UNIVERSIDAD AUTÓNOMA DE MADRID
Facultad de Ciencias
Departamento de Física Teórica

One-dimensional topological insulators in the AIII symmetry class

Memoria de Tesis Doctoral realizada por

Carlos García Velasco

y presentada ante el Departamento de Física Teórica
de la Universidad Autónoma de Madrid
para la obtención del Título de Doctor en Física Teórica.

Tesis Doctoral dirigida por

Belén Paredes Ariza,

Profesora del Arnold Sommerfeld Center for Theoretical Physics,
Ludwig-Maximilians-University Munich.
Profesora honoraria del Departamento de Física Teórica,
Universidad Autónoma de Madrid.

Madrid, julio de 2019

Universidad Autónoma
de Madrid

Contents

List of Figures

Purpose and motivation

The phenomenon of fractionalization was first studied in the context of quantum field theory [1, 2]. Such phenomenon consists of the emergence of excited states for which the particle number takes fractional values, instead of integers [1, 2, 3, 4]. Despite of being initially a theoretical curiosity, its physical realization in condensed matter systems was found not after a long time. In particular, it is realized by the polyacetylene molecule, which is described by the so-called SSH model [3], as well as by conjugated diatomic polymers [5, 6].

From a condensed matter physics point of view, the phenomenon of fractionalization that occurs in the SSH model is due to the fact that such model is a topological insulator [7, 8]. This means that the energy bands, which determine the relation between the energy and the momentum of the electrons in the system, have topological properties characterized by topological invariants. In particular, the topological nature of a one-dimensional condensed matter system, such as the SSH model, is characterized by the Zak phase [9], which is the Berry phase that particles pick up after completing a closed adiabatic path along the whole first Brillouin zone. A non trivial Zak phase is directly related to the existence of zero energy edge states [10, 11, 12], and these states are in fact the ones that lead to the phenomenon of fractionalization.

The fact that an insulator can exhibit topological features, and thus edge states and fractionalization, depends on its symmetry properties. All topological insulators, together with topological superconductors, are classified in ten different symmetry classes, according to the presence or absence of time reversal symmetry, charge conjugation symmetry, also know as particle-hole symmetry, and chiral symmetry [13, 14, 15]. In the particular case of one-dimensional topological insulators, the presence of chiral symmetry is needed in order for the system to be topologically non-trivial [13, 14, 15]. Such symmetry is the composition of time reversal and charge conjugation symmetries, therefore there are only two possibilities for a one-dimensional topological insulator: either it has also both time reversal and charge conjugation symmetries, or none of them. The first situation corresponds to the BDI (chiral orthogonal) symmetry class, while the second one corresponds to the AIII (chiral unitary) symmetry class. The BDI symmetry class is precisely the one to which the SSH model belongs, so that polyacetylene represents a physical realization of such symmetry class. In contrast, the AIII symmetry class lacks, to our knowledge, experimental realization.

On another note, the development of cold atoms experiments during the last decades [16, 17, 18, 19] allows the realization of condensed matter systems in a well controlled environment, which has led to a great progress in the study, simulation and detection of topological insulators, among many other exotic condensed matter systems and phenomena. For instance, the SSH model has been realized in two occasions in cold atoms experiments, in one of them the non-trivial Zak phase that characterizes its topological nature has been measured [20], while in the other the edge states of the system have been prepared and observed [21]. Nevertheless, the phenomenon of fractionalization has never been directly observed in one-dimensional topological insulators.

All this motivated our purposes for the first part of this thesis. These are the following:

- To propose a particular model for a one-dimensional topological insulator in the AIII symmetry class.
- To identify the properties that characterize topological insulators in the AIII class and distinguish them from the ones in the BDI class.
- To design an experimental protocol for the realization of such model.
- To find a new path towards the observation of the phenomenon of fractionalization in one-dimensional systems.

The fundamental ingredient that a one-dimensional model needs for it to be a topological insulator consists of having more than one site per unit cell. In this way, there is a degree of freedom within each unit cell in the lattice, what leads to an internal structure where symmetry transformations can be defined. That is the case of chiral symmetry, sometimes called sub-lattice symmetry, which is essential for a one-dimensional system to be a topological insulator [14, 15]. The SSH model consists of a one-dimensional dimerized lattice with two alternating different tunnelings amplitudes [3, 12], thus it is a one-dimensional lattice with two sites per unit cell.

This notion of one-dimensional lattice with two sites per unit cell can be generalized to the type of models know as ladder models, in which each leg of a ladder represents each of the two types of sites within each unit cell. The SSH model is a particular case of ladder model; nevertheless, a ladder model is in general more complex and its corresponding Hamiltonian contains terms to which a one-dimensional lattice such as the one of the SSH model cannot lead. Our next purpose is focused on these kind of models, whose higher complexity gives rise to new properties and a larger variety of edge states.

Apart from the SSH model, the only topological ladder models that have been investigated so far are: a generalization of the SSH model that belongs to the AIII class [22], which we have designed during the development of this thesis, and is presented in Part I in this work; the so-called Creutz ladder [23], that belongs

to the BDI class; and two variations of the Creutz ladder [24, 25]. Indeed, to our knowledge, there is no systematic study of topological insulators with ladder structure and many topological ladder models might remain unknown. Neither is there a general analysis that allows us to know, in a methodically way ,which ladder models are topological and which ingredients are necessary for a topological ladder model to be in the BDI class, or in the AIII class. In fact, the AIII class has hardly received attention and still lacks experimental realization. Furthermore, apart from the solitons that appear in the SSH model, edge modes in topological ladders have been barely explicitly discussed and, in addition, it has not been clearly specified what characteristic properties distinguish edge modes in the BDI class from edge modes in the AIII class.

All these motivates a second set of purposes for this thesis. These are:

- To carry out a systematic analysis of ladder models, determining what conditions must a ladder model fulfil in order to be topological, as well as the conditions that it must satisfy for it to belong, on one hand, to the BDI class and, on the other hand, to the AIII class.

- To find all ladder architectures that correspond to a model for a topological insulator.

- To investigate what kind of edge states can be found in a topological ladder model, what are their properties and how do these depend on the symmetry class of the model.

On another note, in the last years ladder systems have become a fruitful medium for investigating topological phases of matter, encouraged by the recent achievements in simulating synthetic dimensions [26, 27] and implementing spin-orbit couplings with ultracold atoms [28, 29, 30]. In particular, this feature allows the realization of artificial gauge fields in ladder architectures exhibiting a wide variety of topological phenomena.

Apart from the SSH model, the ladder systems that have been experimentally realized so far are not topological themselves, as a one-dimensional topological insulator, but show properties that are inherited from a two-dimensional Chern insulator or quantum Hall system [31]. For instance, by combining a superlattice structure together with laser-assisted tunneling [32, 33] the characteristic currents that exist in chiral ladders have been observed [34], which are directly related to the edges of two-dimensional Chern insulators.

Ladder systems can also be realized by simulating a synthetic dimension, corresponding each leg to a different internal atomic degree of freedom. This experimental scheme was exploited for the observation of analogous chiral currents in square ladders under effective magnetic fields [35, 36, 37, 38]. Furthermore, more complicated ladder geometries with diagonal couplings have been recently investigated [24, 39, 40].

All these increases our interest in ladder models, as the experimental techniques developed in the last years facilitate the realization of this kind of models with cold atoms in optical lattices.

Objetivo y motivación

El fenómeno de fraccionalización fue estudiado por primera vez en el contexto de teoría cuántica de campos [1, 2]. Dicho fenómeno consiste en la aparición de estados excitados en los que el número de partículas toma valores fraccionados, en lugar de valores enteros [1, 2, 3, 4]. A pesar de haber surgido como una curiosidad teórica, pronto encontró realización en sistemas de materia condensada. En concreto, en la molécula de poliacetileno, descrita por el conocido modelo SSH [3], así como en polímeros diatómicos conjugados [5, 6].

Alejándonos del contexto de teoría cuántica de campos, y adoptando una visión más propia de la materia condensada, el fenómeno de fraccionalización que tiene lugar en el modelo SSH se debe a que dicho modelo es un aislante topológico [7, 8]. Esto quiere decir que las bandas de energía, que determinan la relación entre la energía y el momento de los electrones del sistema, tienen propiedades topológicas caracterizadas a través de invariantes topológicos. En concreto, la naturaleza topológica de un sistema de materia condensada unidimensional, como lo es el modelo SSH, está caracterizada mediante la fase de Zak [9], que consiste en la fase de Berry que obtiene una partícula tras completar un circuito cerrado adiabático a lo largo de toda la primera zona de Brillouin. Una fase de Zak no trivial está directamente relacionada con la existencia de estados de borde de energía cero [10, 11, 12], y son estos estados los que dan lugar al fenómeno de fraccionalización.

El que un aislante pueda o no tener una naturaleza topológica, y por tanto presentar estados de borde y dar lugar al fenónemo de fraccionalización, depende de sus propiedades de simetría. Todos los aislantes topológicos, junto con los superconductores topológicos, se encuentran clasificados en diez clases de simetría diferentes, según la presencia o ausencia de simetría de inversión temporal, simetría de conjugación de carga, también denominada simetría de partícula-hueco, y simetría quiral [13, 14, 15]. En el caso particular de aislantes topológicos unidimensionales, la presencia de simetría quiral es necesaria para que un sistema tenga una topología no trivial [13, 14, 15]. Dicha simetría es la composición de las simetría de inversión temporal y de conjugación de carga, de modo que solo hay dos posibilidades para un aislante topológico unidimensional: o bien presenta también simetría de inversión temporal y de conjugación de carga, o bien ninguna de las dos. El primer caso se corresponde con la clase de simetría BDI (clase ortogonal quiral), mientras que el segundo con la clase de simetría AIII (clase unitaria quiral). La clase de simetría BDI es precisamente a la que pertenece el modelo SSH, por lo tanto el poliacetileno representa una realización física de dicha clase de simetría. Por el contrario, la clase

de simetría AIII no ha sido realizada en ningún experimento hasta ahora.

Por otra parte, el desarrollo de experimentos con átomos fríos en redes ópticas durante las últimas décadas [16, 17, 18, 19] permite la realización de sistemas de materia condensada en un entorno controlado, lo que ha permitido un gran avance en el estudio, la simulación y la detección de aislantes topológicos, entre otros muchos sistemas y fenómenos exóticos de materia condensada. Por ejemplo, el modelo SSH ha sido realizado en experimentos de átomos fríos en redes ópticas en dos ocasiones, en una de ellas se ha medido la fase de Zak no trivial que caracteriza su naturaleza topológica [20], mientras que en otra los estados de borde del modelo han sido preparados y observados [21]. No obstante, el fenómeno de fraccinalización nunca ha sido observado directamente en aislantes topológicos unidimensionales.

Todo esto motivó nuestros objetivos para la primera parte de la tesis. Estos objetivos son los siguientes:

- Proponer un modelo particular de aislante topológico unidimensional representante de la clase de simetría AIII.

- Identificar las propiedades que caracterizan a los aislantes topológicos en la clase de simetría AIII y permiten diferenciarlos de aquellos en la clase BDI.

- Diseñar un protocolo experimental para la realización de dicho modelo.

- Buscar un nuevo camino para la observación del fenómeno de fraccionalización en sistemas unidimensionales.

La característica fundamental que un modelo unidimensional necesita para poder ser un aislante con una topología no trivial, consiste en tener más de un sitio por celda unidad. De este modo, existe un grado de libertad dentro de cada celda de la red, lo que da lugar a una estructura interna en la cual se pueden definir transformaciones de simetría. Este es el caso de la simetría quiral, denominada también simetría de sub-red, la cual es imprescindible para que un sistema unidimensional sea un aislante topológico [14, 15]. El modelo SSH consiste en una red unidimensional dimerizada en la que dos amplitudes de salto diferentes se alternan [3, 12], por lo tanto, consiste en una red unidimensional con dos sitios por celda unidad.

Esta noción de red unidimensional con dos sitios por celda unidad puede ser generalizada al tipo de modelos conocido como modelos de escalera, en los que cada pata de una escalera se corresponde con uno de los dos sitios de cada celda unidad. El modelo SSH es un caso particular de escalera; sin embargo, un modelo de escalera es en general más complejo y su correspondiente Hamiltoniano contiene términos a los que una red unidimensional como la del modelo SSH no podría dar lugar. Nuestro siguiente objetivo se centra en este tipo de modelos, cuya mayor complejidad da lugar a nuevas propiedades y una mayor diversidad de estados de borde.

Aparte del modelo SSH, solo unos pocos modelos de escalera topológicos han sido investigados: una generalización del modelo SSH que pertenece a la clase AIII [22], que hemos desarrollado durante el desarrollo de esta tesis, y presentamos en la Parte I de este trabajo; la denominada escalera de Creutz [23], que pertenece a

la clase BDI; y dos variaciones de la escalera de Creutz [24, 25]. De hecho, hasta donde conocemos, no existe ningún estudio sistemático de aislantes topológicos con estructura de escalera y muchos modelos topológicos de escalera podrían permanecer desconocidos. Tampoco existe un análisis general que permita conocer de manera metódica qué modelos de escaleras son topológicos, y qué ingredientes son necesarios para que un modelo de escalera topológico pertenezca, bien, a la clase BDI o, bien, a la clase AIII. En realidad, la clase AIII no ha recibido apenas atención y sigue sin haber sido realizada en experimentos. Más aún, aparte de los solitones que aparecen en el modelo SSH, los estados de borde de modelos topológicos de escalera han sido escasamente estudiados de manera explícita y no ha sido especificado claramente qué propiedades características diferencian a los estados de borde en la clase BDI de aquellos en la clase AIII.

Todo esto motiva un segundo conjunto de objetivos para esta tesis. Estos son:

- Llevar a cabo un análisis sistemático de los modelos de escalera y determinar qué condiciones debe cumplir un modelo para ser topológico, así como las condiciones que debe satisfacer para pertenecer, por un lado, a la clase BDI, y, por otro lado, a la clase AIII.

- Utilizar los resultados del punto anterior para encontrar todas las arquitecturas de escalera que dan lugar a un modelo de aislante topológico.

- Conocer los estados de borde a los que un modelo de escalera topológico puede dar lugar, cuáles son sus propiedades, y cómo estas se ven afectadas por la clase de simetría del modelo.

Por otro lado, en los últimos años, los sistemas de escalera se han convertido en un medio fructífero para investigar fases topológicas de la materia, fomentados por los logros recientes en la simulación de dimensiones sintéticas [26, 27], y en la implementación de acoplo espín-órbita en experimentos de átomos fríos [28, 29, 30]. En particular, estas técnicas permiten la realización de campos gauge artificiales en arquitecturas de escalera exhibiendo una amplia variedad de fenómenos topológicos.

Además del modelo SSH, los modelos de escalera que han sido realizados experimentalmente hasta ahora no son topológicos en sí mismos, como sistemas unidimensionales, sino que muestran propiedades heredadas de aislantes topológicos bidimensionales o sistemas de efecto Hall cuántico [31]. Por ejemplo, mediante la combinación de una estructura de super-red con acoplo asistido por láser [32, 33], las corrientes características que existen en escaleras quirales han sido observadas [34], las cuales están directamente relacionadas con los estados de borde de aislantes topológicos de Chern bidimensionales.

Los modelos de escalera también pueden ser realizados mediante la simulación de una dimensión sintética, correspondiendo cada pata de la escalera a un grado de libertad atómico interno diferente. Este mecanismo ha sido usado para la observación de corrientes quirales análogas en sistemas de escalera cuadrada sometidos a campos magnéticos efectivos [35, 36, 37, 38]. Además, otras geometrías de escalera más complicadas, con acoplos diagonales, han sido recientemente investigadas [24, 39, 40].

Todo esto aumenta más, si cabe, nuestro interés en los modeles de escalera, ya que las técnicas experimentales desarrolladas en los últimos años permiten la realización de este tipo de modelos en experimentos de átomos fríos en redes ópticas.

Outline

This thesis is structured in four main parts.

Part I es dedicated to the first issues we want to address in this work, namely: proposing a model for a one-dimensional topological insulator in the AIII symmetry class, finding its characteristic properties that distinguish it from a model in the BDI class, and designing an experimental scheme for its physical realization. We present a generalization of the SSH model in the AIII class and show how the different symmetry class is manifested through the momentum of the zero energy edge states. In this way we analyse not only their spatial localization at the edges of the system, but also their momentum, which can be at the same time well defined. In consequence, we find out that the phenomenon of fractionalization occurs also in momentum space, what opens new detection possibilities. Finally, we show how our model can be realized in cold atoms experiments using currently available techniques.

Motivated by the results we obtained in Part I, we developed a quench protocol that exploits the simultaneous good definition of the edge states position and momentum and leads to an interference of fractionalized quasiparticles. The quench consists of changing the Hamiltonian parameters so that the system is taken to its critical point. In this situation the energy bands of the system cross each other at a critical momentum, around which the dispersion relation is almost linear. This, combined with the edge states momentum properties, makes them propagate along the system, while preserving their identity of fractionalized quasiparticles.

In Part III we develop an exhaustive analysis of topological two leg ladder models. We obtain the general form of a topological ladder Hamiltonian in the BDI class, as well as in the AIII class. We analyse the structure of these general Hamiltonians and classify all topological ladder models into six types, being three of them in the BDI class and the other three in the AIII class. We show how all topological ladder models can be obtained by performing a unitary transformation onto a canonical ladder model. By using this canonical ladder model we obtain the edge states wave functions of a any topological ladder model, and characterize each of the six types of topological ladder models through the edge states momentum distribution. Finally, we present all different ladder architectures that lead to a topological model.

In Part IV we study in more detail one of the topological ladder models we presented in Part III. In particular, we analyse the edge states dynamics after a quench to the critical point, and how they depend on the symmetry class of the model. The combination of the good definition of the edge states position and momentum, together with the presence of an effective magnetic field, that makes the system belong to the AIII class, results in the emergence of protected chiral currents.

Preliminaries: Symmetry classes of one-dimensional topological insulators

Topological insulators are classified according to their symmetry properties under time reversal, charge conjugation and chiral transformations [13, 14, 15]. In one dimension, the presence or absence of chiral symmetry determines completely the topological or trivial character of an insulator. Since chiral symmetry is the composition of time reversal and charge conjugation symmetries, thus either both time reversal and charge conjugation symmetries are present or none of them is. These two cases correspond, respectively, to the two distinct symmetry classes of one-dimensional topological insulators: the BDI class and the AIII class (see Fig. 1).

	TR	CC	Chiral	Symmetry Class
Trivial Insulator	-	-	**0**	-
Topological Insulator	**1**	**1**	**1**	**BDI**
Topological Insulator	**0**	**0**	**1**	**AIII**

Figure 1: **Topological classes of 1D insulators.** Symmetry classes for one-dimensional insulators according to the presence (1) or absence (0) of time reversal (TR), charge conjugation (CC) and chiral symmetries.

We consider a Hamiltonian H for a one-dimensional non-interacting topological insulator with translational invariance. This system can be illustrated as a ladder with a leg for each different type of site per unit cell, where every hopping term is represented by a line (see. Fig. 2). The translational invariance allows us to write the Hamiltonian using the momentum representation as:

$$H = -\sum_k \psi_k^\dagger \, M(k) \, \psi_k, \tag{1}$$

being $\psi_k^\dagger$ a vector that contains all creation modes with Bloch momentum k, $\psi_k^\dagger = (\hat{a}_k^\dagger \quad \hat{b}_k^\dagger \ldots)$, and $M(k)$ a hermitian matrix called the *Hamiltonian matrix*.

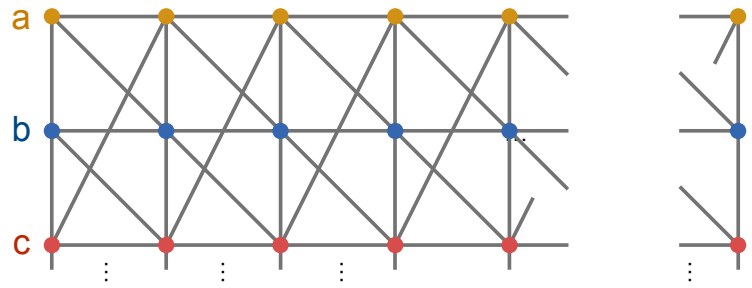

Figure 2: **1D topological insulator.** A model for a 1D topological insulator with translational invariance can be represented as a ladder in which each leg corresponds to a different type of site within every unit cell.

In this context time reversal, charge conjugation and chiral symmetries are transformations acting on the spinor ψ_k that produce a particular change in the Hamiltonian. Time reversal symmetry is an antiunitary transformation $\mathcal{T}$ that leaves the Hamiltonian invariant, charge conjugation symmetry is an antinunitary transformation $\mathcal{C}$ under which the Hamiltonian changes its sign and, finally, chiral symmetry is a unitary transformation $\mathcal{S}$ that changes the sign of the Hamiltonian. That is:

$$\begin{aligned}
&\text{Time reversal:} && \mathcal{T}\,\psi_k = U_T\,(\psi_k)^*, && \mathcal{T}H\mathcal{T}^{-1} = H && (2)\\
&\text{Charge conjugation:} && \mathcal{C}\,\psi_k = U_C\,(\psi_k)^*, && \mathcal{C}H\mathcal{C}^{-1} = -H && (3)\\
&\text{Chiral:} && \mathcal{S}\,\psi_k = U_S\,\psi_k, && \mathcal{S}H\mathcal{S}^{-1} = -H. && (4)
\end{aligned}$$

Where U_T, U_C and U_S are unitary constant matrices. Therefore, time reversal symmetry implies that the eigenstates of the Hamiltonian come in pairs with the same energy but opposite momenta, charge conjugation symmetry implies that they come in pairs with opposite energies and momenta, and finally chiral symmetry implies that they come in pairs with opposite energies and same momentum.

From Eq. (1) it follows that these symmetry operations acting on the Hamiltonian are equivalent to a transformation of the Hamiltonian matrix. Therefore, the conditions for time reversal, charge conjugation and chiral symmetry can be expressed as:

$$\begin{aligned}
&\text{Time reversal:} && \exists\, U_T \,|\quad U_T\,M^*(-k)\,U_T^\dagger = M(k) && (5)\\
&\text{Charge conjugation:} && \exists\, U_C \,|\quad U_C\,M^*(-k)\,U_C^\dagger = -M(k) && (6)\\
&\text{Chiral:} && \exists\, U_S \,|\quad U_S\,M(k)\,U_S^\dagger = -M(k), && (7)
\end{aligned}$$

being U_T, U_C and U_S unitary matrices with no dependence on the momentum.

Part I

Realizing and detecting a topological insulator in the AIII symmetry class

Chapter 1

A model for an AIII topological insulator

1.1 Hamiltonian of the model

Our model for a topological insulator in the AIII symmetry class consists of a dimerized one-dimensional lattice with two different sites per unit cell and two distinct coupling terms. The two hopping amplitudes are J' and $Je^{i\delta}$, being one of them complex so that particles pick up a phase δ when traveling from one unit cell to the next one (Fig. 1.1). This model is described by the following tight-binding Hamiltonian:

$$H_\delta = -\sum_{n}^{N} \left(J' \, \hat{a}_n^\dagger \hat{b}_n + J e^{i\delta} \, \hat{a}_{n+1}^\dagger \hat{b}_n + \text{H.c.} \right), \tag{1.1}$$

being $\hat{a}_n^\dagger$ and $\hat{b}_n^\dagger$ the creation operators of a particle at the sublattice site a_n and b_n, respectively, in the n-th unit cell, and N the total number of unit cells in the lattice.

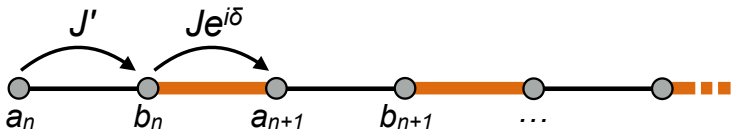

Figure 1.1: **The model.** Schematic illustration of our model for a topological insulator in the AIII class: a one-dimensional dimerized lattice with two different sites per unit cell, a and b, and two tunneling amplitudes J' and $Je^{i\delta}$. Particles pick up a phase δ when travelling from one sublattice site to the same sublattice site in the following lattice cell.

This model is a generalization of the SSH model [3, 12]. In the particular case in which $\delta = 0$ our model becomes the SSH model. As we will show throughout this part of the thesis, the presence of the phase δ is sufficient to:

i) break time reversal and charge conjugation symmetries and, therefore, make the model be a realization of the AIII symmetry class;

ii) make the symmetry protected zero modes that the model exhibits in its topological phase under open boundary conditions have different properties from those present in the case in which $\delta = 0$;

iii) allow the development of an alternative way of observing the phenomenon of fractionalization, in momentum space ,which would not be possible in the BDI class.

1.2 Symmetries of the model

In order to know what are the symmetry properties of the Hamiltonian, we exploit its translational invariance and write it in the momentum representation. The Bloch modes $\hat{a}_k^\dagger$ and $\hat{b}_k^\dagger$, which constitute the momentum basis, are defined from the position basis as:

$$\hat{a}_k^\dagger = \frac{1}{\sqrt{N}} \sum_{n=1}^{N} e^{ikn}\, \hat{a}_n^\dagger \tag{1.2}$$

$$\hat{b}_k^\dagger = \frac{1}{\sqrt{N}} \sum_{n=1}^{N} e^{ikn}\, \hat{b}_n^\dagger, \tag{1.3}$$

being the momentum k quantized as $k = 2\pi m/N$, with $m \in \mathbb{Z}$, and having set the lattice constant to the unit. The Hamiltonian of the system under periodic boundary conditions can be written as:

$$H_\delta = -\sum_k \hat{\psi}_k^\dagger\, M_\delta(k)\, \hat{\psi}_k, \tag{1.4}$$

where $\hat{\psi}_k^\dagger = \begin{pmatrix} \hat{a}_k^\dagger & \hat{b}_k^\dagger \end{pmatrix}$ and being $M_\delta(k)$ the so-called Hamiltonian matrix, which depends on the momentum and takes the form:

$$M_\delta(k) = \left[J' + J\cos(k-\delta)\right]\sigma_x + J\sin(k-\delta)\,\sigma_y. \tag{1.5}$$

Once we know the Hamiltonian matrix of the model, it is straightforward to obtain the symmetry properties of the system. These are the following:

i) Chiral symmetry.

The condition that the Hamiltonian matrix needs to fulfil for the model to present chiral symmetry is that $U_S M_\delta(k) U_S^\dagger = -M_\delta(k)$ for some unitary transformation U_S, called the chiral operator, which does not depend on the momentum (this transformation acts on the space spanned by the two sublattice sites and consists of the

same transformation on every cell in the lattice). By looking at the Hamiltonian matrix, Eq. (1.5), we conclude that the model has always chiral symmetry, for every possible parameter configuration, as it consists of a linear superposition of the two Pauli matrices σ_x and σ_y and thus:

$$\sigma_z M_\delta(k)\sigma_z = -M_\delta(k), \tag{1.6}$$

so that the chiral operator is $U_S = \sigma_z$.

ii) Time reversal and charge conjugation symmetries.

Chiral symmetry is the composition of time reversal and charge conjugation symmetries and our model is always chiral symmetric. Therefore, the condition for time reversal symmetry is all we need to analyse in order to know weather the Hamiltonian exhibits both time reversal and charge conjugation symmetries or none of them. That condition is $U_T M_\delta^*(-k)U_T^\dagger = M_\delta(k)$ for some unitary operator U_T with no dependence on the momentum. In the particular case in which $\delta = 0$ or $\delta = \pi$ the Hamiltonian matrix is such that:

$$M_0^*(-k) = M_0(k), \tag{1.7}$$

and therefore the model is both time reversal and charge conjugation symmetric. These two parameter configurations, $\delta = 0$ and $\delta = \pi$, belong then to the BDI symmetry class [see Fig. 1.2(a)].

On the contrary, in the more general situation in which $\delta \neq 0, \pi$, the model presents neither time reversal symmetry nor charge conjugation symmetry. We have that:

$$\begin{aligned} M_\delta^*(-k) = \begin{pmatrix} 0 & J' + Je^{-i(k+\delta)} \\ J' + Je^{i(k+\delta)} & 0 \end{pmatrix} \neq \\ \neq \begin{pmatrix} 0 & J' + Je^{-i(k-\delta)} \\ J' + Je^{i(k-\delta)} & 0 \end{pmatrix} = M_\delta(k), \end{aligned} \tag{1.8}$$

and there is no unitary matrix U_T such that:

$$U_T M_\delta^*(-k)U_T^\dagger = M_\delta(k). \tag{1.9}$$

In case such unitary transformation existed, it would be necessarily a rotation around the z-axis, as any other unitary operator would add a component proportional to σ_z to the Hamiltonian matrix. A rotation $R_z(\theta)$ of an arbitrary angle θ around the z-axis transforms $M_\delta^*(-k)$ in the following way:

$$\begin{aligned} R_z(\theta)M_\delta^*(-k)R_z^\dagger(\theta) = \begin{pmatrix} 0 & e^{i\theta}\left[J' + Je^{-i(k+\delta)}\right] \\ e^{-i\theta}\left[J' + Je^{i(k+\delta)}\right] & 0 \end{pmatrix} \neq \\ \neq \begin{pmatrix} 0 & J' + Je^{-i(k-\delta)} \\ J' + Je^{i(k-\delta)} & 0 \end{pmatrix} = M_\delta(k). \end{aligned} \tag{1.10}$$

(a)				
δ = 0, π	TIME REVERSAL	$M_0^*(-k) = M_0(k)$	1	**BDI Symmetry Class**
	CHARGE CONJUGATION	$\sigma_z M_0^*(-k)\sigma_z = -M_0(k)$	1	
	CHIRAL SYMMETRY	$\sigma_z M_0(k)\sigma_z = -M_0(k)$	1	

(b)				
δ ≠ 0, π	TIME REVERSAL	$\nexists U_T \mid \quad U_T M_\delta^*(-k)U_T^\dagger = M_\delta(k)$	0	**AIII Symmetry Class**
	CHARGE CONJUGATION	$\nexists U_C \mid \quad U_C M_\delta^*(-k)U_C^\dagger = -M_\delta(k)$	0	
	CHIRAL SYMMETRY	$\sigma_z M_\delta(k)\sigma_z = -M_\delta(k)$	1	

Figure 1.2: **Symmetry class of the model.** Presence (1) or absence (0) of time reversal, charge conjugation and chiral symmetries in our model. (a) On one hand, for $\delta = 0$ or $\delta = \pi$ (cases in which our model becomes the SSH model), the system has chiral, time reversal and charge conjugation symmetries and thus belongs to the BDI class. (b) On the other hand, for $\delta \neq 0, \pi$, the model breaks both time reversal and charge conjugation symmetries while it remains chiral symmetric. Consequently, it is a realization of the AIII class.

As we see, there is no unitary matrix U_T able to fulfil the time reversal symmetry condition. As a result, the presence of a phase $\delta \neq 0, \pi$ breaks both time reversal and charge conjugation symmetries, while keeping chiral symmetry, and thus makes the model belong to the AIII class [see Fig. 1.2(b)].

1.3 Topological nature of the model

The topological nature of the model is characterized through the Zak phase, which is the Berry phase that particles pick up when they complete an adiabatic path across the first Brillouin zone [9]. The Zak phase can be computed as:

$$\mathcal{Z} = -i \oint_{1^{st}\mathcal{BZ}} dk \, \langle k, \delta|_\pm \, \partial_k \, |k, \delta\rangle_\pm, \tag{1.11}$$

where $|k, \delta\rangle_\pm$ are the Bloch eigenstates of the Hamiltonian, that is, the eigenstates for periodic boundary conditions. Therefore, in order to calculate the Zak phase, we first need to obtain the Bloch eigenstates of the Hamiltonian. For that, we consider the Hamiltonian matrix, Eq. (1.5), and write it in the following form:

$$M_\delta(k) = M_0(k - \delta), \tag{1.12}$$

with:

$$M_0(k) = \rho(k)\, \boldsymbol{n}(k) \cdot \boldsymbol{\sigma}, \tag{1.13}$$

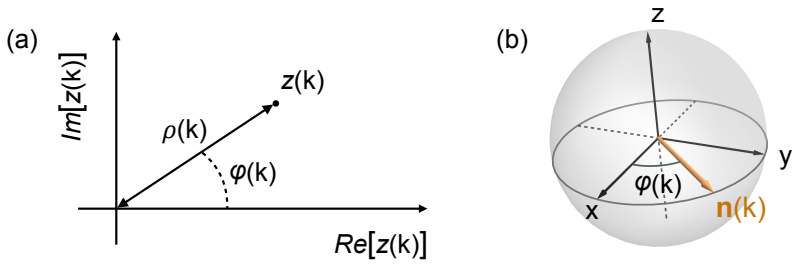

Figure 1.3: **Hamiltonian matrix and isospin.** (a) The Hamiltonian matrix is completely characterized by two functions: $\rho(k)$ and $\varphi(k)$, which are the modulus and argument of the complex function $z(k)$. On one hand, the function $\rho(k)$ determines the two energy bands of the system as $E_\pm(k) = \mp\rho(k-\delta)$. On the other hand, the function $\varphi(k)$ defines a unit vector $\boldsymbol{n}(k)$ that characterizes, through the Bloch sphere representation, the superposition state between the modes $\hat{a}_k^\dagger$ and $\hat{b}_k^\dagger$ that constitutes an eigenstate of the Hamiltonian.

being $\boldsymbol{\sigma}$ a vector containing the three Pauli matrices, and:

$$\rho(k) = \sqrt{J^2 + J'^2 + 2JJ'\cos k}, \tag{1.14}$$

$$\boldsymbol{n}(k) = \cos\varphi(k)\,\hat{x} + \sin\varphi(k)\,\hat{y}, \tag{1.15}$$

where $\varphi(k) = \arg(J' + Je^{ik})$. That is, the Hamiltonian matrix is characterized by the two functions $\rho(k)$ and $\varphi(k)$, which are the modulus and argument of the complex number $z(k) = J' + Je^{ik}$ [see Fig. 1.3(a)]. The angle $\varphi(k)$ corresponds to the azimuthal angle in spherical coordinates of the unit vector $\boldsymbol{n}(k)$ in the three-dimensional space [see Fig. 1.3(b)].

Decomposing the Hamiltonian matrix in this way is really convenient, as its eigenvectors can be easily obtained from the vector $\boldsymbol{n}(k)$ through the Bloch sphere representation. That is, for a particular value of the momentum k the Hamiltonian matrix has two eigenvectors $\hat{n}_\pm(k)$, with eigenvalues $\pm\rho(k)$, which correspond to the vectors $\pm\boldsymbol{n}(k)$ in the Bloch sphere representation:

$$\pm\boldsymbol{n}(k) = \cos\varphi(k)\,\hat{x} + \sin\varphi(k)\,\hat{y} \quad \longrightarrow \quad \hat{n}_\pm(k) = \frac{1}{\sqrt{2}}\begin{pmatrix} 1 \\ \pm e^{i\varphi(k)} \end{pmatrix}. \tag{1.16}$$

The eigenstates of the Hamiltonian are then obtained from the eigenvectors of the Hamiltonian matrix and the two-component momentum creation operator:

$$|k,\delta\rangle_\pm = \hat{\psi}_k^\dagger\,\hat{n}_\pm(k-\delta)\,|0\rangle = \frac{1}{\sqrt{2}}\left(\hat{a}_k^\dagger \pm e^{i\varphi(k-\delta)}\,\hat{b}_k^\dagger\right)|0\rangle\,, \tag{1.17}$$

with energies $E_\pm(k) = \mp\rho(k-\delta)$. Substituting these eigenstates in Eq. (1.11) we can compute the Zak phase:

$$\mathcal{Z} = \frac{1}{2}\oint_{1^{st}\mathcal{BZ}} dk\,\frac{d\varphi}{dk} = \frac{\Delta\varphi}{2} = \begin{cases} 0 & \text{(for winding number 0)} \\ \pi & \text{(for winding number 1).} \end{cases} \tag{1.18}$$

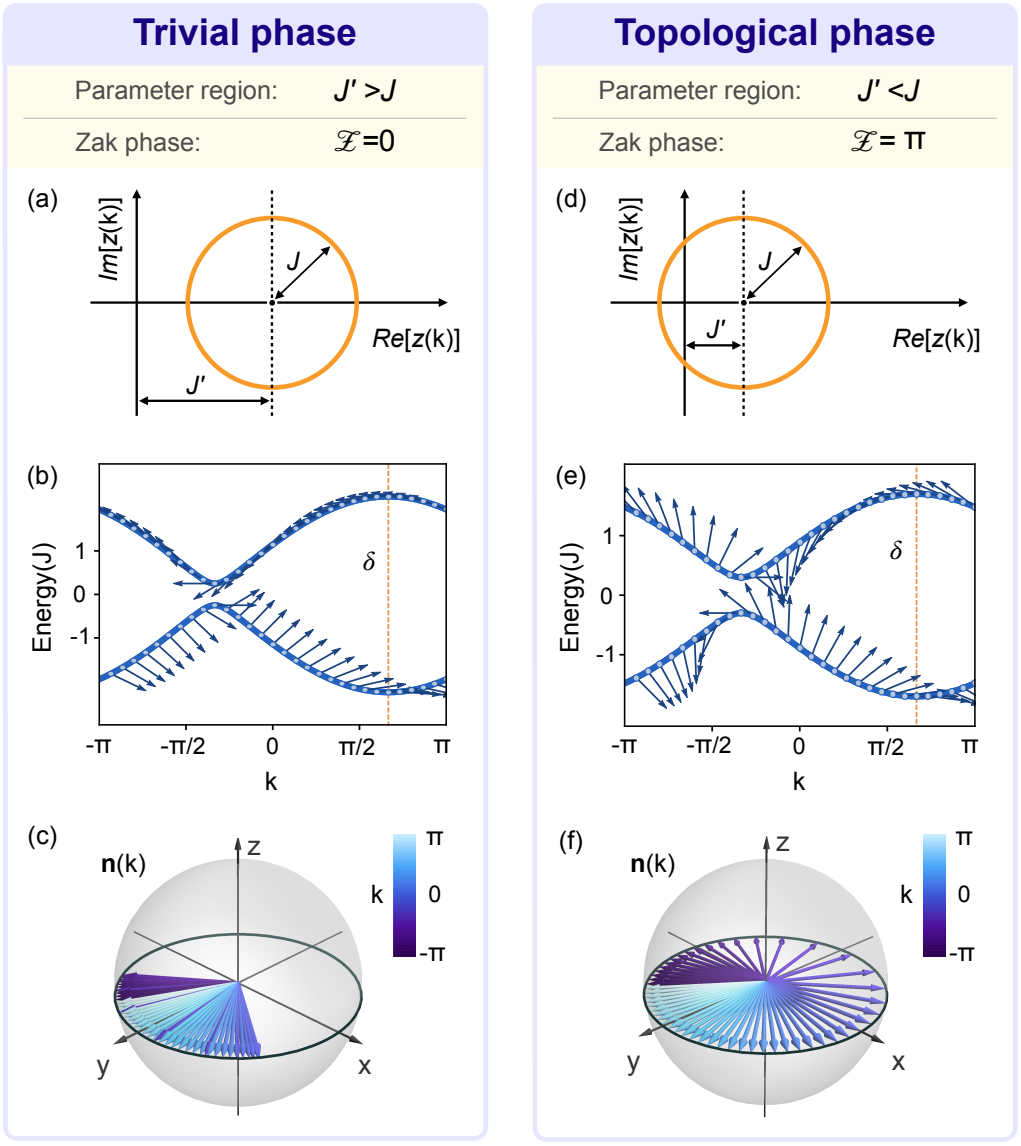

Figure 1.4: **Trivial and topological phases.** Plot of $z(k)$, the energy bands and the isospin vector $\boldsymbol{n}(k)$ in the trivial phase, (a), (b) and (c), and in the topological phase (d), (e) and (f). In the trivial phase, when $J' > J$, the circle that describes the function $z(k)$ does not enclose the origin and, thus, the winding number of the vector $\boldsymbol{n}(k)$ on the xy-plane is 0. On the contrary, in the topological phase, when $J' < J$, the circle described by $z(k)$ encloses the origin and, equivalently, the isospin vector has winding number 1.

As we see, the Zak phase is quantized according to the winding number of the vector $\boldsymbol{n}(k)$ in the xy-plane as the momentum runs over the first Brillouin zone or, equivalently, according to the winding number of $z(k)$ in the complex plane. In this way, the system can be found to be in two distinct topological phases: on one hand, a topologically trivial phase characterized by a Zak phase $\mathcal{Z} = 0$, and on the other hand, a topologically nontrivial phase characterized by a Zak phase $\mathcal{Z} = \pi$.

The complex function $z(k)$ describes a circle of radius J centred at the point $(J', 0)$. Therefore, the system is in its topological phase for $J' < J$, whereas the trivial phase corresponds to $J' > J$, being both phases separated by the critical point $J' = J$ (see Fig. 1.4). To be more precise, the exact values of the Zak phase depends on our definition of the unit cell [20]. The important aspect about the Zak phase is the fact that it is quantized, corresponding each of the two possible values to a distinct topological class distinguished by a different winding number of $z(k)$ and $\boldsymbol{n}(k)$. It is the difference between the Zak phase in the trivial phase and the Zak phase in the topological phase what constitutes an invariant quantity that characterizes the topological nature of the system. Nevertheless, for the sake of simplicity, we use in this work the values $\mathcal{Z} = 0$ and $\mathcal{Z} = \pi$ for the Zak phase in the trivial and topological phases, respectively.

1.4 Analysis of the phase δ

As we have already proved, the presence of a phase δ in one of the two hopping terms in a dimerized lattice model is sufficient to produce the breaking of time reversal and charge conjugation symmetries and, thus, make the model belong to the AIII symmetry class. We obtained this result after following the simplest and more direct procedure, which consists of analysing the condition that the Hamiltonian matrix needs to fulfil for the Hamiltonian to present chiral, time reversal and charge conjugation symmetries.

Nevertheless, it might seem surprising that just a simple phase is all we need in order to get a realization of a distinct class of topological insulators, characterized by different symmetry properties, as we are dealing with a one-dimensional system and one could think that any phase can be removed by means of gauge transformations and, therefore, conclude that all possible phases are irrelevant.

For this reason, we dedicate this section to show a detailed and profound analysis of the role that such phase plays in our model. We provide several ways to realize how relevant the phase δ is and why it is directly related to the breaking of time reversal and charge conjugation symmetries.

1.4.1 Momentum-isospin correspondence

The phase δ has direct implications in the correspondence, established by the Hamiltonian matrix, between the two characteristic physical magnitudes associated to each eigenmode of the system for periodic boundary conditions. These magnitudes are, on one hand, the momentum and, on the other, the isospin vector corresponding to the two-level quantum system formed by the two different sublattice sites.

Momentum shift in a simple lattice

In order to understand the relation between these two physical quantities and the phase δ, we first analyse a more simple model. We consider a one-dimensional

lattice with just one single site per unit cell, that is, the simplest lattice model we can imagine. The Hamiltonian for such lattice model is:

$$H_{\mathrm{s}} = -\sum_{n=1}^{N} \left(t\, \hat{a}_{n+1}^{\dagger} \hat{a}_n + \mathrm{H.c.} \right), \tag{1.19}$$

where t is a real first-neighbour hopping amplitude. If we write the Hamiltonian using the momentum representation we obtain directly its spectral decomposition:

$$H_{\mathrm{s}} = -\sum_{k} 2t \cos k\, \hat{a}_k^{\dagger} \hat{a}_k, \tag{1.20}$$

from which we can identify the eigenstates of the Hamiltonian: $|k\rangle = \hat{a}_k^{\dagger} |0\rangle$. They fulfil the eigenvalue equation:

$$H_{\mathrm{s}} |k\rangle = -2t \cos k\, |k\rangle\,, \tag{1.21}$$

so that the energy associated to the eigenstate $|k\rangle$ is given by the function $E_{\mathrm{s}}(k) = -2t \cos k$.

We know consider another Hamiltonian, which is the result of adding a phase α to every hopping term in the previous model. That is:

$$H_{\mathrm{s}}(\alpha) = -\sum_{n=1}^{N} \left(t e^{i\alpha}\, \hat{a}_{n+1}^{\dagger} \hat{a}_n + \mathrm{H.c.} \right). \tag{1.22}$$

In the momentum basis this new Hamiltonian takes the following form:

$$H_{\mathrm{s}}(\alpha) = -\sum_{k} 2t \cos(k - \alpha)\, \hat{a}_k^{\dagger} \hat{a}_k, \tag{1.23}$$

and, therefore, the states $|k\rangle$,which are the eigenstates of $H_{\mathrm{s}}(\alpha = 0)$, are also eigenstates of the new Hamiltonian for any value that the phase α can take. However, the energy associated to the eigenstate $|k\rangle$ is given by $E_{\mathrm{s}}(k - \alpha)$, as we have that:

$$H_{\mathrm{s}}(\alpha) |k\rangle = E_{\mathrm{s}}(k - \alpha) |k\rangle\,. \tag{1.24}$$

In this way, we can say that a shift in the momentum has been introduced in the Hamiltonian by adding a phase to the hopping terms, that is, by making them complex. It is important to remark that the eigenstates of the Hamiltonian are the same for any value of α. The only thing that depends on such phase is the energy associated to each eigenstate, in such a way that the dispersion relation is the one corresponding to the Hamiltonian with no phase α, but shifted with respect to the momentum by α.

Let us consider the eigenstates $|k\rangle$ of the Hamiltonian with no phase α and perform a momentum relabelling so that we obtain the states $|k - \alpha\rangle$. In general these new states are not eigenstates of the Hamiltonian for any value of α, because

the value of the shifted momentum $k-\alpha$ will not coincide with any of the quantized values of the momentum that form the orthogonal basis $\{|k_n\rangle\}_{n=1}^{N}$, with $k_n = 2\pi n/N$ and $n \in \mathbb{Z}$. Only when $\alpha = 2\pi m/N$, with $m \in \mathbb{Z}$, will the new states still be eigenstates of the Hamiltonian; which is due to the fact that, in that case, the momentum relabelling produces just a rearrangement of the set of eigenstates.

As we see, relabelling the eigenstates is not equivalent to making a shift in the momentum. A genuine shift in the momentum has to be implemented by adding the same phase to all coupling amplitudes in the model. Why is that? What do we mean when we say that a particle occupies a wave function with a certain well-defined linear momentum? We mean that, when we perform a translation in space along a certain direction, this wave function transforms into itself times a complex phase proportional to the translated distance and being the proportionality constant precisely the value of its linear momentum along that particular direction. In other words, the momentum is the generator of the group of translations in space and, thus, a well defined momentum is a consequence of having translational symmetry in space. In the particular case of a system in the lattice, only those translations given by a lattice vector leave the system invariant and, thus, are symmetries. Therefore, the momentum of a particle is the phase that its wave function picks up when a translation of one unit cell is performed, since the momentum, called in this context quaismomentum, is the generator of this discrete group of translations. That is the reason why adding a phase α to all coupling terms in the simple lattice model H_{texts} produces a shift in the momentum.

Momentum shift in a dimerized lattice

On the contrary, in the case of our AIII model things are different due to the fact that it consists of a dimerized lattice and not a simple one.

We start by considering the model with no phase δ, that is the SSH model, whose Hamiltonian is:

$$H_{\delta=0} = -\sum_k \hat{\psi}_k^\dagger \, M_0(k) \, \hat{\psi}_k. \tag{1.25}$$

The eigenstates of this Hamiltonian are made from two quantities. On one hand $\hat{\psi}_k^\dagger$, a two-component creation operator with a particular momentum k. On the other hand $\hat{n}_\pm(k)$, a two-component complex vector that depends on the momentum and determines the superposition state between the modes $\hat{a}_k^\dagger$ and $\hat{b}_k^\dagger$ that constitutes an eigenstate of the Hamiltonian. This vector corresponds, through the Bloch sphere representation, to a unit vector $\pm\boldsymbol{n}(k)$ in the three-dimensional real space, which is determined by the Hamiltonian matrix when we write it as:

$$M_0(k) = \rho(k)\, \boldsymbol{n}(k) \cdot \sigma, \tag{1.26}$$

The two eigenvectors of the Hamiltonian matrix, for a particular momentum value k, are precisely $\hat{n}_\pm(k)$ with energies $\pm\rho(k)$, that is:

$$M_0(k)\, \hat{n}_\pm(k) = \pm\rho(k)\, \hat{n}_\pm(k). \tag{1.27}$$

Therefore, the eigenstates of the Hamiltonian $H_{\delta=0}$ for periodic boundary conditions are:

$$|k, \delta = 0\rangle_{\pm} = \hat{\psi}_k^{\dagger}\, \hat{n}_{\pm}(k)\, |0\rangle\,, \tag{1.28}$$

with energies $\mp\rho(k)$.

What happens if we introduce a non-zero phase δ to the model? In that case the Hamiltonian written in the momentum representation would be:

$$H_{\delta} = -\sum_{k} \hat{\psi}_k^{\dagger}\, M_{\delta}(k)\, \hat{\psi}_k = -\sum_{k} \hat{\psi}_k^{\dagger}\, M_0(k-\delta)\, \hat{\psi}_k. \tag{1.29}$$

If we apply it onto an eigenstate of the former Hamiltonian, $H_{\delta=0}$, we get:

$$H_{\delta}\, |k, 0\rangle_{\pm} = -\sum_{q} \hat{\psi}_q^{\dagger}\, M_0(q-\delta)\, \hat{\psi}_q\, \hat{\psi}_k^{\dagger}\, \hat{n}_{\pm}(k)\, |0\rangle = -\hat{\psi}_k^{\dagger}\, M_0(k-\delta)\, \hat{n}_{\pm}(k)\, |0\rangle\,. \tag{1.30}$$

As we see, the Hamiltonian matrix is evaluated at the momentum value $k-\delta$, whereas the isospin vector is evaluated at k. In order to satisfy the eigenvector equation, both need to be evaluated at the same momentum value. Therefore, the states $|k, 0\rangle_{\pm}$, which are the eigenstates of the Hamiltonian with no phase δ, are no longer eigenstates of the Hamiltonian once the phase δ has been added. This is due to the fact that the Hamiltonian has an internal structure corresponding to the two-level system that constitute the two sites within each unit cell.

In the case of a simple chain, the momentum is the only magnitud that constitutes each eigenstate. Therefore, if a certain state has the appropriate momentum value, i.e. one of the momentum values that form the momentum basis, it will always be an eigenstate of the system, being its corresponding energy the only quantity that depends on the phase α.

On the contrary, in the case of a dimerized lattice there are two physical magnitudes associated to each eigenstate: the momentum and the isospin vector. Having the appropriate momentum value is not enough for a state to be an eigenstate of the Hamiltonian. In addition, the correspondence between its momentum and its isospin vector has to be the same as the one in the Hamiltonian. That is, if there is a phase δ in the model, the Hamiltonian shows a shift in the momentum-isospin correspondence, as the Hamiltonian matrix is evaluated at the momentum value $k-\delta$, whereas the creation and annihilation operators correspond to a momentum value k [see Eq. (1.29)]. As a consequence, the eigenstates of such Hamiltonian must have the same shift between its momentum and isospin in order to be truly eigenstates. The eigenstates of H_{δ} are then:

$$|k, \delta\rangle_{\pm} = \hat{\psi}_k^{\dagger}\, \hat{n}_{\pm}(k-\delta)\, |0\rangle\,, \tag{1.31}$$

and are such that: $H_{\delta}\, |k, \delta\rangle_{\pm} = \mp\rho(k-\delta)\, |k, \delta\rangle_{\pm}$. These states are genuinely different from the eigenstates of $H_{\delta=0}$, and cannot be obtained from them by making a relabelling of the momentum. If we consider an eigenstate of $H_{\delta=0}$, $|k, \delta = 0\rangle_{\pm}$, and just evaluate it at a different momentum $k-\delta$, we will get $|k-\delta, \delta = 0\rangle_{\pm}$. This new state

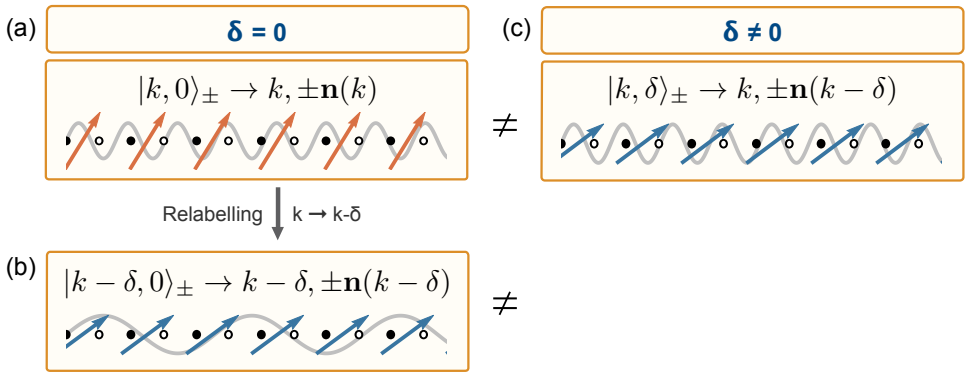

Figure 1.5: **Momentum-isospin correspondence.** (a) The eigenstates of the Hamiltonian $H_{\delta=0}$ are characterized by a momentum k and an isospin vector $\boldsymbol{n}(k)$. (b) Relabelling the momentum of such states gives us a new set of states, with momentum $k-\delta$ and isospin vector $\boldsymbol{n}(k-\delta)$, however the relation between these two magnitudes remains the same. (c) The eigenstates of the Hamiltonian H_δ are characterized by a momentum k and an isospin vector $\boldsymbol{n}(k-\delta)$, what makes them be genuinely different from those eigenstates of $H_{\delta=0}$ (and any relabelling of such states), as they show a distinct momentum-isospin correspondence.

will not be an eigenstate of H_δ, as they do not share the same momentum-isospin correspondence (see Fig. 1.5).

What is the reason for this behavior? It is due to the fact that in a dimerized lattice a shift in the momentum is nothing trivial. In order to perform a shift in the momentum, as in any lattice with a discrete translational symmetry, we need to implement a phase that particles pick up when traveling from one unit cell to the next one. In the simple lattice, this means the same phase for all couplings in the model, whereas for a dimerized lattice this introduces a modification in the isospin vector that determines the Hamiltonian matrix [see Eq. (1.26)].

1.4.2 Equivalence to a ladder Hamiltonian with flux equal to δ

There is and alternative way of seeing how the phase δ determines the symmetry properties of our one-dimensional Hamiltonian and thus its symmetry class. It consists of continuously deforming our one-dimensional Hamiltonian, Eq. (1.1), into the following ladder Hamiltonian:

$$H_{\text{Ladder}} = H_\delta - J'' \sum_n \left(\hat{a}_n^\dagger \hat{b}_{n+1} + \text{h.c.} \right). \tag{1.32}$$

When transforming the one-dimensional model into the ladder model, the phase δ is transformed into a non-zero magnetic flux per plaquette, which is precisely equal to δ [Fig. 1.6(b)]. In the ladder model, it is clear that for $\delta = 0$ the magnetic flux vanishes and the system is time reversal symmetric, whereas for $\delta \neq 0$ the magnetic

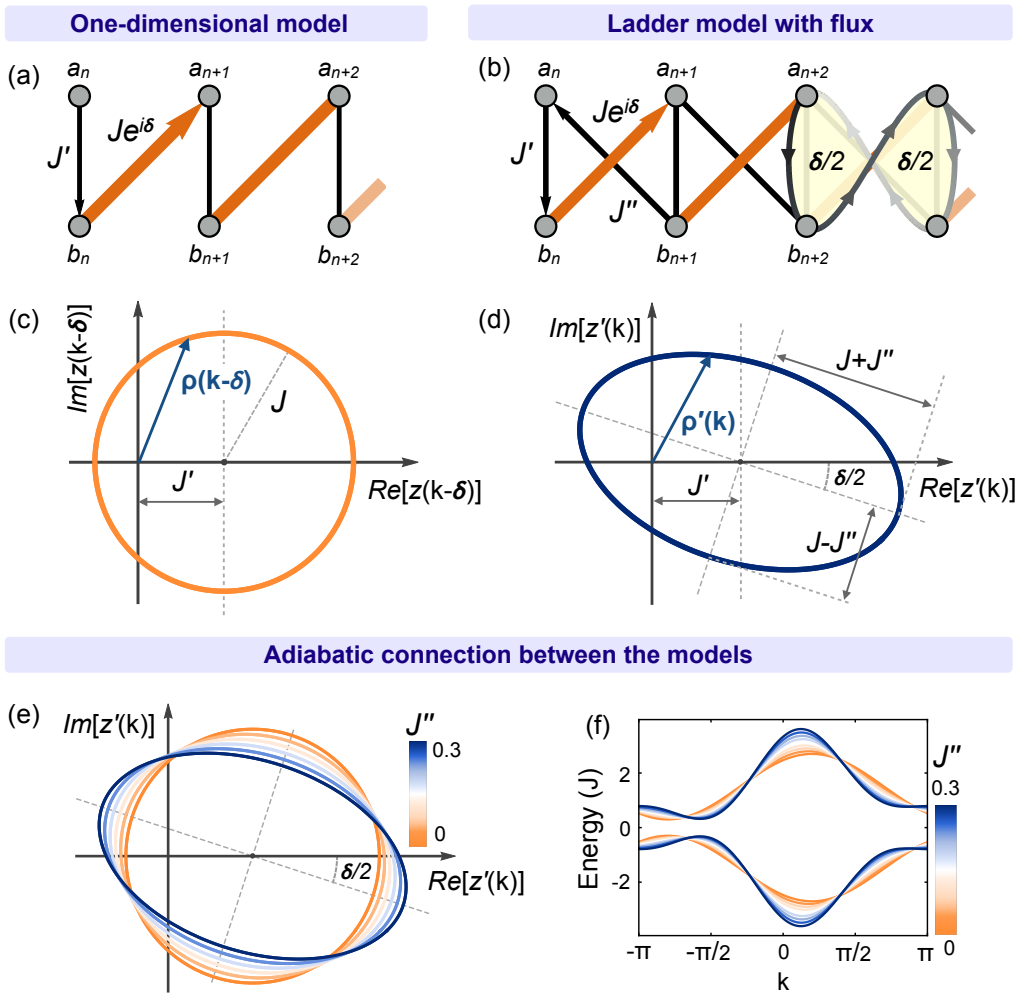

Figure 1.6: **Equivalence to a ladder model with flux.** (a) Schematic illustration of our model for a topological insulator in the AIII class seen as a ladder. It can be deformed into a ladder Hamiltonian (b) in the same symmetry class. Here, the phase δ corresponds to the total phase accumulated along a closed path, and thereby to an effective magnetic flux. For the one-dimensional model ($J = 1.2$, $J' = 0.8$ and $\delta = \pi/5$) the two components of the Hamiltonian matrix describe a circle (c), whereas they describe an ellipse (d) for the ladder model ($J = 1.2$, $J' = 0.8$, $J'' = 0.3$ and $\delta = \pi/5$). (e) Both models can be smoothly connected without crossing the origin in the complex plane. Therefore, their corresponding energy bands can be continuous deformed without closing the gap (f).

flux leads to a time reversal breaking model in the AIII symmetry class. The particular case in which $\delta = \pi$ is an exception, as, although constituting a non-vanishing effective magnetic flux per plaquette, it just introduces a negative sign in one of the tunneling amplitudes. The corresponding Hamiltonian is real so that time reversal and charge conjugation symmetries are preserved and therefore the Hamiltonian belongs to the BDI class. Both Hamiltonians, the one-dimensional one and the lad-

der one, are continuously connected without closing any energy gap, therefore they share the same symmetry properties. As a result, the one-dimensional model is also in the AIII symmetry class for $\delta \neq 0, \pi$.

In order to see how the two Hamiltonians are continuously connected we need to analyse the Hamiltonian matrices and the energy bands. The Hamiltonian matrix of our one-dimensional model, Eq. (1.5), can be written as:

$$M_\delta(k) = \mathrm{Re}\left[z(k-\delta)\right]\sigma_x + \mathrm{Im}\left[z(k-\delta)\right]\sigma_y, \tag{1.33}$$

with:

$$z(k) = J' + Je^{ik}. \tag{1.34}$$

If we draw the function $z(k-\delta)$ on the complex plane, we obtain a circle parametrized by the momentum k of radius J centred at the point $(J', 0)$ [see Fig. 1.6(c)]. The model has two energy bands with energies $E_\pm(k) = \mp\rho(k-\delta)$, where $\rho(k-\delta)$ is given by the distance between the origin and the curve point $z(k-\delta)$ [see Fig. 1.6(c)]. Hence, the energy gap closes only if the curve crosses the origin, something that only happens at the topological transition point $J' = J$.

On the other side, the ladder model H_{Ladder} in Eq. (1.32) corresponds to a Hamiltonian matrix:

$$M_{\mathrm{Ladder}}(k) = \mathrm{Re}\left[z'(k)\right]\sigma_x + \mathrm{Im}\left[z'(k)\right]\sigma_y, \tag{1.35}$$

with

$$z'(k) = z(k-\delta) + J''e^{-ik} \tag{1.36}$$

The new function $z'(k)$ that characterizes the Hamiltonian matrix describes an ellipse with axes $J + J''$ and $|J - J''|$, rotated an angle $\delta/2$ [Fig. 1.6(d)], and the energy bands of the model are given by $E'_\pm(k) = \mp\rho'(k)$, where $\rho'(k)$ corresponds to the distance between the origin and the curve point $z'(k)$ [see Fig. 1.6(d)]

As the tunneling amplitude J'' is increased from zero to a given value, the circle is continuously deformed into the ellipse [Fig. 1.6(e)]. Since this occurs without the curves crossing the origin in the complex plane, the corresponding energy bands are continuously deformed without closing the energy gap [Fig. 1.6(f)]. As a conclusion, both Hamiltonians share the same symmetry properties and thus belong to the same symmetry class. Therefore, our one-dimensional model belongs to the BDI symmetry class only when $\delta = 0, \pi$, being in the AIII symmetry class for $\delta \neq 0, \pi$.

1.4.3 Non-zero average momentum edge modes

There exists a relation between the symmetry class of the Hamiltonian and the momentum of the symmetry protected edge modes that the system exhibits when it is found to be in its topologically non-trivial phase. This correspondence serves to make evident the relevance of the phase δ and its direct relation with the breaking of time reversal and charge conjugation symmetries.

In this context, if a Hamiltonian H presents timer reversal symmetry there is a global unitary transformation U_T such that:

$$U_T\, H\, U_T^\dagger = H. \tag{1.37}$$

Therefore, if a certain state $|e\rangle$ is an eigenstate of the Hamiltonian with some energy E, then the transformed state $U_T\,|e\rangle^*$ is also an eigenstate of the Hamiltonian with the same energy. In case of a non degenerate state, as the edge states, this means that this transformation leaves the state invariant up to a phase, which can be absorbed in the unitary operator U_T. That is:

$$U_T\,|e\rangle^* = |e\rangle\,, \tag{1.38}$$

and consequently, opposite momentum modes are on average equally occupied:

$$\langle e|\,\hat{n}_k\,|e\rangle = \langle e^*|\,\hat{n}_{-k}\,|e^*\rangle = \langle e^*|\,U_T^\dagger\,\hat{n}_{-k}\,U_T\,|e^*\rangle = \langle e|\,\hat{n}_{-k}\,|e\rangle. \tag{1.39}$$

As a result, the momentum density distribution of the edge modes of a time reversal symmetric Hamiltonian is an even function of the momentum and, thus, such states have a zero average momentum.

In Chapter 2 we derive and analyse the wave function of the edge modes of our one-dimensional model and we show that the average momentum of such states is zero only for $\delta = 0$ and $\delta = \pi$. This will prove, in an alternative way, that a phase $\delta \neq 0, \pi$ leads to the breaking of time reversal and charge conjugation symmetries and, therefore, makes the Hamiltonian enter the AIII symmetry class. Furthermore, it also has observable consequences, such as the momentum of the edge modes.

1.4.4 Gauge transformations, topology and boundary conditions

Despite everything we have already explained in this section about the role that the phase δ plays in our one-dimensional model, there is a gauge transformation that removes the phase δ form the system. This unitary is given by:

$$V : \begin{cases} \hat{a}_n^\dagger \longrightarrow e^{i\delta n}\hat{a}_n^\dagger \\ \hat{b}_n^\dagger \longrightarrow e^{i\delta n}\hat{b}_n^\dagger, \end{cases} \tag{1.40}$$

so that, after all, the Hamiltonian with a phase δ and the one with no phase, can be connected through a gauge transformation:

$$V\, H_\delta\, V^\dagger = H_{\delta=0}. \tag{1.41}$$

However, this does not mean that both models are equivalent, nor they share the same symmetry properties.

Why is that? The fundamental reason is that not every unitary operator that can be applied to the Hamiltonian are allowed in the definition of the different symmetries that serve to classify topological insulators. The model can exhibit topological

features because of having two sites per unit cell. This makes the Hamiltonian be able to be written using a spinor-like discrete field $\hat{\psi}_k^\dagger$, and it is in this internal space where the topological properties are found. As a two level-quantum system, this internal space can be described by using the Bloch sphere representation. Chiral symmetry implies that, instead of being able to reach any point in the sphere, the vectors that characterize the system are constrained to a particular plane crossing the center of the sphere. Therefore there are two possible situations that correspond to two distinct topological phases: enclosing the origin forming a complete circle (winding number 1) or forming just an arc that does not enclose the origin and can be continuously deformed into a point (winding number 0). When using the symmetry properties in order to classify distinct topological insulators we need to consider those unitary transformations that preserve the topological nature of the system. In other words, they need to consist of the same unitary transformation applied to every vector in this internal space.

We can give an example that serves to easily visualize this. Let us consider a tight-binding model with two sites per unit cell and translational invariance, so that its corresponding Hamiltonian can be written in momentum space as:

$$H = \sum_k \hat{\psi}_k^\dagger \, \boldsymbol{v}(k) \cdot \boldsymbol{\sigma} \, \hat{\psi}_k^\dagger, \tag{1.42}$$

being $\boldsymbol{v}(k)$ a vector that depends on the momentum. In this way, the system is totally characterized by a finite set of vectors, one for each quantized momentum value. If we were allowed to consider any unitary transformation that can be applied to the whole Hamiltonian in order to define the symmetry transformations, we could define the following unitary:

$$U = \sum_k \hat{\psi}_k^\dagger \, \boldsymbol{u}(k) \cdot \boldsymbol{\sigma} \, \hat{\psi}_k^\dagger, \tag{1.43}$$

choosing each vector $\boldsymbol{u}(k)$ to be orthogonal to each vector $\boldsymbol{v}(k)$, that is: $\boldsymbol{u}(k) \cdot \boldsymbol{v}(k) = 0 \quad \forall k$. Consequently, the unitary operator U is such that $UHU^\dagger = -H$ and thus the Hamiltonian would be chiral symmetric. This means that every Hamiltonian of that kind, which is quite general, would be topologically non-trivial, would represent a topological insulator and would exhibit symmetry protected edge modes, which is clearly not true.

We can consider a more general Hamiltonian than our one-dimensional Hamiltonian in Eq. (1.1), which consist of a dimerized lattice with two different phases in the hopping amplitudes, δ and θ [see Fig. 1.7(a)]. The Hamiltonian of such model is:

$$H_{\delta,\theta} = -\sum_n^N \left(J' e^{-i\theta} \, \hat{a}_n^\dagger \hat{b}_n + J e^{i(\delta-\theta)} \, \hat{a}_{n+1}^\dagger \hat{b}_n + \text{H.c.} \right). \tag{1.44}$$

In the momentum representation this Hamiltonian looks like:

$$H_{\delta,\theta} = -\sum_k \hat{\psi}_k^\dagger \, R_z(\theta) \, M_\delta(k) \, R_z^\dagger(\theta) \hat{\psi}_k, \tag{1.45}$$

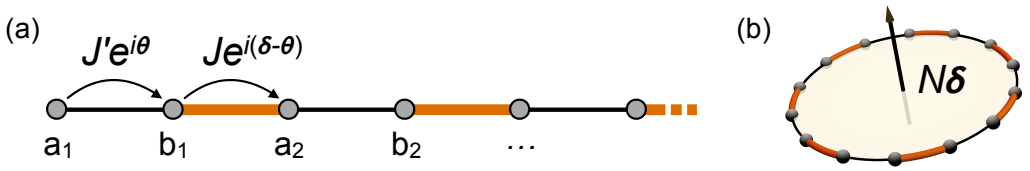

Figure 1.7: **Phase δ as an effective magnetic flux.** (a) In a dimerized one-dimensional lattice with two different complex hopping amplitudes only the sum of the two phases is relevant, i.e. the total phase accumulated when a particle travels from one site to the same type of site in the following cell. In this way, each possible value of δ constitutes a different model that belongs to a continuous set of equivalent models parametrised by the phase θ. All equivalent models are connected by global rotations around the z-axis (see text). (b) When joining the two ends of the lattice particles pick up a phase $N\delta$ when completing a closed path along the whole ring. Therefore, the phase δ is directly related to an effective magnetic flux penetrating the system.

being $M_\delta(k)$ the same Hamiltonian matrix as the one corresponding to our one-dimensional model, Eq. (1.5), and $R_z(\theta) = e^{i\theta\sigma_z/2}$ a rotation around the z-axis of an angle θ.

As we see, the phase θ is an irrelevant quantity, as it can be removed by performing a global unitary transformation, whereas δ is not. This is due to the fact that δ is the total phase accumulated by a particle when travelling from any site in the lattice to the same site in the following lattice cell. As we explained before in this section, this phase constitutes a shift in the momentum and changes the momentum-isospin correspondence. Furthermore, if we consider periodic boundary conditions, it turns out that there is an effective magnetic flux penetrating the ring formed by the whole lattice which is precisely equal to $N\delta$ [see Fig. 1.7(b)]. It is clear then that the phase δ can be removed by a gauge transformation only for open boundary conditions, being a gauge invariant quantity when the system is subjected to periodic boundary conditions. A topological insulator like our model exhibits a bulk-edge correspondence, that is a direct relation between two ways in which its topological nature can be manifested. On one hand, for periodic boundary conditions, it is manifested in the bulk through the non-trivial Zak phase. On the other hand, for open boundary conditions, through the existence of symmetry protected zero modes localized at the edges of the system. Following this bulk-edge correspondence, if the phase δ is relevant and determines the symmetry properties and topological class of the model in the bulk, it has to be the same when we look at the edges of the system.

In conclusion, not every gauge transformation is allowed when considering the symmetry transformations that classify topological insulators. They do not only need to be unitary, but also preserve the topology of the system. In other words, only those that act equally on every vector in the internal space are permitted. Alternatively, we can say that only those unitary transformations that act on the system independently of having periodic or open boundary conditions can be con-

sidered to constitute symmetry transformations. In fact, the gauge transformation in Eq. (1.40), which is not a global transformation, does not commute with a change of the boundary conditions.

Chapter 2

Edge modes in the AIII class

2.1 Emergence of edge modes in the topological phase

When the edges of the one-dimensional lattice are not connected with each other, and thus the system consists of an open chain, the Bloch modes in Eq. (1.3) are no longer the proper eigenstates of the Hamiltonian, as they do not fulfil the open boundary conditions. Nevertheless, they constitute an orthonormal basis of the space of states and are really convenient for obtaining the right eigenstates of the Hamiltonian. For that, we need to consider linear superpositions of two Bloch modes with arbitrary momenta such that their corresponding energy, according to the dispersion relation, are the same. That is, we need to combine the Bloch mode with momentum q with the one with momentum $q' = -q + 2\delta$. Then, we impose the boundary conditions, what gives us, on one hand, the relation between the two coefficients in such linear superposition and, on the other hand, the quantization condition for q.

The eigenmodes of the model for open boundary conditions are:

$$\hat{c}^\dagger_{\pm,q} \propto \sum_n e^{i\delta n} \left[\sin\big(qn - \varphi(q)\big)\hat{a}^\dagger_n \pm \sin qn\, \hat{b}^\dagger_n \right], \tag{2.1}$$

being the quantum number q quantized according to the following equation:

$$q(N+1) - m\pi = \varphi(q), \tag{2.2}$$

where $\varphi(k) = \arg(J' + Je^{ik})$ and being m and integer running from 1 to N. In this way, for each value of m we would obtain a different value of q that satisfies the quantization condition and corresponds to a pair of eigenstates, one for each energy band, with energies $E_\pm(q) = \mp\rho(q)$, being $\rho(q) = |J' + Je^{ik}|$. It is important to notice that the quantum number q, that labels all bulk eigenstates of the Hamiltonian for open boundary conditions, does not coincide with the momentum of such states. A bulk mode of the form in Eq. (2.1) has two different momentum components, one with momentum $q + \delta$ and another one with momentum $-q + \delta$.

There is a region in the parameter space in which the quantization condition has N different solutions, leading to $2N$ bulk eigenstates, N for each energy band.

However, when $J'/J < 1 - 1/(N+1)$ there are just $N-1$ solutions and therefore only $2N-2$ bulk eigenstates of the form in (Eq. 2.1). In that case the two missing eigenstates will be the so-called edge modes or zero modes [see Fig. 2.1(a)].

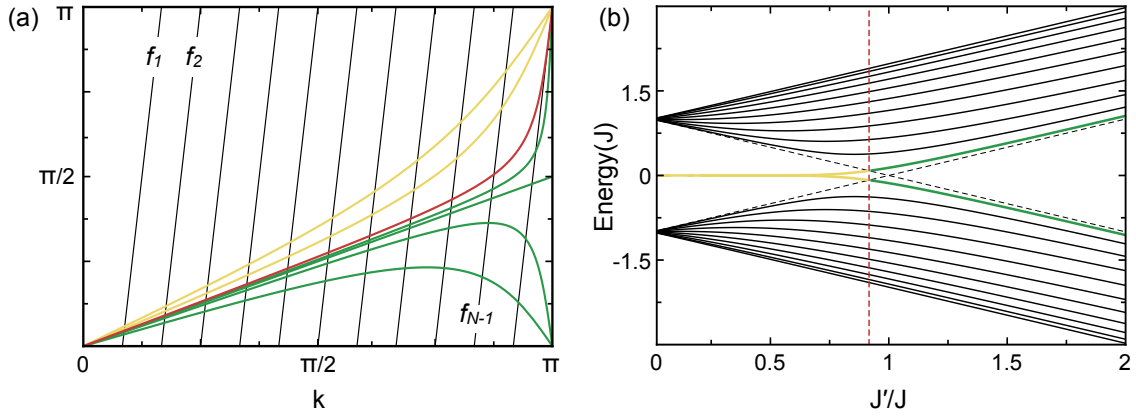

Figure 2.1: **Emergence of edge modes in the topological phase.** (a) Graphic representation of the momentum quantization condition in Eq. (2.1) for a total number of unit cells $N = 11$. The black lines correspond to the functions $f_m(q) = q(N+1) - m\pi$ and the coloured curves to the function $\varphi(q)$ for different values of the ratio between the two hopping amplitudes, J'/J. The crossing points between $\varphi(q)$ and each line $f_m(q)$ correspond to each quantized value of q and, thus, to pairs of bulk eigenstates of the Hamiltonian, one for each energy band. For $J'/J > 1 - 1/(N+1)$, the function $\varphi(q)$ crosses every line $f_m(q)$ and, therefore, there exist $2N$ bulk eigenstates (green curves, corresponding to $J'/J = 1.5$, 1.1, 1 and 0.967 starting from the bottom). For $J'/J < 1 - 1/(N+1)$, the function $\varphi(q)$ crosses just the first $N-1$ lines $f_m(q)$, so that the Hamiltonian exhibits only $2N-2$ bulk eigenstates, being the two missing states the edge modes (yellow curves, corresponding to $J'/J = 0.5$ and 0.7 starting from above). The transition point between the absence and presence of edge modes, $J'/J = 1 - 1/(N+1)$, corresponds to the case in which the slope of the tangent line to the function $\varphi(q)$ (red curve) at $q = \pi$ is equal to the slope of the line $f_N(q)$. (b) Energy diagram for a total number of unit cells $N = 11$. The black curves correspond to the energy of the bulk eigenstates of the Hamiltonian as a function of the ratio J'/J. The green curves are the energy of the lowest energy bulk eigenstate in the upper band and the highest energy bulk eigenstate in the lower band. At the transition point $J'/J = 1 - 1/(N+1)$ (red dashed line), these two eigenstates are no longer in the bulk and they become the two edge states, whose energy is exponentially close to zero (yellow curves).

In this way, if we consider the system to be somewhere in its topologically trivial phase and then we continuously modify the ratio between the two hopping amplitudes J'/J towards the topological phase, the edge modes will not appear exactly at the topological transition point $J' = J$ but slightly later on, when the two tunneling amplitudes are such that $J'/J = 1 - 1/(N+1)$ [see Fig. 2.1(b)]. Consequently, we can say that there are two critical points, one that indicates the topological

phase transition between the two topologically distinct phases and another one that separates the absence and presence of edge modes in the system. Both are quite close to each other and, when considering a large number of unit cells in the lattice, $N >> 1$, they coincide, what stands for a bulk-edge correspondence. In other words, the presence of symmetry protected zero modes at the edges of the system is directly related to a non-trivial topology characterised by the whole set of bulk eigenstates through the Zak phase.

In order to obtain the wave function of the edge modes we need to consider Bloch modes with complex momentum, as there exist no more real solutions to the quantization condition other that the $N-1$ that correspond to the $2N-2$ bulk eigenstates. Combining a mode with momentum $k = \pi + \delta + i\xi$ and another one with momentum $k' = -\pi + \delta - i\xi$, and imposing the boundary conditions we get the two edge modes of the Hamiltonian:

$$\hat{e}^{\dagger}_{\pm} = \frac{1}{\sqrt{2}}\Big(\tilde{a}^{\dagger}_{n=1} \pm \tilde{b}^{\dagger}_{n=N}\Big), \tag{2.3}$$

where:

$$\tilde{a}^{\dagger}_{n=1} = \frac{1}{\sqrt{c}} \sum_{n} e^{i(\pi+\delta)n} \, \sinh \xi(N+1-n) \, \hat{a}^{\dagger}_{n}, \tag{2.4}$$

$$\tilde{b}^{\dagger}_{N=1} = \frac{1}{\sqrt{c}} \sum_{n} e^{i(\pi+\delta)n} \, \sinh \xi n \, \hat{b}^{\dagger}_{n}, \tag{2.5}$$

being $c = \sum_n \sinh^2 \xi n$ a normalization constant and being ξ determined by the following equation:

$$J' \sinh \xi(N+1) = J \sinh \xi N. \tag{2.6}$$

That is, the two edge modes of the Hamiltonian, $\hat{e}^{\dagger}_{\pm}$, are the symmetric and antisymmetric linear combinations of the modes $\tilde{a}^{\dagger}_{n=1}$ and $\tilde{b}^{\dagger}_{n=N}$, which are localized at the left and right edges of the system, respectively. Furthermore, they also exhibit a polarization property, as the mode at the left edge of the lattice occupies only a-modes, whereas the one at the right occupies only b- modes. In other words, the modes localized at opposite ends of the lattice correspond to orthogonal isospin states.

The quantity ξ is the imaginary part of the edge modes momentum, so that its inverse is a length and, as we can see from the edge modes wave functions, it determines the localization length associated to the edge modes spatial density distribution. In this way, if we consider the edge modes to be spatially concentrated in a region much smaller than the size of the whole system, we can take the limit $\xi N >> 1$, what allows us to obtain a approximated expression for ξ:

$$\xi \approx -\log(J'/J). \tag{2.7}$$

As a consequence of this approximated expression for the quantity ξ, the energies of the edge modes, which in general are $\mp\sqrt{J'^2 + J^2 - 2J'J\cosh\xi}$, can also be

approximated and become zero. This approximation holds quite well in most of the topologically non-trivial phase, being not as good in a vicinity of the topological phase transition (see Fig. 2.2). The fact that the energy of the edge modes is almost zero implies that they can be consider to constitute a two-dimensional degenerate eigensubspace and, thus, the two modes from which they are formed, $\tilde{a}^\dagger_{n=1}$ and $\tilde{b}^\dagger_{n=N}$, are also zero energy eigenstates of the Hamiltonian. This is of course not exactly true, just an approximation. If we prepared a particle in the mode localized at one particular edge of the lattice and let it evolve in time under the Hamiltonian of the system, it would not remain the same as a truly eigenstate would do. It would oscillate between itself and the mode localized at the opposite edge. Nevertheless, the time that we would need to wait until it becomes the other mode is really large as it is proportional to the inverse of the absolute value of the edge modes energy.

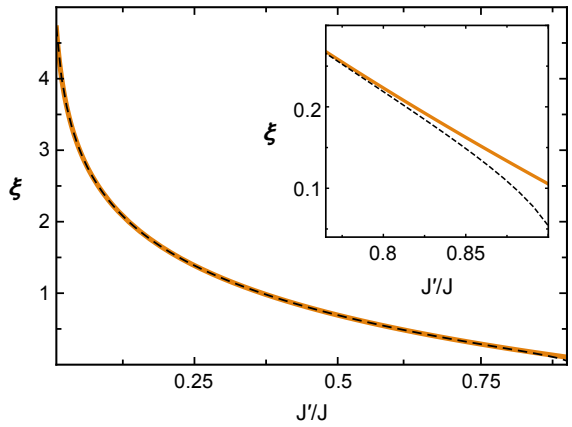

Figure 2.2: **Zero energy approximation.** Plot of the exact value of ξ (black dashed curve) and its approximated value according to the expression in Eq. (2.1) (orange curve) as a function of the ratio between the two hopping amplitudes, J'/J. The approximation fits quite well in most of the topological phase, being not as good in the vicinity of the transition point. As a result, considering the edge modes to have zero energy is a quite good approximation.

2.2 Edge modes momentum and symmetry class

As we have anticipated in Sec. 1.4.3, there is a relation between the topological symmetry class of the Hamiltonian and the edge modes that it exhibits. In other words, the edge modes that correspond to the BDI symmetry class, for $\delta = 0, \pi$ (SSH model), and the ones in the AIII class, for $\delta \neq 0, \pi$, are different and this difference can be measured. As a result, the symmetry class of the system is characterised by the properties of the edge modes.

When we look at the edge modes spatial density distribution, we find no difference at all between the BDI class and the AIII class. In both cases the edge modes are concentrated at the edges of the system [see Fig. 2.3(a) and (c)]. On the

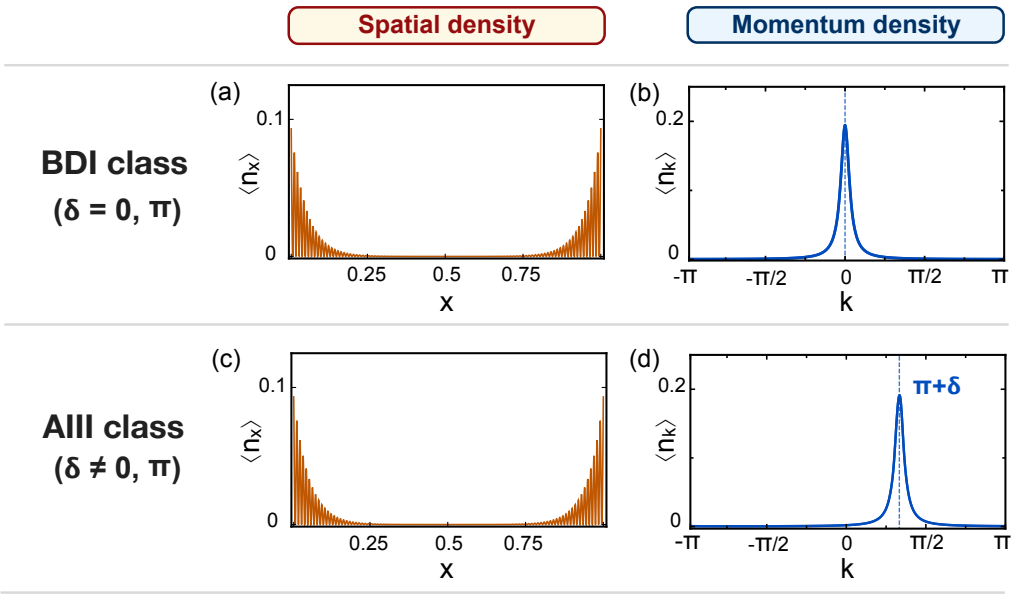

Figure 2.3: **Edge modes momentum and symmetry class.** (a) Spatial density distribution $\langle \hat{n}_x \rangle$ and (b) momentum density distribution $\langle \hat{a}_k^\dagger \hat{a}_k \rangle = \langle \hat{b}_k^\dagger \hat{b}_k \rangle$ of the edge modes for $N = 100$, $J'/J = 0.9$ and $\delta = 0$ (BDI symmetry class). (c) Spatial and (d) momentum density distributions of the edge modes for $N = 100$, $J'/J = 0.9$ and $\delta = -2\pi/3$ (AIII symmetry class). While the edge modes spatial density distributions are the same in both symmetry classes, it is through their momentum distributions how the Hamiltonian symmetry class is manifested. Edge modes in the BDI class have a zero average momentum, imposed by the presence of time reversal symmetry. On the contrary, the AIII symmetry class is characterised by non-zero average momentum edge modes. All data represented in this figure has been obtained by exact numerical diagonalization of the Hamiltonian.

contrary, it is their momentum density distribution what has the information about the Hamiltonian symmetry class. If we look at the edge modes wave functions, Eq. (2.4) and Eq. (2.5), we can identify a momentum term $e^{i(\pi+\delta)n}$, what indicates that their momentum density distribution is shifted by $\pi + \delta$. In the BDI symmetry class, $\delta = 0, \pi$, the edge modes momentum distribution consists of an even function centred at $k = 0$ or $k = \pi$ [see Fig.2.3(b)], so that edge modes in the BDI class have a zero average momentum. In contrast, in the AIII symmetry class, $\delta \neq 0, \pi$, the edge modes density distribution is centred at $k = \pi + \delta$ [see Fig.2.3(d)], so that the edge modes average momentum is different from zero.

This difference between the momentum of the edge modes in the BDI class and in the AIII class is nothing casual. As we explained in Sec. 1.4.3, the presence of time reversal symmetry forces the edge modes to have a zero average momentum. Therefore, edge modes with a non-zero average momentum are a direct consequence of the breaking of time reversal symmetry and constitute a hallmark of the AIII symmetry class.

2.3 Edge modes spatial and momentum localizations

Besides the manifestation of the Hamiltonian symmetry class through the edge modes momentum distribution, studying the edge modes in momentum space has allowed us to find out another interesting feature of such states. Surprisingly, the edge modes are well localized around their average momentum, in addition to their good spatial localization at the edges of the system.

From the edge modes wave functions, Eq. (2.4) and Eq. (2.5), we can compute their spatial localization length, denoted as δx, as the FWHM of their spatial density distribution [see Fig. 2.4(a)]. This localization length can also be approximated by taking the limit $\xi N >> 1$ and is given by:

$$\delta x = N - \frac{1}{\xi}\text{arsinh}\left(\frac{1}{\sqrt{2}}\sinh\xi N\right) \simeq \frac{\log 2}{2\xi}, \tag{2.8}$$

expressed in units of the total size of the system.

In order to get the edge modes momentum localization length, we first need to write them using the momentum basis. In momentum representation the edge modes are:

$$\hat{e}^\dagger_\pm = \frac{1}{\sqrt{2}}\sum_k \left[F(\tilde{k})\,\hat{a}^\dagger_k \pm e^{i\tilde{k}(N+1)}F(-\tilde{k})\,\hat{b}^\dagger_k\right], \tag{2.9}$$

with $F(k) = \frac{1}{\sqrt{Nc}}\sum_n e^{-ikn}\sinh\xi(N+1-n)$ and $\tilde{k} = k - \pi - \delta$. By making an integral instead of a discrete sum we can obtain the following approximation of the function $F(k)$:

$$F(k) = \frac{f(k)}{1+(k/\xi)^2}, \tag{2.10}$$

with:

$$f(k) = \cosh\xi N - i\frac{k}{\xi}\sinh\xi N - e^{-ikN}. \tag{2.11}$$

The real and imaginary parts of $f(k)$ have a well defined parity, being its real part even and its imaginary part odd. Therefore, the modulus square of $f(k)$ is an even function of the momentum. In consequence, $|F(k)|^2 = |F(-k)|^2$ and, thus, the two edge modes components have the same momentum distribution [see Eq. (2.9)]. That is:

$$\langle 0|\,\hat{e}_\pm\,\hat{a}^\dagger_k\,\hat{a}_k\,\hat{e}^\dagger_\pm\,|0\rangle = \langle 0|\,\hat{e}_\pm\,\hat{b}^\dagger_k\,\hat{b}_k\,\hat{e}^\dagger_\pm\,|0\rangle = \frac{1}{2}|F(k-\pi-\delta)|^2. \tag{2.12}$$

The modulus square $|F(k)|^2$ consists of the product between the square of a Cauchy distribution centred at $k = \pi + \delta$ with scale parameter ξ and the even function of the momentum $|f(k)|^2$. The first factor tends to highly localize the distribution around its center. Therefore, in order to get a simpler expression for the edge modes momentum density distribution that allows us to obtain its localization length, we can approximate the second factor by its second order Taylor expansion:

$$|F(k)|^2 \simeq \left[\frac{1}{1+(k/\xi)^2}\right]^2\left[A_0 + A_2(k/\xi)^2\right], \tag{2.13}$$

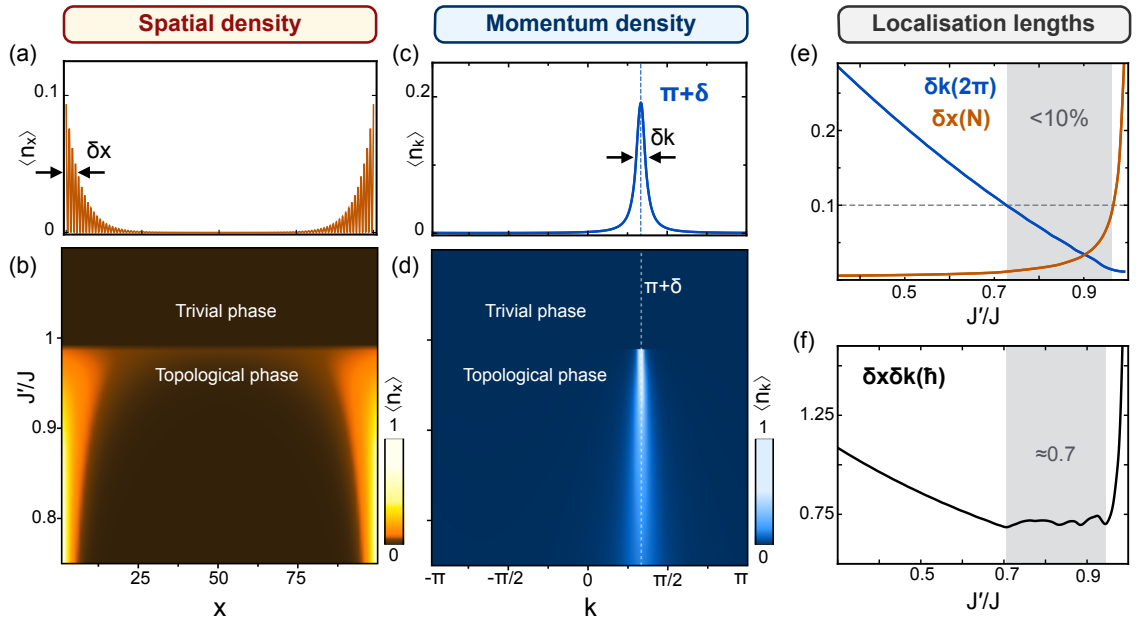

Figure 2.4: **Edge modes spatial and momentum localizations.** (a) Spatial density distribution $\langle \hat{n}_x \rangle$ and (c) momentum density distribution $\langle \hat{a}_k^\dagger \hat{a}_k \rangle = \langle \hat{b}_k^\dagger \hat{b}_k \rangle$ of the edge modes for $N = 100$, $J'/J = 0.9$ and $\delta = -2\pi/3$. (b) Spatial and (d) momentum density distributions of the edge modes as a function of the ratio J'/J for $N = 100$ and $\delta = -2\pi/3$. (e) Edge modes spatial and momentum localization lengths and (f) combined position-momentum uncertainty as a function of the ratio J'/J for $N = 100$. The spatial localization of the edge modes is better the farther to the critical point the system is, whereas their momentum localization behaves in the opposite way. Nevertheless, both magnitudes can be simultaneously well defined, reaching a minimum position-momentum uncertainty of $0.7\hbar$. All data represented in this figure has been obtained by exact numerical diagonalization of the Hamiltonian.

with A_0 and A_2 being constant coefficients. The edge modes localization length in momentum space, defined as the FWHM of their momentum density distribution [see Fig. 2.4(c)] is then given by:

$$\delta k \simeq \xi(1 + A_2/A_0) \simeq 2\xi(1 + \xi^2 N^2 e^{-\xi N}), \tag{2.14}$$

expressed in terms of the total size of the first Brillouin zone. These two expressions for the spatial and momentum localization lengths of the edge modes, Eq. (2.8) and Eq. (2.14), hold for a wide range of parameters.

The bigger the ratio between the two hopping amplitudes J'/J is, the smaller the quantity ξ is [see Eq. (2.1) and Fig. 2.2]. Therefore, by analysing the expressions for the edge modes spatial and momentum localizations, Eq. (2.8) and Eq. (2.14), we can conclude that the spatial localization of the edge modes gets better as the system gets farther from the topological transition point, whereas their momentum

localization gets better as the system gets closer to the topological transition point. This behaviour can be checked and visualized in Fig. 2.4(b) and (d), where we show the edge modes spatial and momentum density distributions as a function of the ratio J'/J, obtained by exact numerical diagonalization of the Hamiltonian.

Interestingly, there is a region in the topological phase where both the position and momentum of the edge modes are well defined and correspond to localization lengths lower than 0.1, in terms of the total size of the lattice and total size of the first Brillouin zone, respectively [see Fig. 2.4(e)]. In that region of the parameter space the product between the spatial and momentum localization lengths reaches its minimum value of $0.7\hbar$, quite close to the minimum possible value it could take according to the Heisenberg uncertainty principle [see Fig. 2.4(f)].

Chapter 3

Experimental realization and observing fractionalization

3.1 Experimental realization

We have developed an experimental protocol for the realization of our one-dimensional model for a topological insulator in the AIII symmetry class (see Fig. 3.1). For that, we need to combine a superlattice structure [20], which serves as a dimerized one-dimensional lattice with two different hopping amplitudes, together with Raman assisted tunneling [32, 33], which allows the implementation of complex tunneling amplitudes. As a result, the following experimental Hamiltonian can be realize:

$$H_{\text{exp}} = -\sum_{n}^{N} \left(J' \, e^{i(2n-1)\delta} \, \hat{a}_n^\dagger \hat{b}_n + J e^{i2n\delta} \, \hat{a}_{n+1}^\dagger \hat{b}_n + \text{H.c.} \right). \tag{3.1}$$

It is not exactly the same Hamiltonian as the one in Eq. (1.1) that corresponds to our model. However, both Hamiltonians are equivalent and are connected through the following gauge transformation:

$$\begin{cases} \hat{a}_n^\dagger \; \rightarrow \; \hat{a}_n^\dagger, \\ \hat{b}_n^\dagger \; \rightarrow \; e^{i(2n-1)\delta} \, \hat{b}_n^\dagger. \end{cases} \tag{3.2}$$

The reason why the experimental Hamiltonian and the theoretical one are equivalent to each other is the fact that the total phase accumulated by a particle after travelling from a particular site in the lattice to the same site in the following lattice cell is always δ [see Fig. 3.1(b)]. Therefore, the two Hamiltonians can be connected by means of this gauge transformation both for periodic and for open boundary conditions, as the effective magnetic flux that penetrates the sample for periodic boundary conditions is in both cases $N\delta$ [see Fig. 3.1(c)].

The gauge transformation that connects the experimental and the theoretical Hamiltonians can be written in the momentum representation as $\hat{a}_k^\dagger(\hat{b}_k^\dagger) \rightarrow \hat{a}_k^\dagger(\hat{b}_{k-2\delta}^\dagger)$. In consequence, the edge modes in the experimental gauge have the

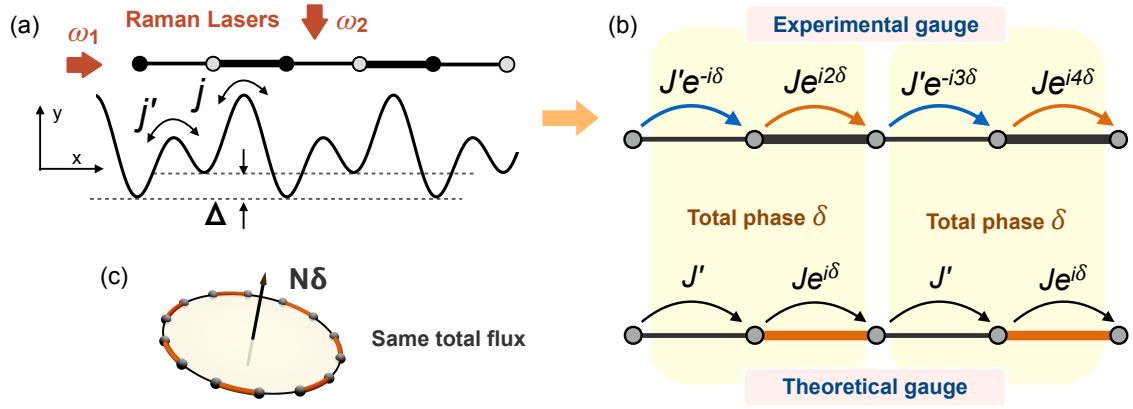

Figure 3.1: **Experimental scheme.** (a) A doble well potential with energy offset Δ is created from the superposition of two standing waves, forming a one-dimensional dimerized lattice with tunneling amplitudes j and j'. A pair of Raman lasers is added along the $-x$ and $-y$ directions with frequencies ω_1 and ω_2, such that $\omega_1 - \omega_2 = \Delta/\hbar$. This produces a laser assisted tunneling that leads to the Hamiltonian in Eq. (3.1). (b) Schematic representation of the experimental Hamiltonian and the theoretical one. Both Hamiltonians are equivalent, as the total phase accumulated by a particle when travelling from a site in the lattice to the same site in the next lattice cell is always δ. (c) In both cases the effective magnetic flux that penetrates the ring formed by the lattice under periodic boundary conditions is $N\delta$.

following form:

$$\hat{e}^{\dagger}_{\mathrm{exp},\pm} = \frac{1}{\sqrt{2}} \sum_n \left(e^{i(\pi+\delta)n} \sinh \xi (N+1-n)\, \hat{a}^{\dagger}_n \pm e^{i(\pi-\delta)n} \sinh \xi n\, \hat{b}^{\dagger}_n \right), \tag{3.3}$$

so that the mode located at the left edge of the system has momentum $\pi + \delta$, whereas the one at the right edge has momentum $\pi - \delta$. In this way, for the BDI symmetry class ($\delta = 0, \pi$) the two edge modes are localized at the same position in momentum space ($k = \pi$ or $k = 0$). In contrast, for the AIII symmetry class ($\delta \neq 0, \pi$) they are localized at opposite momenta ($k = \pi + \delta$ and $k = \pi - \delta$). This splitting is a distinctive feature of the AIII symmetry class and is not possible in the BDI symmetry class, as the presence of time reversal symmetry forces the edge modes to be at the same momentum position. As we show in the following, this feature of the AIII symmetry class allows us to directly observe fractionalization in momentum space.

3.2 Observing fractionalization in the AIII model

The phenomenon of fractionalization was first studied in the context of quantum field theory and consist of the appearance of excitations carrying a fractionalized particle number in some soliton quantum field theories [1, 2, 41, 42]. Such field theories are

not present in the Standard Model of particle physics and, thus, such fractionalized excitations do not exist as conventional free particles in nature. However, some condensed matter systems can serve as physical realizations of such soliton field theories and, therefore, give rise to fractionalized particles, which in this context are called *quasiparticles*.

That is the case of our one-dimensional model for a topological insulator. At a filling factor such that all states of negative energy are occupied, this many body state can be interpreted as a Dirac sea on top of which particles and antiparticles (holes) can be created, by occupying positive energy states and emptying negative energy states, respectively. In that situation, and when the system is in its topological phase, the lowest energy excitation that can be created, which corresponds to one of the edge modes, is described by a discretized version of a soliton quantum field theory with fractionalized excitations. Therefore, it inherits the property of fractionalization.

What does exactly the phenomenon of fractionalization mean in the context of a condensed matter system and not a soliton field theory? In order to understand the correspondence between these two levels, the soliton quantum field theory and the topological insulator that realizes it at a very specific filling factor, we need to compare two situations. On one hand, a fermion occupying an edge state with no more occupied states; and, on the other hand, the situation in which a fermion occupies the same edge state and all negative energy states are also occupied, which represent the vacuum of the field theory.

3.2.1 Fractionalization in position space

We start by considering the many body state in which all bulk states in the lower energy band plus the negative energy edge state are occupied. This many body state is:

$$|\Phi_+\rangle = \hat{e}_+^\dagger \prod_q \hat{c}_{+,q}^\dagger |0\rangle, \tag{3.4}$$

being $\hat{c}_{+,q}^\dagger$ the bulk modes in Eq. (2.1). We want to know what is the spatial density distribution, denoted as ν_x, for such many body state. That is, the expected value of the particle number operator $\hat{n}_x$; being $\hat{n}_{x=2n-1} = \hat{a}_n^\dagger \hat{a}_n$ and $\hat{n}_{x=2n} = \hat{b}_n^\dagger \hat{b}_n$, runing x from 1 to $2N$ and n from 1 to N.

First, it is convenient to define the two following projectors:

$$P_\pm = \hat{e}_\pm^\dagger \, |0\rangle\langle 0| \, \hat{e}_\pm + \sum_q \hat{c}_{\pm,q}^\dagger \, |0\rangle\langle 0| \, \hat{c}_{\pm,q}, \tag{3.5}$$

which correspond to the subspaces generated by all positive and negative energy states, respectively. Now, we can write an expression for the spatial density distribution corresponding to the many body state $|\Phi_+\rangle$ using such projectors:

$$\nu_x = \langle 0| \, \hat{e}_+ \, \hat{n}_x \, \hat{e}_+^\dagger \, |0\rangle + \sum_q \langle 0| \, \hat{c}_{+,q} \, \hat{n}_x \, \hat{c}_{+,q}^\dagger \, |0\rangle = \mathrm{tr}\big(\hat{n}_x \, P_+\big) = 1 - \mathrm{tr}\big(\hat{n}_x \, P_-\big), \tag{3.6}$$

where we have used the fact that $P_+ + P_- = \mathbb{I}$ and $\mathrm{tr}\big(\hat{n}_x\big) = 1$.

Due to the presence of chiral symmetry, the chiral operator $U_S : \hat{a}_n^\dagger(\hat{b}_n^\dagger) \to \hat{a}_n^\dagger(-\hat{b}_n^\dagger)$ transforms every positive energy eigenstate into a negative energy eigenstate and vice versa, so that $U_S P_\pm U_S^\dagger = P_\mp$. For this reason, together with the fact that the chiral operator leaves the density operator $\hat{n}_x$ invariant, we have that $\mathrm{tr}\big(\hat{n}_x\, P_+\big) = \mathrm{tr}\big(\hat{n}_x\, P_-\big)$. Therefore, substituting in Eq. (3.6), we get:

$$\nu_x = 1 - \mathrm{tr}\big(\hat{n}_x\, P_-\big) = 1 - \mathrm{tr}\big(\hat{n}_x\, P_+\big) = 1 - \nu_x \implies \nu_x = \frac{1}{2}. \tag{3.7}$$

In this way, the many body state $|\Phi_+\rangle$, that consists of having all negative energy states occupied, corresponds to a flat spatial density distribution.

Now we consider the resulting state of adding a fermion, occupying the positive energy edge mode, to that flat density profile:

$$|\Phi_{\mathrm{qp}}\rangle = \hat{e}_-^\dagger |\Phi_+\rangle = \hat{e}_-^\dagger \hat{e}_+^\dagger \prod_q \hat{c}_{+,q}^\dagger |0\rangle. \tag{3.8}$$

In this many-body state both edge modes are occupied. Therefore the modes $\tilde{a}_{n=1}^\dagger$ and $\tilde{b}_{n=N}^\dagger$ are also occupied and we have:

$$\Big(\tilde{a}_{n=1}^\dagger \tilde{a}_{n=1} - \nu_x\Big)|\Phi_{\mathrm{qp}}\rangle = \frac{1}{2}\,|\Phi_{\mathrm{qp}}\rangle, \tag{3.9}$$

$$\Big(\tilde{b}_{n=N}^\dagger \tilde{b}_{n=N} - \nu_x\Big)|\Phi_{\mathrm{qp}}\rangle = \frac{1}{2}\,|\Phi_{\mathrm{qp}}\rangle. \tag{3.10}$$

This result states that the many-body state $|\Phi_{\mathrm{qp}}\rangle$, with a fermion on top of a flat background, is an exact eigenstate of the number operators $\tilde{a}_{n=1}^\dagger \tilde{a}_{n=1} - \nu_x$ and $\tilde{b}_{n=N}^\dagger \tilde{b}_{n=N} - \nu_x$. Therefore, we can say that two fractionalized quasiparticles with particle number $1/2$ exist at the edges of the system. Analogously, we can define the quasihole sate:

$$|\Phi_{\mathrm{qh}}\rangle = \hat{e}_+ |\Phi_+\rangle = \prod_q \hat{c}_{+,q}^\dagger |0\rangle, \tag{3.11}$$

which is the result of removing a fermion from the flat density many-body state in Eq. (3.4) and satisfies:

$$\Big(\tilde{a}_{n=1}^\dagger \tilde{a}_{n=1} - \nu_x\Big)|\Phi_{\mathrm{qh}}\rangle = -\frac{1}{2}\,|\Phi_{\mathrm{qh}}\rangle, \tag{3.12}$$

$$\Big(\tilde{b}_{n=N}^\dagger \tilde{b}_{n=N} - \nu_x\Big)|\Phi_{\mathrm{qh}}\rangle = -\frac{1}{2}\,|\Phi_{\mathrm{qh}}\rangle. \tag{3.13}$$

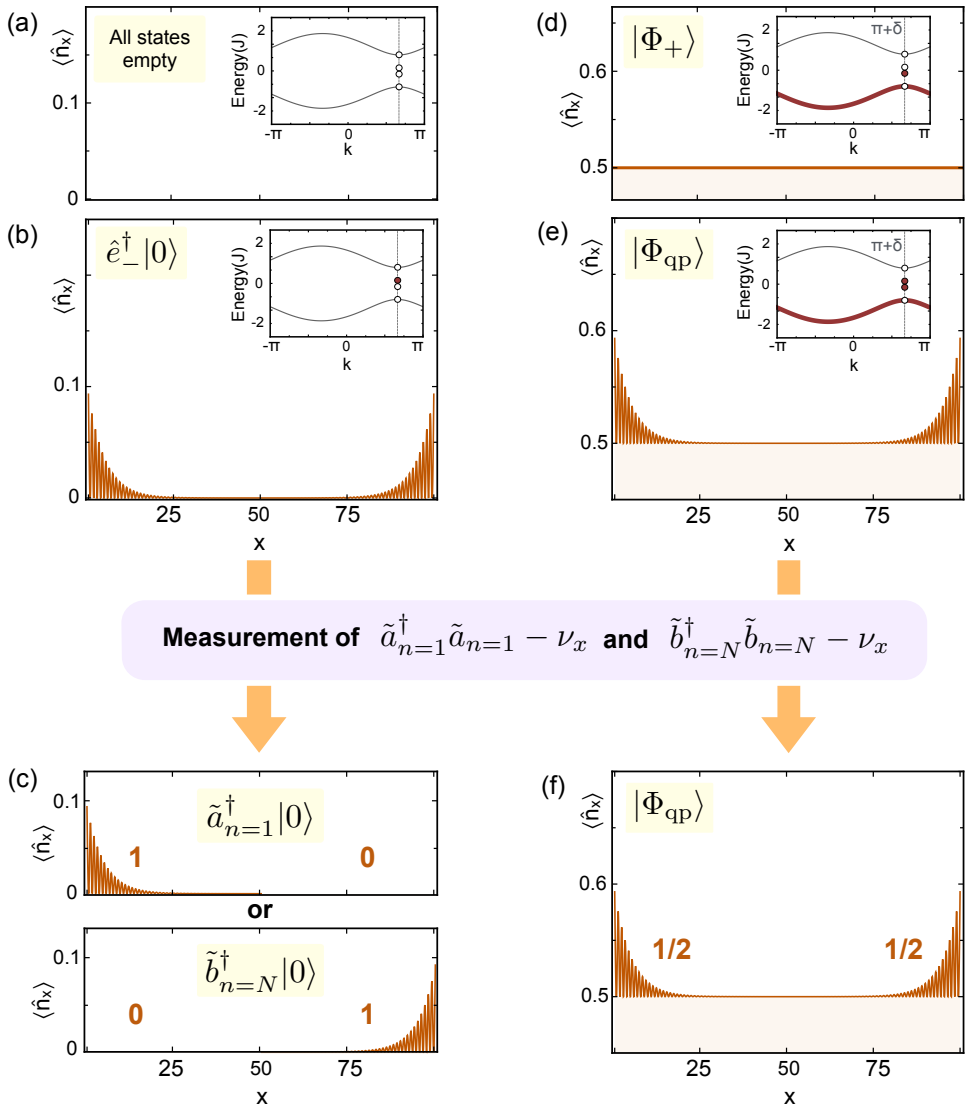

Figure 3.2: **Fractionalization in a one-dimensional topological insulator.** (b) Spatial density distribution of a fermion occupying the edge mode $\hat{e}_-^\dagger$, being all other eigenstates of the Hamiltonian empty. (c) After measuring the number operators $\tilde{a}_{n=1}^\dagger\tilde{a}_{n=1}-\nu_x$ and $\tilde{b}_{n=N}^\dagger\tilde{b}_{n=N}-\nu_x$ the state of the fermion will be $\tilde{a}_{n=1}^\dagger|0\rangle$ or $\tilde{b}_{n=N}^\dagger|0\rangle$, being both possibilities equally probable. In this case the fermion is found to be at one of the two edges of the system. (d) Spatial density distribution of the many-body state $|\Phi_+\rangle$, in which all bulk modes in the lower energy band plus one edge mode are occupied, see Eq. (3.4). (e) Spatial density distribution of the many-body state $|\Phi_{\rm qp}\rangle$, consisting of a fermion added to a flat background density, see Eq. (3.8). (f) The measurement of $\tilde{a}_{n=1}^\dagger\tilde{a}_{n=1}-\nu_x$ and $\tilde{b}_{n=N}^\dagger\tilde{b}_{n=N}-\nu_x$ leaves the state of the system invariant and gives the outcomes 1/2 and 1/2, what indicates that two quasiparticles of fractional charge 1/2 exist at the edges of the chain on top of a flat background density. All data in this figure has been obtained by exact numerical diagonalization of our Hamiltonian H_δ for $J'/J=0.9$, $\delta=-2\pi/3$ and $N=100$.

As we have already mentioned, in order to better understand the phenomenon of fractionalization in our one-dimensional model, we can compare two different situations: a fermion occupying one edge state wave function and a fermion occupying the same state but on top of the flat density distribution that corresponds to the many-body state in Eq. (3.4).

In the first case [see Fig. 3.2(a) and (b)] we have a particle whose wave function is the superposition between two states, each of them localized at each edge of the system. Thereby, if we measure the number operators $\tilde{a}^{\dagger}_{n=1}\tilde{a}_{n=1}-\nu_x$ and $\tilde{b}^{\dagger}_{n=N}\tilde{b}_{n=N}-\nu_x$ we will obtain the outcome 1 for one of them and the outcome 0 for the other, being the two alternatives equally probable. In other words, the particle will be found at one edge of the chain and its state after the measurement will be $\tilde{a}^{\dagger}_{n=1}|0\rangle$ or $\tilde{b}^{\dagger}_{n=N}|0\rangle$ [see Fig. 3.2(c)].

In contrast, in the second situation the system is in a many-body state consisting of a fermion on top of a flat background density [see Fig. 3.2(d) and (e)]. As we have explained, see Eq. (3.9) and Eq. (3.10), this state is an eigenstate of the number operators $\tilde{a}^{\dagger}_{n=1}\tilde{a}_{n=1}-\nu_x$ and $\tilde{b}^{\dagger}_{n=N}\tilde{b}_{n=N}-\nu_x$. Therefore, if we measure such number operators we will always obtain the outcome 1/2 for both of them and the state of the system after the measurement will remain the same [see Fig. 3.2(f)]. That is, a fermion occupying an edge mode behaves in a different way, depending on whether it has been added to a flat background many-body state or not. And the reason behind this difference is the fact that the flat background many-body state represents the vacuum of a soliton field theory in which excitations with fractional particle number arise.

3.2.2 Fractionalization in momentum space

Up to now, we have discussed the phenomenon of fractionalization in position space. However, the well definition of the edge modes momentum leads to an interesting result: fractionalization also occurs in momentum space.

In the following we show how our analysis of the edge modes momentum makes possible the observation of the phenomenon of fractionalization in momentum space, which represents a new alternative way in addition to the position space. Furthermore, the fact that the edge modes in the AIII symmetry class have a momentum different from 0 and π facilitates the observation of fractionalization, as we explain later on in this section.

The momentum representation of the edge modes, see Eq. (2.9) and Eq. (2.10), allows as to decompose them as:

$$\hat{e}^{\dagger}_{\pm}=\frac{1}{\sqrt{2}}\Big(\tilde{a}^{\dagger}_{k=\pi+\delta}\pm\tilde{b}^{\dagger}_{k=\pi+\delta}\Big), \tag{3.14}$$

with:

$$\tilde{a}^\dagger_{k=\pi+\delta} = \sum_k F(k-\pi-\delta)\,\hat{a}^\dagger_k, \tag{3.15}$$

$$\tilde{b}^\dagger_{k=\pi+\delta} = \sum_k e^{i(k-\pi-\delta)(N+1)}\,F(-k+\pi+\delta)\,\hat{b}^\dagger_k, \tag{3.16}$$

being $\tilde{a}^\dagger_{k=\pi+\delta}$ and $\tilde{b}^\dagger_{k=\pi+\delta}$ two momentum components highly localized in momentum space at $k=\pi+\delta$.

In order to show the phenomenon of fractionalization in momentum space we proceed in the same way as we did in the previous section for the position space. We start by considering the many-body state $|\Phi_+\rangle$, in which all negative energy eigenstates of the Hamiltonian are occupied, see Eq. (3.4). We denote by ν_k its corresponding momentum density distribution, which consists of the expected value of $\hat{a}^\dagger_k\hat{a}_k$. Using the projectors defined in Eq. (3.5) and following the same reasoning as before we can easily prove that this momentum density distribution is also flat:

$$\nu_k = \mathrm{tr}\Big(\hat{a}^\dagger_k\hat{a}_k P_+\Big) = 1-\mathrm{tr}\Big(\hat{a}^\dagger_k\hat{a}_k P_-\Big) = 1-\nu_k \implies \nu_k = \frac{1}{2}. \tag{3.17}$$

In the same way, the momentum density distribution for $\hat{b}^\dagger_k\hat{b}_k$ is also uniform and equal to 1/2. Adding a fermion to this flat background density leads to the many-body state $|\Phi_{\mathrm{qp}}\rangle$, in which both edge modes are occupied. Therefore, the two momentum modes $\tilde{a}^\dagger_{k=\pi+\delta}$ and $\tilde{b}^\dagger_{k=\pi+\delta}$ are also occupied and we have:

$$\Big(\tilde{a}^\dagger_{k=\pi+\delta}\tilde{a}_{k=\pi+\delta}-\nu_k\Big)|\Phi_{\mathrm{qp}}\rangle = \frac{1}{2}\,|\Phi_{\mathrm{qp}}\rangle, \tag{3.18}$$

$$\Big(\tilde{b}^\dagger_{k=\pi+\delta}\tilde{b}_{k=\pi+\delta}-\nu_k\Big)|\Phi_{\mathrm{qp}}\rangle = \frac{1}{2}\,|\Phi_{\mathrm{qp}}\rangle. \tag{3.19}$$

This result states that two quasiparticles of fractional charge 1/2 exist in momentum space at the position $k+\pi+\delta$.

What are the implications for the experiment? In the experimental gauge, the edge modes are [see Eq. (3.3)]:

$$\hat{e}^\dagger_{\mathrm{exp},\pm} = \frac{1}{\sqrt{2}}\Big(\tilde{a}^\dagger_{\mathrm{exp},k=\pi+\delta} \pm \tilde{b}^\dagger_{\mathrm{exp},k=\pi-\delta}\Big), \tag{3.20}$$

with:

$$\tilde{a}^\dagger_{\mathrm{exp},k=\pi+\delta} = \sum_k F(k-\pi-\delta)\,\hat{a}^\dagger_k, \tag{3.21}$$

$$\tilde{b}^\dagger_{\mathrm{exp},k=\pi+\delta} = \sum_k e^{i(k-\pi+\delta)(N+1)}\,F(-k+\pi-\delta)\,\hat{b}^\dagger_k. \tag{3.22}$$

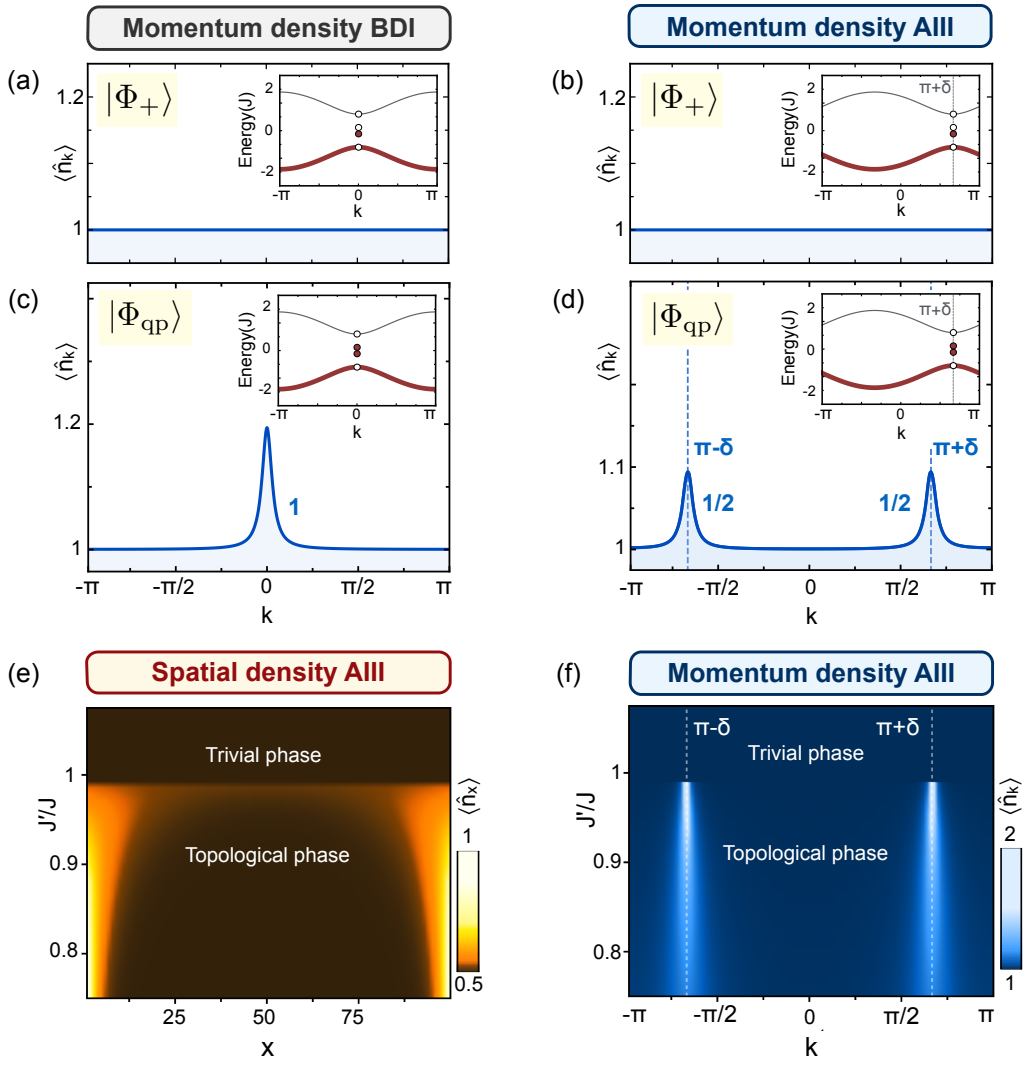

Figure 3.3: **Direct observation of fractionalization in the AIII class.** (a)-(d). Momentum density distributions (a), (c) for the BDI symmetry class ($\delta = 0$), and (b), (d) the AIII symmetry class ($\delta = -2\pi/3$), for $N = 100$ and $J'/J = 0.9$. For both symmetry classes the many body state $|\Phi_+\rangle$, see Eq. (3.4), corresponds to a flat momentum density distribution (a), (b). For the state $|\Phi_{\rm qp}\rangle$, in which a fermion is added to the flat background, the momentum density distribution in the BDI symmetry class (c) shows a single peak of charge 1 at momentum $k = \pi$ (plotted shifted at $k = 0$). In contrast, in the AIII symmetry class (d), the momentum density distribution shows two peaks of charge 1/2 localized at momenta $\pi \pm \delta$. (e), (f) Simultaneous fractionalization in position and momentum space in the AIII symmetry class. (e) Spatial density distribution and (f) momentum density distribution for the many body state $|\Phi_{\rm qp}\rangle$, such that the upper band is empty, as a function of the ratio between the two hopping amplitudes J'/J for $N = 100$ and $\delta = -2\pi/3$. In the topological phase two peaks of charge 1/2 arise at the edge of the chain and also at momenta $\pi \pm \delta$ in momentum space.

That is, the two momentum modes that form the edge states are localized at different positions in the momentum space. The mode $\tilde{a}$ is localized in position space at the left edge of the chain and at momentum $k = \pi + \delta$ in momentum space, whereas the mode $\tilde{b}$ is localized in position space at the right edge of the system and at momentum $k = \pi - \delta$ in momentum space.

This means a significant difference between the BDI symmetry class and the AIII symmetry class. For the BDI class ($\delta = 0, \pi$) a particle added to a uniform background will consist of two quasiparticles bound together at the same momentum position. The momentum distribution will show a single peak at momentum $k = \pi$ or $k = 0$ enclosing a total charge 1 [Fig. 3.3(c)]. For the AIII case, in contrast, a particle added to a uniform background will split into two halves located at opposite momenta $(\pi - \delta, \pi + \delta)$. The momentum distribution will show two peaks, each enclosing a 1/2 charge [Fig. 3.3(d)]. In the AIII class splitting of the fermion occurs therefore both in position and momentum spaces [Fig. 3.3(e),(f)]. The splitting in momentum is a direct consequence of the non-zero momentum of the edge modes, which is in turn a direct manifestation of the breaking of time reversal symmetry characterizing the AIII class.

Part II

Interference of fractionalized quasiparticles in a one-dimensional topological insulator

Chapter 4

Interference of fractionalized quasiparticles

4.1 Quench to the critical point

We have designed a quench protocol for the one-dimensional model H_δ in which two fractionalized quasiparticles move along the system at constant velocity and almost without dissipation. They interfere with each other and keep on moving until they reach the edges of the system. Afterwards, they bounce and repeat the same process over and over.

Such dynamics emerges after quenching the ratio between the two hopping amplitudes from the topological phase to the critical point:

$$H_\delta(J' < J) \longrightarrow H_\delta(J' = J), \tag{4.1}$$

and is the consequence of two ingredients:

i) The uniform background spatial density of the many-body state $|\Phi_+\rangle$ [Eq. (3.4)], in which all bulk eigenstates in the lower energy band plus one edge mode are occupied, does not evolve in time. Thereby, quasiparticles can be defined on top on that flat background density at any time.

ii) At the critical point, the gap between two energy bands of the system closes at $k = \pi + \delta$ [see Fig.4.1(b)]. Therefore, the dispersion relation is almost linear around that momentum value, which is precisely the momentum at which the edge modes are localized in momentum space. The simultaneous good definition of both the position and the momentum of the edge modes, together with an almost linear dispersion relation, makes them propagate at constant velocity along the system while preserving their good spatial and momentum localizations.

The combination of *i)* and *ii)* leads to quench dynamics in which two quasiparticles move along the system on top of a uniform background density and interfere with each other. In the following sections we explain in detail such process.

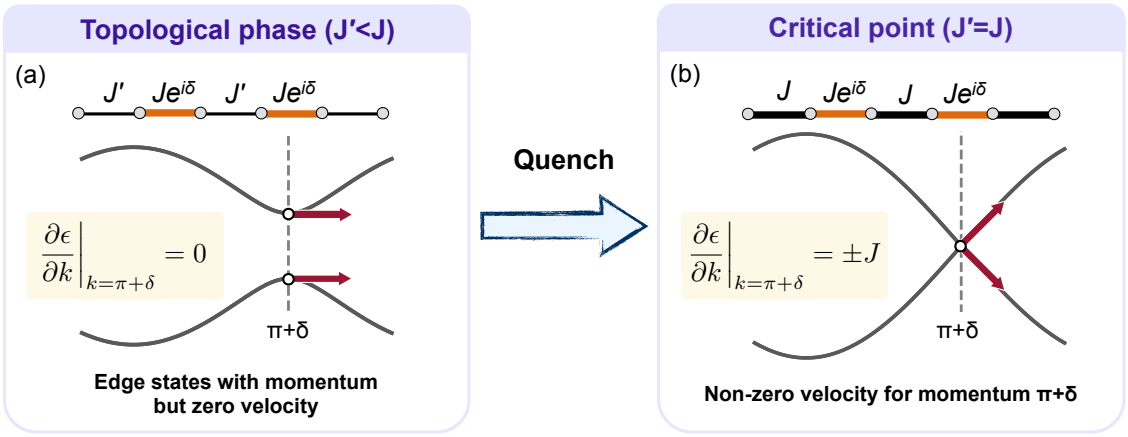

Figure 4.1: **Quench to the critical point.** The system is prepared somewhere in its topologically non-trivial phase, so that two quasiparticles exist at the edges of the chain. For that, we need $J' < J$. In that situation, (a), the two edge modes have momentum $\pi + \delta$ and no velocity. After quenching the ratio between the two hopping amplitudes to $J'/J = 1$, the edge modes are localized in momentum space where the gap has been closed and the dispersion relation is almost linear (b). In consequence, they have a non-zero velocity and propagate along the system.

4.2 Absence of evolution of flat background

We want to compute the spatial density distribution of the many-body state $|\Phi_+\rangle$ as a function of time, that is:

$$\nu_x(t) = \langle\Phi_+|\, U^\dagger(t)\, \hat{n}_x\, U(t)\, |\Phi_+\rangle, \tag{4.2}$$

where $U(t) = \exp(-itH_\delta/\hbar)$ is the time evolution operator.

In order to compute this spatial density evolution we start by exploiting the chiral symmetry of the Hamiltonian. First, the chiral operator U_S transforms every positive energy eigenstate into a negative energy eigenstate and vice versa, and thus $U_S\,|\Phi_-\rangle = |\Phi_+\rangle$, where $|\Phi_-\rangle$ is the many-body state in which all positive energy eigenstates are occupied. Second, the chiral operator is such that $U_S^\dagger\, H\, U_S = -H$, so that $U_S^\dagger\, U(t)\, U_S = U(-t)$. Furthermore, it leaves the number operator $\hat{n}_x$ invariant. The combination of these three properties implies that the spatial density distribution of the many-body state $|\Phi_+\rangle$ at positive time t is equal to the spatial density distribution of the many-body state $|\Phi_-\rangle$ at negative time $-t$. That is:

$$\begin{aligned}\nu_x(t) =& \langle\Phi_+|\, U^\dagger(t)\, \hat{n}_x\, U(t)\, |\Phi_+\rangle = \langle\Phi_-|\, U_S^\dagger\, U^\dagger(t)\, \hat{n}_x\, U(t)\, U_S\, |\Phi_-\rangle = \\ & \langle\Phi_-|\, U^\dagger(-t)\, U_S^\dagger\, \hat{n}_x\, U_S\, U(-t)\, |\Phi_-\rangle = \langle\Phi_-|\, U^\dagger(-t)\, \hat{n}_x\, U(-t)\, |\Phi_-\rangle \end{aligned} \tag{4.3}$$

We can simplify this computation by using the unitary transformation V that connects the Hamiltonian with a phase δ to the one with no phase at all, that is:

$V\,H_\delta\,V^\dagger = H_{\delta=0}$ [see Eq. (1.40)]. We have:

$$\begin{aligned}\langle\Phi_-|\,U^\dagger(-t)\,\hat{n}_x\,U(-t)\,|\Phi_-\rangle = \\ &\overset{a}{=} \langle\Phi_-^{\delta=0}|\,V\,U^\dagger(-t)\,\hat{n}_x\,U(-t)\,V^\dagger\,|\Phi_-^{\delta=0}\rangle = \\ &\overset{b}{=} \langle\Phi_-^{\delta=0}|\,U^\dagger_{\delta=0}(-t)\,V\,\hat{n}_x\,V^\dagger\,U_{\delta=0}(-t)\,|\Phi_-^{\delta=0}\rangle = \\ &\overset{c}{=} \langle\Phi_-^{\delta=0}|\,U^\dagger_{\delta=0}(-t)\,\hat{n}_x\,U_{\delta=0}(-t)\,|\Phi_-^{\delta=0}\rangle = \\ &\overset{d}{=} \langle\Phi_-|\,U^\dagger(t)\,\hat{n}_x\,U(t)\,|\Phi_-\rangle. \end{aligned} \tag{4.4}$$

Here, we have used that (a) $|\Phi_\pm\rangle = V^\dagger\,|\Phi_\pm^{\delta=0}\rangle$. We have also used that (b) the quench does not change the value of δ and thereby the time evolution operator for arbitrary δ is connected to the one for $\delta = 0$ through the same unitary V:

$$U(t) = V U_{\delta=0}(t) V^\dagger. \tag{4.5}$$

Moreover, we have used that (c) the density operator $\hat{n}_x$ is invariant under V, since V only introduces a local phase shift. Finally we have that (d) for $\delta = 0$ the system has time reversal symmetry and thus we can invert the time evolution. The result can be generalized for any δ following the same reasoning and using again (a), (b) and (c).

From Eq. (4.3) and Eq. (4.4) we conclude that the two many-body states $|\Phi_+\rangle$ and $|\Phi_-\rangle$ show the same spatial density distribution at all times. In addition, the evolved projectors $P_+(t)$ and $P_-(t)$, which correspond to the subspaces generated by all negative and positive eigenstates of the Hamiltonian, respectively [see Eq. (3.5)], sum to identity at any time. In consequence, we have:

$$\nu_x(t) = \mathrm{tr}\Big(\hat{n}_x P_+(t)\Big) = 1 - \mathrm{tr}\Big(\hat{n}_x P_-(t)\Big) = 1 - \mathrm{tr}\Big(\hat{n}_x P_+(t)\Big) = 1 - \nu_x(t), \tag{4.6}$$

what leads us to the final result:

$$\nu_x(t) = \frac{1}{2}. \tag{4.7}$$

In conclusion, the flat background density of the many-body state $|\Phi_+\rangle$ remains constant in time.

4.3 Free propagation of edge modes

The spatial density distribution of the edge modes at time t is given by:

$$\langle e_\pm|\,U^\dagger(t)\,\hat{n}_x\,U(t)\,|e_\pm\rangle, \tag{4.8}$$

being $|e_\pm\rangle \equiv \hat{e}^\dagger_\pm|0\rangle$ and $U(t)$ the time evolution operator.

As we did before, we can use the unitary transformation V that connects the Hamiltonian with a phase δ to the one with no phase to simplify this computation.

We have:

$$\begin{aligned}\langle e_\pm|\, U^\dagger(t)\,\hat{n}_x\,U(t)\,|e_\pm\rangle = \\ &\overset{a}{=} \langle e_{\pm,\delta=0}|\, V\,U^\dagger(t)\,\hat{n}_x\,U(t)\,V^\dagger\,|e_{\pm,\delta=0}\rangle = \\ &\overset{b}{=} \langle e_{\pm,\delta=0}|\, U^\dagger_{\delta=0}(t)\,V\,\hat{n}_x\,V^\dagger\,U_{\delta=0}(t)\,|e_{\pm,\delta=0}\rangle = \\ &\overset{c}{=} \langle e_{\pm,\delta=0}|\, U^\dagger_{\delta=0}(t)\,\hat{n}_x\,U_{\delta=0}(t)\,|e_{\pm,\delta=0}\rangle. \end{aligned} \tag{4.9}$$

Where we have used that (a) $|e_\pm\rangle = V^\dagger\,|e_{\pm,\delta=0}\rangle$, (b) $U(t) = VU_{\delta=0}(t)V^\dagger$, and (c) the density operator $\hat{n}$ is invariant under V. In conclusion, we can compute the edge states spatial density evolution for $\delta = 0$, as we know that the result holds for arbitrary δ.

For $\delta = 0$ the time evolution Hamiltonian is:

$$H_{\text{Quench}} = H_{\delta=0}(J = J') = -\sum_{x=1}^{2N} \hat{d}^\dagger_x \hat{d}_{x+1} + \text{h.c.}, \tag{4.10}$$

where $\hat{d}^\dagger_{2n-1} \equiv \hat{a}^\dagger_n$ and $\hat{d}^\dagger_{2n} \equiv \hat{b}^\dagger_n$, with $n = 1, ..., N$. The eigenstates of this time evolution Hamiltonian are:

$$|q\rangle = \sum_{x=1}^{2N} \sin qx\, \hat{d}^\dagger_x, \tag{4.11}$$

with eigenvalues $\epsilon(q) = -2J\cos q$, where $q = m\pi/2L$, $m = 1, ..., 2N$ and $L = N + 1/2$. The edge eigenstates of $H_{\delta=0}$ (before the quench, with $J' < J$), are:

$$|e_{\pm,\delta=0}\rangle = \frac{1}{\sqrt{2}}\big(\,|l\rangle \pm |r\rangle\,\big), \tag{4.12}$$

being $|l\rangle = \tilde{a}^\dagger_{n=1}\,|0\rangle$ and $|r\rangle = \tilde{b}^\dagger_{n=N}\,|0\rangle$ the edge modes located at the let and right ends of the system, respectively [see Eq. (2.4) and Eq. (2.5)]. They are written in terms of the $\hat{d}^\dagger_x$ modes as:

$$|l\rangle = \sum_{x=1}^{2N} \sin\frac{\pi}{2}x\,\psi(x)\,\hat{d}^\dagger_x\,|0\rangle\,, \tag{4.13}$$

$$|r\rangle = \sum_{x=1}^{2N} \cos\frac{\pi}{2}x\,\psi(2L-x)\,\hat{d}^\dagger_x\,|0\rangle\,, \tag{4.14}$$

with:

$$\psi(x) = \begin{cases} 0, & x < 1, \\ \frac{1}{\sqrt{\kappa}}\sinh\frac{\xi}{2}(2N+1-x), & 1 \le x \le 2N, \\ 0, & x > 2N, \end{cases} \tag{4.15}$$

being $\kappa = \sum_{x=1}^{2N} \sinh^2(\xi x/2)$ a normalization constant. It is convenient to define the following states:

$$|l_j^{\pm}\rangle = \sum_{x=1}^{2N} e^{\pm i\frac{\pi}{2}x}\, \psi(x+1-j)\, \hat{d}_x^{\dagger}\, |0\rangle\,, \tag{4.16}$$

$$|r_j^{\pm}\rangle = \sum_{x=1}^{2N} e^{\pm i\frac{\pi}{2}x}\, \psi(j+1-x)\, \hat{d}_x^{\dagger}\, |0\rangle\,. \tag{4.17}$$

On one hand, $|l_j^{\pm}\rangle$ is a state of momentum $\pm\pi/2$ with a spatial density distribution equal to the spatial density distribution of the state $|l\rangle$ but shifted a distance $j+1$, so that it reaches its maximum value at position $x = j$ [see Fig. 4.2(a) and (b)]. On the other hand, $|r_j^{\pm}\rangle$ is a state of momentum $\pm\pi/2$ with a spatial density distribution equal to the spatial density distribution of the state $|r\rangle$ but shifted a distance $2N-j$, so that it reaches its maximum value at position $x = j$ [see Fig. 4.2(c) and (d)].

Using these states, the edge states in Eq. (4.13) and Eq. (4.14) can be decomposed into two components of opposite momenta:

$$|l\rangle = \frac{1}{2i}\Big(\, |l_1^{+}\rangle - |l_1^{-}\rangle\, \Big), \tag{4.18}$$

$$|r\rangle = \frac{1}{2}\Big(\, |r_{2N}^{+}\rangle + |r_{2N}^{-}\rangle\, \Big). \tag{4.19}$$

In order to compute the time evolution of the edge states, we first write them using the basis $\{|q\rangle\}$ of eigenstates of the quench Hamiltonian, see Eq. (4.11). We have:

$$|l_j^{\pm}\rangle = \frac{e^{\pm i\frac{\pi}{2}(j-1)}}{2i} \sum_q \left[e^{iq(j-1)}\, G\left(-q \mp \frac{\pi}{2}\right) - e^{-iq(j-1)}\, G\left(q \mp \frac{\pi}{2}\right) \right] |q\rangle\,, \tag{4.20}$$

$$|r_j^{\pm}\rangle = \frac{e^{\pm i\frac{\pi}{2}(j+1)}}{2i} \sum_q \left[e^{iq(j+1)}\, G\left(q \pm \frac{\pi}{2}\right) - e^{-iq(j+1)}\, G\left(-q \pm \frac{\pi}{2}\right) \right] |q\rangle\,, \tag{4.21}$$

where:

$$G(q) = \sum_{x=1}^{2N} e^{-iqx}\psi(x). \tag{4.22}$$

Here, we have used the fact that the wave functions of $|l_j^{\pm}\rangle$ and $|r_j^{\pm}\rangle$ are concentrated around the position $x = j$, so that regions far away from that position do not contribute to the scalar products $\langle q\,|l_j^{\pm}\rangle$ and $\langle q\,|r_j^{\pm}\rangle$. As the wave function of $|l_j^{\pm}\rangle$ is concentrated to the right of $x = j$, see Fig. 4.2(b), the expression in Eq. (4.20) holds for any j not close to $2N$. Similarly, the expression in Eq. (4.21) holds for j not close to 1, as the wave function of $|r_j^{\pm}\rangle$ is localized to the left of $x = j$, see Fig. 4.2(d).

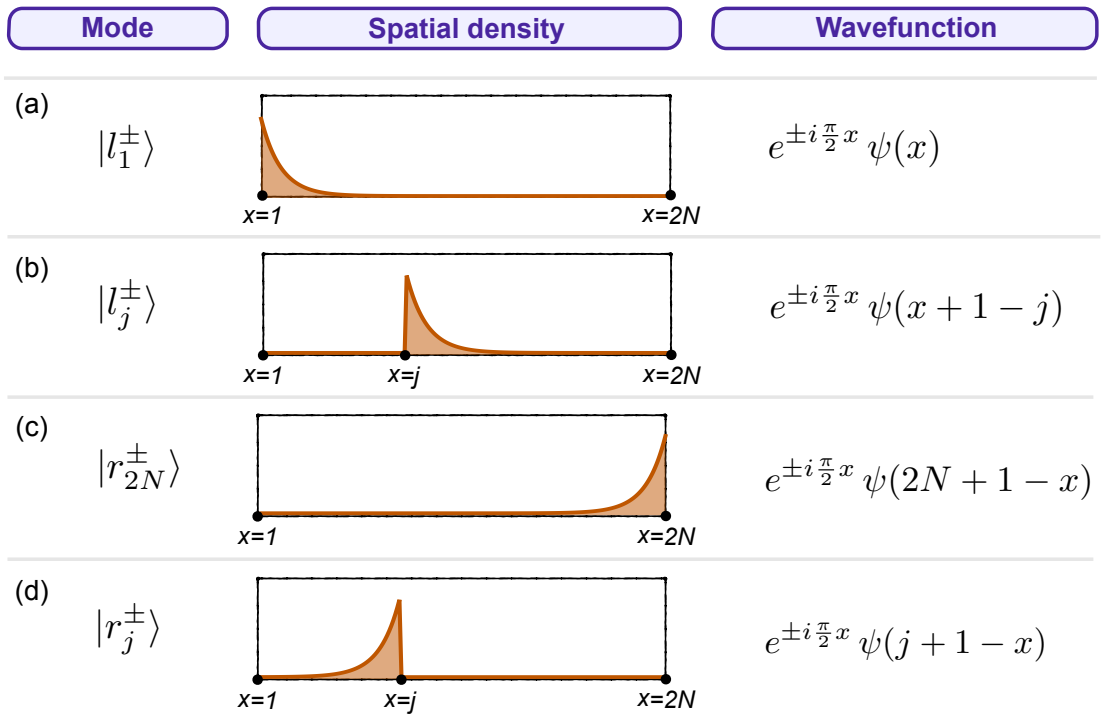

Figure 4.2: **Edge modes decomposition and shifted modes.** The edge modes of $H_{\delta=0}$, as well as their time evolution after the quench $H_{\delta=0}(J'<J) \longrightarrow H_{\delta=0}(J'=J)$, can be written using the states $|l_j^{\pm}\rangle$ and $|r_j^{\pm}\rangle$. (a) The states $|l_1^{\pm}\rangle$ are localized at the left edge of the system and form the left edge eigenstate of $H_{\delta=0}$, see Eq. (4.18). (b) For an arbitrary j, the states $|l_j^{\pm}\rangle$ consist of the the same spatial density distribution, but shifted so that its maximum value corresponds to the position $x=j$. (c) The states $|r_{2N}^{\pm}\rangle$ are localized at the right edge of the system and form the right edge eigenstate of $H_{\delta=0}$, see Eq. (4.19). (d) For arbitrary j, the states $|r_j^{\pm}\rangle$ show a shifted spatial density distribution with its maximum value at position $x=j$. The superscript $\pm$ in all states indicates a factor $e^{\pm i\pi x/2}$ in the wave function, so that the state has momentum $\pm\pi/2$.

Once we have the edge states written in terms of the basis of eigenstates of the quench Hamiltonian, we can easily compute their time evolution as:

$$U(t)\,|l_1^{\pm}\rangle = \frac{1}{2i}\sum_q e^{-it\epsilon(q)/J}\left[G\left(-q\mp\frac{\pi}{2}\right)-G\left(q\mp\frac{\pi}{2}\right)\right]|q\rangle\,, \tag{4.23}$$

$$U(t)\,|r_{2N}^{\pm}\rangle = \frac{e^{\pm i\pi(N+1/2)}}{2i}\sum_q e^{-it\epsilon(q)/J}\left[G\left(q\pm\frac{\pi}{2}\right)-G\left(-q\pm\frac{\pi}{2}\right)\right]|q\rangle\,, \tag{4.24}$$

being the time t expressed in units of $\hbar/J$. Here, we have used that $e^{\pm iq(2N+1)}=1$, as $q=m\pi/(N+1/2)$ with $m=1,...,2N$.

Now, we use two important properties of the edge modes. On one hand, they are localized in momentum space at $\pm\pi/2$, where the second derivative of the quench

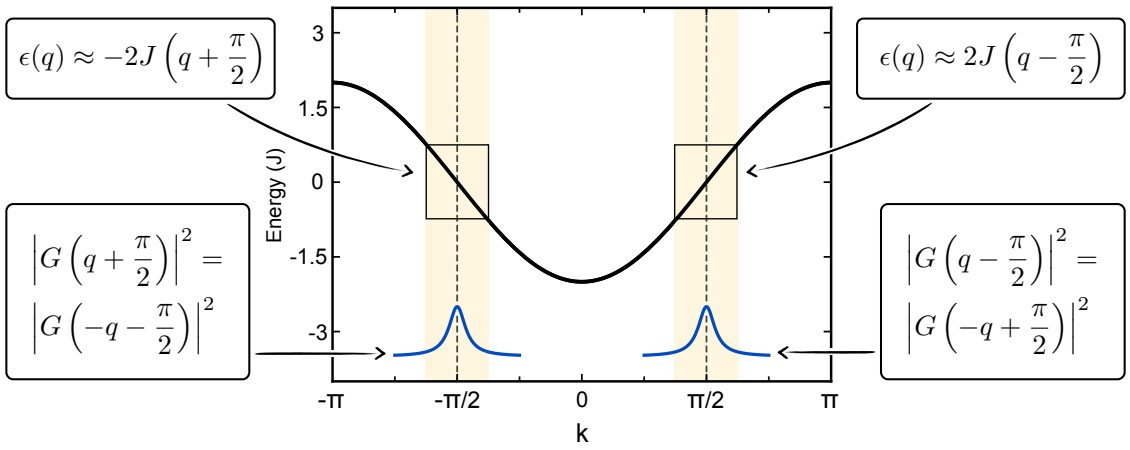

Figure 4.3: **Linear dispersion relation approximation.** Dispersion relation of the quench Hamiltonian $H_{\delta=0}(J' = J)$ (black line) and detail of the edge modes momentum distribution (blue lines). The dispersion relation is almost linear for momenta close to the values $\pm\pi/2$. This property, together with the well localization of the edge modes in momentum space at precisely those particular values, allows us to make the approximation $\epsilon(q) \approx \pm 2J(q \mp \pi/2)$.

Hamiltonian dispersion relation vanishes. On the other hand, they are well localized around that values, as we explained in Chapter 2. In consequence, their time evolution is governed by an almost linear dispersion relation, see Fig. 4.3. The first order Taylor expansion of the dispersion relation of the quench Hamiltonian at momentum $q = \pm\pi/2$ is:

$$\epsilon(q) = -2J\cos q = \pm 2J\left(q \mp \frac{\pi}{2}\right) + \mathcal{O}\left(\left(q \mp \frac{\pi}{2}\right)^3\right), \tag{4.25}$$

and therefore we can approximate the dynamical phase in the time evolution as:

$$-it\epsilon(q)/J \approx \mp i2t\left(q \mp \frac{\pi}{2}\right). \tag{4.26}$$

By substituting this approximation in Eq. (4.23) and Eq. (4.24), we get the time evolution of $|l_1^{\pm}\rangle$ and $|r_{2N}^{\pm}\rangle$:

$$U(t)\,|l_1^{\pm}\rangle = \frac{e^{i\pi t}}{2i}\sum_q \left[e^{\pm i2tq}\,G\left(-q \mp \frac{\pi}{2}\right) - e^{\mp i2tq}\,G\left(q \mp \frac{\pi}{2}\right)\right]|q\rangle\,, \tag{4.27}$$

$$U(t)\,|r_{2N}^{\pm}\rangle = \frac{e^{\pm i\pi(N+\frac{1}{2})}e^{i\pi t}}{2i}\sum_q \left[e^{\pm i2tq}\,G\left(q \pm \frac{\pi}{2}\right) - e^{\mp i2tq}\,G\left(-q \pm \frac{\pi}{2}\right)\right]|q\rangle\,, \tag{4.28}$$

We have used the approximation $\epsilon(q) \approx 2J(q-\pi/2)$ in the terms with $G(-q+\pi/2)$ and $G(q-\pi/2)$, as they are concentrated around the momentum $\pi/2$; and the approximation $\epsilon(q) \approx -2J(q+\pi/2)$ in the terms with $G(-q-\pi/2)$ and $G(q+\pi/2)$, as they are localised at the momentum $-\pi/2$.

Comparing Eq. (4.27) with Eq. (4.20) we see that the state $|l_1^{\pm}\rangle$ becomes the state $|l_{1+2t}^{\pm}\rangle$ at time $\pm t$; and comparing Eq. (4.28) with Eq. (4.21) we see that the state $|r_{2N}^{\pm}\rangle$ becomes the state $|r_{2N-2t}^{\pm}\rangle$ at time $\mp t$. That is:

$$U(\pm t)\,|l_1^{\pm}\rangle = |l_{1+2j}^{\pm}\rangle\,, \tag{4.29}$$

$$U(\mp t)\,|r_{2N}^{\pm}\rangle = |r_{2N-2t}^{\pm}\rangle\,. \tag{4.30}$$

In other words, the state $|l_1^{+}\rangle$, with momentum $\pi/2$ and localized at the left edge of the chain, moves towards the bulk after the quench and evolves *into* $|l_{1+2j}^{+}\rangle$ [see Fig. 4.4(a)]. On the contrary, the state $|l_1^{-}\rangle$ cannot move in the direction of its momentum $-\pi/2$, as it is already at the left edge of the system. Therefore it evolves *from* the state $|l_{1+2t}^{-}\rangle$ [see Fig. 4.4(a)]. Analogously, the two modes at the right edge of the system, $|r_{2N}^{+}\rangle$ and $|r_{2N}^{-}\rangle$ evolve *from* $|r_{2N-2t}^{+}\rangle$ and *into* $|r_{2N-2t}^{-}\rangle$, respectively [see Fig. 4.4(b)].

This results hold for t smaller that N, so that the wave packets do not have enough time to reach the opposite edge of the chain. If we evaluate Eq. (4.27) and Eq. (4.28) for an evolution time $T = N + 1/2$, we get:

$$U(T)\,|l_1^{\pm}\rangle = \frac{e^{i\pi(N+\frac{1}{2})}}{2i}\sum_q \left[G\left(-q \mp \frac{\pi}{2}\right) - G\left(q \mp \frac{\pi}{2}\right)\right]|q\rangle\,, \tag{4.31}$$

$$U(T)\,|r_{2N}^{\pm}\rangle = \frac{\pm 1}{2i}\sum_q \left[G\left(-q \pm \frac{\pi}{2}\right) - G\left(q \pm \frac{\pi}{2}\right)\right]|q\rangle\,, \tag{4.32}$$

where we have used that $e^{\pm i2Tq} = 1$ as $q = m\pi/(N+1/2)$ with $m = 1, .., 2N$. Comparing Eq. (4.31) and Eq. (4.32) with Eq. (4.20) and Eq. (4.21), respectively, we conclude that:

$$U(T)\,|l_1^{\pm}\rangle = \pm\,|r_{2N}^{\mp}\rangle\,, \tag{4.33}$$

$$U(T)\,|r_{2N}^{\pm}\rangle = \pm\,|l_1^{\mp}\rangle\,, \tag{4.34}$$

that is, after time T each state becomes the state of opposite momentum located at the opposite edge of the system [see Fig. 4.4(c) and (d)].

Combining the results in Eq. (4.29), Eq. (4.30) and Eq. (4.33) we can compute the time evolution of the left edge mode:

$$U(t)\,|l\rangle \overset{a}{=} \frac{1}{2i}\left[U(t)\,|l_1^{+}\rangle - U(t-T)U(T)\,|l_1^{-}\rangle\right] \overset{b}{=} \frac{1}{2i}\left[|l_{1+2t}^{+}\rangle + U(t-T)\,|r_{2N}^{+}\rangle\right] \overset{c}{=}$$
$$\frac{1}{2i}\left[|l_{1+2t}^{+}\rangle + |r_{2t-1}^{+}\rangle\right] = \frac{1}{2i}\sum_{x=1}^{2N} e^{i\frac{\pi}{2}x}\left[\psi(x-2t) + \psi(2t-x)\right]\hat{d}_x^{\dagger}\,|0\rangle\,. \tag{4.35}$$

Here, we have first (a) separated $|l\rangle$ into the two different momentum components $|l_1^{+}\rangle$ and $|l_1^{-}\rangle$, as well as decomposed the time evolution operator that acts on the negative momentum component as the product of two time evolution operators: $U(t) = U(t-T)U(T)$. Then (b) the positive momentum component $|l_1^{+}\rangle$ propagates

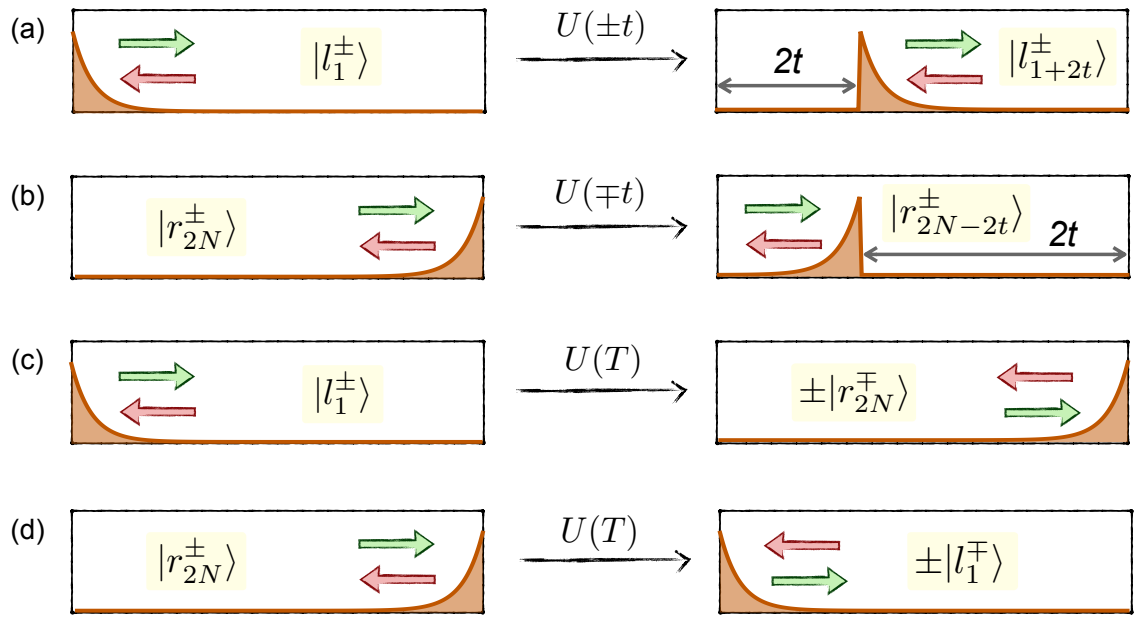

Figure 4.4: **Time evolution of edge modes components.** (a), (b) The states $|l_1^+\rangle$ and $|r_{2N}^-\rangle$ are localized at the left and right edges of the system and have momentum $\pi/2$ and $-\pi/2$, respectively. Therefore, they can propagate towards the bulk at constant velocities and we have that: $U(t)\,|l_1^+\rangle = |l_{1+2t}^+\rangle$ and $U(t)\,|r_{2N}^-\rangle = |r_{2N-2t}^-\rangle$. In contrast, the states $|l_1^-\rangle$ and $|r_{2N}^+\rangle$ have momentum towards the edges of the system, and thus they evolve from the states $|l_{1+2t}^-\rangle$ and $|r_{2N-2t}^+\rangle$, respectively. (c), (d) For an evolution time $T = N+1/2$, each state gets its spatial density distribution reflected with respect to the center of the chain and its momentum inverted. In this way, we have: $U(T)\,|l_1^{\pm}\rangle = \pm\,|r_{2N}^{\mp}\rangle$ and $U(T)\,|r_{2N}^{\pm}\rangle = \pm\,|l_1^{\mp}\rangle$.

during time t and becomes $|l_{1+2t}^+\rangle$, whereas the negative momentum component $|l_1^-\rangle$ evolves during time T and becomes $|r_{2N}^+\rangle$, getting its spatial density distribution reflected and its momentum inverted. Finally (c) the reflected component $|r_{2N}^+\rangle$ evolves backwards in time and becomes $|r_{2t-1}^+\rangle$. In this way, the two initial components form a wave packet centred at position $2t$ with momentum $\pi/2$ that moves towards the bulk at a constant velocity [see Fig. 4.5].

Analogously, the results in Eq. (4.29), Eq. (4.30) and Eq. (4.34) allow us to compute the time evolution of the right edge mode:

$$\begin{aligned} U(t)\,|r\rangle =& \frac{1}{2}\left[U(t-T)U(T)\,|r_{2N}^+\rangle + U(t)\,|r_{2N}^-\rangle\right] = \\ & \frac{1}{2}\left[U(t-T)\,|l_1^-\rangle + |r_{2N-2t}^-\rangle\right] = \frac{1}{2}\left[|l_{1+2(T-t)}^-\rangle + |r_{2T-2t}^-\rangle\right] = \\ & \frac{1}{2}\sum_{x=1}^{2N} e^{-i\frac{\pi}{2}x}\left[\psi(x-2N-1+2t) + \psi(2N+1-2t-x)\right]\hat{d}_x^\dagger\,|0\rangle\,. \end{aligned} \tag{4.36}$$

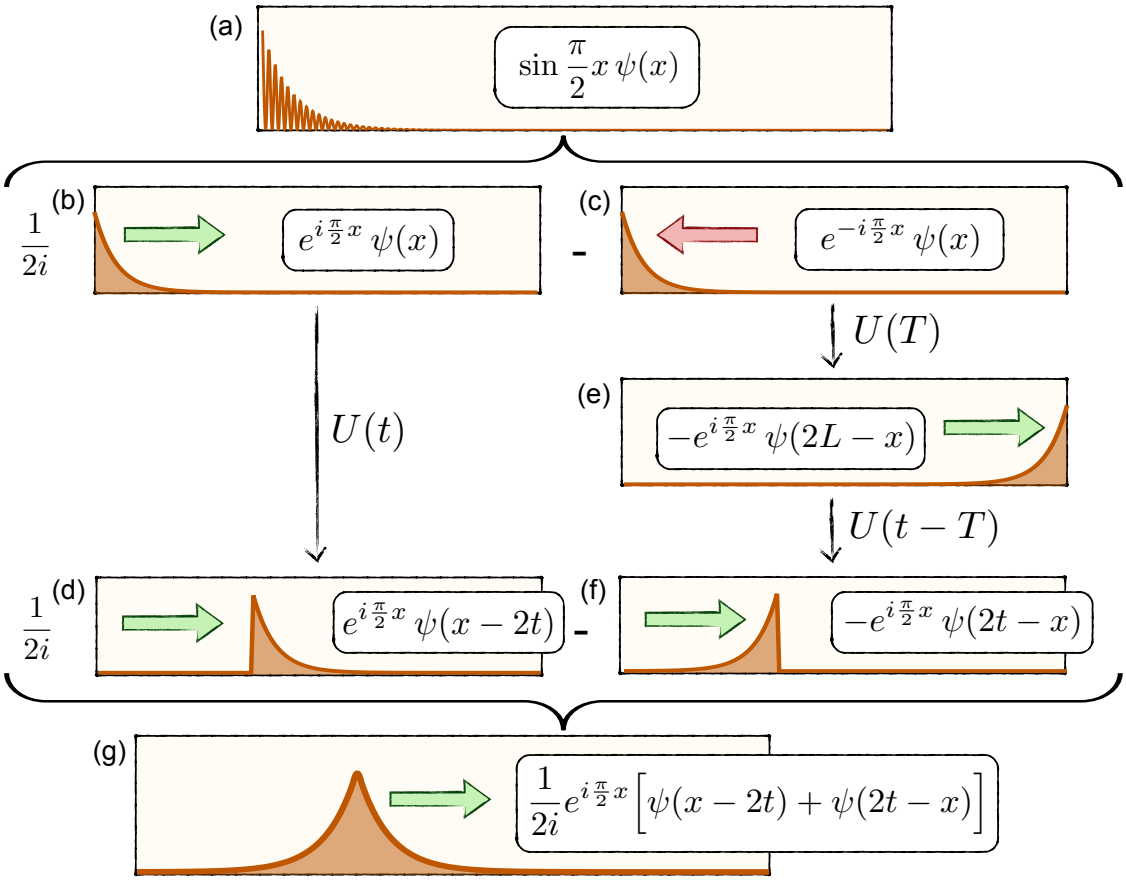

Figure 4.5: **Edge modes free propagation.** The initial edge mode located at the left side of the system, (a), is decomposed into two components, (b) and (c), of opposite momenta $\pm\pi/2$. The component with positive momentum, (b), moves to the right and gets its spatial density distribution shifted by a distance $2t$ at time t, (d). The component with negative momentum, (c), cannot move to the left as it is already at the edge of the system. We can picture its time evolution in two steps. First, it evolves during time T and gets its spatial density distribution reflected and its momentum inverted, (e). Then, it evolves backwards in time travelling a distance $2(T-t)$ to the left, (f). Finally, we sum the two components and get a wave packet that moves freely through the system at constant velocity, (g). The time evolution of the state localized at the right edge of the system, $|r\rangle$, can be visualise in a similar way.

Therefore, the state $|r\rangle$ evolves in time forming a wave packet centred at position $x = 2N + 1 - 2t$ with momentum $-\pi/2$ that moves towards the bulk at constant velocity.

From Eq. (4.33) and Eq. (4.34) we can obtain the time evolution of both edge

states, $|l\rangle$ and $|r\rangle$, at time T:

$$U(T)\,|l\rangle = \frac{1}{2i}U(T)\big(\,|l_1^+\rangle - |l_1^-\rangle\,\big) = \frac{1}{2i}\big(\,|r_{2N}^-\rangle + |r_{2N}^+\rangle\,\big) = -i\,|r\rangle\,, \tag{4.37}$$

$$U(T)\,|r\rangle = \frac{1}{2}U(T)\big(\,|r_{2N}^+\rangle + |r_{2N}^-\rangle\,\big) = \frac{1}{2}\big(\,|l_1^-\rangle - |l_1^+\rangle\,\big) = -i\,|l\rangle\,, \tag{4.38}$$

As we see, each edge state becomes the other one after time T, so that the same process is repeated over and over.

4.4 Interference of quasiparticles

We have obtained two results: after performing a quench to the critical point *i)* the uniform flat background density corresponding to the many body state $|\Phi_+\rangle$ remains constant, and *ii)* the edge states move freely through the system with almost no dissipation, reaching the opposite edges of the system, bouncing and repeating the same process again and again. Combining these two results, we get the time evolution of the many body state $|\Phi_{\rm qp}\rangle$ in which two quasiparticles exist at the edges of the system, and conclude that the quasiparticles preserve their identity during the time evolution. We have:

$$\Big[\tilde{d}^\dagger_{x=2t}\tilde{d}_{x=2t} - \nu_x\Big]\,|\Phi_{\rm qp}(t)\rangle = \frac{1}{2}\,|\Phi_{\rm qp}(t)\rangle\,, \tag{4.39}$$

with:

$$\tilde{d}^\dagger_{x=2t} = \frac{1}{2i}\sum_{x=1}^{2N} e^{i\frac{\pi}{2}x}\,[\psi(x-2t) + \psi(2t-x)]\,. \tag{4.40}$$

Which states that at time t there is a fractionalized quasiparticle with charge $1/2$ over the flat background density occupying the mode $\tilde{d}^\dagger_{x=2t}$, localized at position $x = 2t$. Analogously, there is another fractionalized quasiparticle at position $x = 2N + 1 - 2t$.

In this way, the edge states $|l\rangle$ and $|r\rangle$, located initially at the left and right edges of the system [see Fig. 4.6(b)i], evolve in time forming two wave packets that move towards the bulk keeping their good spatial and momentum localizations [see Fig. 4.6(b)ii]. They meet at the center of the system, interfere constructively with each other [see Fig. 4.6(b)iii] and continue moving until they reach the opposite edge of the lattice [see Fig. 4.6(b)iv]. At this point the two initial states are restored [see Fig. 4.6(b)v], so that the same process is repeated over and over [see Fig. 4.6(a)].

This dynamics is a consequence of the simultaneous good spatial and momentum localizations of the edge modes, together with the fact that, in the critical point, the dispersion relation of the Hamiltonian is almost linear at momentum $k = \pi + \delta$, where the edge modes are located in momentum space. The linear dispersion relation approximation holds for long evolution times, as the edge states remain localized at momentum $k = \pi + \delta$ [see Fig. 4.6(c)].

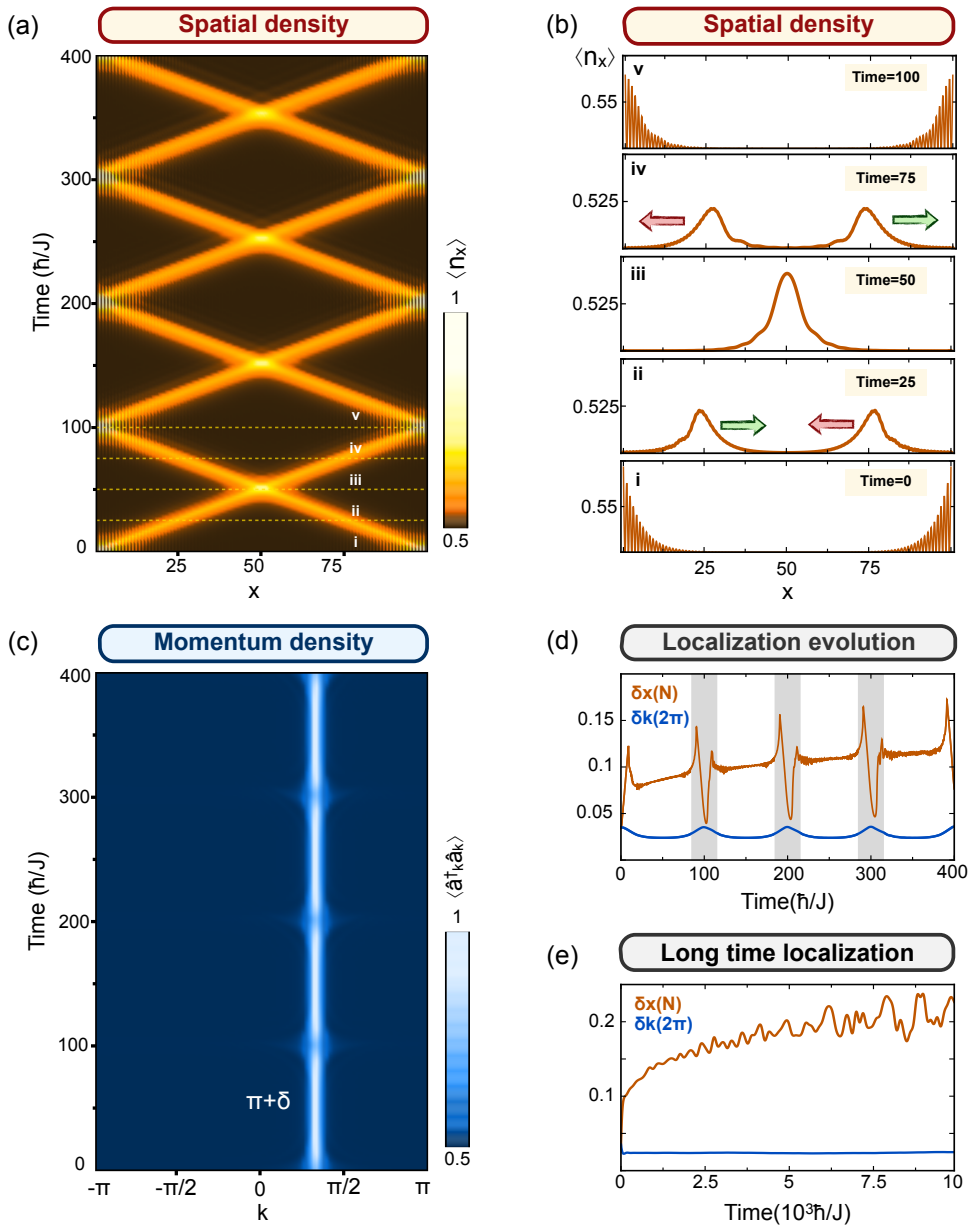

Figure 4.6: **Interference of fractionalized quasiparticles.** Time evolution of the many-body state with two fractional quasiparticles after a quench to the critical point. Parameters are $N = 100$ and $\delta = -2\pi/3$. The Hamiltonian is quenched from $J'/J = 0.9$ to $J'/J = 1$. In position space, (a) and (b), the two quasiparticles keep their definition and move towards the bulk in opposite directions on top of a uniform and constant background of density $\nu_x = 1/2$. They interfere at the center of the system, travelling back and forth with almost no dissipation. In momentum space, (c), quasiparticles keep their good localization at $\pi + \delta = \pi/3$. The spatial and momentum localization lengths remain almost constant in time, (d) and (e), with small oscillations occurring when quasiparticles bounce at the edges of the system (d).

In Fig. 4.6(d) we show how the spatial and momentum localization lengths of the edge modes evolve in time. At the beginning of the time evolution the spatial localization length increases, as the wave packet that moves along the system consists of the sum of two edge mode wave functions [see Fig. 4.4(g)], and thus has a larger spatial extension. In consequence, the momentum localization length decreases, keeping the position-momentum uncertainty constant. This localization lengths remain almost constant, with oscillations every time the quasiparticles bounce at the edges of the system [grey regions in Fig. 4.6(d)]. For long evolution times, the edge modes remain well localized in momentum space, whereas their spatial localization gets worse. Nevertheless, the spatial localization length increases slowly in time, being $\delta x \approx 0.2$ after the edge modes have travelled the whole system a hundred times [see Fig. 4.6(e)].

Part III

Classification of topological ladder models

Chapter 5

Hamiltonian characterization of topological ladder models

In this work we study models for non-interacting one-dimensional topological insulators with two different sites per unit cell, translational symmetry and in which only couplings that change the lattice index by one unit at most are allowed. That is what we call here a ladder model (see Fig. 5.1).

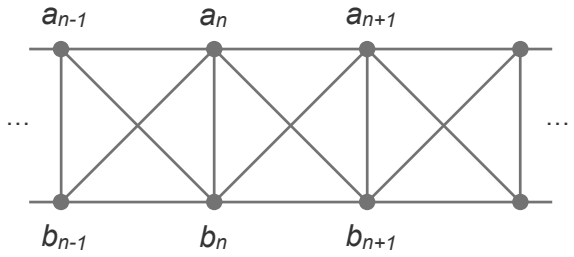

Figure 5.1: **Ladder model.** Schematic illustration of a ladder model. Each leg corresponds to one of the two different sites per unit cell and all possible couplings are represented by lines.

We denote as $\hat{a}_n^\dagger$ and $\hat{b}_n^\dagger$ the operators that create a particle in the sublattice site a_n and b_n of the n-th lattice cell, respectively. The most general ladder model corresponds to the following Hamiltonian:

$$H = -\sum_{n=1}^{N} \left(\psi_n^\dagger \, C \, \psi_n + \psi_{n+1}^\dagger \, T \, \psi_n + \psi_n^\dagger \, T^\dagger \, \psi_{n+1} \right), \tag{5.1}$$

where $\psi_n^\dagger = \begin{pmatrix} \hat{a}_n^\dagger & \hat{b}_n^\dagger \end{pmatrix}$, N is the total number of unit cells in the lattice, C is a 2×2 hermitian matrix and T a general complex 2×2 matrix. Both matrices have no dependence on the lattice index n, as we are considering the model to be translational invariant. We change to the momentum representation and write the Hamiltonian H as:

$$H = -\sum_{k} \psi_k^\dagger \, M(k) \, \psi_k, \tag{5.2}$$

where:

$$M(k) = C + e^{-ik}\, T + e^{ik}\, T^\dagger \tag{5.3}$$

is the Hamiltonian matrix. As any 2×2 hermitian matrix, it can be written as:

$$M(k) = \lambda(k)\mathbb{I} + \rho(k)\, \boldsymbol{n}(k) \cdot \boldsymbol{\sigma}, \tag{5.4}$$

being $\mathbb{I}$ the identity and $\boldsymbol{\sigma}$ a vector containing the three Pauli matrices. Here $\lambda(k)$ and $\rho(k)$ are real functions and $\boldsymbol{n}(k)$ is a real unit vector in the 3-dimensional space. The Hamiltonian matrix depends on the momentum only through the sine and cosine functions [see Eq. (5.3)] and therefore the vector $\boldsymbol{n}(k)$ can be decomposed as:

$$\rho(k)\, \boldsymbol{n}(k) = \boldsymbol{n}_0 + \boldsymbol{n}_c \cos k + \boldsymbol{n}_s \sin k, \tag{5.5}$$

being $\boldsymbol{n}_0$, $\boldsymbol{n}_c$ and $\boldsymbol{n}_s$ three constant vectors.

In the following we show how the symmetry class of a ladder Hamiltonian is determined by the properties of these three vectors. We also identify the general form of a ladder Hamiltonian in the BDI symmetry class and a ladder Hamiltonian in the AIII symmetry class. For that, we first impose chiral symmetry and obtain the most general Hamiltonian of a topologically nontrivial ladder model. Afterwards, we impose time reversal symmetry and distinguish between ladder Hamiltonian in the BDI class and a ladder Hamiltonian in the AIII class.

5.1 Ladder Hamiltonian with chiral symmetry

We consider the Hamiltonian matrix of a general ladder model, Eq. (5.4). It can be proved that it has chiral symmetry if and only if $\lambda(k) = 0$ and the vector $\boldsymbol{n}(k)$ lives in a plane that crosses the origin (see Appendix A for the details). That is, the conditions for chiral symmetry are:

$$M(k) = \rho(k)\, \boldsymbol{n}(k) \cdot \boldsymbol{\sigma}, \tag{5.6}$$

$$\{\boldsymbol{n}_0,\, \boldsymbol{n}_c,\, \boldsymbol{n}_s\} \text{ are linearly dependent.} \tag{5.7}$$

In other words, the Hamiltonian matrix has no component proportional to the identity and the three components of $\boldsymbol{n}(k)$ lie in a common plane. As a consequence, we can choose a particular orthonormal basis within that plane made by just two vectors $\boldsymbol{n}_1$ and $\boldsymbol{n}_2$ and write the Hamiltonian matrix as a combination of $\sigma_1 = \boldsymbol{n}_1 \cdot \boldsymbol{\sigma}$ and $\sigma_2 = \boldsymbol{n}_2 \cdot \boldsymbol{\sigma}$, being $\{\sigma_1, \sigma_2\} = 0$.

In conclusion, the most general ladder model for a topological insulator corresponds to a Hamiltonian matrix of the form:

$$M(k) = f_1(k)\, \sigma_1 + f_2(k)\, \sigma_2, \tag{5.8}$$

with $\{\sigma_1, \sigma_2\} = 0$ and being $f_1(k)$ and $f_2(k)$ two real functions that depend on the momentum through the sine and cosine functions. Defining:

$$\sigma_3 = -(i/2)\, [\sigma_1, \sigma_2]\,, \tag{5.9}$$

it follows that $\sigma_3 M(k) \sigma_3 = -M(k)$. Therefore we can identify the orthogonal direction to the plane where $\boldsymbol{n}(k)$ lives with the unitary operator that fulfils the chiral condition (7), that is: $U_S = \sigma_3$.

5.2 Ladder Hamiltonian in the BDI class

We consider a general Hamiltonian matrix with chiral symmetry, written as in Eq. (5.6). By imposing the condition for time reversal symmetry in Eq. (5), it can be proved (see Appendix A for the details) that the Hamiltonian has time reversal symmetry if and only if:

$$\boldsymbol{n}_s \cdot \boldsymbol{n}_0 = 0 \tag{5.10}$$

$$\boldsymbol{n}_s \cdot \boldsymbol{n}_c = 0. \tag{5.11}$$

In other words, the even and odd components of the Hamiltonian matrix must be perpendicular to each other. Combining this with the second condition for chiral symmetry, Eq. (5.7), it follows that the Hamiltonian matrix of a BDI model must be a combination of two Pauli matrices along perpendicular directions, corresponding each to an even and an odd function of the momentum, respectively. This means that there exist real parameters α, β and γ and a particular choice of the orthonormal basis $\{\boldsymbol{n}_1, \boldsymbol{n}_2\}$ such that:

$$f_1(k) = \alpha + \beta \cos k \tag{5.12}$$

$$f_2(k) = \gamma \sin k. \tag{5.13}$$

Therefore, the most general Hamiltonian for a ladder model in the BDI symmetry class corresponds to a matrix of the form:

$$M(k) = (\alpha + \beta \cos k)\, \sigma_1 + \gamma \sin k\, \sigma_2, \tag{5.14}$$

where α, β and γ are real parameters and $\{\sigma_1, \sigma_2\} = 0$. A Hamiltonian of this form has chiral symmetry because it is a particular case of Eq. (5.8), and it has time reversal symmetry since:

$$\sigma_2 \sigma_y M^*(-k) \sigma_y \sigma_2 = M(k). \tag{5.15}$$

Chiral and time reversal symmetries imply charge conjugation symmetry, therefore the condition for charge conjugation symmetry is also fulfilled. We can identify the time reversal and charge conjugation transformations that satisfy the respective symmetry conditions, Eq. (5) and Eq. (6), as: $U_T = \sigma_2 \sigma_y$ and $U_C = \sigma_1 \sigma_y$.

5.3 Ladder Hamiltonian in the AIII class

A model in the AIII symmetry class has chiral symmetry but is not time reversal symmetric. Therefore, it corresponds to a Hamiltonian matrix of the form in Eq. (5.8) that cannot be written as in Eq. (5.14).

In addition to the form in Eq. (5.8), the Hamiltonian matrix of a chiral model can be written in an alternative way, using the basis formed by $\boldsymbol{n}_c$ and $\boldsymbol{n}_s$. Since

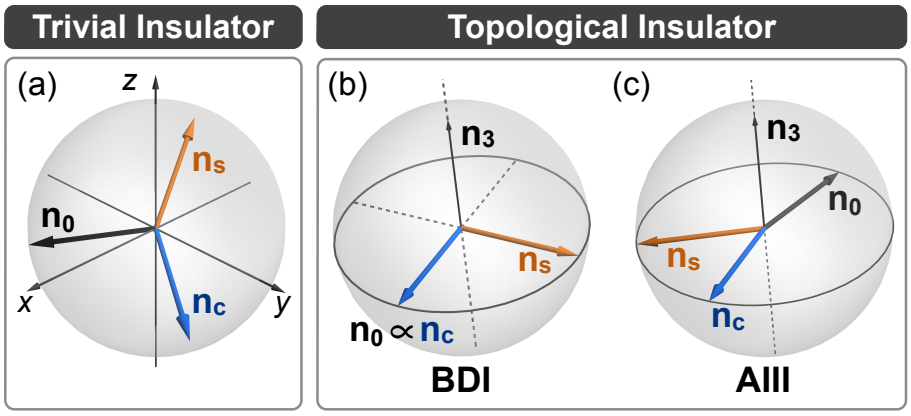

Figure 5.2: **Geometrical classification of ladder Hamiltonians.** The symmetry class of a ladder model is determined by the geometry of its Hamiltonian matrix $M(k) = (\boldsymbol{n}_0 + \boldsymbol{n}_c \cos k + \boldsymbol{n}_s \sin k) \cdot \boldsymbol{\sigma}$. In the most general case it corresponds to a normal insulator (a). When all the components lie in a common plane the system has chiral symmetry and, thus, exhibits topological properties. The orthogonal direction to that plane, denoted by the unit vector $\boldsymbol{n}_3$, corresponds to the chiral symmetry operator: $U_S = \sigma_3 = \boldsymbol{n}_3 \cdot \boldsymbol{\sigma}$. If the odd component is normal to the even ones, the system is in the BDI class (b), whereas it belongs to the AIII class otherwise (c). For the shake of clarity all vectors are represented with the same modulus, although they are in general different.

the components of the Hamiltonian matrix of a chiral model lie in a common plane, there exist real parameters α, β, η and γ such that:

$$M(k) = (\alpha + \beta \cos k)\, \sigma_c + (\eta + \gamma \sin k)\, \sigma_s, \tag{5.16}$$

with $\sigma_c = (\boldsymbol{n}_c \cdot \boldsymbol{\sigma})/|\boldsymbol{n}_c|$ and $\sigma_s = (\boldsymbol{n}_s \cdot \boldsymbol{\sigma})/|\boldsymbol{n}_s|$.

Comparing this expression to the general Hamiltonian matrix of a BDI model, Eq. (5.14), we conclude that the most general Hamiltonian for a ladder model in the AIII class corresponds to a Hamiltonian matrix of the form in Eq. (5.16) with $\eta \neq 0$ and/or $\{\sigma_c, \sigma_s\} \neq 0$. In other words, the model must break at least one of the two conditions $\eta = 0$ and $\{\sigma_c, \sigma_s\} = 0$ in order to be in the AIII class, which are equivalent to the time reversal conditions in Eq. (5.10) and Eq. (5.11).

In this way, we use two different representations for the Hamiltonian matrix of a chiral ladder. The first one, Eq. (5.8), uses an orthonormal basis $\{\boldsymbol{n}_1, \boldsymbol{n}_2\}$ and, thus, two anticommuting Pauli matrices $\boldsymbol{\sigma}_1$ and $\boldsymbol{\sigma}_2$. The second one, Eq. (5.16), in contrast, uses two Pauli matrices $\boldsymbol{\sigma}_c$ and $\boldsymbol{\sigma}_s$ whose anticommutator is in general different from zero. They are combinations of $\boldsymbol{\sigma}_1$ and $\boldsymbol{\sigma}_2$ and the four of them lie in the same plane. The first representation has the advantage of using an orthonormal basis, which is easier to deal with. On the other hand, in the second representation the functions $\sin k$ and $\cos k$ are separated in different components, which is more convenient in some situations. Only for the BDI class these two representations coin-

cide and the even and odd components of the Hamiltonian matrix can be separated in orthogonal directions.

In conclusion, the symmetry class of a ladder model for a topological insulator is determined by the geometry of the Hamiltonian matrix. Decomposing it as $M(k) = (\boldsymbol{n}_0 + \boldsymbol{n}_c \cos k + \boldsymbol{n}_s \sin k) \cdot \boldsymbol{\sigma}$, the model is topologically non-trivial only when all components lie in a common plane, corresponding to a topologically trivial insulator otherwise [Fig. 5.2(a)]. In the former case, the system belongs to the BDI class if the even and odd components are perpendicular to each other [Fig. 5.2(b)], whereas it is in the AIII class in the most general situation [Fig. 5.2(c)].

Chapter 6

6 types os topological ladder models and 6 types of Wilson fermion configurations

6.1 Topological characterization of a ladder model.

As we explained in Chapter 5, a ladder model with chiral symmetry corresponds to a Hamiltonian matrix that can be written using two different representations. On one hand:

$$M(k) = \rho(k)\, \boldsymbol{n}(k) \cdot \boldsymbol{\sigma}, \tag{6.1}$$

being the vector $\boldsymbol{n}(k)$ confined in a particular plane; that is, there exists a unitary vector $\boldsymbol{n}_3$ such that $\boldsymbol{n}_3 \cdot \boldsymbol{n}(k) = 0\ \forall k \in 1^{st}\mathcal{BZ}$. On the other hand, we can define another two unitary vectors $\boldsymbol{n}_1$ and $\boldsymbol{n}_2$ such that the three of them, $\{\boldsymbol{n}_1, \boldsymbol{n}_2, \boldsymbol{n}_3\}$, form an orthonormal basis. Therefore, the Hamiltonian matrix can also be written as:

$$M(k) = f_1(k)\, \sigma_1 + f_2(k)\, \sigma_2, \tag{6.2}$$

with $\{\sigma_1, \sigma_2\} = 0$, being $\sigma_j = \boldsymbol{n}_j \cdot \boldsymbol{\sigma}, \quad j = 1, 2$ and $f_1(k)$ and $f_2(k)$ two real functions of the momentum. Both ways of writing the Hamiltonian matrix can be related by defining the complex function $z(k)$ and the real function $\varphi(k)$ as:

$$z(k) = \rho(k)\, e^{i\varphi(k)} = f_1(k) + i f_2(k), \tag{6.3}$$

so that $\boldsymbol{n}(k) = \cos\varphi(k)\, \boldsymbol{n}_1 + \sin\varphi(k)\, \boldsymbol{n}_2$. In this way $\varphi(k)$ is the azimuth angle of the vector $\boldsymbol{n}(k)$ when using spherical coordinates if we choose the three cartesian coordinates x, y and z in the directions of $\boldsymbol{n}_1$, $\boldsymbol{n}_2$ and $\boldsymbol{n}_3$, respectively (see Fig. 6.1). Hence, the eigenvectors of the Hamiltonian matrix are easy to obtain, as they correspond to the vectors $\pm\boldsymbol{n}(k)$ in the Bloch sphere representation. That is:

$$\pm\boldsymbol{n}(k) \longrightarrow U \begin{pmatrix} 1 \\ \pm e^{i\varphi(k)} \end{pmatrix}, \tag{6.4}$$

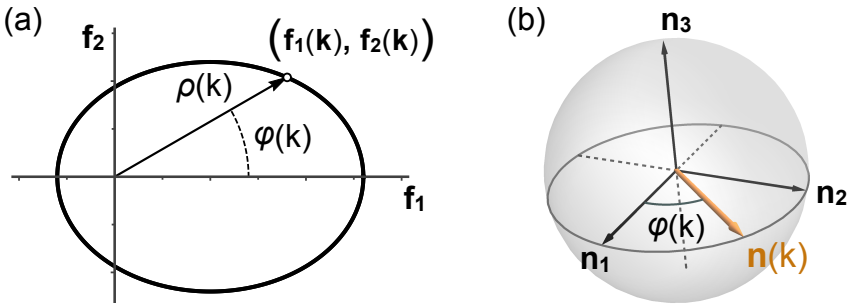

Figure 6.1: **Hamiltonian matrix curve of a ladder model.** (a) A ladder model with chiral symmetry is characterized by the functions $f_1(k)$ and $f_2(k)$, which describe a closed curve in the plane. This curve determines the two energy bands of the system as $E_\pm(k) = \mp\rho(k)$, being $\rho(k)$ the distance from each point to the origin. (b) In addition, each point in the curve determines also an angle $\varphi(k)$, which defines an isospin vector $\boldsymbol{n}(k)$ that characterizes each eigenstate. The presence of chiral symmetry makes the vector $\boldsymbol{n}(k)$ be constrained to the plane generated by the two vectors $\boldsymbol{n}_1$ and $\boldsymbol{n}_2$.

being U the rotation that transforms $\sigma_x(\sigma_y)$ into $\sigma_1(\sigma_2)$ and corresponding each of the two possibilities $\pm$ to each of the two different energy bands. The eigenmodes of the Hamiltonian under periodic boundary conditions are therefore:

$$|k\rangle_\pm = \begin{pmatrix}\hat{a}_k^\dagger & \hat{b}_k^\dagger\end{pmatrix} \frac{1}{\sqrt{2}} U \begin{pmatrix}1 \\ \pm e^{i\varphi(k)}\end{pmatrix} |0\rangle\,, \tag{6.5}$$

whose corresponding energies are:

$$E_\pm(k) = \mp\rho(k) = \mp\sqrt{f_1^2(k) + f_2^2(k)}. \tag{6.6}$$

Once we have obtained the Bloch modes, i.e. the eigenstates of the Hamiltonian for periodic boundary conditions, we can compute the Zak phase, which characterizes the topological nature of the system. It consists of the geometrical phase acquired by a particle when completing an adiabatic path across the whole first Brillouin zone, that is:

$$\mathcal{Z} = -i \oint_{1^{st}BZ} dk\, \langle k|_\pm\, \partial_k\, |k\rangle_\pm = \frac{1}{2} \oint_{1^{st}BZ} dk\, \frac{d\varphi(k)}{dk} = \frac{\Delta\varphi}{2}. \tag{6.7}$$

As we see, the Zak phase is quantized according to the winding number around the origin of $z(k)$ in the complex plane and, equivalently, to the winding number of the vector $\boldsymbol{n}(k)$ around the origin in the plane generated by the two vectors $\boldsymbol{n}_1$ and $\boldsymbol{n}_2$ (see Fig. 6.2). When the curve encloses the origin (winding number 1) the system is in a topological phase and correspodns to a Zak phase $\mathcal{Z} = \pi$. On the contrary, if the curve does not enclose the origin (winding number 0) the system is in a trivial phase and $\mathcal{Z} = 0$.

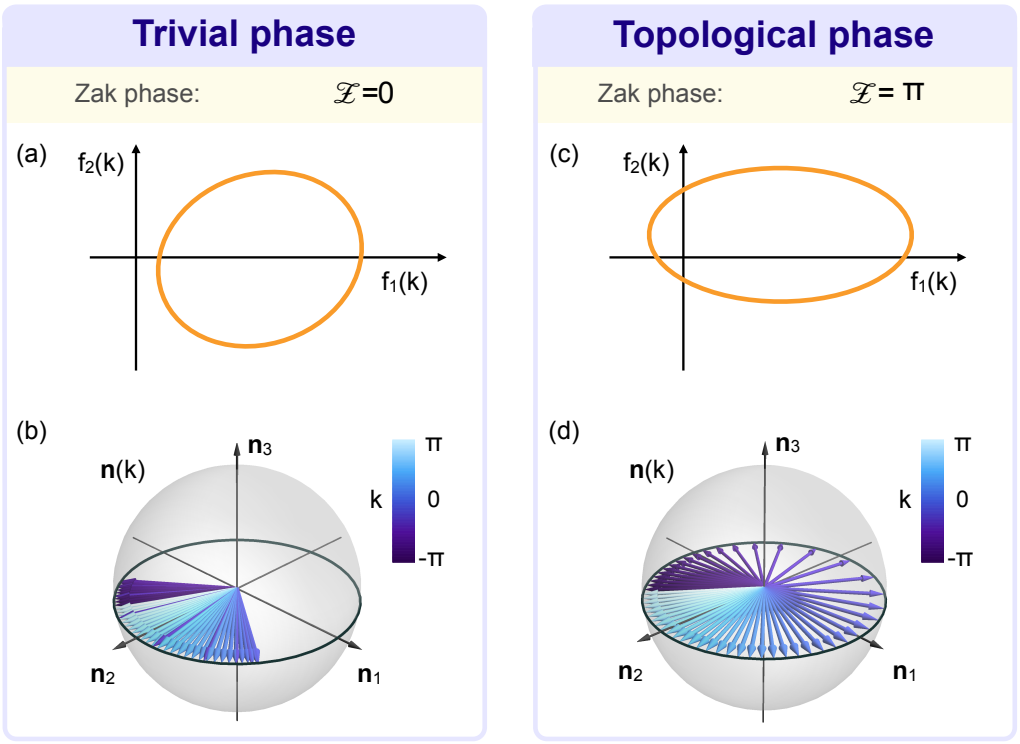

Figure 6.2: **Topological characterization of a ladder model.** The trivial and topological phases of a ladder model are characterized and distinguished by the Zak phase. In the trivial phase the curve drawn by the Hamiltonian matrix in the complex plane, $z(k) = f_1(k) + if_2(k)$, does not enclose the origin (a), so that the vector $\boldsymbol{n}(k)$ on the Bloch sphere describes a circular arc as the momentum varies across the Brillouin zone (b). This situation corresponds to a Zak phase $\mathcal{Z} = 0$. On the other hand, when the system is in the topologically non-trivial phase, $z(k)$ encloses the origin (c), and the vector $\boldsymbol{n}(k)$ describes a closed circumference (d). In this case the Zak phase takes the value $\mathcal{Z} = \pi$.

In this way, the presence of chiral symmetry makes the Hamiltonian matrix live on the plane generated by $\boldsymbol{n}_1$ and $\boldsymbol{n}_2$, where the functions $f_1(k)$ and $f_2(k)$ define a closed curve parametrized by the momentum. These two functions completely characterize the ladder model, being the particular directions of the vectors $\boldsymbol{n}_1$ and $\boldsymbol{n}_2$ irrelevant as they can be changed by performing a global unitary transformation. On one hand, the winding number of the curve determines weather or not the system is found to be in its topological phase. On the other hand, each point in the curve, given by a particular value of the momentum k, determines an angle $\varphi(k)$ and a distance to the origin $\rho(k)$. The first function defines an isospin vector $\boldsymbol{n}(k)$, which corresponds through the Bloch sphere representation to the particular superposition between the modes $\hat{a}_k^\dagger$ and $\hat{b}_k^\dagger$ that constitutes an eigenstate of the Hamiltonian, Eq. (6.5), while the second function gives us the energy of such modes, Eq. (6.6).

The topological characterization of a ladder model is quite similar to the topological characterization of a dimerized lattice, which we explained in Chapter 1. The

reason for that is, on one hand, the fact that a dimerized lattice is a particular case of a ladder model and, on the other hand, chiral symmetry is the only ingredient we need to derive the quantization of the Zak phase and the appearance of two topologically distinct phases. Chiral symmetry constrains the Hamiltonian matrix to be in a plane and, in that plane, all information about the Hamiltonian is encoded in the complex function $z(k)$, the functions $f_1(k)$ and $f_2(k)$ or the functions $\rho(k)$ and $\varphi(k)$. The difference between a ladder model and a dimerized lattice is that for a ladder model these functions are more general. In consequence, a ladder model can exhibit properties inaccessible for a dimerized lattice, as well as richer edge modes.

6.2 6 types of topological ladder models

In this section we analyse the different types of energy bands that a topological ladder model can exhibit. We pay special attention to the number of energy gaps between the two bands, as well as their width and location in the first Brillouin zone. These aspects are quite relevant since, as we show in Chapter 8, they are directly related to the properties of the symmetry protected edge modes that a topological ladder model give rise to. In this way, we have classified all possible topological ladder models into six different types, three of them belonging to the BDI symmetry class, and another three in the AIII symmetry class.

6.2.1 3 types of topological ladder models in the BDI class

As we concluded in Chapter 6, the Hamiltonian matrix of a topological ladder model in the BDI symmetry class has the following form:

$$M(k) = f_1(k)\,\sigma_1 + f_2(k)\,\sigma_2, \tag{6.8}$$

with $\{\sigma_1, \sigma_2\} = 0$ and:

$$\begin{cases} f_1(k) = \alpha + \beta\,\cos k \\ f_2(k) = \gamma\,\sin k \end{cases}, \tag{6.9}$$

being α, β and γ three real parameters. Therefore the curve drawn by the Hamiltonian matrix in the complex plane, $z(k) = f_1(k) + i f_2(k)$, is an ellipse with its center located at the point $(\alpha, 0)$ and whose horizontal and vertical axes are given by $|\beta|$ and $|\gamma|$, respectively. That is:

$$\left[\frac{f_1(k) - \alpha}{\beta}\right]^2 + \left[\frac{f_2(k)}{\gamma}\right]^2 = 1. \tag{6.10}$$

The two energy bands of such topological ladder model are:

$$E_{\pm}(k) = \mp\rho(k) = \mp\sqrt{\alpha^2 + \gamma^2 + 2\alpha\beta\cos k + (\beta^2 - \gamma^2)\cos^2 k}. \tag{6.11}$$

The energy bands are distinguished by a global sign, $E_{\pm}(k) = \mp\rho(k)$, so that the energy gaps will be located at the minima of the function $\rho(k)$. Being q a certain minimum of such function, the width of the corresponding energy gap will be

$E_{gap} = 2\rho(q)$.

Taking into account the location and width of the energy gaps we can distinguish three types of topological ladder models in the BDI symmetry class. On one hand, the number of energy gaps cannot be larger than two, as the curve described by the Hamiltonian matrix in the complex plane is an ellipse. On the other hand, the presence of time reversal symmetry makes the energy bands be symmetric with respect to the momentum, that is: $E_{\pm}(-k) = E_{\pm}(k)$. Therefore there are three distinct possibilities, namely: *i)* a single energy gap located at momentum $q = 0$ or $q = \pi$ (as the momenta $k = \pi$ and $k = -\pi$ are identified), *ii)* two energy gaps of the same width located at opposite momenta $q_1 = q$ and $q_2 = -q$, with $q \neq 0, \pi$, and *iii)* two energy gaps with, in general, different widths and located at the momentum values $q_1 = 0$ and $q_2 = \pi$. We call these three cases the *SSH-like* model, the *balanced* BDI model and the *imbalanced* BDI model, respectively.

***i)* SSH-like model**

The SSH model corresponds to the particular case in which $|\beta| = |\gamma|$, so that the ellipse that characterizes the Hamiltonian matrix in the complex plane collapses into a circle [see Fig. 6.3(a1)]. As a consequence the function $\rho(k)$ has just one minimum and, therefore, the energy bands show a single energy gap, which can be located at momentum $q = 0$ or $q = \pi$ [see Fig. 6.3(a2)]. For $\alpha\beta > 0$, the energy gap is found to be at $q = 0$, whereas it is located at $q = \pi$ for $\alpha\beta < 0$.

In the case in which $|\beta| \neq |\gamma|$, so that the two axes of the ellipse in the complex plane are different from each other, there is a region in the parameter space in which the corresponding ellipse has an eccentricity low enough for the bands to have a single energy gap, located at the same position as in the SSH model. This more general model is what we call the SSH-like model and is defined by the condition $|\alpha\beta| \geq |\beta^2 - \gamma^2|$.

To see this, we consider the first derivative with respect to the momentum of the lower energy band of a general BDI ladder model [see Eq. (6.11)]:

$$\rho'(k) = -\frac{1}{\rho(k)} \sin k \left[\alpha\beta + (\beta^2 - \gamma^2)\cos k\right]. \tag{6.12}$$

It is straightforward to conclude that a momentum q needs to fulfil one of the following conditions in order to be a minimum (or a maximum) of the band: *i)* $\sin q = 0$, or *ii)* $\cos q = -\alpha\beta/(\beta^2 - \gamma^2)$. In the case in which $|\alpha\beta| > |\beta^2 - \gamma^2|$ condition *ii)* does not define a real value for q and, therefore, there are only two solutions: $q = 0$ and $q = \pi$, one will correspond to a maximum and the other to a minimum. This is precisely the case for the SSH-like model. In the particular case in which $|\alpha\beta| = |\beta^2 - \gamma^2|$ condition *ii)* can be indeed satisfied by a real value of the momentum, however the solution coincides with one of the solutions of condition *i)* and thus this situation represents another case of SSH-like model. Finally, when $|\alpha\beta| < |\beta^2 - \gamma^2|$, there are four different solutions. Among them, two will be minima

and the other two maxima. This last situation includes the two other types of BDI ladder models different from the SSH-like model.

Nevertheless, the edge modes of the SSH-like model are not significantly different from the ones that appear in the SSH model (see Chapter 8), which is a simpler and widely known model. Therefore, we will often use the SSH model as a representative of the first type of topological ladder model in the BDI class, instead of using the slightly more general SSH-like model.

***ii)* Balanced BDI model**

This model corresponds to the situation in which $|\alpha\beta| < |\beta^2 - \gamma^2|$, what implies that the upper band has two maxima and two minima, and $|\beta| > |\gamma|$, so that the horizontal axis of the ellipse in the (f_1, f_2)-plane is bigger than the vertical one [see Fig. 6.3(b1)]. In this situation, the minima are located at $q_1 = q$ and $q_2 = -q$ with $\cos q = -\alpha\beta/(\beta^2 - \gamma^2)$ and the maxima are found at $k = 0$ and $k = \pi$. In this way, the energy gaps between the two bands are located at opposite momenta $\pm q$ and, as a consequence of time reversal symmetry, their widths are the same [see Fig. 6.3(b2)].

***iii)* Imbalanced BDI model**

The third type of BDI ladder model corresponds to the last possibility: $|\alpha\beta| < |\beta^2 - \gamma^2|$ and $|\beta| < |\gamma|$, so that the ellipse in the (f_1, f_2)-plane has a vertical axis bigger than its horizontal axis [see Fig. 6.3(c1)]. As in the balanced BDI model, the imbalanced BDI model is characterized by two minima and two maxima in its energy bands. However, their locations are interchanged, being the minima located at $q_1 = 0$ and $q_2 = \pi$, whereas the maxima take place at $\pm q$ with $\cos q = -\alpha\beta/(\beta^2 - \gamma^2)$. Therefore, while the locations of the energy gaps are fixed at $q_1 = 0$ and $q_2 = \pi$, their widths can be in general different [see Fig. 6.3(c2)].

It is illuminating to draw the parameter space of a general topological ladder model in the BDI symmetry class and identify the region corresponding to each one of the three types of BDI ladder models. The condition $|\alpha\beta| \geq |\beta^2 - \gamma^2|$, that defines the SSH-like model, can be written in terms of the ratios $|\beta/\alpha|$ and $|\gamma/\alpha|$. If we define $x = |\beta/\alpha|$ and $y = |\gamma/\alpha|$, the SSH-like model corresponds to the region whose boundaries are given by the following functions:

$$y = \sqrt{x^2 - x}, \tag{6.13}$$

$$y = \sqrt{x^2 + x}, \tag{6.14}$$

which are asymptotically close to the lines $y = x - 1/2$ and $y = x + 1/2$, respectively. Therefore, the SSH-like model region in the parameter space corresponds approximately to a stripe of width $1/\sqrt{2}$ whose center is given by the line $|\beta/\alpha| = |\gamma/\alpha|$ (SSH model), corresponding the two remaining regions to the balanced and imbalanced BDI models [see Fig. 6.4(e)].

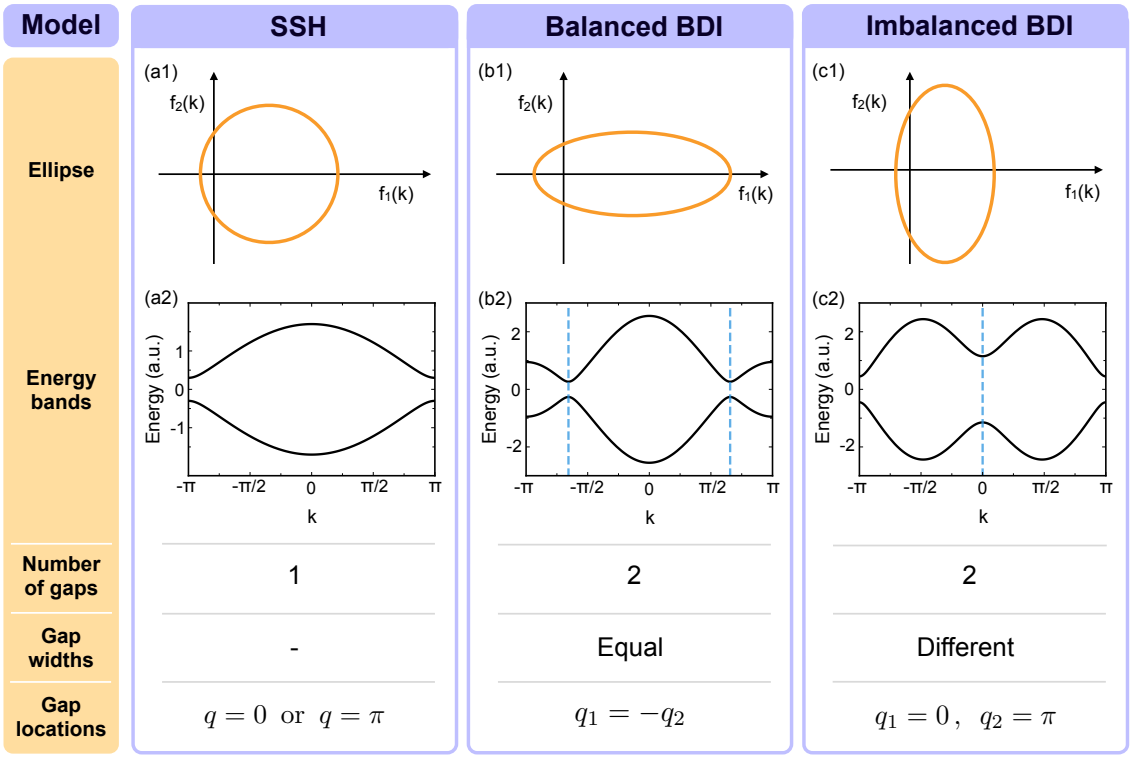

Figure 6.3: **3 types of topological ladder models in the BDI class.** There are three types of topological ladder models in the BDI symmetry class, which are distinguished and characterized by their energy gap configurations. (a) The SSH model (as the representative of a slightly more general model, the SSH-like model) corresponds to a circumference in the (f_1, f_2)-plane and a single energy gap between the two energy bands of the system. This gap is located at $q = 0$ or $q = \pi$, depending on the relative sign between the Hamiltonian parameters α and β (see text). (b) The balanced BDI model corresponds to an ellipse in the (f_1, f_2)-plane whose horizontal axis is bigger than the vertical one, so that there are two energy gaps of the same width and located at opposite momenta $q_1 = q$ and $q_2 = -q$, with $\cos q = \alpha\beta/(\gamma^2 - \beta^2)$. (c) The imbalanced BDI model is characterized by a Hamiltonian matrix that draws an ellipse in the (f_1, f_2)-plane with a vertical axis bigger than the horizontal one, and thus there are two gaps between the energy bands, located at momentum $q_1 = 0$ and $q_2 = \pi$. In general, each gap has a different width.

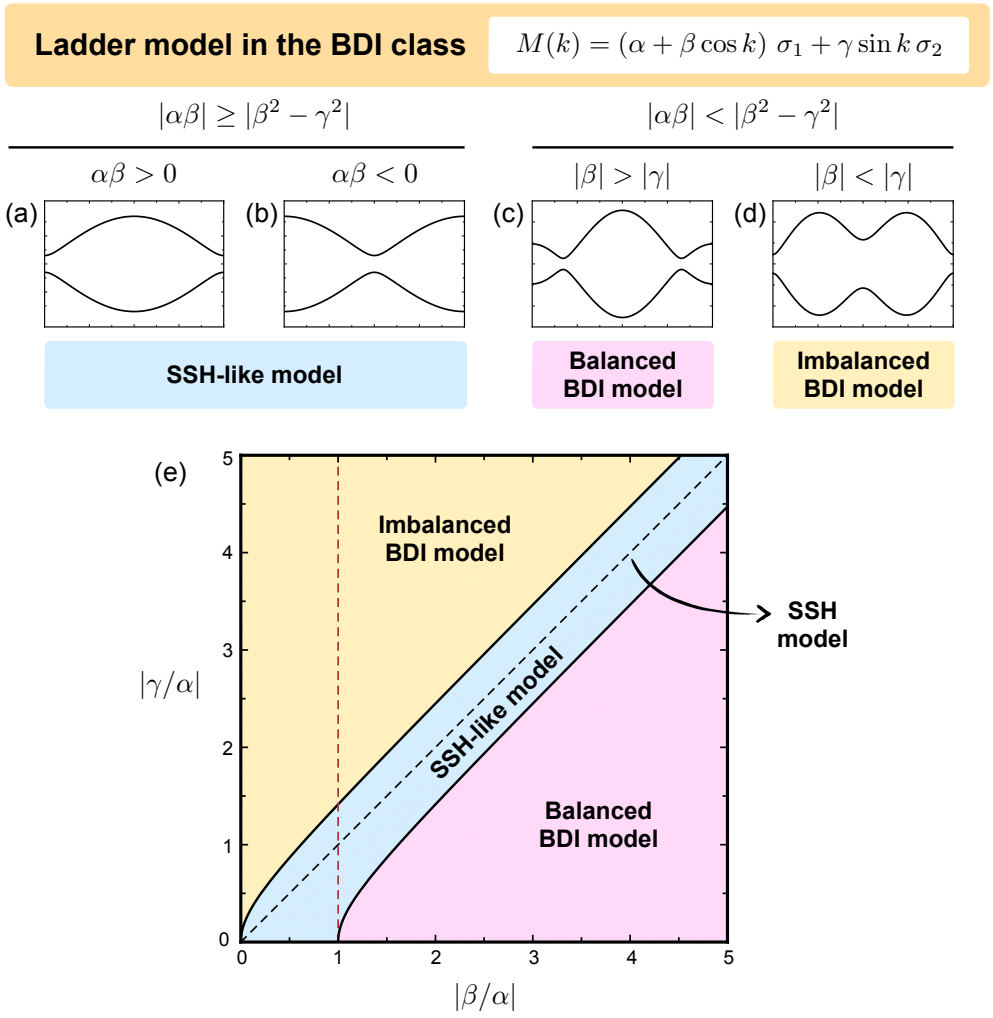

Figure 6.4: **Classification of BDI ladder models.** A general ladder model in the BDI symmetry class can be classified into one of three different types according to the parameters of its Hamiltonian matrix $M(k) = (\alpha + \beta \cos k)\, \sigma_1 + \gamma \sin k\, \sigma_2$. For $|\alpha\beta| \geq |\beta^2 - \gamma^2|$, it corresponds to the SSH-like model, which is characterized by (a) a single energy gap located at $q = 0$ if $\alpha\beta > 0$ or (b) a single energy gap located at $q = \pi$ for $\alpha\beta < 0$. The SSH model is a representative of this type and corresponds to the particular case in which $|\beta| = |\gamma|$. On the other hand, when $|\alpha\beta| < |\beta^2 - \gamma^2|$, the system corresponds to the balanced BDI model for $|\beta| > |\gamma|$ and to the imbalanced BDI model for $|\beta| < |\gamma|$. The former one is characterized through its energy bands by (c) the presence of two energy gaps of the same width located at opposite momenta, whereas the last one gives rise to (d) a pair of energy gaps of the different widths at momenta $q = 0$ and $q = \pi$. (e) Parameter space of a general BDI ladder model, where the two axes correspond to the quantities $|\beta/\alpha|$ and $|\gamma/\alpha|$. The blue region corresponds to the SSH-like model, the pink one to the balance BDI model and the yellow one to the imbalance BDI model. The dashed black line corresponds to the SSH model and the dashed red line indicates the critical point that separates the trivial phase, $|\alpha| > |\beta|$, from the topological one, $|\alpha| < |\beta|$.

6.2.2 3 types of topological ladder models in the AIII class

From Chapter 5, we know that a topological ladder model in the AIII symmetry class is characterized by a Hamiltonian matrix of the form:

$$M(k) = (\alpha + \beta \cos k)\, \sigma_c + (\eta + \gamma \sin k)\, \sigma_s, \tag{6.15}$$

being $\eta \neq 0$ and/or $\{\sigma_c, \sigma_s\} \neq 0$. This implies that, if we write the Hamiltonian matrix using two anti-commuting Pauli matrices σ_1 and σ_2 as:

$$M(k) = f_1(k)\, \sigma_1 + f_2(k)\, \sigma_2, \tag{6.16}$$

the two functions $f_1(k)$ and $f_2(k)$ describe an ellipse such that, in contrast to the BDI case, its center can be located anywhere in the plane and its axes can be rotated with respect to the abscises and ordinates axes. As a consequence, the energy gap configurations that a topological ladder model in the AIII class can exhibit are richer than those in the BDI class, as they are not constrained by the presence time reversal symmetry. Analogously to the classification of BDI ladder models, we can distinguish three distinct kinds of topological ladder models in the AIII symmetry class, characterized by a different energy gap configuration, namely: *i)* a single energy gap located at momentum $q \neq 0, \pi$, *ii)* two energy gaps of the same width located at *not opposite momenta* q_1 and q_2, and *iii)* two energy gaps with different widths and located at any momentum values q_1 and q_2, excluding the case in which $q_1 = 0$ and $q_2 = \pi$. We call these three cases the *circular* AIII model, the *balanced* AIII model and the *imbalanced* AIII model, respectively.

i) Circular AIII model

In the case in which $|\beta| = |\gamma|$ the curve described by the Hamiltonian matrix in the complex plane is a circle [see Fig. 6.5(a1)]. Therefore the energy bands give rise to a single energy gap, which is located at any momentum q different from 0 and π [see Fig. 6.5(a2)], as these two particular cases take place only in the BDI class. Nevertheless, not only the specific case in which $|\beta| = |\gamma|$ corresponds to this gap configuration. Analogously to the SSH model and the SSH-like model, the case $|\beta| = |\gamma|$ is just a particular model within a larger region in parameter space in which the Hamiltonian matrix ellipse has an eccentricity low enough for the energy bands to have a single energy gap. For the sake of simplicity, we refer to this type of AIII ladder models as the circular AIII model, since the case $|\beta| = |\gamma|$ (the only situation in which the Hamiltonian matrix curve is truly a circle) is the simplest representative of this family of models and there is no significant distinction between any of them.

ii) Balanced AIII model

This model corresponds to the case in which the Hamiltonian matrix ellipse is such that one of its axes crosses the origin [see Fig. 6.5(b1)], so that the points

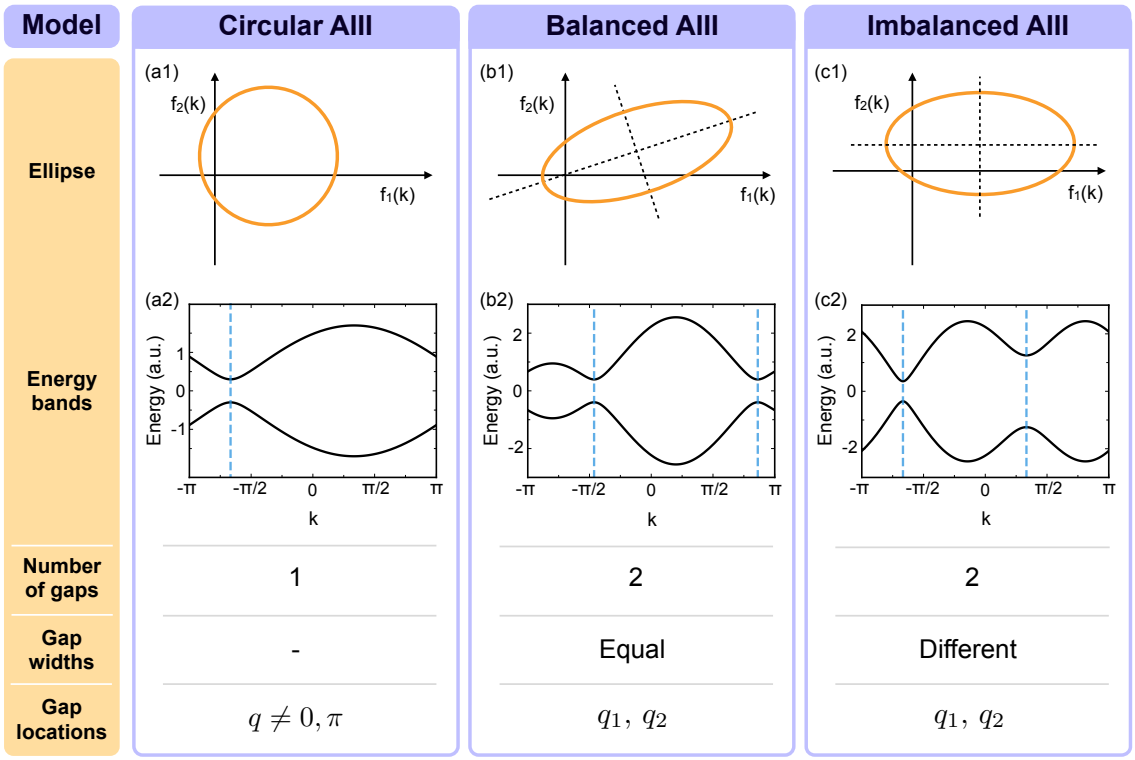

Figure 6.5: **3 types of topological ladder models in the AIII class.** There are three types of topological ladder models in the AIII symmetry class, characterized by distinc energy gap configurations. (a) The circular AIII model corresponds to an ellipse in the (f_1, f_2)-plane whose eccentricity is low enough for the energy bands to have a single gap. Due to the lack of time reversal symmetry, this energy gap is located at $q \neq 0, \pi$. In this figure we show the particular case in which the Hamiltonian matrix ellipse is actually a circumference, which represents the simplest circular AIII model. (b) The balanced AIII model corresponds to a Hamiltonian matrix ellipse such that one of its axis crosses the origin, so that there are two energy gaps of the same width. The lack of time reversal symmetry implies that they are located at not opposite momenta: q_1 and q_2 with $q_1 \neq -q_2$. (c) The imbalanced AIII model corresponds to the most general situation. Therefore, it shows two energy gaps of different widths and located at any positions in momentum space; excluding the case in which $q_1 = 0$ and $q_2 = \pi$, as it would correspond to the imbalanced BDI model.

associated to the minima of the upper band are at the same distance from the origin and, thus, there are two energy gaps of the same width between the two energy bands [see Fig. 6.5(b2)]. These energy gaps cannot be located at opposite momenta, as this would correspond to the BDI class. That is, the gaps are located at q_1 and q_2 with $q_1 \neq -q_2$.

***iii)* Imbalanced AIII model**

Finally, the imbalanced AIII model consists of the more general case, in which the Hamiltonian matrix ellipse does not correspond to any of the previous situations [see Fig. 6.5(c1)]. In this case the energy bands show a pair of energy gaps with different widths and located at any momenta q_1 and q_2 [see Fig. 6.5(c2)], excluding the case $q_1 = 0$ and $q_2 = \pi$ as it corresponds to the imbalanced BDI model.

6.3 6 types of Wilson fermion configurations

A ladder model with chiral symmetry and a Fermi energy between the two bands can be interpreted as a discretized description of a fermion, where a whole in the filled sea of negative energy states represents an antiparticle.

When there is a gap between the two bands the fermion is massive, whereas it is massless at the critical point, where the two bands cross each other. The simplest ladder model describing a fermion with a kinetic and a mass term is called the naive lattice transcription of the Dirac equation [43]. Each of the two momentum values at which the upper band reaches a local minimum corresponds to a pole of the propagator and thus to a different specie of fermion [44]. In the context of particle physics this was called the doubling problem and was solved by Wilson [45], who added another kinetic term so that one of the fermions gets heavier, leaving only one light fermion.

In the context of condensed matter, the naive Dirac fermion corresponds to a trivial insulator, whereas the Wilson fermion corresponds to a topological ladder in the BDI symmetry class, more precisely to the Creutz ladder [23]. It describes two Wilson fermions of different masses localized at momenta $k = 0$ and $k = \pi$. After considering the most general ladder model Hamiltonian we have found more possible Wilson fermion configurations, as well as a relation between the symmetry class of a topological ladder model and the set of Wilson fermions that it describes.

There are six distinct Wilson fermion configurations that a ladder model can exhibit, and they correspond to the six different types of ladder models we showed in the previous section. The SSH model corresponds to just one fermion, which is massive, and appears at momentum $k = 0$ or $k = \pi$. Therefore we say that it is a non chiral Wilson fermion. The balanced BDI model shows two fermions of the same mass, since both energy gaps in this kind of ladder model have the same width. The energy gaps appear at opposite momenta and, thus, the two corresponding fermions have opposite chirality. The imbalance BDI model describes two fermions with different masses, being both of them non chiral, as the energy gaps are located in momentum space at $k = 0$ and $k = \pi$. The circular AIII model shows a single Wilson fermion, which is massive and chiral, as the energy gap is located at any momentum different from 0 and π. The balanced AIII model describes two chiral fermions of the same mass, and whose chiralities are not opposite to each other. Finally, the imbalanced AIII model corresponds to the most general case in which

there are two chiral fermions of different masses [see Fig. 6.6].

As we see, there are two variables: the number of Wilson fermions and their masses. A topological ladder model can describe one or two fermions and, in the second case, they can have equal masses (balanced models) or different masses (imbalanced models). The presence of time reversal symmetry in the BDI class forces the Wilson fermions to be non chiral, or, in case there are two fermions with the same mass, have opposite chirality. On the contrary, in the AIII class all fermions are chiral, what is a manifestation of the breaking of time reversal symmetry. In consequence, there are six different Wilson fermion configurations that characterize each type of topological ladder model.

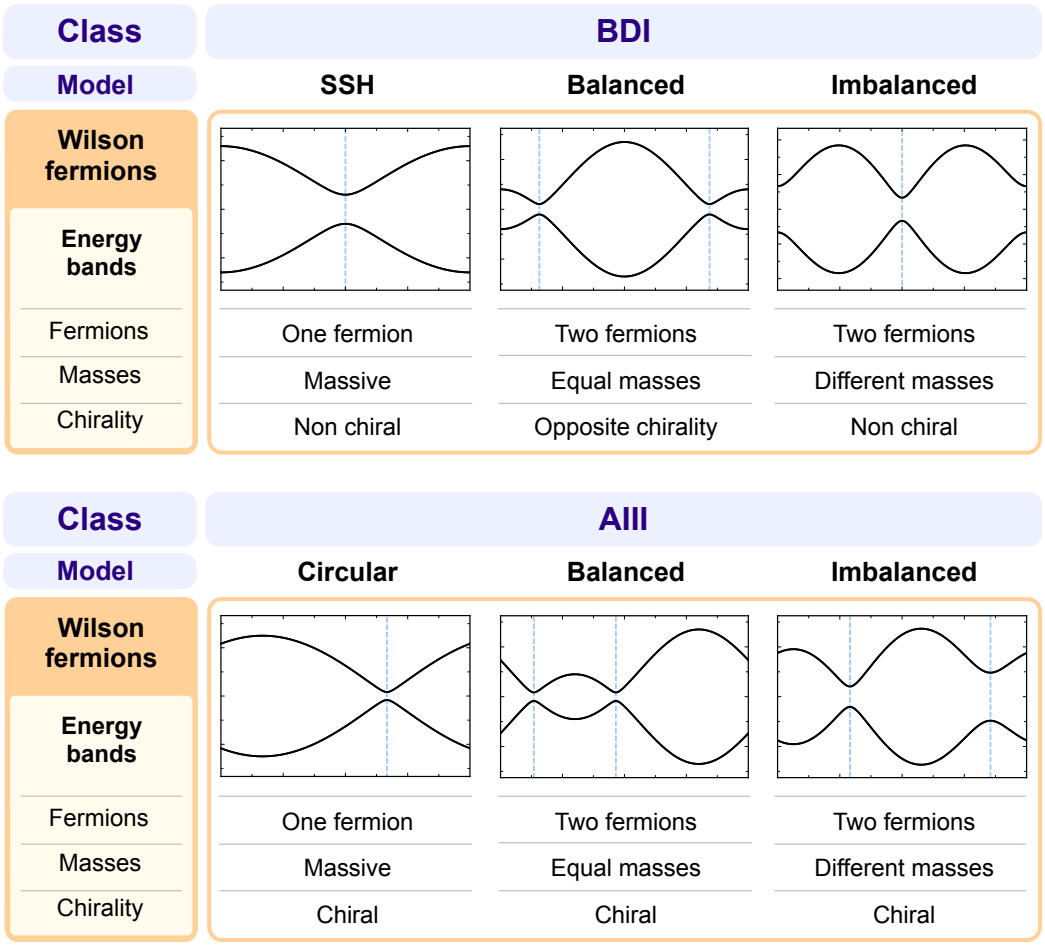

Figure 6.6: **Wilson fermion configurations of a ladder model.** There are three different configurations of Wilson fermions that a ladder model in the BDI class can describe, and another three in the AIII class. Each of this six possibilities is characterized by three aspects. First, the number of fermions, which can be one or two. Second, in case there are two fermions, weather they have the same mass or not. Third, the chirality of the fermions, which is related to the symmetry class of the ladder model (see text).

Chapter 7

Canonical topological ladder model: the bowtie ladder

7.1 The bowtie ladder architecture

From Chapters 5 and 6, we know that a topological ladder model is characterized by two real functions of the momentum, $f_1(k)$ and $f_2(k)$, or alternatively by the real functions $\rho(k)$ and $\varphi(k)$, being these four functions related through the expression $\rho(k)e^{i\varphi(k)} = f_1(k) + if_2(k)$. The Hamiltonian matrix of a topological ladder model can then be written in terms of such functions as:

$$M(k) = f_1(k)\,\sigma_1 + f_2(k)\,\sigma_2, \tag{7.1}$$

being σ_1 and σ_2 two anti-commuting Pauli matrices given by two orthogonal unitary vectors in the 3-dimensional real space; that is: $\sigma_j = \boldsymbol{n}_j \cdot \boldsymbol{\sigma}$ with $\boldsymbol{n}_1 \cdot \boldsymbol{n}_2 = 0$.

The particular directions of the vectors $\boldsymbol{n}_1$ and $\boldsymbol{n}_2$ are irrelevant as they can be changed by performing a global unitary transformation. In this way, we can focus on a particular choice for $\boldsymbol{n}_1$ and $\boldsymbol{n}_2$ and study the corresponding ladder architecture and Hamiltonian. If we take $\boldsymbol{n}_1 = \hat{x}$ and $\boldsymbol{n}_2 = \hat{y}$ we obtain a particular realization of a topological ladder model. It constitutes a *canonical* ladder model, as every topological ladder model can be obtained from it by applying the appropriate unitary transformation.

We start by considering the Hamiltonian matrix of such canonical ladder. For that we need to substitute in Eq. 7.1 σ_1 and σ_2 by σ_x and σ_y, respectively. In this way, and using the functions $\rho(k)$ and $\varphi(k)$ instead of $f_1(k)$ and $f_2(k)$, the canonical ladder Hamiltonian matrix takes the following form:

$$M(k) = \rho(k)\,\left[\cos\varphi(k)\,\sigma_x + \sin\varphi(k)\sigma_y\right] = \rho(k)\begin{pmatrix} 0 & e^{-i\varphi(k)} \\ e^{i\varphi(k)} & 0 \end{pmatrix}, \tag{7.2}$$

so that the canonical ladder Hamiltonian in the momentum representation is:

$$H_{\rm c} = -\sum_k \rho(k)\left(e^{-i\varphi(k)}\,\hat{a}_k^\dagger \hat{b}_k + e^{i\varphi(k)}\,\hat{b}_k^\dagger \hat{a}_k\right). \tag{7.3}$$

The Hamiltonian matrix of any topological ladder model depends on the momentum only through the two functions $\sin k$ and $\cos k$, or alternatively through e^{ik} and e^{-ik} (see Chapter 5). Therefore, the most general Hamiltonian matrix corresponds to the case in which $\rho(k)e^{i\varphi(k)}$ is a general complex linear combination of the three functions 1, e^{ik} and e^{-ik}, that is:

$$\rho(k)e^{i\varphi(k)} = e^{-i\theta}\left(Je^{i\phi/2} + te^{-i\delta}e^{ik} + t'e^{i\delta}e^{-ik}\right). \tag{7.4}$$

Being J, t and t' three real and positive parameters and θ, ϕ and δ three phases. We have chosen a particular parametrization of the phases which, without loss of generality, is really convenient in order to make a physical interpretation of them, as we will show in the following. In order to see how the canonical ladder Hamiltonian looks like in the position representation, we substitute $\rho(k)e^{i\varphi(k)}$ by its expression in (7.4) in the Hamiltonian in momentum space (7.3) and thus obtain:

$$H_{\mathrm{c}} = -\sum_n \left(Je^{i(\theta-\phi/2)}\,\hat{a}_n^\dagger \hat{b}_n + te^{i(\delta+\theta)}\,\hat{a}_{n+1}^\dagger \hat{b}_n + t'e^{-i(\delta-\theta)}\,\hat{a}_n^\dagger \hat{b}_{n+1} + \mathrm{h.c.}\right). \tag{7.5}$$

In this way, we can identify the three parameters J, t and t' as the amplitudes of a vertical and two diagonal couplings in the ladder, respectively. Therefore, due to its ladder architecture, we call this model the *bowtie* ladder model (see Fig. 7.1).

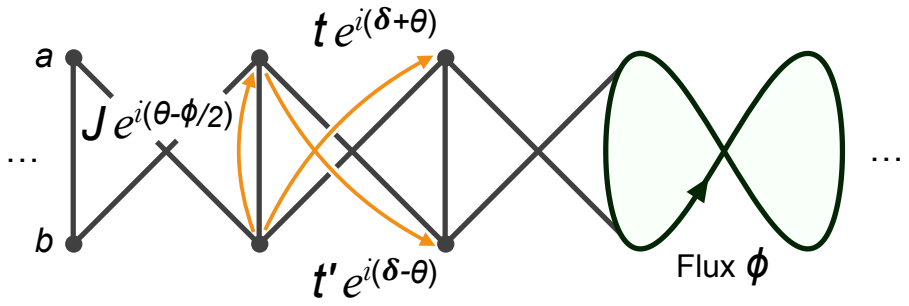

Figure 7.1: **The bowtie ladder.** Schematic illustration of the bowtie ladder, which is a canonical ladder model, as any other ladder model can be obtained by performing the appropriate unitary transformation onto this model. The bowtie ladder consists of three different hopping terms: one vertical coupling and two diagonal couplings. This ladder geometry allows the construction of closed paths that define finite areas. A particle that completes the elementary path $a_n \to b_{n+1} \to a_{n+1} \to b_n \to a_n$ gets a phase ϕ, which is then interpreted as an effective magnetic flux penetrating the ladder.

In order to see which role plays each parameter in the bowtie ladder Hamiltonian, we go back to the momentum representation and write the Hamiltonian as:

$$H_{\mathrm{c}} = -\sum_k \begin{pmatrix}\hat{a}_k^\dagger & \hat{b}_k^\dagger\end{pmatrix} R_z(\theta)\, M_{\mathrm{c}}(k)\, R_z^\dagger(\theta) \begin{pmatrix}\hat{a}_k \\ \hat{b}_k\end{pmatrix}, \tag{7.6}$$

where $R_z(\theta) = e^{i\theta\sigma_z/2}$ is a rotation of an angle θ around the z-axis and:

$$M_{\rm c}(k) = \left[J\cos\frac{\phi}{2} + (t+t')\cos(k-\delta)\right]\sigma_x + \left[J\sin\frac{\phi}{2} + (t-t')\sin(k-\delta)\right]\sigma_y. \quad (7.7)$$

By inspecting the bowtie ladder Hamiltonian matrix $M_{\rm c}(k)$, as well as the bowtie ladder geometry in Fig. 7.1, we can identify three different phases in the model, with three distinct physical meanings. These are:

- *Effective magnetic flux ϕ*

  The phase ϕ determines the total phase accumulated by a particle completing a closed path in the ladder. A non-vanishing accumulated phase along a closed path corresponds to an effective magnetic flux penetrating the area defined by the path. Therefore, we can identify the phase ϕ as an effective magnetic flux. All closed paths that can be defined in the canonical ladder are obtained as a combination of the elementary path $a_n \to b_{n+1} \to a_{n+1} \to b_n \to a_n$. As we show in the next sections, the phase ϕ affects the symmetries of the Hamiltonian and the properties of the edge states.

- *Shift δ in the momentum-isospin correspondence.*

  The phase δ produces a shift in the Hamiltonian matrix with respect to the momentum [see Eq.(7.7)]. This produces a shift in the correspondence between the momentum of each eigenstate and its associated vector in the Bloch sphere, which makes them be genuinely different from those eigenstates corresponding to the case in which there is no phase δ. This phase also affects the symmetries of the Hamiltonian and the properties of the edge states, as we show in the following sections and Chapter 8.

- *Irrelevant phase θ.*

  The phase θ produces a rotation around the z-axis [see Eq.(7.6)], which is a global unitary operation and does not affect the symmetries of the system. In the following we neglect this phase for simplicity being all possible rotations around the z-axis included in our analysis by adding the phase θ as shown in Fig. 7.1.

7.2 Symmetry properties of the bowtie ladder

7.2.1 The $(\boldsymbol{n}_0, \boldsymbol{n}_c, \boldsymbol{n}_s)$-decomposition

In order to know what are the symmetries of the bowtie ladder Hamiltonian and how they depend on the different parameters present in the model, we decompose its Hamiltonian matrix as $M_{\rm c}(k) = (\boldsymbol{n}_0 + \boldsymbol{n}_c\cos k + \boldsymbol{n}_s\sin k)\cdot\boldsymbol{\sigma}$, being:

$$\begin{cases} \boldsymbol{n}_0 = J\cos(\phi/2)\,\hat{x} + J\sin(\phi/2)\,\hat{y}, \\ \boldsymbol{n}_c = (t+t')\cos\delta\,\hat{x} - (t-t')\sin\delta\,\hat{y}, \\ \boldsymbol{n}_s = (t+t')\sin\delta\,\hat{x} + (t-t')\cos\delta\,\hat{y}. \end{cases} \quad (7.8)$$

a) Chiral symmetry

It is clear that the bowtie ladder Hamiltonian has chiral symmetry, as the three vectors $\boldsymbol{n}_0$, $\boldsymbol{n}_c$ and $\boldsymbol{n}_s$ lie in the xy-plane. The Hamiltonian matrix is a linear combination of σ_x and σ_y, Eq. (7.7) and therefore $\sigma_z M_c(k)\sigma_z = -M_c(k)$; so that the chiral symmetry condition, Eq. (7), is always fulfilled with $U_S = \sigma_z$.

b) Time reversal and charge conjugation symmetries

There are two conditions that a ladder model has to fulfil in order to be time reversal symmetric, which are: $\boldsymbol{n}_c \cdot \boldsymbol{n}_s = 0$ and $\boldsymbol{n}_0 \cdot \boldsymbol{n}_s = 0$ (see Chapter 5). These two conditions applied to the bowtie ladder imply:

$$\boldsymbol{n}_c \cdot \boldsymbol{n}_s = 0 \quad \rightarrow \quad tt' \sin 2\delta = 0, \tag{7.9}$$

$$\boldsymbol{n}_0 \cdot \boldsymbol{n}_s = 0 \quad \rightarrow \quad t \sin\left(\delta + \frac{\phi}{2}\right) + t' \sin\left(\delta - \frac{\phi}{2}\right) = 0. \tag{7.10}$$

The first time reversal condition, Eq. (7.9), implies that δ can only take the values 0, $\pm\pi/2$ and π. When $\delta = 0$ or π, the second time reversal condition, Eq. (7.10), is fulfilled only if $\phi = 0$, whereas it is satisfied for $\phi = \pi$ when $\delta = \pm\pi/2$. Therefore there are four different configurations of the bowtie ladder parameters whose corresponding Hamiltonian exhibits time reversal symmetry. In the presence of chiral symmetry, either both time reversal and charge conjugation symmetries are present in the model, or none of them is. Consequently, these four configurations belong to the BDI symmetry class, whereas any other configuration of parameters corresponds to the AIII symmetry class. As a result, we obtain Fig. 7.2, where we show the symmetries of the bowtie ladder Hamiltonian and their dependence on its parameters.

ϕ	δ	Time reversal	Charge conjugation	Chiral symmetry	Symmetry Class
0	0, π	1	1	1	**BDI**
π	±π/2	1	1	1	**BDI**
Otherwise		0	0	1	**AIII**

Figure 7.2: **Bowtie ladder symmetry class**. Presence (1) or absence (0) of time reversal, charge conjugation and chiral symmetries in the bowtie ladder Hamiltonian. The symmetries of the bowtie ladder Hamiltonian are determined by the phases of its couplings, namely: δ and ϕ. Only four particular configurations of parameters correspond to a Hamiltonian that belongs to the BDI symmetry class, being in the AIII class otherwise.

7.2.2 Hamiltonian matrix structure

Alternatively, we can obtain the symmetries of the canonical ladder by analasyng its Hamiltonian matrix.

There are two ways in which the Hamiltonian matrix of a ladder with chiral symmetry can be written. On one hand, using two anticommuting Pauli matrices, σ_1 and σ_2, and two functions of the momentum $f_1(k)$ and $f_2(k)$. This representation is easier to deal with as it uses the orthonormal basis $\{\boldsymbol{n}_1, \boldsymbol{n}_2\}$. However, these two vectors are not unique, since we can choose any other orthogonal basis within the plane in which the Hamiltonian matrix lives; therefore, the two functions $f_1(k)$ and $f_2(k)$ are also not unique and there is no systematic way in which we can read the symmetry class of the Hamiltonian by looking at these functions.

On the other hand, we can separate the component of the Hamiltonian matrix that goes with $\sin k$ and the one with $\cos k$, what is more convenient in order to read the symmetries of the Hamiltonian. Nevertheless, this second representation uses two Pauli matrices, σ_c and σ_s, whose anticommutator is in general different from zero. In this way, we can write in general:

$$M(k) = (\alpha + \beta \cos k)\, \sigma_c + (\eta + \gamma \sin k)\, \sigma_s. \tag{7.11}$$

Once we have expressed the Hamiltonian matrix of a ladder model using this representation it is straightforward to read its symmetries. *The model belongs to the BDI class if and only if* $\{\sigma_c, \sigma_s\} = 0$ *and* $\eta = 0$, *being in the AIII class otherwise.* In other words, only in the BDI case the odd and even components of the Hamiltonian matrix can be separated in orthogonal directions (see Chapter 5).

The bowtie ladder Hamiltonian matrix is written using the first representation in Eq.(7.7). If we write it using the second representation we get:

$$\begin{aligned} M_{\mathrm{c}}(k) =& \sqrt{t^2 + t'^2 + 2tt' \cos 2\delta} \left(\frac{J \cos\delta \cos(\phi/2)}{t + t'} - \frac{J \sin\delta \sin(\phi/2)}{t - t'} + \cos k \right) \sigma_c + \\ &+ \sqrt{t^2 + t'^2 - 2tt' \cos 2\delta} \left(\frac{J \sin\delta \cos(\phi/2)}{t + t'} + \frac{J \cos\delta \sin(\phi/2)}{t - t'} + \sin k \right) \sigma_s \end{aligned} \tag{7.12}$$

where the two Pauli matrices σ_c and σ_s are:

$$\sigma_c = \frac{(t + t') \cos\delta\, \sigma_x - (t - t') \sin\delta\, \sigma_y}{\sqrt{t^2 + t'^2 + 2tt' \cos 2\delta}}, \quad \sigma_s = \frac{(t + t') \sin\delta\, \sigma_x + ((t - t') \cos\delta\, \sigma_y}{\sqrt{t^2 + t'^2 - 2tt' \cos 2\delta}}. \tag{7.13}$$

Therefore, the two conditions that must be satisfied in order for the Hamiltonian to be time reversal symmetric are:

$$\{\sigma_c, \sigma_s\} = \frac{4\, tt' \sin 2\delta\, \mathbb{I}}{\sqrt{(t^2 + t'^2)^2 - (2tt' \cos 2\delta)^2}} = 0 \tag{7.14}$$

$$\eta = J \sqrt{t^2 + t'^2 - 2tt' \cos 2\delta} \left(\frac{\sin\delta \cos(\phi/2)}{t + t'} + \frac{\cos\delta \sin(\phi/2)}{t - t'} \right) = 0. \tag{7.15}$$

The first condition implies that $\delta = 0, \pm\pi/2$ or π. When $\delta = 0$ or π, $\eta \propto \sin(\phi/2)$ and thus $\phi = 0$. In the case $\delta = \pm\pi/2$, $\eta \propto \cos(\phi/2)$ and therefore $\phi = \pi$. In this way, we obtain the same result as before, using the three vectors $\boldsymbol{n}_0$, $\boldsymbol{n}_c$ and $\boldsymbol{n}_s$ (see Fig. 7.2).

7.3 Bowtie ladder topological phase.

The simplest way of writing the bowtie ladder Hamiltonian matrix is using the form $M_c(k) = f_1(k)\sigma_x + f_2(k)\sigma_y$. From Eq. (7.7) we can identify the functions $f_1(k)$ and $f_2(k)$ and see that they satisfy the following ellipse equation:

$$\left[\frac{f_1(k) - J\cos(\phi/2)}{t + t'}\right]^2 + \left[\frac{f_2(k) - J\sin(\phi/2)}{t - t'}\right]^2 = 1, \tag{7.16}$$

so that the curve described by the Hamiltonian matrix in the complex plane is an ellipse centred at the point $(J\cos(\phi/2), J\sin(\phi/2))$ and whose horizontal and vertical axes are $t + t'$ and $|t - t'|$, respectively (see Fig. 7.3). Form this ellipse equation we can obtain the condition that defines the region in the parameter space in which the system exhibits a topologically non-trivial nature. Such condition is determined by imposing that the ellipse encloses the origin and thus the Zak phase takes the value π. This condition is:

$$J\sqrt{t^2 + t'^2 - 2tt'\cos\phi} < |t^2 - t'^2|. \tag{7.17}$$

It is important to mention that we exclude the case in which $t = t'$ from our analysis, as it corresponds to a trivial Hamiltonian. From Eq. (7.7) we see that the component that goes with $\sin(k - \delta)$ in the Hamiltonian matrix vanishes in this situation and thus the Hamiltonian matrix ellipse collapses into a line [see Eq. (7.16)]. Therefore, the corresponding winding number is always zero and the model cannot access a topologically non-trivial phase.

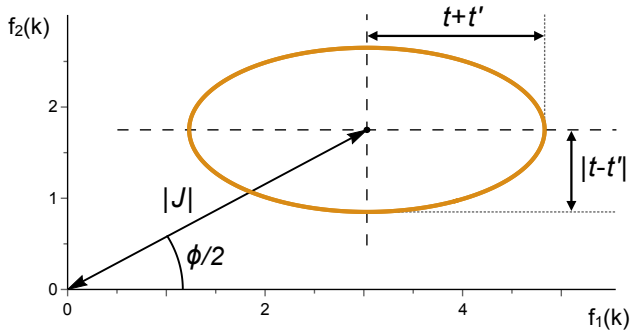

Figure 7.3: **Bowtie ladder Hamiltonian matrix ellipse.** , The curve described by the bowtie ladder Hamiltonian matrix is an ellipse centred at $(J\cos(\phi/2), J\sin(\phi/2))$ and with axes $t + t'$ and $||t| - |t'||$. From the corresponding ellipse equation we can derive the condition that the parameters need to fulfil for the Hamiltonian to be topologically non-trivial [Eq. (7.17)].

7.4 Bowtie ladder in the BDI symmetry class

Among the four different parameter configurations of the bowtie ladder Hamiltonian that belong to the BDI symmetry class (see Fig. 7.2), the bowtie ladder model can explore all different types of BDI ladder models, namely: the SSH model, the balanced BDI model and the imbalanced BDI model.

i) Bowtie ladder realizing the SSH model

The bowtie ladder collapses into a one-dimensional dimerized lattice if we set one of the two diagonal coupling amplitudes to zero; that is, $t = 0$ or $t' = 0$. In both cases the system becomes a chain with just two alternate couplings (see Fig. 7.4) and thus the phase ϕ becomes redundant and can be neglected, as in a one-dimensional chain no closed path defining a finite area can be constructed (apart from the path formed by the whole system when considering closed boundary conditions). Evaluating the time reversal conditions, Eq. (7.9) and Eq. (7.10), for $t = 0$ or $t' = 0$ we see that the corresponding Hamiltonian belongs to the BDI symmetry class only if $\delta = 0$ or $\delta = \pi$, being in the AIII class otherwise (see Fig. 7.5).

These two different ways in which the bowtie ladder becomes a one-dimensional dimerized lattice are realizations of the SSH model. They are connected to each other by applying the unitary transformation σ_x, which interchanges $\hat{a}_n^\dagger$ with $\hat{b}_n^\dagger$ and

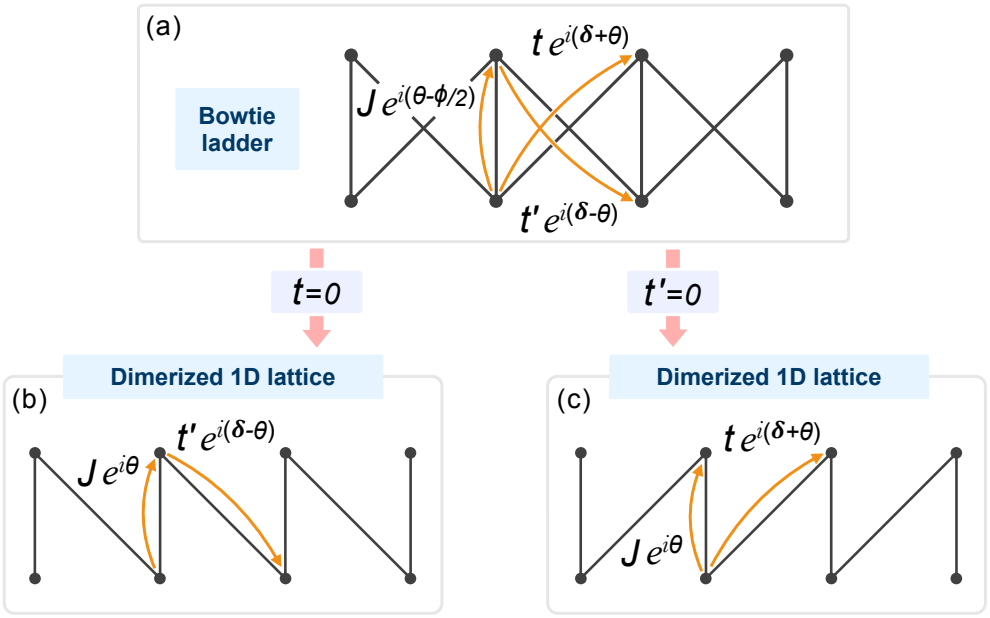

Figure 7.4: **1D dimerized lattice from the canonical ladder.** The canonical ladder (a) can collapse into a one-dimensional dimerized lattice by setting one of the two diagonal coupling amplitudes to zero. That is, making $t' = 0$ (b) or $t = 0$ (c).

δ	Time reversal	Charge conjugation	Chiral symmetry	Class
0,π	1	1	1	**BDI**
Otherwise	0	0	1	**AIII**

Figure 7.5: **Symmetry class of the bowtie ladder as a dimerized chain.** Presence (1) or absence (0) of time reversal, charge conjugation and chiral symmetries in the bowtie ladder Hamiltonian when the ladder has collapsed into a one-dimensional dimerized lattice. In this case all symmetry properties of the system are determined by the phase δ. The Hamiltonian belongs to the BDI symmetry class for $\delta = 0$ and $\delta = \pi$, whereas it belongs to the AIII class otherwise.

consists of flipping the ladder with respect to a central horizontal line (see Fig. 7.6), and therefore we only need to consider and analyse one of them. We choose the case given by setting $t' = 0$, whose Hamiltonian matrix is:

$$M(k) = (J \pm t\cos k)\,\sigma_x \pm t \sin k\,\sigma_y. \tag{7.18}$$

The $\pm$ options correspond to $\delta = 0$ and $\delta = \pi$, respectively. This Hamiltonian matrix is characterized by the fact that the ellipse in the complex plane has collapsed into a circumference [see Fig. 7.7(a)], which is centred at the point $(J, 0)$ and whose radius is t, so that the system is in a topologically non-trivial phase if $J < t$.

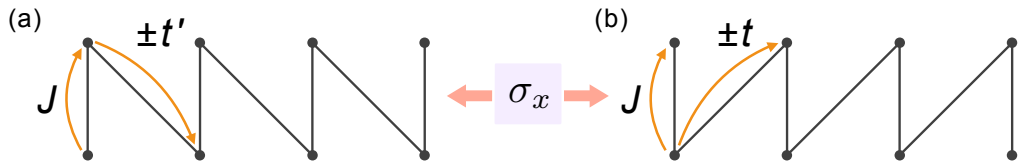

Figure 7.6: **SSH model from the canonical ladder.** The SSH model is obtained from the canonical ladder Hamiltonian by removing one of the two diagonal couplings, that is, taking $t = 0$ (a) or $t' = 0$ (b), as well as removing all phases in the tunneling amplitudes. This two possibilities correspond to different Hamiltonians which, nevertheless, are connected by applying the unitary σ_x.

ii) Bowtie ladder realizing the balanced BDI model

In the case in which the three coupling amplitudes present in the bowtie ladder Hamiltonian are non zero, there are four different configurations of parameters that correspond to a Hamiltonian in the BDI symmetry class. Two with $\phi = 0$ and another two with $\phi = \pi$ (see Fig. 7.2). The Hamiltonian matrices for the first two, with no effective magnetic flux, are the following:

$$M(k) = [J \pm (t + t')\cos k]\;\sigma_x \pm (t - t')\sin k\,\sigma_y, \tag{7.19}$$

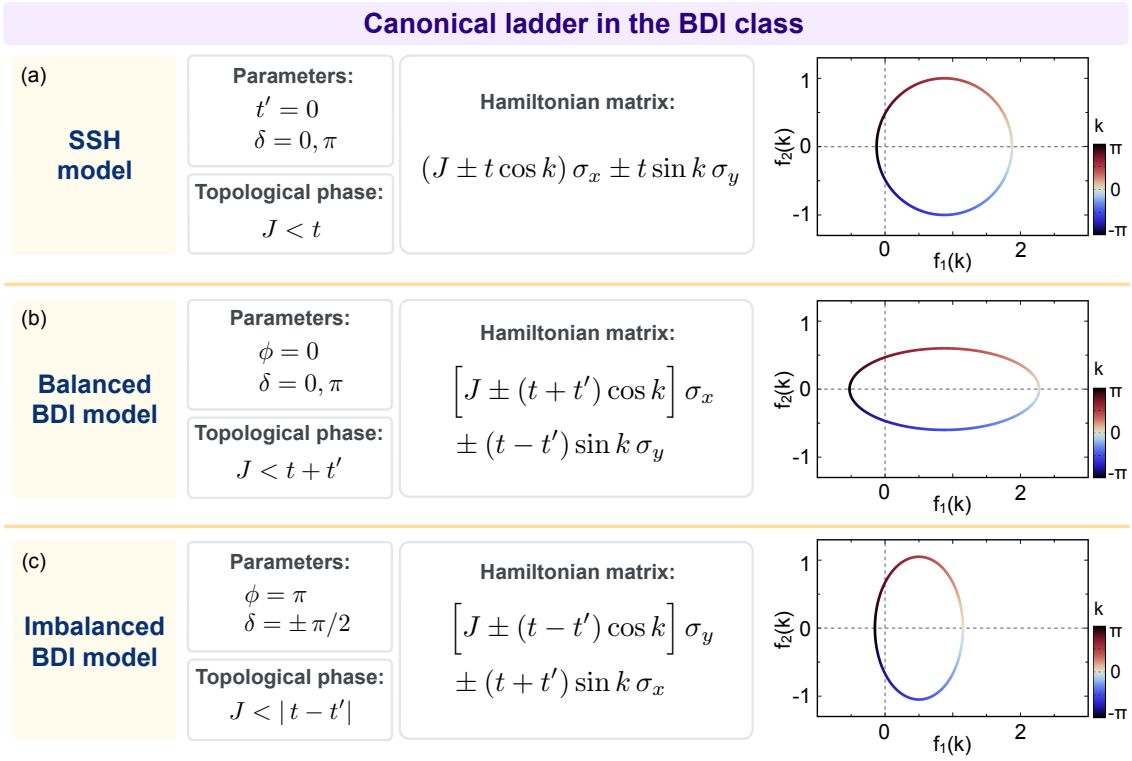

Figure 7.7: **Bowtie ladder in the BDI class.** The bowtie ladder serves as a canonical ladder model and allows us to explore and realize all types of topological ladder models. In particular, the three distinct types of BDI ladder models can be achieved by choosing the appropriate parameters configuration. Taking $t' = 0$ and $\delta = 0$ or $\delta = \pi$, it realizes the SSH model (a). For $\phi = 0$ and $\delta = 0$ or $\delta = \pi$, it corresponds to the balanced BDI model (b). Finally, for $\phi = \pi$ and $\delta = \pi/2$ or $\delta = -\pi/2$, we obtain a realization of the imbalanced BDI model.

where the $\pm$ correspond to the cases $\delta = 0$ and $\delta = \pi$, respectively. These Hamiltonian matrices are characterized by the fact that the horizontal axis of the corresponding ellipse is always bigger than the vertical one [see Fig. 7.7(b)], so that these two configurations of the bowtie ladder are realizations of the balanced BDI model (as well as the SSH-like model for a small region in the parameter space (see Fig. 6.4). The condition for a non-trivial topology takes in this case the particular form $J < t + t'$.

iii) Bowtie ladder realizing the imbalanced BDI model

The other two configurations of the bowtie ladder that realize BDI models, with $\phi = \pi$, correspond to the Hamiltonian matrices:

$$M(k) = \left[J \mp (t - t')\cos k\right]\,\sigma_y \pm (t + t')\sin k\,\sigma_x, \tag{7.20}$$

where the $\mp$ correspond to the cases $\delta = \pm\pi/2$. The ellipses described by these Hamiltonian matrices are characterized by a horizontal axis smaller than the vertical

one, considering the horizontal direction the one where the centre of the ellipse is located [see Fig. 7.7(c)]. Consequently, these two configurations of the bowtie ladder realize the imbalanced BDI model, as well as the SSH-like model in a small region in the parameter space (see Fig. 6.4). The condition for a non-trivial topology takes the form $J < |t - t'|$.

7.5 Bowtie ladder in the AIII class

There are two ways in which the bowtie ladder can break time reversal symmetry and, thus, belong to the AIII symmetry class. On one hand, by shifting the momentum-isospin correspondence, what can be done by adding a phase δ. On the other hand, by adding an effective magnetic flux per plaquette ϕ. We analyse each case separately.

7.5.1 Shift in the momentum-isospin correspondence

Any model in the BDI symmetry class with Hamiltonian matrix $M(k)$ can be taken to the AIII symmetry class by adding a shift δ in the momentum-isospin relation; that is, transforming $M(k)$ into $M(k-\delta)$. In the presence of this phase δ the Hamiltonian matrix has a different form and breaks time reversal and charge conjugation symmetries. The bulk modes differ from those corresponding to the case in which there is no phase δ, being characterized by a different momentum-isospin relation.

To show these results, we start by considering a ladder model in the BDI class, whose Hamiltonian matrix, as we know from Chapter 5, can be written as:

$$M(k) = (\alpha + \beta \cos k)\, \sigma_1 + \gamma \sin k\, \sigma_2, \tag{7.21}$$

with $\{\sigma_1, \sigma_2\} = 0$ and being α, β and γ three real parameters. The Bloch eigenstates of these model are given by Eq. (6.5) and the corresponding energies are $E_{\pm}(k) \mp \rho(k)$, with:

$$\rho^2(k) = \alpha^2 + \gamma^2 + 2\alpha\beta \cos k + (\beta^2 - \gamma^2) \cos^2 k. \tag{7.22}$$

If we introduce a shift δ with respect to the momentum, we obtain a new Hamiltonian matrix, $M(k-\delta)$, which can be decomposed as:

$$\begin{aligned} M(k-\delta) =& \sqrt{\beta^2 \cos^2\delta + \gamma^2 \sin^2\delta} \left(\frac{\alpha \cos\delta}{\beta} + \cos k \right) \sigma_c + \\ & \sqrt{\beta^2 \sin^2\delta + \gamma^2 \cos^2\delta} \left(\frac{\alpha \sin\delta}{\beta} + \sin k \right) \sigma_s, \end{aligned} \tag{7.23}$$

with $\sigma_c \propto \beta \cos\delta\, \sigma_1 - \gamma \sin\delta\, \sigma_2$ and $\sigma_s \propto \beta \sin\delta\, \sigma_1 + \gamma \cos\delta\, \sigma_2$. Comparing this matrix with the general form of the Hamiltonian matrix of a ladder model with chiral symmetry, Eq. (5.16), we conclude that it belongs to the BDI symmetry class

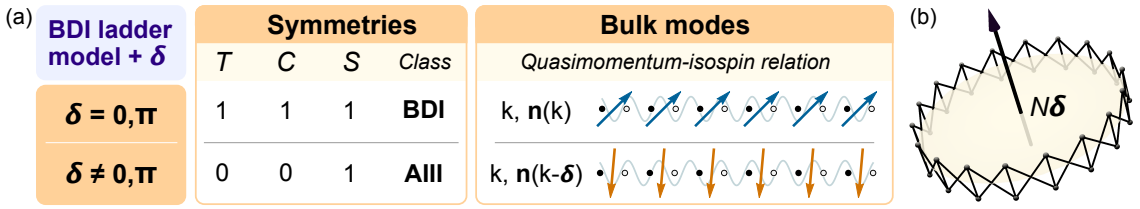

Figure 7.8: **Shift in the momentum-isospin correspondence.** (a) Each ladder model in the BDI class can be generalized by adding a phase δ. In the presence of a phase $\delta \neq 0, \pi$ time reversal and charge conjugation symmetries are broken and the model belongs to the AIII class. In this case the bulk modes exhibit a different momentum-isospin relation. (b) For periodic boundary conditions and N unit cells a total phase $N\delta$ is acquired by particles when completing a closed path along the whole system.

if and only if:

$$\eta = \frac{\alpha \sin\delta}{\beta}\sqrt{\beta^2 \sin^2\delta + \gamma^2 \cos^2\delta} = 0, \tag{7.24}$$

$$\{\sigma_c, \sigma_s\} \propto (\beta^2 - \gamma^2)\sin\delta\cos\delta = 0. \tag{7.25}$$

These two conditions are fulfilled simultaneously only if $\sin\delta = 0$, that is: for $\delta = 0$ and $\delta = \pi$. The phase δ that appears in the bowtie ladder parametrization (see Fi. 7.1) plays precisely this role, that is, introduces a shift in the Hamiltonian matrix with respect to the momentum. As a consequence, all ladder models in the BDI symmetry class come in pairs ($\delta = \delta_0, \delta = \delta_0 + \pi$), whose corresponding Hamiltonian matrices have the form:

$$M(k) = (\alpha \pm \beta\cos k)\,\sigma_1 \pm \gamma \sin k\,\sigma_2. \tag{7.26}$$

They are particular cases of a more general one with a phase $\delta = \delta_0 + \delta'$. This more general model belongs to the BDI class for $\delta' = 0, \pi$, whereas it belongs to the AIII class otherwise [see Fig. 7.8(a)].

The Bloch eigenstates for $\delta' \neq 0$ are:

$$|k, \delta'\rangle_\pm = \begin{pmatrix}\hat{a}_k^\dagger & \hat{b}_k^\dagger\end{pmatrix} \frac{1}{\sqrt{2}}\, U \begin{pmatrix} 1 \\ \pm e^{i\phi(k-\delta')}\end{pmatrix} |0\rangle\,. \tag{7.27}$$

The phase δ' produces a shift in the correspondence between the momentum and the isospin of each eigenstate, which are the two quantities that characterize them. As a consequence, the set of eigenmodes of the Hamiltonian for $\delta' \neq 0$ (AIII class) is genuinely different from the set of eigenmodes of the Hamiltonian for $\delta' = 0$ (BDI class) [see Fig. 7.8(a)].

In this way, the phase δ of the bowtie ladder model plays the same role that the phase δ did in the model for a topological insulator in the AIII class that we study in Part I and Part II of this thesis. It is in fact a generalization, what means

that shifting the momentum-isospin correspondence is a systematic way of breaking time reversal symmetry and can be donde in every ladder model. In the case of the bowtie ladder, when considering periodic boundary conditions, the phase δ also results in an effective magnetic flux $N\delta$ penetrating the ring formed by the whole system [see Fig. 7.8(b)].

The bowtie ladder model in the presence of a phase δ can realize each of the three different types of AIII ladder models, namely: the circular AIII model the balanced AIII model and the imbalanced AIII model.

***i)* Bowtie ladder realizing the circular AIII model**

This case corresponds to the situation in which one of the two diagonal couplings of the bowtie ladder have been set to zero, so that the system became a dimerized one-dimensional lattice (see Fig. 7.4). Both cases, taking $t = 0$ or $t' = 0$, are connected by applying a global unitary transformation. Therefore, we can consider only the case $t' = 0$, for which the Hamiltonian matrix is:

$$M(k) = \Big[J + t\cos(k-\delta)\Big]\,\sigma_x + t\sin(k-\delta)\,\sigma_y. \tag{7.28}$$

It describes a circle in the complex plane [see Fig. 7.9(a)] and corresponds to two energy bands with a single gap at momentum $q = \pi+\delta$. Therefore, it is a realization of the circular AIII model, and is precisely the model we study in Part I and Part II in this thesis. The condition for the system to be in its topologically non trivial phase is $J < t$.

***ii)* Bowtie ladder realizing the balanced AIII model**

In case in which the three different hopping amplitudes of the model are different from zero and $\phi = 0$, the bowtie ladder Hamiltonian matrix is:

$$M(k) = \Big[J + (t+t')\cos(k-\delta)\Big]\,\sigma_x + (t-t')\sin(k-\delta)\,\sigma_y. \tag{7.29}$$

This Hamiltonian matrix corresponds to an ellipse whose horizontal axis is bigger than the vertical one [see Fig. 7.9(b)] and two energy bands with two gaps of the same width located at $q_1 = \delta + q$ and $q_2 = \delta + q$ with:

$$q = \arccos\left[\frac{-J(t+t')}{4tt'}\right]. \tag{7.30}$$

Therefore, it is a realization of the balanced AIII model. The condition for a non trivial topology takes in this case the form $J < t + t'$.

***iii)* Bowtie ladder realizing the imbalanced AIII model**

For an effective magnetic flux $\phi = \pi$, the Hamiltonian matrix is:

$$M(k) = \big[J - (t-t')\cos(k-\delta')\big]\,\sigma_y + (t+t')\sin(k-\delta')\,\sigma_x, \tag{7.31}$$

where $\delta' = \delta - \pi/2$. The Hamiltonian matrix ellipse has then a horizontal axis smaller than the vertical one, considering the horizontal direction the one where the centre of the ellipse is located [see Fig. 7.9(c)]. In consequence, the model has two gaps between the energy bands, which have different widths and are located at $q_1 = \delta'$ and $q_2 = \delta' + \pi$. Thereby, it is a realization of the imbalanced AIII model. The condition for a non-trivial topology takes the form $J < |t - t'|$.

7.5.2 Effective magnetic flux per plaquette

We know that if we add a phase $\delta \neq 0, \pi$ to a particular bowtie ladder parameter configuration in the BDI class, we obtain a model in the AIII class. The Hamiltonian matrix of the new model will be equal to the Hamiltonian matrix of the BDI model to which the phase δ has been added, but with a shift of δ with respect to the momentum.That is:

$$M_{\mathrm{c}}(k;\delta) = M_{\mathrm{c}}(k-\delta;0). \tag{7.32}$$

In consequence, the Hamiltonian matrix curve will remain the same, being the momentum that corresponds to each point in the ellipse the only thing that is different. The energy bands are also shifted with respect to the momentum:

$$E_{\pm}(k;\delta) = E_{\pm}(k-\delta;0), \tag{7.33}$$

so that the number of energy gaps and their widths are not affected by the phase δ. However, their location in momentum space does actually change. In the SSH model there is a single energy gap at $q = 0$ or $q = \pi$; after adding a phase δ to such model we obtain the circular AIII model, with a single gap at $q = \delta$ or $q = \pi + \delta$. Analogously, adding a phase δ to the balanced BDI model and the imbalanced BDI model turns them into the balanced AIII model and the imbalanced AIII model, respectively.

Furthermore, most AIII ladder models can only be realized by adding a phase δ to a BDI ladder model. That is the case of the circular AIII model and the balanced AIII model. If an AIII ladder model has a single gap at $q \neq 0, \pi$, or two gaps of the same width, we can add a phase δ to them such that we obtain a single gap at $q = 0$, for the first case, and two gaps at opposite momenta in the second case. These new configurations are in the BDI class, what means that any circular AIII model and any balanced AIII model can be taken to the BDI class by adding the appropriate phase δ to them. On the contrary, not every imbalanced AIII model can be taken to the BDI class by shifting the momentum-isospin correspondence, but only those in which the distance between the two energy gaps is exactly π, and therefore a phase δ can be added such that one gap is shifted to $q_1 = 0$ and the other to $q_2 = \pi$.

As a result, we can conclude that a ladder model in the AIII class in which time reversal symmetry is broken by the presence of an effective magnetic field, such as the bowtie ladder with $\phi \neq 0, \pi$, is a realization of the imbalanced AIII model in which the distance between the two energy gaps is different from π . All other possible ladder models in the AIII class, namely: the circular AIII model, the balanced AIII model and the imbalance AIII model with a distance of π between

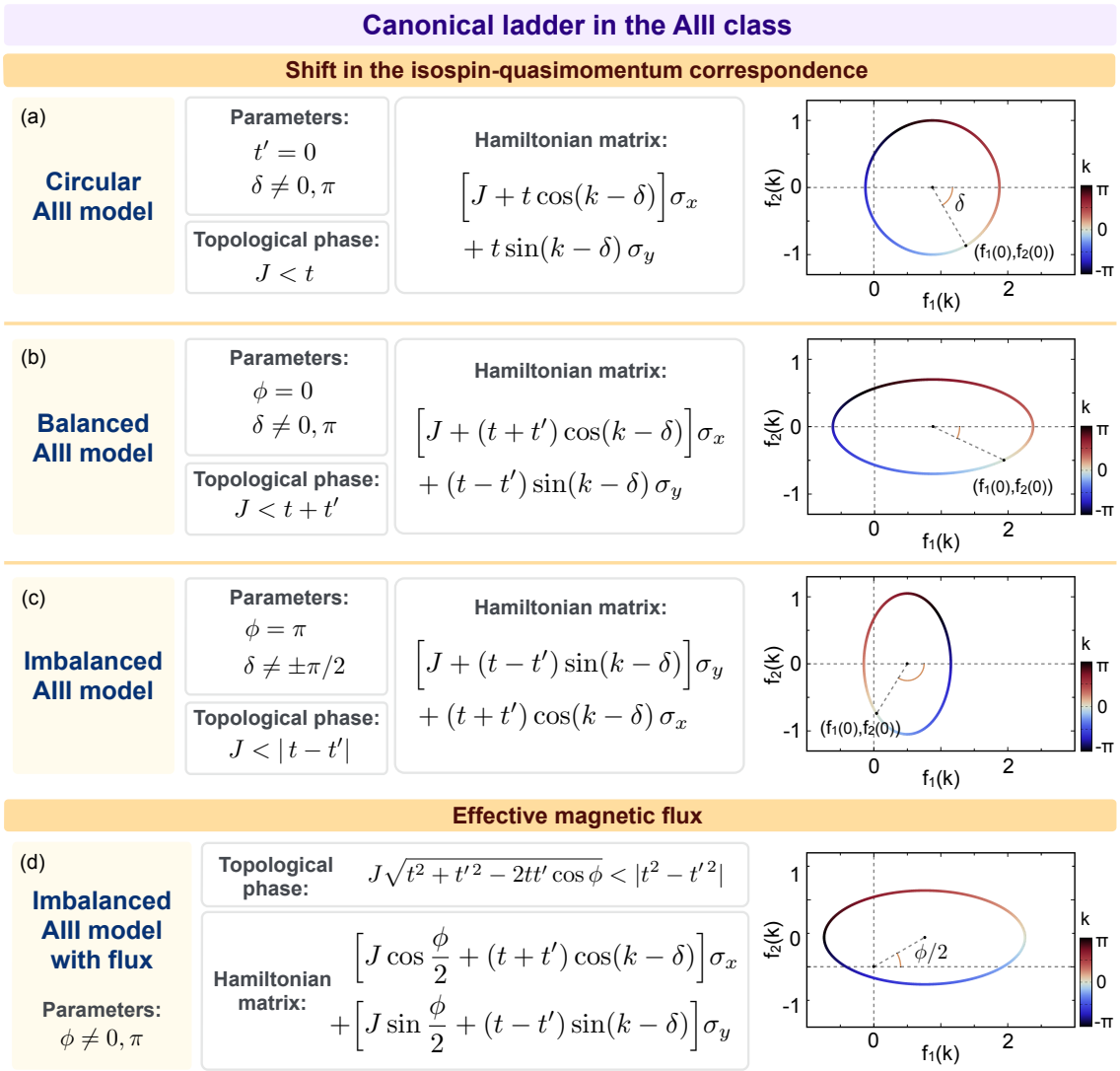

Figure 7.9: **Bowtie ladder in the AIII class.** The bowtie ladder needs at least one of two ingredients in order to break time reversal symmetry and realize a model in the AIII class: a phase δ that introduces a shift in the momentum-isospin correspondence or an effective magnetic flux ϕ. In the first case, the bowtie ladder realizes the circular AIII model (a), the balanced AIII model (b) and a particular case of the imbalance AIII model (c), in which the distance between the two energy gaps is π. In the second case, for $\phi \neq 0, \pi$, the bowtie ladder realizes the most general imbalance AIII model (d), in which the distance between the two energy gaps is different from π.

the two energy gaps, can be taken to the BDI class by adding a phase δ. The only values that the effective magnetic field can take in the BDI class are $\phi = 0$ and $\phi = \pi$, and the phase δ does not change the value of the effective magnetic field. Therefore, $\phi = 0$ or $\phi = \pi$ for those three types of AIII ladder models.

The bowtie ladder model with $\phi \neq 0, \pi$ corresponds to the Hamiltonian matrix

in Eq. 7.7, which describes an ellipse centred at $(J\cos\phi/2, J\sin\phi/2)$ and with axes $t+t'$ and $|t-t'|$ [see Fig. 7.9(d)]. It is a realization of the imbalanced AIII model and the condition that defines its topologically non trivial phase is the one in Eq. 7.17.

Chapter 8

Topological ladder edge states

The topological nature of a ladder model with chiral symmetry is manifested, for open boundary conditions, in the existence of topologically protected edge modes. They are located at the edges of the system, have almost zero energy and appear when the system is in its topological phase. Here we first obtain their wave function and then present their main properties, namely: they can be localized both in position and momentum spaces, and their momentum distribution is directly related to the number and masses of the Wilson fermions described by the model, as well as to the symmetry class of the Hamiltonian.

8.1 Edge states wave function

In order to derive the wave function of the edge modes of a topological ladder model, we focus on the bowtie ladder. As a canonical ladder model, any other ladder model can be obtained from it by performing a global unitary transformation. Therefore, once we obtain the edge modes of the bowtie ladder, it is straightforward to generalize the result to any ladder model. For it, we exploit the symmetries of the bowtie ladder model and also make a zero energy approximation.

8.1.1 Inversion-reflection-conjugation symmetry

The bowtie ladder model has an inversion-reflection-conjugation (IRC) symmetry, which can be used in order to obtain important information about the wave function of the edge modes. We consider the bowtie ladder and define the unitary transformation W as:

$$W : \begin{cases} \hat{a}_n^\dagger \longrightarrow \hat{b}_{N+1-n}^\dagger \\ \hat{b}_n^\dagger \longrightarrow \hat{a}_{N+1-n}^\dagger. \end{cases} \tag{8.1}$$

It is clearly a unitary transformation, as it rearranges the elements of the position basis. This operation consists of a reflection of the ladder with respect to a central vertical line and an inversion that interchanges the a and b modes with each other (see Fig. 8.1). This unitary transformation modifies the momentum creation

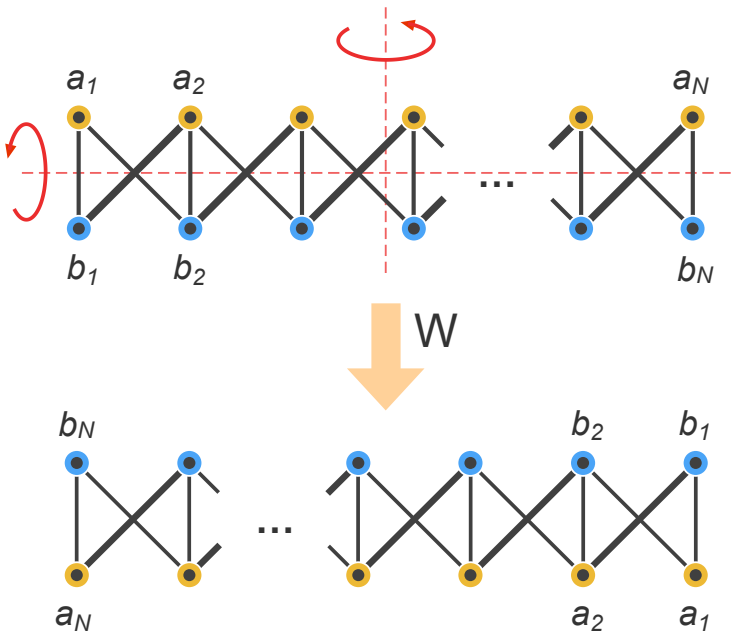

Figure 8.1: **IRC-symmetry of the bowtie ladder.** Schematic illustration of the unitary operator W, which produces a reflection and an inversion of the ladder. This transformation together with the complex conjugation leaves the bowtie ladder Hamiltonian invariant and, thus, represents a symmetry of the system.

operators in the following way:

$$\hat{a}_k^\dagger = \frac{1}{\sqrt{N}} \sum_n e^{ikn}\, \hat{a}_n^\dagger \xrightarrow{W} e^{ik(N+1)} \frac{1}{\sqrt{N}} \sum_n e^{-ikn}\, \hat{b}_n^\dagger = e^{ik}\, \hat{b}_{-k}^\dagger, \tag{8.2}$$

where we have used that $e^{ikN} = 1$. Therefore, the unitary W takes the following form in the momentum representation:

$$W : \begin{cases} \hat{a}_k^\dagger \longrightarrow e^{ik}\, (\hat{b}_k^\dagger)^* \\ \hat{b}_k^\dagger \longrightarrow e^{ik}\, (\hat{a}_k^\dagger)^*. \end{cases} \tag{8.3}$$

Applying this inversion-reflection transformation to the bowtie ladder Hamiltonian is equivalent to compute its complex conjugated:

$$\begin{aligned} H_\mathrm{c} = -\sum_k \rho(k) \left[e^{-i\varphi(k)}\, \hat{a}_k^\dagger \hat{b}_k + e^{i\varphi(k)}\, \hat{b}_k^\dagger \hat{a}_k \right] \xrightarrow{W} W H_\mathrm{c} W^\dagger = \\ -\sum_k \rho(k) \left[e^{i\varphi(k)}\, \hat{b}_k^\dagger \hat{a}_k + e^{-i\varphi(k)}\, \hat{a}_k^\dagger \hat{b}_k \right]^* = H_\mathrm{c}^*. \end{aligned} \tag{8.4}$$

Therefore the canonical Hamiltonian is invariant under the composition of the unitary transformation W and the anti-unitary transformation K, the complex conjugation. Moreover, both transformations commute with each other (the unitary

transformation W consists in a permutation of the elements of the position basis, so that it corresponds to a real matrix in such representation with only 0's and 1's as entries), in this way:

$$(WH_cW^\dagger)^* = WH_c^*W^\dagger = H_c. \tag{8.5}$$

As a consequence, if a certain vector $|e\rangle$ is an eigenstate of the Hamiltonian with a corresponding energy E the transformed state $W|e\rangle^*$ is also an eigenstate with the same energy. For non degenerate states, as the edge modes, this means that the transformed state is proportional to itself. Since the transformation preserves the norm, the transformed state is equal to itself up to a phase:

$$V|e\rangle^* = e^{i\omega}|e\rangle. \tag{8.6}$$

The phase ω can be absorbed into the state by redefining $|e\rangle = e^{i\omega/2}|e\rangle$, and thus we can consider without loss of generality that:

$$V|e\rangle^* = |e\rangle. \tag{8.7}$$

Being $\psi_a(n)$ and $\psi_b(n)$ the two components of the edge mode wave function, that is:

$$|e\rangle = \sum_n \begin{pmatrix}\hat{a}_n^\dagger & \hat{b}_n^\dagger\end{pmatrix}\begin{pmatrix}\psi_a(n)\\ \psi_b(n)\end{pmatrix}|0\rangle, \tag{8.8}$$

the transformed state is:

$$W|e\rangle^* = \sum_n \begin{pmatrix}\hat{a}_n^\dagger & \hat{b}_n^\dagger\end{pmatrix}\begin{pmatrix}\psi_b^*(N+1-n)\\ \psi_a^*(N+1-n)\end{pmatrix}|0\rangle, \tag{8.9}$$

and thus the IRC symmetry implies:

$$\psi_b(n) = \psi_a^*(N+1-n). \tag{8.10}$$

As a result the edge state can be expressed in terms of just one wave function $\psi(n)$ as:

$$|e\rangle = \frac{1}{\sqrt{2}}\sum_n \begin{pmatrix}\hat{a}_n^\dagger & \hat{b}_n^\dagger\end{pmatrix}\begin{pmatrix}\psi(n)\\ \psi^*(N+1-n)\end{pmatrix}|0\rangle. \tag{8.11}$$

8.1.2 Chiral symmetry and edge states polarization

The presence of chiral symmetry makes all eigenstates come in pairs of opposite energy, being the two eigenstates of each pair connected by the chiral operator U_S. That is, being the edge mode $|e\rangle$ in Eq.(8.11) an eigenstate of the bowtie ladder Hamiltonian with some energy E, then the state $U_S|e\rangle$ is another eigenstate with energy $-E$. In the case of the bowtie ladder Hamiltonian the chiral operator is $U_S = \sigma_z$, therefore the two edge modes are:

$$|e_\pm\rangle = \frac{1}{\sqrt{2}}\sum_n \begin{pmatrix}\hat{a}_n^\dagger & \hat{b}_n^\dagger\end{pmatrix}\begin{pmatrix}\psi(n)\\ \pm\psi^*(N+1-n)\end{pmatrix}|0\rangle, \tag{8.12}$$

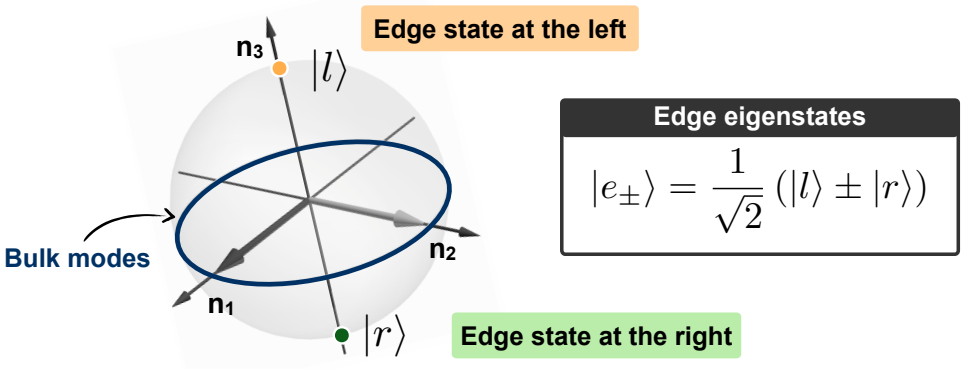

Figure 8.2: **Edge modes polarization.** The edge eigenstates of the Hamiltonian, $|e_\pm\rangle$, consist of the symmetric and antisymmetric superpositions of the edge states $|l\rangle$ and $|r\rangle$, which are localized at the left and right edges of the system. The isospin state of these two edge states are the ones given by the eigenvectors of the chiral operator. This correlation between the isospin of each edge modes and the edge where it is located is what we call the edge modes polarization. If we place all eigenstates of the Hamiltonian in the Bloch sphere, the bulk modes are on the equator and the edge modes are at the poles; being the equator the circumference formed by the intersection of the sphere and the plane where the Hamiltonian matrix lives, so that the poles correspond to the direction of the chiral operator $U_S = \boldsymbol{n}_3 \cdot \boldsymbol{\sigma}$.

which satisfy: $U_S\,|e_\pm\rangle = |e_\mp\rangle$.

The edge modes are located at the edges of the system and the most general wave function $\psi(n)$ can be decompose into two different parts:

$$\psi(n) = \psi_l(n) + \psi_r(n), \tag{8.13}$$

being $\psi_l(n)$ and $\psi_r(n)$ located at the left and right ends of the ladder, respectively. In this way, we can decompose the edge modes in the following way:

$$|e_\pm\rangle = \frac{1}{2}\Big(\,|l_\pm\rangle + |r_\pm\rangle\,\Big), \tag{8.14}$$

where:

$$|l_\pm\rangle = \sum_n \begin{pmatrix}\hat{a}_n^\dagger & \hat{b}_n^\dagger\end{pmatrix} \begin{pmatrix}\psi_l(n) \\ \pm\psi_r^*(N+1-n)\end{pmatrix} |0\rangle\,, \tag{8.15}$$

$$|r_\pm\rangle = \sum_n \begin{pmatrix}\hat{a}_n^\dagger & \hat{b}_n^\dagger\end{pmatrix} \begin{pmatrix}\psi_r(n) \\ \pm\psi_l^*(N+1-n)\end{pmatrix} |0\rangle\,, \tag{8.16}$$

so that the edge modes would be made from four different components: two located at the left end of the ladder, $|l_\pm\rangle$, and another two at the right edge, $|r_\pm\rangle$. On the other hand, apart from being spatially located at the ends of the ladder, the edge modes are chacterized by the property of having almost zero energy. Furthermore, we can consider regions in the parameter space in which the energy of the edge modes

is arbitrary close to zero so that we can make the approximation of zero energy, which is equivalent to consider the size of the system to be infinite compared to the spatial extension of the edge modes wave packets. In this situation the edge modes are annihilated by the Hamiltonian: $H_c\,|e_\pm\rangle = 0$. However, the Hamiltonian is a local operator, as it connects each site in the ladder with itself and the sites within the same and the adjacent unit cells. As a consequence, the edge modes can be eigenstates of the Hamiltonian with zero energy only if the two components from which they are formed are also annihilated by the Hamiltonian, since they are separated by an arbitrary long distance. That is:

$$H_c\,|e_\pm\rangle = 0 \implies H_c\,|l_\pm\rangle = H_c\,|r_\pm\rangle = 0, \tag{8.17}$$

which would imply that the four states $|l_+\rangle$, $|l_-\rangle$,$|r_+\rangle$ and $|r_-\rangle$ are zero energy eigenstates of the Hamiltonian. In this situation the two original edge modes of the system would split into four different edge modes, what has no sense. The origin of this contradiction is found in the assumption that the wavefunction $\psi(n)$ has two components located at each edge of the ladder. Therefore, we conclude that it must be located at one particular edge. For instance, let us consider the case in which it is localized at the left side of the system. Then, the edge modes would be written as:

$$|e_\pm\rangle = \frac{1}{\sqrt{2}}\Big(\,|l\rangle \pm |r\rangle\,\Big), \tag{8.18}$$

where $|l\rangle$ and $|r\rangle$ are states localized at the left and right edges of the system, respectively:

$$|l\rangle = \sum_n \psi(n)\,\hat{a}_n^\dagger\,|0\rangle \tag{8.19}$$

$$|r\rangle = \sum_n \psi^*(N+1-n)\,\hat{b}_n^\dagger\,|0\rangle\,. \tag{8.20}$$

In conclusion, the edge states which are exact eigenstates of the Hamiltonian, $|e_\pm\rangle$, are composed of two edge states, $|l\rangle$ and $|r\rangle$, which are localized at a single edge of the system. In the zero energy approximation, and due to the local nature of the Hamiltonian, the edge modes $|l\rangle$ and $|r\rangle$ can be considered to be also eigenstates of the system. The presence of chiral symmetry implies that the two edge exact eigenstates $|e_\pm\rangle$ must be transformed by the chiral operator into each other. This means that the subspace spanned by the edge eigenstates $|e_\pm\rangle$, which is the same as the one spanned by the two single-edge modes $|l\rangle$ and $|r\rangle$, is invariant under the chiral operator. Since the single-edge modes are separated by an arbitrary long distance and the chiral operator acts locally, the only possible situation is that they are eigenstates of the chiral operator. Let us choose the edge mode at the left size of the system to be the one corresponding to the eigenvalue $+1$ and the one at the right to the eigenvalue -1, that is:

$$U_S\;|l\rangle = |l\rangle\,, \tag{8.21}$$

$$U_S\;|r\rangle = -\,|r\rangle\,. \tag{8.22}$$

So that the isospin state of each single-edge mode, i.e. the vector that corresponds to the $a-b$ internal degree of freedom, corresponds to one of the two orthogonal eigenvectors of the chiral operator, which stands for a *polarization* property of the edge modes (see Fig. 8.2). In the case of the bowtie ladder, for which $U_S = \sigma_z$, this means that the left edge mode occupies only a-sites in the ladder, whereas the right edge mode occupies only b-sites. The edge eigenstates of the Hamiltonian are then formed as the symmetric and antisymmetric superpositions of the edge modes $|l\rangle$ and $|r\rangle$, see Eq. 8.14, and fulfil the relation $U_S\,|e_\pm\rangle = |e_\mp\rangle$.

Finally, we could ask ourselves what decides the particular polarization of the edge modes. That is, when does the edge mode located at the left end of the system occupy a-modes and when b-modes? It turns out that it depends on the two diagonal couplings of the bowtie ladder. For $t > t'$ the edge mode at the left occupies a-modes and the one at the right b-modes, whereas the polarization is the opposite for $t < t'$. In the first situation, when $t > t'$, we can get arbitrary close to the limit case $t' = 0$. At that point the ladder becomes a dimerized $(a-b)$ chain, where the left edge is an a-site and the right edge a b-site. In contrast, for $t < t'$, the ladder can be continuously connected to an $(b-a)$ chain, where the left edge is a b-site and the right one an a-site. Both situations cannot be continuously connected without a phase transition, as the point $t = t'$ corresponds to a trivial topology, for which there are no edge modes (see Chapter 7).

8.1.3 Zero energy approximation

A very good approximation of the edge modes wave function can be obtained by considering them to be zero energy eigenstates of the Hamiltonian.

We start by separating the bowtie ladder Hamiltonian for periodic boundary conditions, H_{prdc}, into two parts: the bowtie ladder Hamiltonian for open boundary conditions, H_{open}, and an edge Hamiltonian, H_{edge}. That is:

$$H_{\text{prdc}} = H_{\text{open}} + H_{\text{edge}}, \tag{8.23}$$

being:

$$H_{\text{edge}} = -te^{i\delta}\,\hat{a}_1^\dagger \hat{b}_N - t'e^{i\delta}\,\hat{b}_1^\dagger \hat{a}_N + \text{H.c.} \tag{8.24}$$

We consider the edge modes in Eq. (8.12) and impose that they are zero energy eigenstates of the Hamiltonian for open boundary conditions:

$$H_{\text{open}}\,|e_\pm\rangle \approx 0, \tag{8.25}$$

so that, in terms of the Hamiltonian for periodic boundary conditions and the edge Hamiltonian, we have:

$$H_{\text{prdc}}\,|e_\pm\rangle - H_{\text{edge}}\,|e_\pm\rangle \approx 0. \tag{8.26}$$

First, we compute the result of applying the Hamiltonian for periodic boundary conditions to the edge modes, $H_{\text{prdc}}\,|e_\pm\rangle$. For that we write the edge modes in the momentum representation, which is more convenient inasmuch as the Hamiltonian

for periodic boundary conditions is easily written in such basis. Defining the function $F(k)$ as:

$$F(k) = \frac{1}{\sqrt{N}} \sum_{n=1}^{N} e^{-ikn} \psi(n), \tag{8.27}$$

the edge modes can be written as:

$$|e_{\pm}\rangle = \frac{1}{\sqrt{2}} \sum_{k} \begin{pmatrix} \hat{a}_k^\dagger & \hat{b}_n^\dagger \end{pmatrix} \begin{pmatrix} F(k) \\ \pm e^{-ik} F^*(k) \end{pmatrix} |0\rangle \,. \tag{8.28}$$

The bowtie ladder Hamiltonian for periodic boundary condition is:

$$H_{\text{prdc}} = -\sum_{k} \rho(k) \begin{pmatrix} \hat{a}_k^\dagger & \hat{b}_n^\dagger \end{pmatrix} \begin{pmatrix} 0 & e^{-i\varphi(k)} \\ e^{i\varphi(k)} & 0 \end{pmatrix} \begin{pmatrix} \hat{a}_k \\ \hat{b}_k \end{pmatrix}, \tag{8.29}$$

so that the result of applying it to the edge modes is:

$$H_{\text{prdc}} |e_{\pm}\rangle = -\frac{1}{\sqrt{2}} \sum_{k} \rho(k) \begin{pmatrix} \hat{a}_k^\dagger & \hat{b}_n^\dagger \end{pmatrix} \begin{pmatrix} \pm e^{-ik} e^{-i\varphi(k)} F^*(k) \\ e^{i\varphi(k)} F(k) \end{pmatrix} |0\rangle \,. \tag{8.30}$$

Secondly, we compute the result of applying the edge Hamiltonian to the edge modes, $H_{\text{edge}} |e_{\pm}\rangle$. For that we need to take into account the polarization of the edge modes, that is, the edge mode at the left size of the system occupies only a-modes, whereas the one at the right occupies only b-modes. Therefore, only two sites are affected by the edge Hamiltonian, a_1 and b_N, and we get:

$$H_{\text{edge}} |e_{\pm}\rangle = -\frac{t}{\sqrt{2}} \Big[e^{-i\delta} \, \psi(1) \, \hat{b}_N^\dagger \pm e^{i\delta} \, \psi^*(1) \, \hat{a}_1^\dagger \Big] |0\rangle \,, \tag{8.31}$$

which in momentum representation takes the form:

$$H_{\text{edge}} |e_{\pm}\rangle = \frac{t}{\sqrt{2N}} \sum_{k} \begin{pmatrix} \hat{a}_k^\dagger & \hat{b}_n^\dagger \end{pmatrix} \begin{pmatrix} \pm e^{-ik} e^{i\delta} \psi^*(1) \\ e^{-i\delta} \, \psi(1) \end{pmatrix} |0\rangle \,. \tag{8.32}$$

From (8.26), (8.30) and (8.32) we obtain:

$$F(k) = -\frac{1}{\sqrt{N}} \, t \, e^{-i\delta} \, \psi(1) \, \frac{e^{-i\varphi(k)}}{\rho(k)}, \tag{8.33}$$

and thus the edge modes are easily written in momentum representation as:

$$|l\rangle = \frac{1}{\sqrt{\kappa}} \sum_{k} \frac{e^{-i\varphi(k)}}{\rho(k)} \, \hat{a}_k^\dagger \, |0\rangle \,, \tag{8.34}$$

$$|r\rangle = \frac{1}{\sqrt{\kappa}} \sum_{k} \frac{e^{-ik} e^{i\varphi(k)}}{\rho(k)} \, \hat{b}_k^\dagger \, |0\rangle \,, \tag{8.35}$$

being κ a normalization constant.

8.2 Edge states general properties

Once we have obtained a quite good approximation for the edge modes wave functions, Eq. (8.34) and Eq. (8.35), we can derive their more relevant properties. These are:

- The edge states are localized in momentum space at the positions of the energy gaps between the two energy bands.
- The edge states are located in position space at the ends of the ladder.
- The edge states can be simultaneously well localized in momentum and position spaces.
- The symmetry class of a topological ladder model is manifested through the edge states momentum distribution.

8.2.1 Edge states in momentum space

The momentum density distribution of the edge states can be easily obtained from their wave functions, Eq.(8.34) and Eq.(8.35). Both states have the same momentum density distribution:

$$\langle \hat{n}_k \rangle = \frac{1}{\kappa\, \rho^2(k)}, \tag{8.36}$$

where $\hat{n}_k = \hat{a}_k^\dagger \hat{a}_k + \hat{b}_k^\dagger \hat{b}_k$. Due to the polarization property of the edge states we know that, in the particular case of the bowtie ladder, the edge state located at the left end of the system occupies only a-modes, whereas the one at the right end occupies only b-modes. Therefore:

$$\langle l|\, \hat{a}_k^\dagger \hat{a}_k\, |l\rangle = \langle r|\, \hat{b}_k^\dagger \hat{b}_k\, |r\rangle = \frac{1}{\kappa\, \rho^2(k)} \tag{8.37}$$

$$\langle r|\, \hat{a}_k^\dagger \hat{a}_k\, |r\rangle = \langle l|\, \hat{b}_k^\dagger \hat{b}_k\, |l\rangle\,. \tag{8.38}$$

In general, for an arbitrary topological ladder model, the edge state located at each end of the system occupies one of the two orthogonal superpositions of a-modes and b-modes corresponding to each eigenvector of the chiral operator U_S. Nevertheless, the momentum distribution $\langle \hat{n}_k \rangle$, understood as the probability for a particle that occupies a certain state to be found with the momentum value k, regardless of its isospin, depends only on the function $\rho(k)$, that is, the energy bands of the system. In this way, we only need to analyse Eq. (8.36) in order to learn about the properties of the edge states in momentum space.

The maxima of the momentum density distribution of the edge modes, $\langle \hat{n}_k \rangle$, will be located at the minima of the function $\rho(k)$. Being q_j a minimum of $\rho(k)$, which

correspond to the location of an energy gap between the two bands, we can make a second order expansion of $\rho(k)$ around that minimum:

$$\rho(k) \approx \frac{E_j}{2} + \frac{(k-q_j)^2}{2m_j}, \tag{8.39}$$

begin E_j the gap width and m_j the mass of the Wilson fermion associated to that gap, which is given by:

$$\frac{1}{m_j} = \left.\frac{d^2\rho(k)}{dk^2}\right|_{k=q_j}. \tag{8.40}$$

In this way we can approximate the edge states momentum distribution around q_j by:

$$\langle \hat{n}_k \rangle \approx \frac{4}{\kappa\, E_j^2}\left[1 + \left(\frac{k-q_j}{\xi_j}\right)^2\right]^{-2}, \tag{8.41}$$

being $\xi_j = \sqrt{m_j\, E_j}$. As we see, the edge states momentum distribution takes the form of the square of a Cauchy distribution around each energy gap and, therefore, we can conclude that the edge states are strongly localized in momentum space at the position of the energy gaps of the system.

The edge states momentum distribution shows a peak for each energy gap between the two bands, being $4/\kappa\, E_j^2$ the height of each peak and $\delta k_j = 2\xi_j\sqrt{\sqrt{2}-1}$ its corresponding FWHM. We can obtain the probability associated to each peak by making an approximation and integrating over a continuum momentum

$$\text{prob}_j \approx \int_{-\infty}^{\infty} dk \frac{4}{\kappa\, E_j^2}\left[1 + \left(\frac{k-q_j}{\xi_j}\right)^2\right]^{-2} = \frac{2\pi}{\kappa}\sqrt{\frac{m_j}{E_j^3}}. \tag{8.42}$$

As a consequence, taking into account the fact that the energy bands correspond to the distance from the origin to the points of an ellipse, in case there are two different energy gaps between the bands, and thus two different peaks in the edge states momentum distribution, the probability associated to the peak placed at the smallest energy gap momentum will be larger.

As a result, we can establish a correspondence between the edge states present in a topological ladder model and the Wilson fermions described by such model, according to which:

- The number of Wilson fermions is equal to the number of momentum components that constitute the edge modes.

- The momenta at which the Wilson fermions arise correspond to the location of the edge modes momentum components.

- The masses of the Wilson fermions correspond to the relative weights of the edge modes momentum components, in such a way that:

(i) If two Wilson fermions have the same masses, the corresponding momentum components contribute equally to the edge modes.

(ii) If two Wilson fermions have different masses, the momentum peak associated to the lightest fermion is better defined, so that its corresponding component is predominant in the edge states wave function.

8.2.2 Edge states in position space

In the case of the position space, each edge sate shows a different density distribution. However, they are not independent from each other, as the wave function of the edge state $|r\rangle$ can be obtained by complex conjugating and reflecting the wave function of the edge state $|l\rangle$, see Eq. (8.19) and Eq. (8.20). We have:

$$\langle l|\,\hat{n}_x\,|l\rangle = |\psi(x)|^2 \tag{8.43}$$

$$\langle r|\,\hat{n}_x\,|r\rangle = |\psi(N+1-x)|^2, \tag{8.44}$$

being $\hat{n}_x = \hat{a}_x^\dagger \hat{a}_x + \hat{b}_x^\dagger \hat{b}_x$ the particle number operator at position x, regardless of the isospin state. In the same way that occurs in momentum space, in position space the two edge states occupy different orthogonal isospin states, given by the chiral operator. Nevertheless, the position density distributions in Eq. (8.43) and Eq. (8.44) are valid for any ladder model.

We first consider the edge state located at the left side of the system, Eq. (8.34). As we already know, it is mostly located in momentum space around the energy gap momenta and, therefore, we can decompose such edge mode in several momentum components. For that, we need to make an expansion of the function $e^{-i\varphi(k)}$ around q_j, being q_j a minimum of $\rho(k)$. The value of $\varphi(k)$, for k close to q_j, will be equal to $\varphi(q_j)$ plus some phase $\delta\varphi_j$, and thus:

$$e^{-i\varphi(k)} = e^{-i[\varphi(q_j)+\delta\varphi_j]} = e^{-i\varphi(q_j)}(\cos\delta\varphi_j - i\sin\delta\varphi_j) \tag{8.45}$$

From Fig. 8.3 we can compute first and second order approximations for the sine and cosine of the variation of $\varphi(k)$ with respect to $\varphi(q_j)$. Taking into account that $\rho(q_j) = E_j/2$ and using the second order expansion of $\rho(k)$ around q_j in Eq. (8.39) we obtain:

$$\cos\delta\varphi_j \approx 1 - \left(\frac{k-q_j}{\xi_j}\right)^2 \tag{8.46}$$

$$\sin\delta\varphi_j \approx \sqrt{2}\left(\frac{k-q_j}{\xi_j}\right) \tag{8.47}$$

By using this expansion of $\varphi(k)$ at each energy gap momentum we can write the edge mode $|l\rangle$ as a sum of different momentum components:

$$|l\rangle = \sum_j |l_j\rangle\,, \tag{8.48}$$

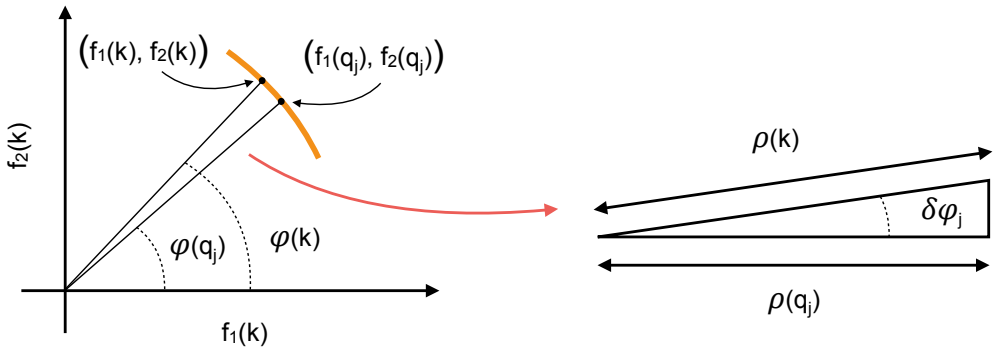

Figure 8.3: **Function $\varphi(k)$ around the momentum of an energy gap.** For a momentum k close to q_j, being q_j the location of an energy gap between the two bands can be written as $\varphi(q_j)$ plus some variation $\delta\varphi_j$, which can be computed in terms of $\rho(k)$ and $\rho(q_j)$ (see text).

running j over the number of energy gaps of the system and being:

$$|l_j\rangle \approx \frac{2}{\sqrt{\kappa}} \sum_k \frac{e^{-i\varphi(q_j)} \left[1 - \left(\frac{k-q_j}{\xi_j}\right)^2 - i\sqrt{2}\left(\frac{k-q_j}{\xi_j}\right)\right]}{E_j + \left(\frac{k-q_j}{\xi_j}\right)^2} \hat{a}_k^\dagger |0\rangle \,. \tag{8.49}$$

We compute the inverse Fourier transform of this momentum wave function and thus obtain the component $|l_j\rangle$ in the position representation:

$$|l_j\rangle \approx \frac{\sqrt{2}(\sqrt{2}-1)}{\sqrt{\kappa}} \sqrt{\frac{m_j}{E_j}}\, e^{-i\varphi(q_j)} \sum_n e^{iq_j n}\, e^{-\xi_j n}\, \hat{a}_n^\dagger\, |0\rangle \,. \tag{8.50}$$

As we see, the spatial wave function consists of two factors: $e^{iq_j n}$, which means that the momentum distribution is centred at the value q_j, as we already new, and $e^{-\xi_j n}$, which is a decaying exponential whose maximum value corresponds to the position $n = 1$. The spatial density distribution of such state is then:

$$\langle l_j|\, \hat{n}_x\, |l_j\rangle \approx \frac{2(3-2\sqrt{2})}{\kappa} \frac{m_j}{E_j}\, e^{-2\xi_j n}, \tag{8.51}$$

Analogously, the edge mode $|r\rangle$ can also be decomposed in different momentum modes:

$$|r\rangle = \sum_j |r_j\rangle \,, \tag{8.52}$$

being:

$$|r_j\rangle \approx \frac{\sqrt{2}(\sqrt{2}-1)}{\sqrt{\kappa}} \sqrt{\frac{m_j}{E_j}}\, e^{i\varphi(q_j)}\, e^{-iq_j(N+1)} \sum_n e^{iq_j n}\, e^{-\xi_j(N+1-n)}\, \hat{b}_n^\dagger\, |0\rangle \,, \tag{8.53}$$

since we know that the spatial wave function of $|r\rangle$ can be obtained by complex conjugating and reflecting the wave function of $|l\rangle$, see Eq. (8.19) and Eq. (8.20). The spatial density distribution of the component $|r_j\rangle$ is then:

$$\langle r_j|\,\hat{n}_x\,|r_j\rangle \approx \frac{2(3-2\sqrt{2})}{\kappa}\,\frac{m_j}{E_j}\,e^{-2\xi_j(N+1-n)}. \tag{8.54}$$

In this way, we conclude that the edge states $|l\rangle$ and $|r\rangle$ are localized at the left and right edges of the system, decaying their spatial density distribution exponentially towards the bulk. Each edge mode component $|l_j\rangle$ and $|r_j\rangle$ has a FWHM of $\delta x_j = \log 2/(2\xi_j)$.

8.2.3 Simultaneous momentum-position localization

From the approximated momentum and spatial density distributions of the edge states, Eq. (8.41), Eq. (8.51) and Eq. (8.54), and their corresponding localization lengths, $\delta k_j = 2\xi_j\sqrt{\sqrt{2}-1}$ and $\delta x_j = \log 2/(2\xi_j)$, we know that the larger an energy gap is, the better defined the position of the corresponding edge states component is and the worse defined its momentum is. However, there is a region in the parameter space for which both the momentum and the position of the edge modes can be simultaneously well defined.

This property of simultaneous position and momentum localization makes possible quench dynamics in which the edge states form well defined wave packets that travel along the system at a constant velocity keeping their identity for long evolution times. This dynamics leads to the interference of fractionalized quasiparticles studied in Part II, as well as to topologically protected chiral currents, which we show in Part IV of this thesis.

8.2.4 Complex momentum interpretation

The quantity ξ_j, defined for each energy gap as $\xi_j = \sqrt{m_j E_j}$, scales the wave function of the edge states component associated to each energy gap, as well as its momentum and position density distributions, Eq. (8.41), Eq. (8.51) and Eq. (8.54). In this way, it also determines the edge sates localization lengths in position and momentum spaces. But, is this just a quantity we defined in order to write things in a more compact way, or can it be physically interpreted?

In Part I of this thesis we obtained the exact wave functions of the edge modes of a one-dimensional dimerized lattice, that realizes the SSH model or the circular AIII model. In that case, after trying to find all eigenstates of the Hamiltonian for open boundary conditions, we end up with a quantization condition for which there are only $N-1$ solutions when the system is in its topologically non trivial phase. Therefore, we found only $2N-2$ bulk eigenstates of the Hamiltonian, Fig. 2.1. As there are no more real solutions to that quantization conditions, we needed to consider Bloch modes with complex momentum, combine them and impose the boundary conditions. The real part of the such momentum turned out to be the

value at which the edge states momentum distribution is centred and coincides with the position of the energy gap of the system, whereas its imaginary part scales the edge states wave function and determines their position and momentum localization lengths.

We could think that the reason for the edge states to have a momentum that corresponds to the energy gap location in momentum space is that this is the momentum at which the energy bands cross each other at the topological transition point, as the edge states have almost zero energy and the crossing point between the bands is the only one that corresponds to an energy equal to zero. However, if we modify the parameters of a model in such a way that the locations of the energy gaps change, the momentum of the edge modes will also change and follow the energy gaps, even though the crossing point of the energy bands at the critical point could correspond to a different momentum. For example, a ladder model with two energy gaps will show edge states with two momentum components, one for each gap, whereas the energy bands cross each other at just one point at the phase transition.

If we evaluate the dispersion relation of the dimerized lattice model for a complex momentum $k = q + i\xi$, we will obtain in general something complex. However, if we choose q to be a minimum or a maximum of the function $\rho(k)$ we will obtain a real quantity. The reason for that is that the function $\rho(k)$, in the case of a dimerized lattice model [see Eq. (1.14)], is even with respect to the locations of its maximum and minimum. Therefore, if we make a power series expansion around that values, all odd terms vanish, which are the ones that contribute to the imaginary part of $\rho(k = q + i\xi)$. Then, we choose the minimum and not the maximum because we want the energy to be zero or close to zero.

In the case of a topological ladder model, finding the edge states "by hard", considering linear superpositions of different momentum modes and imposing the boundary conditions, is mucho more difficult than in a dimerized lattice. In fact, it is much more convenient to use the symmetries of the bowtie ladder, which serves a canonical ladder model, and obtain the edge states wave functions as we did in this chapter. Nevertheless, we can still make an analogy between the edge states we obtained and complex momentum modes that serves us to interpret the quantities ξ_j that appear in the edge sates wave functions.

If we have a topological ladder model with energy bands $E_{\pm}(k) = \mp\rho(k)$ and want to find out eigenstates of zero energy, we can consider a mode with momentum $q_j + i\xi_j$, being q_j a minimum of $\rho(k)$. In order to compute the corresponding energy, we make a second order expansion of $\rho(k)$ at $k = q_j$. That is:

$$\rho(k) \approx \frac{E_j}{2} + \frac{(k - q_j)^2}{2m_j}. \tag{8.55}$$

The fact that q_j is a minimum of $\rho(k)$, and thus the first order term in this expansion vanishes and the second order one is positive, allows the energy corresponding to a complex momentum $q_j + i\xi$ to be zero. In fact, we can find the value of ξ by

imposing a zero energy:

$$\rho(q_j + i\xi_j) \approx \frac{E_j}{2} - \frac{\xi_j^2}{2m_j} = 0 \implies \xi_j = \sqrt{m_j E_j}, \tag{8.56}$$

and we obtain precisely what we have previously defined. This means that the quantity ξ_j, associated to a particular energy gap located at q_j, is the imaginary part that we need to add to the momentum of a state of momentum q_j in order for it to have zero energy, according to a second order approximation. The type of wave function that we obtain if we evaluate a momentum mode at the complex momentum $q_j + i\xi_j$, is: $e^{iq_j n}e^{-\xi_j n}$, which is precisely the approximated wave function we have obtained for each momentum component of the edge state $|l\rangle$.

Despite all this, this is just an analogy that serves to make an interpretation of the parameter ξ_j. In the case of the SSH model and the circular AIII model, we can obtain the exact edge eigenstates by considering complex momentum modes and finding the particular linear superposition that constitutes an eigenstate of the Hamiltonian and fulfils the boundary conditions. However, in the more general case of a ladder model, this would be much more difficult, if able.

8.2.5 Symmetry class correspondence

In Part I we study a one-dimensional dimerized lattice model for a topological insulator, which is in general in the AIII class and can be in the BDI class for two very particular parameter configurations. When studying the edge states of the model we saw that there is no significant difference between the spatial density distribution of the edge states in the BDI class and those in the AIII class. In contrast, it is the momentum density distribution of the edge states what allow us to distinguish between both symmetry classes. The edge states of a topological ladder model behave in the same way, establishing a correspondence between the symmetry class of a topological ladder model and the momentum distribution of the edge modes that such model exhibits. The BDI class is characterized by edge modes with a symmetric momentum distribution, and thus with a zero average momentum, whereas the AIII class corresponds to edge modes with an asymmetric momentum distribution, or a nonzero average momentum.

8.3 6 types of topological ladder edge states

To conclude this chapter, we know that the edge states of a topological ladder model are determined by the two functions $\rho(k)$ and $\varphi(k)$, which are given by the Hamiltonian matrix curve, as well as by the chiral operator U_S. The exact edge

eigenstates of a topological ladder Hamiltonian are $|e_\pm\rangle = (|l\rangle \pm |r\rangle)/\sqrt{2}$, being:

$$|l\rangle = \frac{1}{\sqrt{\kappa}} \sum_k \frac{e^{-i\varphi(k)}}{\rho(k)} \hat{\psi}_k^\dagger \hat{u}_+ |0\rangle \,, \tag{8.57}$$

$$|r\rangle = \frac{1}{\sqrt{\kappa}} \sum_k \frac{e^{-ik} e^{i\varphi(k)}}{\rho(k)} \hat{\psi}_k^\dagger \hat{u}_- |0\rangle \,, \tag{8.58}$$

where $\hat{u}_\pm$ are the eigenvectors of the chiral operator with eigenvalues ± 1, expressed using the basis formed by the eigenvectors of σ_z, so that for $U_S = \sigma_z$ we have that $\hat{\psi}_k^\dagger \hat{u}_+ = \hat{a}_k^\dagger$ and $\hat{\psi}_k^\dagger \hat{u}_- = \hat{b}_k^\dagger$.

The states $|l\rangle$ and $|r\rangle$ are localized at the left and right edges of the ladder, respectively, decaying their spatial density distributions exponentially towards the bulk. Their spatial localization depends on the quantities ξ_j, defined for each energy gap, but does not take into account the locations of the gaps. In consequence, we cannot tell any significant difference between the BDI class and the AIII class or between different types of ladder models, when we look at the edge states spatial density distribution. In contrast, it is through their momentum distribution how both symmetry classes can be distinguished, as well as different types of ladder models. The edge states are localized in momentum space at the positions of the energy gaps, being the relative weight of each momentum component determined by the corresponding gap width and the mass of the associated Wilson fermion. In this way, each of the six different types of topological ladder models corresponds to a distinct type of edge states, characterized by their momentum density distribution.

There are three different types of edge modes that can exist in a BDI topological ladder, corresponding each to a different way of obtaining a symmetric momentum density distribution, imposed by the presence of chiral symmetry. The SSH model has edge states with a single momentum component, which is located at $q = 0$ or $q = \pi$, the only two possibilities for a zero average momentum [see Fig. 8.4(a)]. The balanced BDI model has edge states of two equally weighted momentum components, therefore they are located at opposite momenta so that the average momentum is zero [see Fig. 8.4(b)]. Finally, the imbalanced BDI model has edge states with two differently weighted momentum components. The presence of time reversal symmetry makes them be located at $q_1 = 0$ and $q_2 = \pi$ [see Fig. 8.4(c)].

In the AIII symmetry class there are three distinct types of edge states, one for each type of AIII ladder model. The circular AIII model has edge states with just one momentum component, located at momentum $q \neq 0, \pi$, so that time reversal symmetry is broken [see Fig. 8.5(a)]. The balanced AIII model has edge states with two equally weighted components, located at not opposite momenta, so that their average momentum is different from zero [see Fig. 8.5(b)]. At last, the imbalanced AIII model has edge states with two components of different weights, which can be located at any momentum values, excluding the case in which one component has momentum 0 and the other π [see Fig. 8.5(c)].

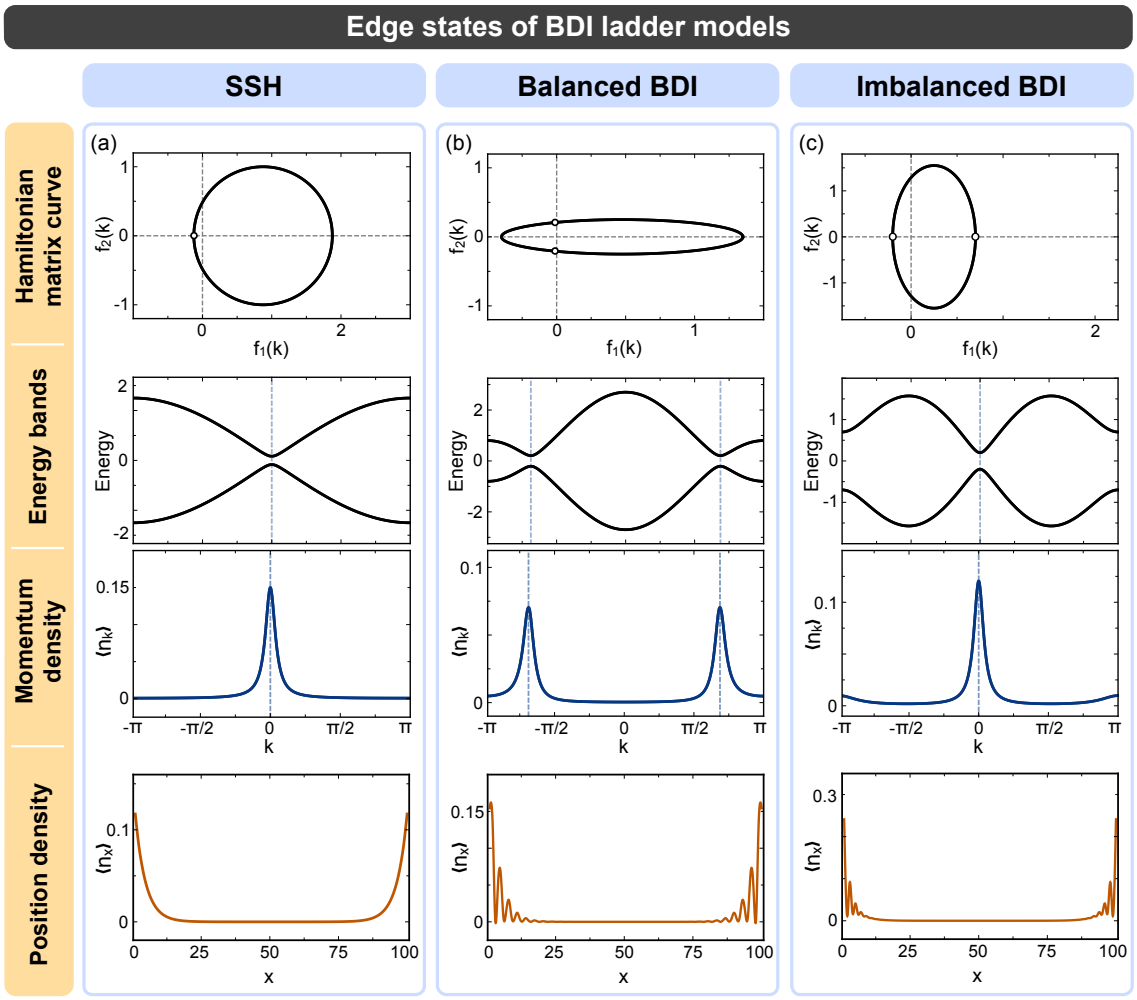

Figure 8.4: **Edge states in the BDI class.** In this figure we show the Hamiltonian matrix curve, the energy bands, and the edges states momentum and position density distributions for each of the three different types of topological ladder models in the BDI class, namely: (a) the SSH model, (b) the balanced BDI model, and (c) the imbalanced BDI model. Each of them is characterized by the edge states momentum density distribution, which is related to the number and masses of the Wilson fermions described by the model. In this way, the edge states momentum density distribution shows a single peak at momentum 0 or π for the SSH model, two peaks of the same height located at opposite momenta for the balanced BDI model, and two peaks of different height located at momenta 0 and π for the imbalanced BDI model. The momentum and position density distributions we show here have been obtained by exact numerical diagonalization of the bowtie ladder Hamiltonian for parameters: $J = 0.875$, $t = 1$, $t' = 0$, $\delta = \pi$ and $\phi = 0$ (SSH model); $J = 0.95$, $t = 1$, $t' = 0.75$, $\delta = 0$ and $\phi = 0$ (balanced BDI model); and $J = 0.25$, $t = 1$, $t' = 0.55$, $\delta = \pi/2$ and $\phi = \pi$ (imbalanced BDI model).

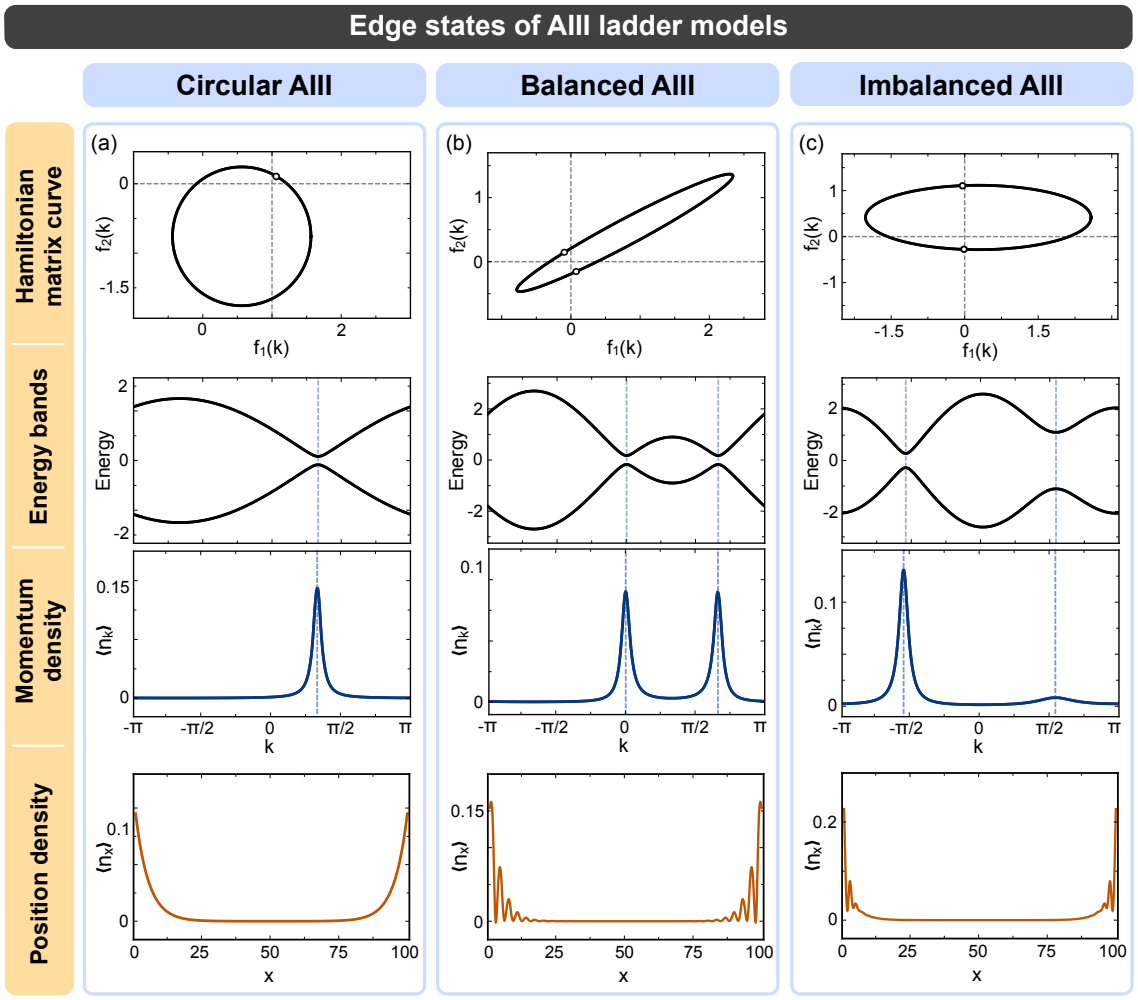

Figure 8.5: **Edge states in the AIII class.**In this figure we show the Hamiltonian matrix curve, the energy bands, and the edges states momentum and position density distributions for each of the three different types of topological ladder models in the AIII class, namely: (a) the circular AIII model, (b) the balanced AIII model, and (c) the imbalanced model. Each of them is characterized by the edge states momentum density distribution, which is related to the number and masses of the Wilson fermions described by the model. In this way, the edge states momentum density distribution shows a single peak at any momentum different from 0 and π for the cricular AIII model, two peaks of the same height located at not opposite momenta for the balanced AIII model, and two peaks of different height located at any momenta, excluding the situation in which one is located at momentum 0 and the other at momentum π, for the imbalanced AIII model. The momentum and position density distributions we show here have been obtained by exact numerical diagonalization of the bowtie ladder Hamiltonian for parameters: $J = 0.875$, $t = 1$, $t' = 0$, $\delta = -2\pi/3$ and $\phi = 0$ (circular AIII model); $J = 0.9$, $t = 1$, $t' = 0.8$, $\delta = -2\Pi/3$ and $\phi = 0$ (balanced AIII model); and $J = 0.5$, $t = 1.5$, $t' = 0.8$, $\delta = 0$ and $\phi = 5\pi/8$ (imbalanced AIII model).

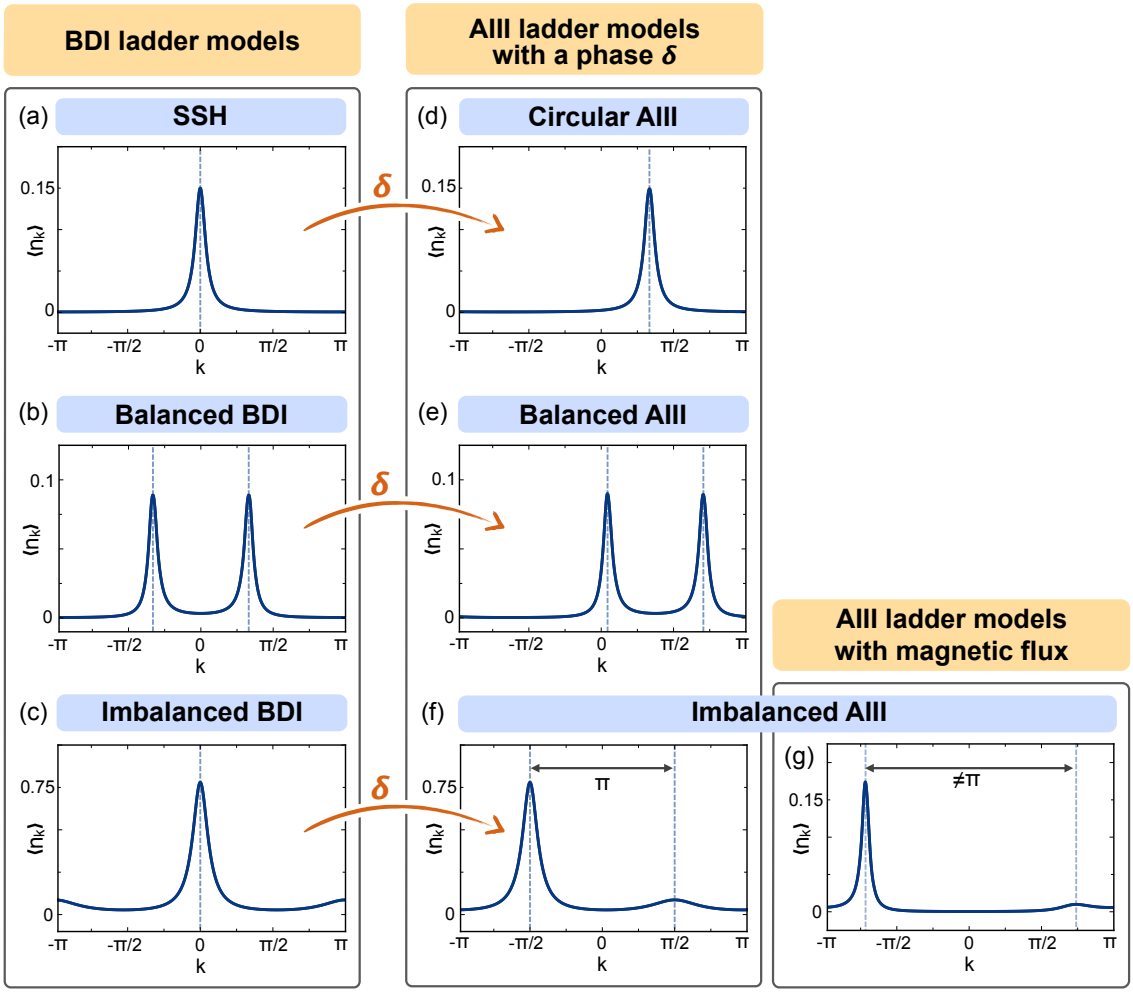

Figure 8.6: **Connection between BDI and AIII ladder models.** Adding a phase δ to ladder models in the BDI class, makes the model enter the AIII class and affects the edge states by shifting their momentum density distribution. In this way, the SSH model (a), the balanced BDI model (b) and the imbalanced BDI model (c) are connected in a one-to-one correspondence to the circular AIII model (d), the balanced AIII model (e) and a particular case of the imbalanced AIII model (f), respectively. The most general imbalanced AIII model, in which the edge states show a momentum distribution with two peaks separated by a distance different from π (e), has no correspondence in the BDI class and is realized by ladder configurations with an effective magnetic flux. Here we show the edge states momentum density distributions for different parameter configurations of the bowtie ladder Hamiltonian, corresponding each to one of the cases mentioned above. This parameters configurations are: (a) $J = 0.875$, $t = 1$, $t' = 0$, $\delta = \pi$ and $\phi = 0$; (b) $J = 0.9$, $t = 1$, $t' = 0.8$, $\delta = \pi$ and $\phi = 0$; (c) $J = 0.2$, $t = 1$, $t' = 0.55$, $\delta = \pi/2$ and $\phi = \pi$; (d) $J = 0.875$, $t = 1$, $t' = 0$, $\delta = -2\pi/3$ and $\phi = 0$; (e) $J = 0.9$, $t = 1$, $t' = 0.8$, $\delta = -5\pi/8$ and $\phi = 0$; (f) $J = 0.2$, $t = 1$, $t' = 0.55$, $\delta = 0$ and $\phi = \pi$; and (g) $J = 1$, $t = 1$, $t' = 0.6$, $\delta = 0$ and $\phi = \pi/8$. All momentum density distributions have been obtained by exact numerical diagonalization of the Hamiltonian.

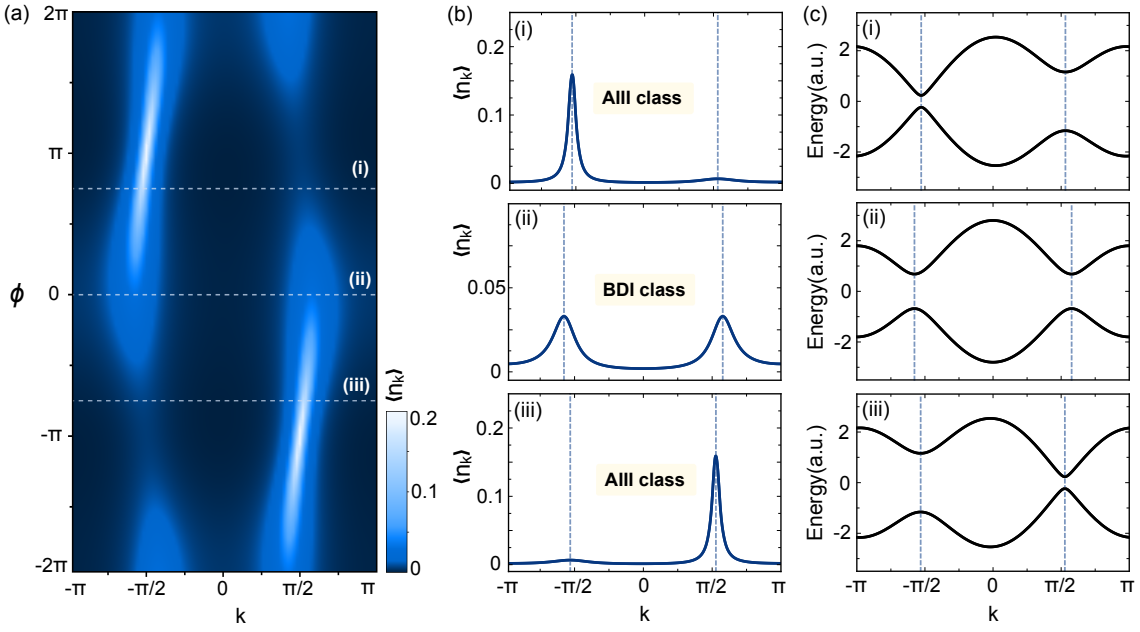

Figure 8.7: **Edge states under an effective magnetic flux.** (a) Momentum density distribution of the edge states of the bowtie ladder Hamiltonian with parameters $J = 0.5$, $t = 1.5$, $t' = 0.8$ and $\delta = 0$, as a function of the effective magnetic flux ϕ. (b) Edge states momentum density distribution and (c) energy bands of the bowtie ladder Hamiltonian for the same parameter configurations and (i) $\phi = 3\pi/4$, (ii) $\phi = 0$, and (iii) $\phi = -3\pi/4$. The edge states momentum density distributions have been obtained by exact numerical diagonalization of the bowtie ladder Hamiltonian.

In Cahpter 8 we analysed how the bowtie ladder Hamiltonian can break time reversal symmetry and, thus, enter the AIII class. We concluded that the model needs at least one of the following two ingredients: a shift in the momentum-isospin correspondence introduced by the presence of a phase δ, and an effective magnetic flux ϕ. Furthermore, we know what type of AIII ladder models are obtained after adding a phase δ or an effective magnetic flux ϕ to each of the three types of BDI ladder models. That is, adding a phase δ to the SSH model, the balanced BDI model and the imbalanced BDI model results into the circular AIII model, the balanced AIII model and the imbalanced AIII model, respectively. However, the imbalanced AIII model that can be achieved by this means is just a particular case, in which the distance in momentum space between the two energy gaps remains constant and equal to π. The most general imbalanced AIII model corresponds to the case in which there is an effective magnetic flux ϕ penetrating the ladder.

This correspondence between BDI and AIII ladder models is quite evident when we look at the edge states. Introducing a shift in the momentum-isospin correspondence in a ladder model means changing the Hamiltonian matrix $M(k)$ into $M(k-\delta)$. Therefore, the two functions $\rho(k)$ and $\varphi(k)$ are transformed into $\rho(k-\delta)$ and $\varphi(k-\delta)$. By looking at the edge states in the momentum representation, Eq. (8.57) and Eq. (8.58), we can easily deduce that their momentum density dis-

tributions will be also shifted. That is:

$$\langle \hat{n}_k \rangle_\delta = \langle \hat{n}_{k-\delta} \rangle_{\delta=0}. \tag{8.59}$$

In Fig. 8.6 we show the relation between the edge states of the three types of BDI ladder models and the edge states of the three types of AIII ladder models.

In addition, we show in Fig. 8.7 how the edge states momentum distribution depends on the value of an effective magnetic flux ϕ. For $\phi = 0$, the edge states show two equally weighted peaks in their momentum density distribution located at opposite momenta. This configuration corresponds to the balanced BDI model. For a non zero effective magnetic flux, the relative weight of each momentum component changes, as well as their location in momentum space. In this case the system realizes the imbalanced AIII model. For $\phi = \pm\pi$, the distance between the two momentum peaks is exactly π, and therefore there model could be brought to the BDI class by introducing a phase $\delta = \pm\pi/2$ that would shift the momentum peaks to $q_1 = 0$ and $q_2 = \pi$. That situation would correspond to the imbalance BDI model.

Chapter 9

Ladder geometries

Here we present all ladder geometries that realize a model for a topological insulator. For that, we first consider the most general ladder model and impose the time reversal and chiral symmetry conditions. After that, we obtain all possible parameter configurations that correspond to a topological model. Each of them will lead to a different ladder geometry. Finally, we analyse a couple of ladder models that we consider to be more relevant.

9.1 General ladder and symmetry conditions

We consider the most general ladder geometry, which contains two horizontal tunneling amplitudes, one for each leg of the ladder, two diagonal tunneling amplitudes, one vertical tunneling amplitude that connects the two sites in the same lattice cell, and two on-site energy terms. All these parameters are contained in the matrices C and T, being the most general ladder Hamiltonian written in terms of these matrices as in Eq. (5.1). Our purpose is to obtain all different ladder architectures that realize a model for a topological insulator. Therefore, we look for ladder geometries that fulfil the two chiral symmetry conditions: Eq. (5.6) and Eq. (5.7). According to the first one, the Hamiltonian matrix must have no component proportional to the identity. This implies that the two on-site energy terms and the two horizontal couplings, one for each leg of the ladder, must be opposite to each other. Therefore, the matrices C and T for the most general ladder model that satisfies the first condition for chiral symmetry are:

$$C = \begin{pmatrix} \epsilon & Je^{i\theta} \\ Je^{-i\theta} & -\epsilon \end{pmatrix}, \qquad T = e^{i\delta} \begin{pmatrix} J' & te^{i(\phi_1+\theta)} \\ t'e^{i(\phi_2-\theta)} & -J' \end{pmatrix}. \tag{9.1}$$

Where ϵ is a real parameter that corresponds to the on-site energies, J, J', t and t' are real parameters that correspond to the vertical, horizontal and diagonal coupling amplitudes and θ, δ, ϕ_1 and ϕ_2 are real parameters that correspond to the four independent phases in the coupling terms [see Fig. 9.1(a)].

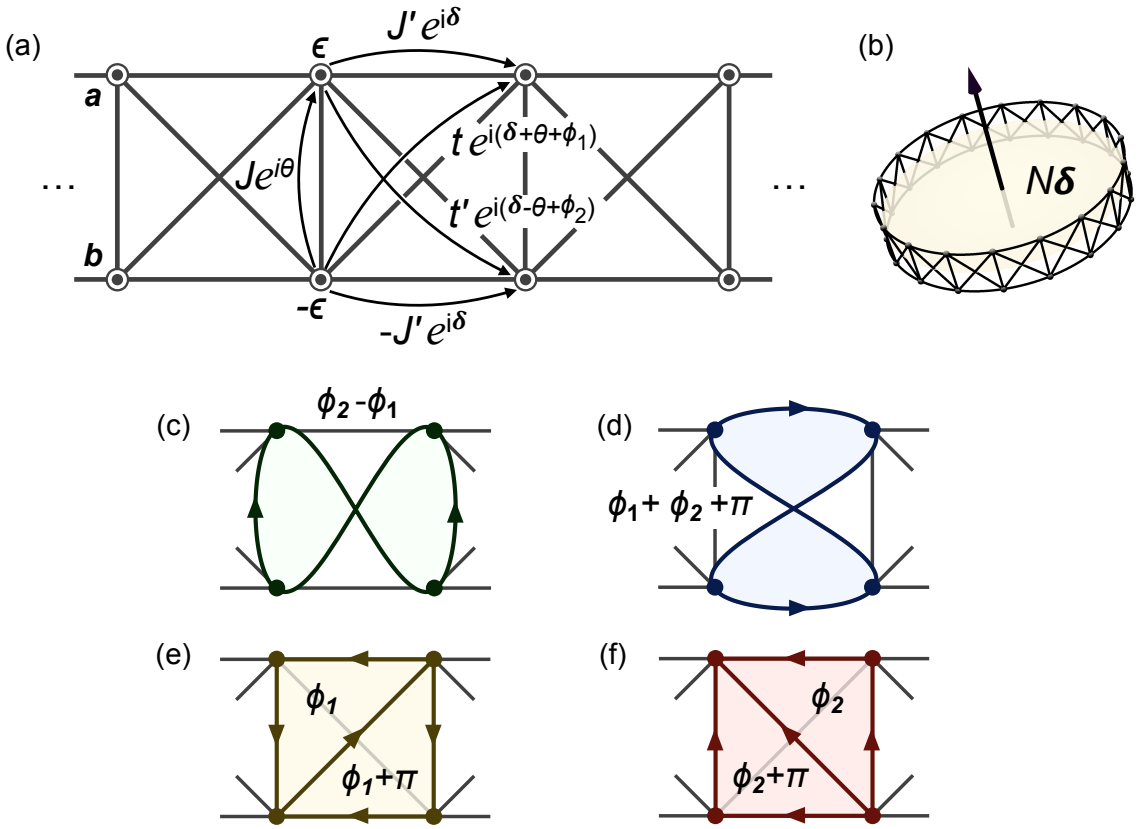

Figure 9.1: **General topological ladder model.** (a) Schematic illustration of the most general ladder model that can exhibit chiral symmetry. The phases of the tunneling amplitudes are parametrized, without loss of generality, so that they have a direct physical interpretation. The phase θ produces a general rotation on the Hamiltonian matrix and is irrelevant. The phase δ changes the correspondence between the momentum and the isospin associated to each eigenstate, as well as leads to a phase $N\delta$ hat particles pick up every time they complete a closed path along the whole system when there are periodic boundary conditions (b). Finally, the two phases ϕ_1 and ϕ_2 are related to the different effective magnetic fluxes that the ladder can exhibit (c), (d), (e) and (f).

We have chosen a parametrization of the phases which, without loss of generality, is convenient in order to make a physical interpretation of them, as we show in the following.

The Hamiltonian can be written in momentum representation as:

$$H = -\sum_k \psi_k^\dagger \, R_z(\theta) \, M(k) \, R_z^\dagger(\theta) \, \psi_k, \tag{9.2}$$

where $R_z(\theta) = e^{i\theta\sigma_z/2}$ is a rotation of an angle θ around the z-axis and:

$$M(k) = \begin{pmatrix} \epsilon + 2J\cos(k-\delta) & z^*(k-\delta) \\ \\ z(k-\delta) & -\epsilon - 2J\cos(k-\delta) \end{pmatrix}, \tag{9.3}$$

being $z(k) = J + te^{i(k-\phi_1)} + t'e^{-i(k-\phi_2)}$. From the form of this Hamiltonian matrix we can distinguish three kind of phases in the ladder parameters:

- *Effective magnetic fluxes ϕ_1 and ϕ_2*

  The two parameters ϕ_1 and ϕ_2 determine the total phase accumulated by a particle completing a closed path in the ladder and, thus, they can be identified as effective magnetic fluxes penetrating the ladder. All closed paths that can be defined in the ladder are obtained as a combination of four elementary paths [Fig. 9.1(c), (d), (e) and (f)]. These phases ϕ_1 and ϕ_2 affect the symmetries of the Hamiltonian and the properties of the edge states.

- *Shift δ in the momentum-isospin correspondence.*

  The phase δ produces a shift in the Hamiltonian matrix with respect to the momentum, Eq. (9.3), so that it introduces a shift in the correspondence between the momentum of each eigenstate and its associated vector in the Bloch sphere, which makes them be genuinely different from those eigenstates corresponding to the case in which there is no phase δ. This phase is a generalization of the the phase δ that appears in the bowtie ladder and in the one-dimensional dimerized lattice studied in Part I and Part II.

- *Irrelevant phase θ.*

  The phase θ produces a rotation around the z-axis, Eq. (9.2), which is a global unitary operation and does not affect the symmetries of the system. Therefore we neglect this phase for simplicity and each model we study includes all possible rotations around the z-axis by adding the phase θ as shown in Fig. 9.1(a).

This analysis of the phases present in the most general topological ladder Hamiltonian is analogous to the one we did for the bowtie ladder in Chapter 7: one phase can be removed by applying a global unitary transformation and, thus, it can be neglected; another one produces a shift in the isospin-quasimomentum relation; and the rest correspond to effective magnetic fluxes penetrating the ladder. In fact, the bowtie ladder parametrized as in Fig. 7.1 corresponds to the particular case of the general ladder in Fig. 9.1 in which $\epsilon = 0$, $J' = 0$, $\theta = -\phi/2$, $\phi_1 = \phi/2$ and $\phi_2 = -\phi/2$.

Our purpose is to find all parameter configurations that correspond to a topological model in the BDI class or in the AIII class. For that, we decompose the Hamiltonian matrix in Eq. (9.3) as $M(k) = (\boldsymbol{n}_0 + \boldsymbol{n}_c \cos k + \boldsymbol{n}_s \sin k) \cdot \boldsymbol{\sigma}$, being:

$$\begin{aligned} \boldsymbol{n}_0 &= J\,\hat{x} + \epsilon\,\hat{z} \\ \boldsymbol{n}_c &= (t\,c_1 + t'c_2)\,\hat{x} - (t\,s_1 - t's_2)\,\hat{y} + 2J'\cos\delta\,\hat{z} \\ \boldsymbol{n}_s &= (t\,s_1 + t's_2)\,\hat{x} + (t\,c_1 - t'c_2)\,\hat{y} + 2J'\sin\delta\,\hat{z}, \end{aligned} \tag{9.4}$$

where $c_i = \cos(\phi_i + \delta)$ and $s_i = \sin(\phi_i + \delta)$. In order for the Hamiltonian to be chiral symmetric, the three vectors $\boldsymbol{n}_0$, $\boldsymbol{n}_c$ and $\boldsymbol{n}_s$ must be linear dependent, Eq. (5.7), which means that the determinant of the matrix formed by their components must

be zero. Imposing this requirement we obtain the condition for chiral symmetry in terms of the ladder parameters:

$$\epsilon \left(t^2 - t'^2\right) - 2JJ' \left(t \cos\phi_1 - t' \cos\phi_2\right) = 0. \tag{9.5}$$

The conditions for time reversal symmetry are $\boldsymbol{n}_c \cdot \boldsymbol{n}_s = 0$ and $\boldsymbol{n}_0 \cdot \boldsymbol{n}_s = 0$, Eq. (5.10) and Eq. (5.11). Imposing them we obtain the conditions that the parameters of the model must fulfil for it to have time reversal symmetry:

$$2J'\epsilon \sin\delta + Jt \sin(\delta + \phi_1) + Jt' \sin(\delta + \phi_2) = 0 \tag{9.6}$$

$$2tt' \sin(2\delta + \phi_1 + \phi_2) + 2J'^2 \sin 2\delta = 0. \tag{9.7}$$

9.2 Finding all topological ladder configurations

9.2.1 Imposing chiral symetry

In order to obtain all ladder geometries realizing a model for a topological insulator we first remark on two ingredients which are needed for a ladder geometry to be chiral symmetric:

1. *Opposite horizontal couplings.*

   The chiral symmetry implies that the Hamiltonian matrix has no component proportional to the identity. As a consequence, the two horizontal tunneling amplitudes must have the same modulus and opposite sing. That is, either both terms appear in the ladder configuration or none of them does.

2. *Non-vanishing diagonal couplings.*

   If a model has no diagonal couplings, that is $t = t' = 0$, the condition for chiral symmetry (9.5) is fulfilled independently of the rest of the parameters. However, such a model will always be in a trivial phase. To see this we consider the most general ladder model with no diagonal couplings, see Fig. 9.2, whose corresponding Hamiltonian matrix is: $M(k) = [\epsilon + 2J' \cos(k - \delta)]\ \sigma_z + J\,\sigma_x$. There is no component with $\sin k$ and therefore the curve described in the complex plane is a line, whose winding number is 0.

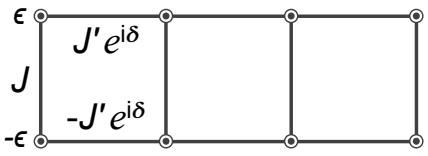

Figure 9.2: **Square ladder.** Schematic illustration of the most general ladder model with no diagonal couplings. Despite of being chiral symmetric, it is always in a trivial phase.

In this way, when looking for topological ladder models we have to discard all configurations with only one horizontal coupling and consider only those with at least one diagonal coupling. To find them we first consider those models with just one diagonal coupling and secondly those with two.

i) Models with one diagonal coupling.

- *Models with $J = 0$ or $J' = 0$.*

  First we consider ladder geometries with just two couplings, being one of them diagonal. In this situation the chiral symmetry condition, Eq. (9.5), implies that $\epsilon = 0$, so that there are no on-site energy terms in the Hamiltonian. This case includes four ladder geometries (see Fig. 9.3).

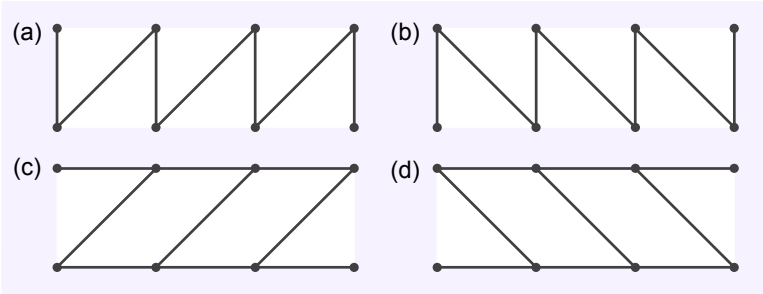

Figure 9.3: **Ladder geometries with chiral symmetry (i).** Topological ladder geometries with one diagonal coupling and no on-site energy.

- *Models with vertical and horizontal couplings J and J'.*

  In this situation the condition for chiral symmetry, Eq. (9.5), constitutes a constraint to the on-site energy $\epsilon = (2JJ'/t)\cos\phi$, where t is the diagonal coupling in the model and ϕ can be ϕ_1 or ϕ_2. This case includes two ladder geometries (see Fig. 9.4).

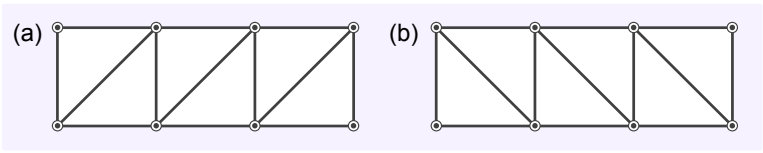

Figure 9.4: **Ladder geometries with chiral symmetry (ii).** Topological ladder geometries with one diagonal coupling and constrained on-site energy.

ii) Models with two diagonal couplings.

- *Models with $J = 0$ or $J' = 0$.*

  In this case the second term in the chiral condition, Eq. (9.5), vanishes and therefore $\epsilon(t^2 - t'^2) = 0$, so that $\epsilon = 0$ or $t = t'$. Then, there are two configurations

for each ladder geometry in this situation: one with no on-site energy and two independent diagonal couplings and another one with on-site energy and two diagonal couplings of the same amplitude. There are three ladder geometries of this kind. One with just the two diagonal couplings [Fig. 9.5(a)], another having, in addition, the vertical tunneling J [Fig. 9.5(b)], and finally the one with the horizontal coupling J' [Fig. 9.5(c) and (d)]. The first two correspond to a trivial model when the two diagonal couplings are the same, which means that the only possibility is having $\epsilon = 0$ and $t \neq t'$. The last case, in contrast, corresponds to a topological model in both situations. In this way we obtain four different ladder models.

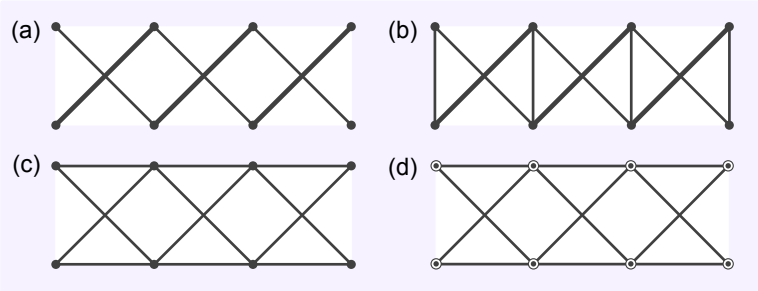

Figure 9.5: **Ladder geometries with chiral symmetry (iii).** Topological ladder geometries with two diagonal terms.

- *Models with vertical and horizontal couplings J and J'.*

  In this case we can distinguish two situations:

  1. If the two diagonal couplings are the same, $t = t'$, the first term in the chiral condition, Eq. (9.5), vanishes and, thus, the on-site energy can take any value. The chiral condition is then fulfilled if $\cos\phi_1 = \cos\phi_2$. This gives us two models, one with $\phi_1 = \phi_2$ and another with $\phi_1 = -\phi_2$. However, the second possibility corresponds to a trivial topology so there is only one model with this configuration [Fig. 9.6(a)].
  2. If the two diagonal couplings are different, $t \neq t'$, the chiral condition implies a constraint to the on-site energy $\epsilon = 2JJ'\left(t\cos\phi_1 - t'\cos\phi_2\right)/(t^2 - t'^2)$. This corresponds to the last model [Fig. 9.6(b)].

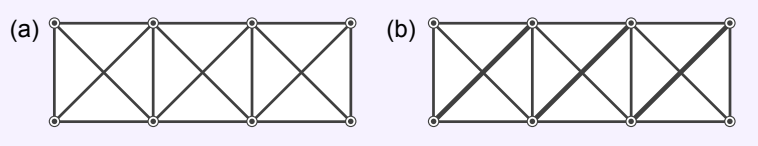

Figure 9.6: **Ladder geometries with chiral symmetry (iv).** Topological ladder geometries with two diagonal terms.

In this way we have obtained twelve topological ladder geometries, Fig. 9.3, Fig. 9.4, Fig. 9.5 and Fig. 9.6. However, some of them correspond to a Hamiltonian matrix of the form: $M(k) = \beta \cos k\, \sigma_c + \gamma \sin k\, \sigma_s$, which means that they are always in a topological phase and have no phase transition, as the curve described by the Hamiltonian matrix is an ellipse centred at the origin whose winding number is always 1. This special behaviour occurs because they are the particular case in which $J = 0$ of a more general geometry. Therefore, we do not need to consider them. These ladder geometries are the ones in Fig.9.3(c) and (d), Fig. 9.5(a) and Fig.9.5(c), which are particular cases of the models in Fig.9.4(a) and (b), Fig. 9.5(b) and Fig.9.6(b), respectively.

9.2.2 Imposing time reversal symmetry

In order to find all ladder models in the BDI class and in the AIII class we need to impose the two time reversal symmetry conditions, Eq. (9.6) and Eq. (9.7), to the topological ladder geometries we have obtained beforehand. When they are fulfilled we have a realization of the BDI class, whereas it corresponds to the AIII class otherwise. By inspecting those conditions we see that they are trivially fulfilled if all phases vanish, which is obvious as this case corresponds to a real Hamiltonian. Nevertheless, there are other solutions to the time reversal symmetry conditions that correspond to complex Hamiltonians. In order to obtain them, we have to evaluate the time reversal symmetry conditions for each particular geometry and find the values of δ, ϕ_1 and ϕ_2 for which they are satisfied.

As an example, we consider the ladder geometry in Fig. 9.5(b). The two time reversal symmetry conditions for this particular case are:

$$J(t + t') \sin\delta \cos\frac{\phi}{2} + J(t - t') \cos\delta \sin\frac{\phi}{2} = 0 \tag{9.8}$$

$$4tt' \sin\delta \cos\delta = 0, \tag{9.9}$$

being ϕ the only effective magnetic flux in this ladder. The solutions to these equations are: $\phi = 0, \delta = 0, \pi$ or $\phi = \pi, \delta = \pm\pi/2$, which correspond to four different BDI models with this particular ladder geometry [see Fig. 9.7(c)].

Analogously, the time reversal symmetry conditions can be easily analysed for all other ladder geometries. As a result, we present in Fig. 9.7 and Fig. 9.8 all ladder models with chiral symmetry and detail the parameter configurations for which they belong to the BDI class and to the AIII class. As we see, all parameter configurations that correspond to a model in the BDI class come in pairs, corresponding the two configurations within each pair to two different values of the phase δ that differ in π. The reason for that is that any BDI model can be generalized by introducing a shift in the momentum-isospin correspondece, which makes the model break time reversal symmetry and enter the AIII class. Only when such shift is equal to 0 or π the model is still in the BDI class. We explain this in detail in Chapter 7 for the bowtie ladder Hamiltonian, however, the analysis can be applied to any ladder model.

(a)

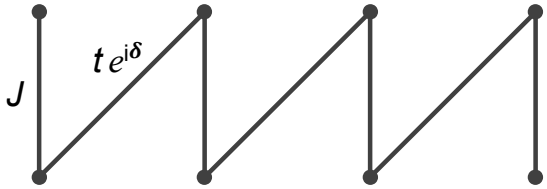

δ	Class
0, π	BDI
Otherwise	AIII

(b)

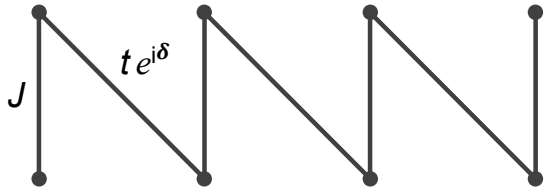

δ	Class
0, π	BDI
Otherwise	AIII

(c)

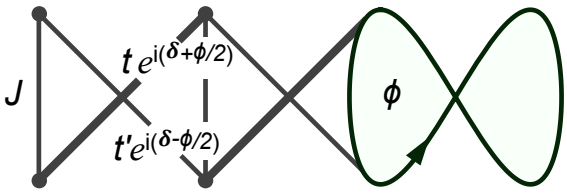

ϕ	δ	Class
0	0, π	BDI
π	±π/2	BDI
Otherwise		AIII

(d)

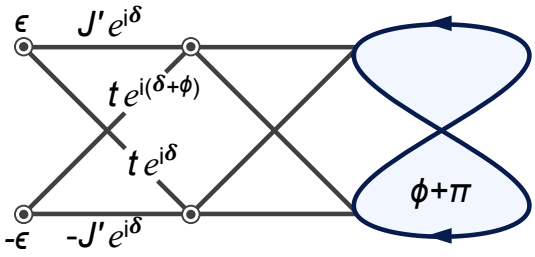

ϕ	δ	Class
0	0, π	Trivial
π	0, π	BDI
Otherwise		AIII

Figure 9.7: **Topological ladder models (i).** Here we show all topological ladder models. For each of them, we specify in a table which parameter configurations correspond to a model in the BDI symmetry class and which to a model in the AIII symmetry class. Ladder models (a) and (b) are in fact one-dimensional dimerized lattice models, which can only realize the SSH model and the circular AIII model. The rest of the ladder models preset in this figure can access all types of topological ladder models (continues in the next page).

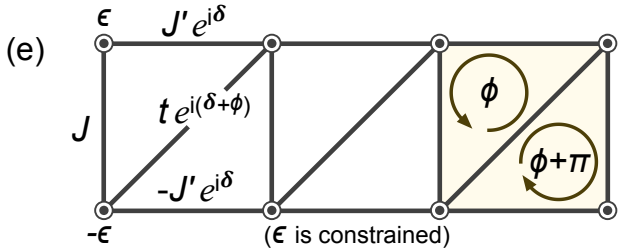

ϕ	δ	Class
0, π	0, π	BDI
±π/2	±π/2	BDI
Otherwise		AIII

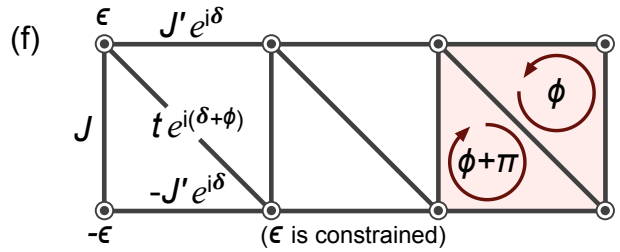

ϕ	δ	Class
0, π	0, π	BDI
±π/2	±π/2	BDI
Otherwise		AIII

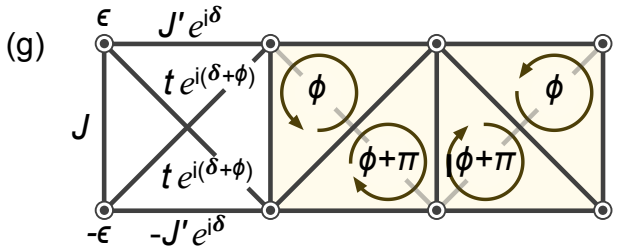

ϕ	δ	ϵ	Class
0,π	Any	Any	Trivial
±π/2	±π/2	0	BDI
Otherwise			AIII

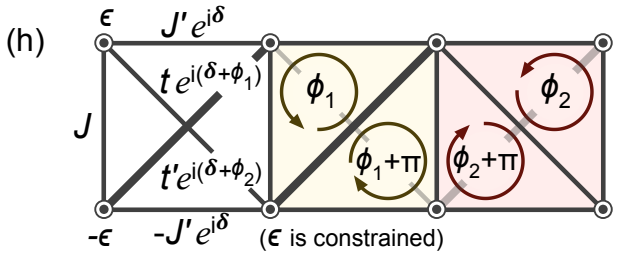

ϕ_1	ϕ_2	δ	Class
0,π	0,π	0,π	BDI
±π/2	±π/2	±π/2	BDI
Otherwise			AIII

Figure 9.8: **Topological ladder models (ii).** In ladder models (c), the bowtie ladder, and (h), one of the diagonal couplings is represented with a thicker line. This indicates that the two diagonal tunneling amplitudes must have different values, otherwise the model would be topologically trivial. A double circle in every site indicates the presence of an on-site energy term in the Hamiltonian. The chiral symmetry condition imposes a constraint to the on-site energy in ladder models (e) and (f), for which $\epsilon = (2JJ'/t)\cos\phi$, and in model (h), for which $\epsilon = 2JJ'(t\cos\phi_1 - t'\cos\phi_2)/(t^2 - t'^2)$.

Among the eight different topological ladder models we present in Fig. 9.7 and Fig. 9.8, the first two, (a) and (b), consist of a one-dimensional dimerized lattice, which we have already deeply analysed in Parts I and II of this thesis. In fact, both ladder models are essentially the same, as one can be obtained by applying σ_x to the other, which consists basically of flipping the ladder. The third ladder model, (c), is actually the bowtie ladder, which we have studied in Chapter 7. Furthermore, we know that it serves as a canonical ladder model, as the bowtie ladder Hamiltonian is the most general ladder Hamiltonian we can imagine up to a global unitary transformation. Therefore, all other ladder models in Fig. 9.7 and Fig. 9.8 can be obtain from the bowtie ladder by performing the appropriate rotation.

Nevertheless, we highlight and show in more detail two particular ladder geometries, (d) and (g), and indicate how to connect them to the canonical ladder. Models (e), (f) and (h) have a constraint in their on-site energy ϵ, which has to take a very particular value that depends on all other parameters, including the effective magnetic fluxes. The moment the on-site energy ϵ has not the appropriate value, chiral symmetry is broken and the model would not be even topological. This would imply a difficulty from an experimental point of view, and therefore we consider these particular ladder geometries of less interest.

9.3 The hourglass ladder

As the first remarkable example of a topological ladder model different from the bowtie ladder, we consider ladder (a) in Fig. 9.9, which we call the *hourglass* ladder and whose Hamiltonian is:

$$H_{\rm hg} = -\sum_n \epsilon\,(\hat{a}_n^\dagger \hat{a}_n - \hat{b}_n^\dagger \hat{b}_n) + \Big[J' e^{i\delta}\,(\hat{a}_{n+1}^\dagger \hat{a}_n - \hat{b}_{n+1}^\dagger \hat{b}_n) + t\, e^{i(\delta+\phi/2)}\,(\hat{a}_{n+1}^\dagger \hat{b}_n - \hat{b}_{n+1}^\dagger \hat{a}_n) + \text{h.c.}\Big]. \tag{9.10}$$

By changing to the momentum representation we obtain the corresponding Hamiltonian matrix, which is:

$$M_{\rm hg}(k) = [\epsilon + 2J'\cos(k-\delta)]\;\sigma_z + 2t\sin(k-\delta-\phi/2)\,\sigma_y. \tag{9.11}$$

As we can see, the Hamiltonian matrix lives on the yz-plane, so that it can be connected to the bowtie ladder Hamiltonian matrix by performing a rotation around the x axis (see Fig. 9.9). That is:

$$H_D\, M(k)\, H_D^\dagger = \begin{pmatrix} 0 & w^*(k) \\ w(k) & 0 \end{pmatrix}, \tag{9.12}$$

where $H_D = (\sigma_x + \sigma_z)/2$ is the Hadamard transformation and:

$$w(k) = \epsilon + 2J'\cos(k-\delta) - i\,2t\sin(k-\delta-\phi/2). \tag{9.13}$$

Now that the Hamiltonian matrix has the canonical form, in which only the off-diagonal terms are different from zero, it can be directly related to the canonical ladder Hamiltonian matrix, which is:

$$M_c(k) = \begin{pmatrix} 0 & z^*(k) \\ z(k) & 0 \end{pmatrix}, \tag{9.14}$$

with:

$$z(k) = J_c + t_c e^{i(k-\delta_c-\phi_c/2)} + t'_c e^{-i(k-\delta_c+\phi_c/2)}. \tag{9.15}$$

Both models are identified by taking $w(k) = z(k)$, what establishes a relation between the parameters of the first model, ϵ, J', t, ϕ and δ, and the ones of the canonical ladder: J_c, t_c, t'_c, ϕ_c and δ_c.

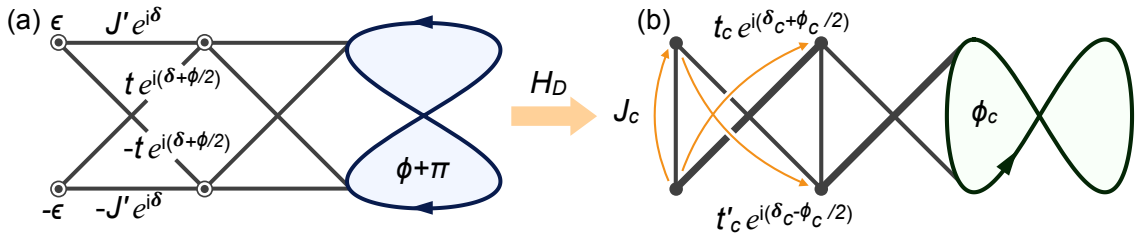

Figure 9.9: **The hourglass ladder.** Schematic illustration of the hourglass ladder. Its Hamiltonian matrix lives on the yz-plane and is connected to the bowtie ladder Hamiltonian matrix by applying the unitary $H_D = (\sigma_x + \sigma_z)/\sqrt{2}$.

9.4 The box ladder

Another remarkable topological ladder model is ladder (a) in Fig. 9.10 which we call the box ladder and whose Hamiltonian is:

$$H_{\text{box}} = -\sum_n \epsilon\,(\hat{a}_n^\dagger \hat{a}_n - \hat{b}_n^\dagger \hat{b}_n) + \Big[J' e^{i\delta}\,(\hat{a}_{n+1}^\dagger \hat{a}_n - \hat{b}_{n+1}^\dagger \hat{b}_n) + t\, e^{i(\delta+\phi)}\,(\hat{a}_{n+1}^\dagger \hat{b}_n + \hat{b}_{n+1}^\dagger \hat{a}_n) + J\,\hat{a}_n^\dagger \hat{b}_n + \text{h.c.}\Big]. \tag{9.16}$$

The corresponding Hamiltonian matrix is:

$$M_{\text{box}}(k) = [\epsilon + 2J'\cos(k-\delta)]\;\sigma_z + [J + 2t\cos(k-\delta-\phi)]\;\sigma_x. \tag{9.17}$$

It is on the xz-plane and is connected to the canonical ladder Hamiltonian matrix by applying two combined rotations, which are: $R_1 = e^{i\pi(\sigma_x+\sigma_y+\sigma_z)/3\sqrt{3}}$ and $R_2 = e^{i\Theta\sigma_z/2}$, where $\Theta = \arctan(J/\epsilon)$. In this way:

$$R_2 R_1\, M_{\text{box}}(k)\, R_1^\dagger R_2^\dagger = \begin{pmatrix} 0 & v^*(k) \\ v(k) & 0 \end{pmatrix}, \tag{9.18}$$

being:

$$v(k) = \sqrt{\epsilon^2 + J^2} + 2J' \cos(k - \delta)e^{-i\Theta} + i2t \sin(k - \delta - \phi)e^{-i\Theta}. \tag{9.19}$$

The condition $v(k) = z(k)$ [see Eq. (9.15)] establishes the relation between the parameters of the box ladder model and the ones of the canonical ladder.

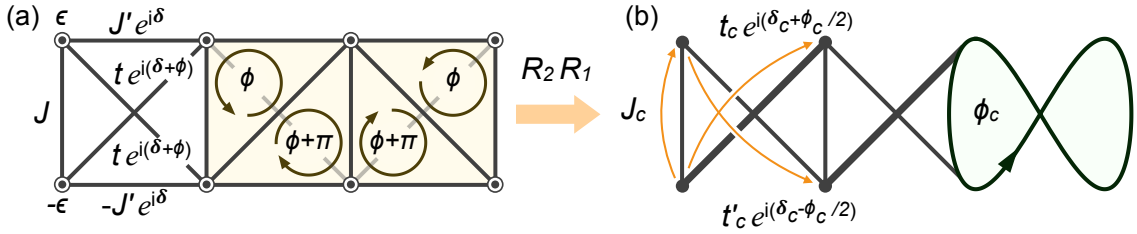

Figure 9.10: **The box ladder.** Schematic illustration of the box ladder. Its Hamiltonian matrix lives on the xz-plane and is connected to the canonical ladder Hamiltonian matrix by applying the unitary transformations R_1 and R_2 (see text).

There are three ladder models studied in previous works which are particular cases of this ladder configuration. The first one is the Creutz ladder [23], which corresponds to ladder (a) in Fig. 9.10 for $\epsilon = 0$, $\delta = -\pi/2$ and $\phi = \pi/2$. The second one is the imbalance Creutz ladder [24], which corresponds to ladder (a) in Fig. 9.10 for $J = 0$, $\delta = \pi/2$, $\phi = \pi/2$ and $J' = t$. Finally, the third one is the shifted Creutz ladder [25], which corresponds to ladder (a) in Fig. 9.10 for $\epsilon = 0$, $\delta = 0$ and $\phi = -\pi/2$.

Part IV

Protected chiral currents in an AIII ladder

Chapter 10

The hourglass ladder model

The simultaneous momentum and position definition of the edge states of a dimerized lattice, that we explained in Part I of this thesis, leads to the interesting dynamics we presented in Part II. After our systematic analysis of topological ladder models, presented in Part III, we have found that, on one hand, the simultaneous good definition of the edge states momentum and position is a common property of all ladder models, and, on the other hand, the more complexity of a ladder system, in comparison to a dimerized one dimensional lattice, leads to several types of edge states with richer properties, reflected in their momentum density distributions.

In this way, we wanted to investigate what kind of edge states dynamics can be found in a ladder system and how they depend on the presence of an effective magnetic flux. In this Part IV of the thesis we show the emergence of protected chiral currents in a ladder model which are the direct consequence of the edge states properties and the breaking of time reversal symmetry by an effective magnetic flux.

10.1 Hamiltonian of the model

We consider the two-leg ladder model given by the following tight-binding Hamiltonian:

$$H = -\sum_{n}^{N} \epsilon \left(\hat{a}_n^\dagger \hat{a}_n - \hat{b}_n^\dagger \hat{b}_n \right) + \Big\{ J' \left(\hat{a}_{n+1}^\dagger \hat{a}_n - \hat{b}_{n+1}^\dagger \hat{b}_n \right) + J e^{i\phi/2} \left(\hat{a}_{n+1}^\dagger \hat{b}_n - \hat{b}_{n+1}^\dagger \hat{a}_n \right) + \text{H.c.} \Big\}, \tag{10.1}$$

where $\hat{a}_n^\dagger (\hat{b}_n^\dagger)$ are the particle creation operators for a particle on the sublattice site $a_n(b_n)$ in the nth lattice cell.

As it can be seen from the Hamiltonian, the model consists in two opposite on-site energies, two opposite horizontal couplings and two diagonal tunneling amplitudes. In addition, the two diagonal hopping terms are complex so that particles pick up a phase ϕ when completing the closed path $a_n \to b_{n+1} \to b_n \to a_{n+1} \to a_n$ [see Fig.10.1]. Therefore the phase ϕ can be interpreted as the Aharonov-Bohm phase

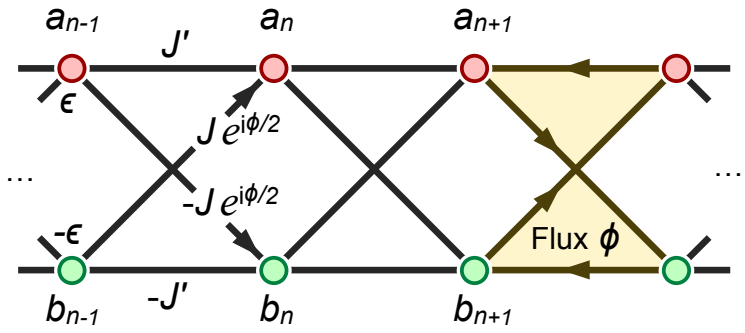

Figure 10.1: **The Model.** Two-leg ladder model for a 1D topological insulator with horizontal and diagonal hopping amplitudes J' and J and on-site energy ϵ. Particles completing a closed path pick up a phase ϕ, which represents an effective magnetic flux penetrating the ladder.

corresponding to an effective magnetic flux penetrating the ladder. This ladder model corresponds to the hourglass ladder, that we presented in Chapter 9.

10.2 Symmetries of the model

For $\phi = 0$, when no magnetic flux penetrates the ladder, the Hamiltonian of the model, Eq. (10.1), is in the BDI symmetry class; otherwise time reversal symmetry is broken and the Hamiltonian belongs to the AIII symmetry class. This can be seen by writing the Hamiltonian in momentum space as:

$$H = -\sum_k \begin{pmatrix} \hat{a}_k^\dagger & \hat{b}_k^\dagger \end{pmatrix} M(k) \begin{pmatrix} \hat{a}_k \\ \hat{b}_k \end{pmatrix}, \tag{10.2}$$

being the Hamiltonian matrix:

$$M(k) = (\epsilon + 2J' \cos k)\, \sigma_z + 2J \sin\left(k - \frac{\phi}{2}\right) \sigma_y. \tag{10.3}$$

The Hamiltonian is chiral symmetric for any value of ϕ, as $\sigma_x M(k) \sigma_x = -M(k)$. Therefore, the chiral operator is $U_S = \sigma_x$. For $\phi = 0$, $M^*(-k) = M(k)$, therefore it is also time reversal symmetric and thus belongs to the BDI class. In contrast, for $\phi \neq 0$, $M^*(-k;\phi) = M(k;-\phi)$, and there is no unitary U_T such that $U_T M(k;-\phi) U_T^\dagger = M(k;\phi)$. To see this, we decompose the Hamiltonian matrix as:

$$M(k) = (\epsilon + 2J' \cos k)\, \sigma_z + 2J \cos\left(\frac{\phi}{2}\right) \sin k\, \sigma_y - 2J \sin\left(\frac{\phi}{2}\right) \cos k\, \sigma_y. \tag{10.4}$$

Computing the complex conjugate of this Hamiltonian matrix and inverting the momentum is equivalent to invert the sign of the magnetic flux ϕ:

$$M^*(-k) = (\epsilon + 2J' \cos k)\, \sigma_z + 2J \cos\left(\frac{\phi}{2}\right) \sin k\, \sigma_y + 2J \sin\left(\frac{\phi}{2}\right) \cos k\, \sigma_y. \tag{10.5}$$

In order for a unitary operator U_T to transform $M^*(-k)$ into $M(k)$, it should leave the two first terms in Eq. (10.5) invariant whereas it should produce a change in the sign of the third one. In general this is simply not possible as the second and third terms consist in the same Pauli matrix σ_y, so that there is no unitary transformation that leaves one invariant and changes the sign of the other one. The only possible solution is that one of these two terms vanishes. This leads to two options: either $\sin(\phi/2) = 0$ and thus the time reversal symmetry condition is fulfilled for $U_T = \mathbb{I}$, or $\cos(\phi/2) = 0$ and therefore the model is time reversal symmetric with $U_T = \sigma_z$. The first case corresponds to a zero magnetic flux, $\phi = 0$, whereas the second one corresponds to an effective magnetic flux $\phi = \pm\pi$. Nevertheless, the last case corresponds to a Hamiltonian matrix:

$$M(k; \phi = \pi) = \epsilon\, \sigma_z + 2(J'\, \sigma_z \mp J\, \sigma_y)\, \cos k, \tag{10.6}$$

which corresponds to a line whose winding number is always zero. Therefore, although being time reversal symmetric, the case in which $\phi = \pm\pi$ corresponds to a trivial topology.

As final conclusion, the Hamiltonian of our model belongs to the BDI symmetry class for $\phi = 0$, it corresponds to a trivial topology for $\phi = \pm\pi$ and it is in the AIII symmetry class otherwise, when some effective magnetic flux $\phi \neq 0, \pm\pi$ penetrates the ladder.

10.3 Topological phase transitions

The Hamiltonian matrix of the model is written as $M(k) = f_1(k)\, \sigma_z + f_2(k)\, \sigma_y$, being:

$$f_1(k) = \epsilon + 2J' \cos k, \tag{10.7}$$

$$f_2(k) = 2J \sin(k - \phi/2). \tag{10.8}$$

Therefore (see Chapter 6 for the details), if we define the two real functions $\rho(k)$ and $\varphi(k)$ as $\rho(k)e^{i\varphi(k)} = f_1(k) + if_2(k)$, the eigenstates of the Hamiltonian for periodic boundary conditions are:

$$|k\rangle_\pm = \begin{pmatrix} \hat{a}_k^\dagger & \hat{a}_k^\dagger \end{pmatrix} U \frac{1}{\sqrt{2}} \begin{pmatrix} 1 \\ \pm e^{i\varphi(k)} \end{pmatrix} |0\rangle\,, \tag{10.9}$$

where $U = e^{i\pi\sigma_y/4} = (\mathbb{I} + i\sigma_y)/\sqrt{2}$, and being their corresponding energies:

$$E_\pm = \mp\rho(k) = \mp\sqrt{(\epsilon + 2J' \cos k)^2 + 4J^2 \sin^2(k - \phi/2)}, \tag{10.10}$$

which constitute the two energy bands of the system.

In this way, the Hamiltonian matrix determines a closed curve in the complex plane, which is given by $z(k) = f_1(k) + if_2(k)$. This curve is in general an ellipse, whose parameters depend on the on-site energy, hopping amplitudes and flux present

in the model, and defines the two functions $\rho(k)$ and $\varphi(k)$ as the modulus and phase of each point in the curve. Moreover, the Zak phase is quantized according to the winding number of $z(k)$, so that the system is in its topologically non-trivial phase as long as the Hamiltonian matrix ellipse encloses the origin in the plane.

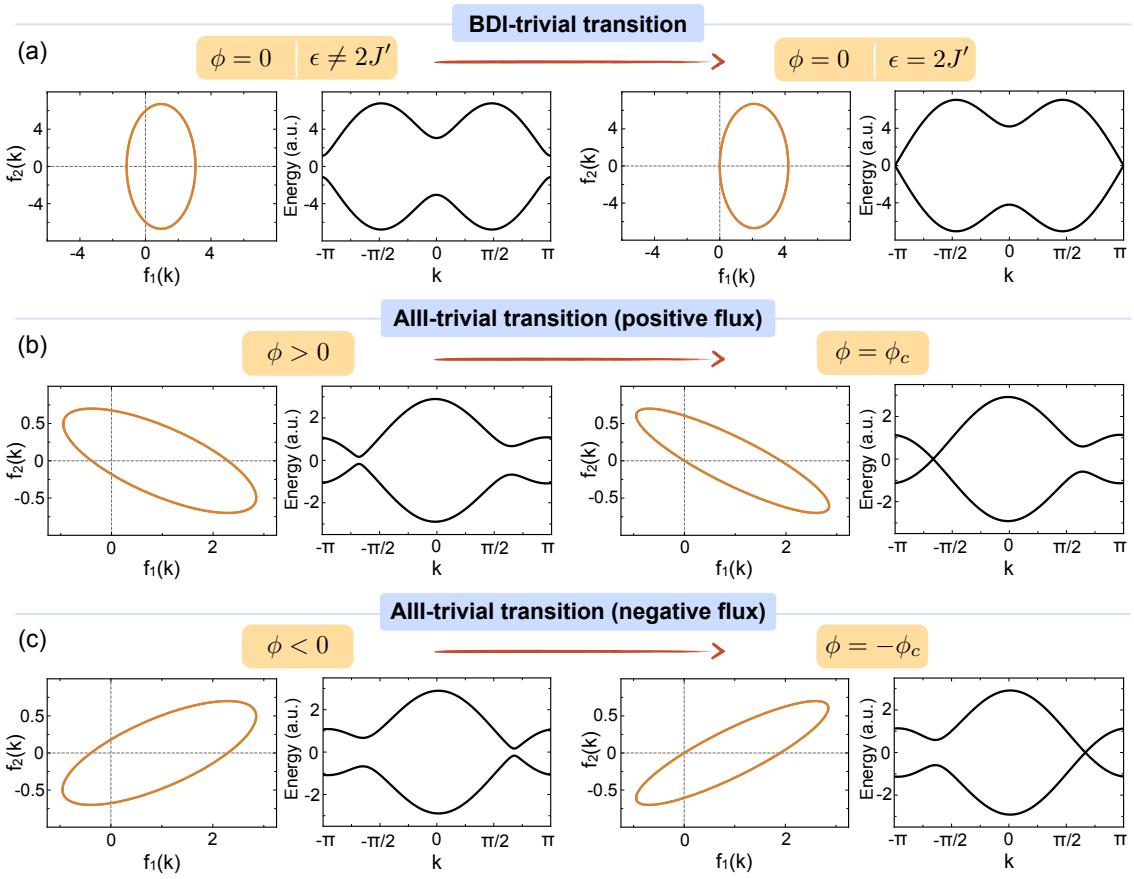

Figure 10.2: **Topological phase transitions.** The model can undergo three different kind of phase transitions: a BDI-trivial transition and two AIII-trivial transitions. A transition from the BDI class, when there is no magnetic flux penetrating the ladder, occurs for $\epsilon = 2J'$, situation in which the energy bands touch each other at momentum $k = \pi$ (a). In the presence of a positive magnetic flux, the system reaches the critical point between the AIII class and its trivial phase when $\phi = \phi_c$. In this case the upper and lower bands close at $k_c = \phi_c/2 - \pi$ (b). Finally, when the ladder is subjected to a negative magnetic flux, the Hamiltonian experiences a transition from the AIII class to its trivial phase when $\phi = -\phi_c$. At this point the band gap closes at $k = -\phi_c/2 + \pi$ (c). Parameters values used in this figura are: (a) $\epsilon = 0.95$, $J' = 1.05$, $J = 3.35$ and $\phi = 0$ before the transition and $\epsilon = 2.1$, $J' = 1.05$, $J = 3.35$ and $\phi = 0$ at the critical point; (b) $\epsilon = J' = 0.95$, $J = 0.35$ and $\phi = \pi/2$ before the transition and $\epsilon = J' = 0.95$, $J = 0.35$ and $\phi = 2\pi/3$ at the critical point; (c) $\epsilon = J' = 0.95$, $J = 0.35$ and $\phi = -\pi/2$ before the transition and $\epsilon = J' = 0.95$, $J = 0.35$ and $\phi = -2\pi/3$ at the critical point.

By looking at the functions $f_1(k)$ and $f_2(k)$, Eq. (10.7) and Eq. (10.8), we conclude that the condition for the model to be in its non-trivial topological phase is:

$$\epsilon < 2J' \cos(\phi/2). \tag{10.11}$$

For $\phi = 0$ the model is topologically nontrivial if $\epsilon < 2J'$ and thus a topological transition from the BDI class to a trivial phase occurs at $\epsilon = 2J'$, where the energy bands touch each other at momentum π [see Fig. 10.2(a)]. In the presence of a magnetic flux per plaquette ϕ, the model is in a topological phase as long as the amplitude of the flux does not exceed a critical value $\phi_c = 2\arccos(\epsilon/2J')$. Thereby the model undergoes a transition from the AIII class to a trivial phase at $\phi = \pm\phi_c$, for which the two bands cross each other at the critical momentum $k_c = \pm\phi_c/2 \mp \pi$ [see Fig. 10.2(b) and (c)].

If $\epsilon > 2J'$, the system is in its topologically trivial phase, see Eq. (7.17). Since we are interested in analysing the edge states, which only exist in the topological phase, we will consider the situation in which $\epsilon \leq 2J'$. Thus, the critical magnetic flux ϕ_c is always well defined by the equation $\cos(\phi_c/2) = \epsilon/(2J')$. Therefore, we can use ϕ_c instead of ϵ as a parameter of the model

10.4 Edge states

For open boundary conditions, in the topological phase, the model exhibits two symmetry protected zero modes. From Chapter 8 we know that these states are $|e_\pm\rangle = (|l\rangle \pm |r\rangle)/\sqrt{2}$, being:

$$|l\rangle = \frac{1}{\sqrt{\kappa}} \sum_k \frac{e^{-i\varphi(k)}}{\rho(k)} \hat{x}^\dagger_{+,k}, \tag{10.12}$$

$$|r\rangle = \frac{1}{\sqrt{\kappa}} \sum_k \frac{e^{-ik}e^{i\varphi(k)}}{\rho(k)} \hat{x}^\dagger_{-,k}, \tag{10.13}$$

with $\hat{x}^\dagger_{\pm,k} = \hat{a}^\dagger_k \pm \hat{b}^\dagger_k$. The state $|l\rangle$ is localized at the left edge of the system, whereas the state $|r\rangle$ is localized at the right edge of the ladder. The are polarized, meaning that they have orthogonal isospin states, which correspond to the two eigenvectors of the chiral operator $U_S = \sigma_x$. In addition to their good localization in position space at the edges of the ladder, they are also well localized in momentum space at the positions of the gaps between the two energy bands. In this way, they can be considered to be formed by several momentum components, one for each energy gap in the system. The smaller an energy gap is, the more prominent the corresponding momentum component in the edge states wave function is (all these features of the edge states are explained in detailed in Chapter 8).

For $\phi = 0$, the system has time reversal symmetry and thus belongs to the BDI symmetry class. In that case the Hamiltonian matrix is:

$$M(k) = (\epsilon + 2J' \cos k)\ \sigma_z + 2J \sin k\, \sigma_y. \tag{10.14}$$

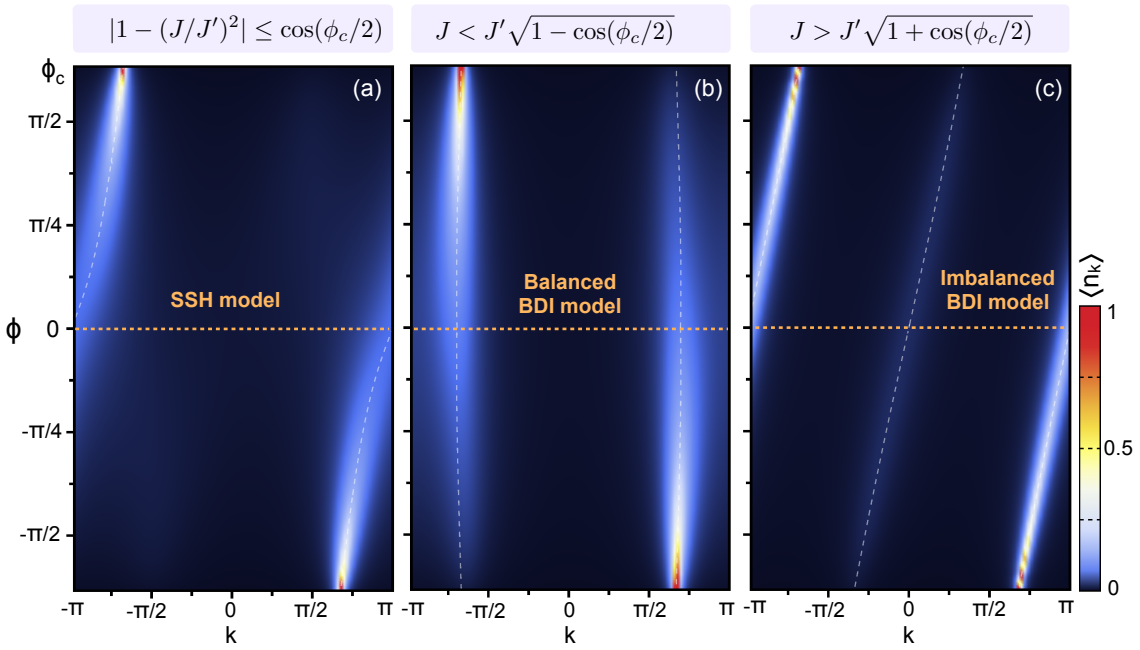

Figure 10.3: **Edge states momentum distribution.** Plot of the edge states momentum distribution as a function of the effective magnetic flux ϕ. For $\phi = 0$ the model belongs to the BDI class. It realizes the SSH-like model, the balanced BDI model and the imbalanced BDI model for $|1-(J/J')^2| \leq \cos\phi_c/2$, $J < J'\sqrt{1-\cos\phi_c/2}$ and $J > J'\sqrt{1+\cos\phi_c/2}$, respectively. This three situations correspond to edge states whose momentum density distribution shows one peak at momentum $k = \pi$ (a), two peaks of the same hight at opposite momenta (b) and two peaks of different hight located at $k = 0$ and $k = \pi$ (c). The presence of a non zero magnetic flux ϕ, modifies the location and relative weight of the peaks in such a way that, for $\phi = \pm\phi_c$, the edge states are mostly located at the critical momentum $k_c = \pm\phi_c/2 \mp \pi$. Parameters values used in this figure are: (a) $\epsilon = J' = J = 0.95$; (b) $\epsilon = J' = 0.95$ and $J = 0.35$; and (c) $\epsilon = J' = J = 0.95$ and $J = 3.35$. In all cases $\phi_c = 2\pi/3$.

Depending on the values of the three parameters ϵ, J and J', this Hamiltonian matrix can corresponds to the Hamiltonian matrix of each one of the three different types of ladder models in the BDI class (see Chapter 6), corresponding each of them to a different type of edge states. The are three possibilities.

When $|1-(J/J')^2| \leq \cos\phi_c/2$ the hourglasss ladder realizes the SSH-like model for $\phi = 0$, which has just one gap between the energy bands, located at momentum $k = \pi$. Therefore, the edge states momentum distribution shows a single peak at $k = \pi$. When an effective magnetic flux ϕ is added, this peak is shifted and deformed, so that when the magnetic flux reaches one of the two critical values, $\phi = \pm\phi_c$, the momentum peak is located at $k_c = \pm\phi_c/2 \mp \pi$, where the gap is closed [see Fig. 10.3(a)]. The second possibility takes place for $J < J'\sqrt{1-\cos\phi_c/2}$, which corresponds to $|1-(J/J')^2| > \cos\phi_c/2$ and $J < J'$. In this case the hourglass

ladder realizes the balanced BDI model for $\phi = 0$, a thus there are two gaps of the same width at opposite momentum. In consequence, the edge modes momentum distribution shows two identical peaks at momenta q_1 and q_2, being:

$$q_1 = -q_2 = \arccos\left[\frac{\cos(\phi_c/2)}{1-(J/J')^2}\right] - \pi. \tag{10.15}$$

The presence of a flux ϕ enhances one of the two peaks, while reduces the other one, depending on its sign, as well as changes slightly their position. Close to the critical values of the flux, $\pm\phi_c$, one momentum peak is located at $k_c = \pm\phi_c/2 \mp \pi$ while the other one is almost totally suppressed [see Fig. 10.3(b)].

Finally, for $J > J'\sqrt{1+\cos\phi_c/2}$, what means that $|1-(J/J')^2| > \cos\phi_c/2$ and $J > J'$, the hourglass ladder realizes the imbalanced BDI model for $\phi = 0$. In that situation, there are two gaps between the energy bands, one at momentum $k = 0$ and another one, of smaller width, at $k = \pi$. The edge modes are then mostly located at momentum π and slightly at momentum 0. The flux ϕ enhances and moves the momentum peak at π, reaching the value k_c for $\phi = \pm\phi_c$ [see Fig. 10.3(c)].

Chapter 11

Protected chiral currents

11.1 Quench to the critical point

We want to design a quench protocol in which the edge states form well defined wave packets that travel along the system. For that we need two ingredients: on one hand, the edge states should be well defined both in momentum and position spaces; and, on the other hand, the dispersion relation of the time evolution Hamiltonian has to be almost linear in the region where the edge states are located in momentum space. Thereby, we need a quench to the critical point, in which the two bands cross each other and thus the dispersion relation is almost linear around that crossing point.

As we explained in Chapter 10, at the critical point, the hourglass ladder Hamiltonian can belong to the BDI class or to the AIII class. Our purpose is precisely to analyse the properties and differences of the edge states dynamics after a quench in the BDI class and a quench in the AIII class. In each case, the energy bands cross each other at a different momentum. Therefore, in order to make the momentum of the edge states coincide with that critical momentum, we need to choose carefully the values of the Hamiltonian parameters before the quench. In the following we explain in detail how these two quenches have to be done.

11.1.1 Quench in the BDI class

The critical point of the hourglass ladder Hamiltonian, when it belongs to the BDI symmetry class, corresponds to $\epsilon = 2J'$, which is equivalent to having $\phi = \phi_c$ with $\phi_c = 0$. At this situation the energy bands cross each other at the critical momentum $k_c = \pi$. Therefore, we are interested in edge states mostly localized in momentum space at $k = \pi$. That is the case for the SSH-like model and the imbalanced BDI model [see Fig. 10.3(a) and (c)].

We choose the imbalanced BDI model, as it corresponds to a larger region in parameter space and thus we can modify more freely the parameter values [see Fig. 6.4(e)]. This model is realized by the hourglass ladder for $J > J'\sqrt{1+\cos\phi_c/2}$. In this case, the edge states have two peaks in their momentum distribution, one at $k = 0$ and another one at $k = \pi$. The gap al $k = \pi$ is smaller that the one at

$k = 0$, therefore the corresponding edge states momentum component is much more prominent [see Fig. 11.1(a)]. At the critical point the dispersion relation is almost linear around the critical momentum $k_c = \pi$, where the two bands cross each other [see Fig. 11.1(c)].

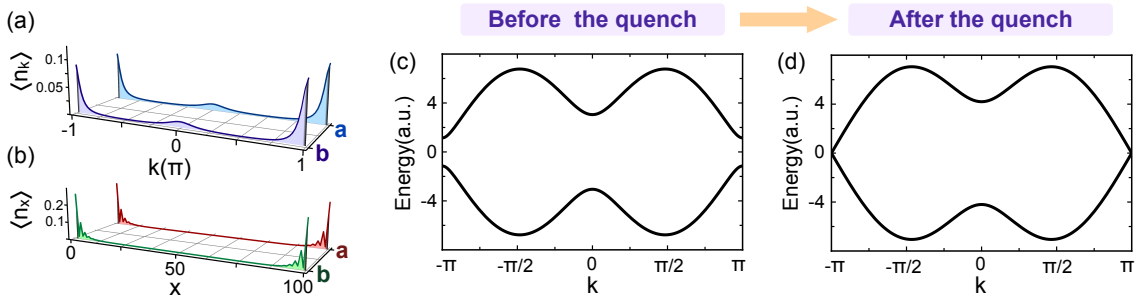

Figure 11.1: **Quench in the BDI class.** (a) Momentum density distribution and (b) spatial density distribution of the edge states for $\epsilon = 0.95$, $J' = 1.05$, $J = 3.35$ and $\phi = 0$. The edge states are mostly located at $k = \pi$ in momentum space, which is the point at which the two energy bands cross each other at the critical point. (b) Energy bands of the hourglass ladder Hamiltonian before the quench, for $\epsilon = 0.95$, $J' = 1.05$, $J = 3.35$ and $\phi = 0$, and (c) after the quench, for $\epsilon = 2.1$, $J' = 1.05$, $J = 3.35$ and $\phi = 0$.

11.1.2 Quench in the AIII class

There are two ways in which the hourglass ladder Hamiltonian can reach its critical point in the AIII class: with a positive magnetic flux $\phi = \phi_c$ or with a negative magnetic flux $\phi = -\phi_c$. The two energy bands of the Hamiltonian cross each other at the critical point at $k_c = \pm\phi_c/2 \mp \pi$, being $\phi = \pm\phi_c$. Therefore, in order for the edge states to be localized in momentum space close to k_c, we need to consider the case in which $J < J'\sqrt{1 - \cos\phi_c/2}$ [see Fig.10.3(b)].

In this situation, the edge states are made of two momentum components, one located at $k = q_1$ and another one at $k = q_2$, depending these two values on the magnetic flux ϕ. For $\phi = 0$ the Hamiltonian realizes the balanced BDI model and both edge states momentum components have the same relative weights, being:

$$q_1(\phi = 0) = -q_2(\phi = 0) = \arccos\left[\frac{\cos(\phi_c/2)}{1 - (J/J')^2}\right] - \pi. \tag{11.1}$$

In the presence of a magnetic flux $\phi \neq 0$, one of the two momentum peaks is enhanced while the other is lessened, as well as their position is slightly changed [see Fig. 10.3(b)]. For a positive magnetic flux, the peak at q_1 gets increased, being the peak at q_2 diminished. Close to the critical point $\phi = \phi_c$ the edge states are almost totally localized at q_1 in momentum space, getting q_1 closer to $k_c = \phi_c/2 - \pi$ the closer the system is to the critical point. For a negative magnetic flux, the edge states behaviour is the opposite, being the momentum peak at q_2 the one that gets

enhanced, and getting q_2 closer to $k_c = -\phi_c + \pi$ the closer the system is to the critical point $\phi = -\phi_c$.

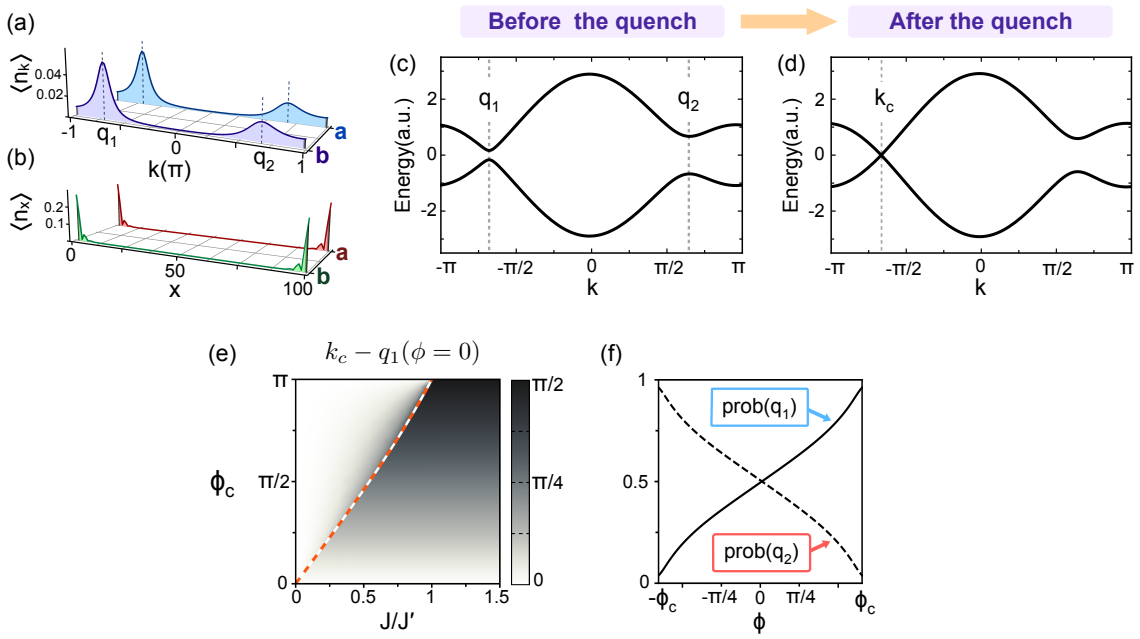

Figure 11.2: **Quench in the AIII class.** (a) Momentum density distribution and (b) spatial density distribution of the edge states for $\epsilon = J' = 0.95$, $J = 0.35$ and $\phi = \pi/4$. The edge states are mostly located in momentum space at $k = q_1$, for a positive magnetic flux, and at $k = q_2$, for a negative magnetic flux. (f) The relatives weights of both momentum components can be chosen by selecting the appropriate value of ϕ. (b) Energy bands of the hourglass ladder Hamiltonian before the quench, for $\epsilon = J' = 0.95$, $J = 0.35$ and $\phi = \pi/2$, and (c) after the quench, for $\epsilon = J' = 0.95$, $J = 0.35$ and $\phi = \phi_c = 2\pi/3$. (e) Difference between the momentum of the edge modes for $\phi = 0$ and the critical momentum k_c at which the energy bands cross each other. When $J < J'\sqrt{1 - \cos\phi_c/2}$ this difference is almost zero, whereas it depends linearly on the magnetic flux otherwise. The curve $J = J'\sqrt{1 - \cos\phi_c/2}$ is plotted in a red dashed line. (f) Relative weights associated to the two edge states momentum peaks, at q_1 and q_2, for $\epsilon = J' = 0.95$ and $J = 0.35$, as a function of the magnetic flux.

Therefore, the quench protocol in the AIII class for a positive magnetic flux is the following. We prepare the system with parameters such that $J < J'\sqrt{1 - \cos\phi_c/2}$ and a magnetic flux $\phi > 0$, so that the edge states are mostly located at q_1 in momentum space [see Fig. 11.2(a)]. Then the magnetic flux is suddenly taken to $\phi = \phi_c$, and thus the energy bands cross each other at the critical momentum $k_c = \phi_c/2 - \pi$, where they are almost linear [see Fig. 11.2(d)]. By looking at Eq. (11.1) we notice that if $(J/J') << 1$, the value of q_1 will almost not depend on the value of the magnetic flux and be really close to k_c. That is precisely what we want, so that the edge states are localized at a momentum for which the dispersion

relation after the quench is almost linear. Since we are considering the region in the parameter space defined by $J < J'\sqrt{1-\cos\phi_c/2}$, the condition $(J/J') << 1$ can be easily fulfilled, and the difference between $q_1(\phi = 0)$ and k_c is low enough [see Fig. 11.2(e)]. The protocol for a quench in the AIII class with a negative magnetic flux is exactly the same, we only need to change the sign of the magnetic flux and consider q_2 instead of q_1.

11.2 Free propagation of the edge states

The dynamics of the edge states can be derived at the same time both for the quench in the BDI class and for the one in the AIII class. In both cases the Hamiltonian parameters before the quench are such that $\epsilon/2J' < \cos\phi_c/2$ and then they are quenched so that $\epsilon/2J' = \cos\phi_c/2$. That is:

$$H\left(\frac{\epsilon}{2J'} < \cos\frac{\phi}{2}\right) \xrightarrow{\text{Quench}} H\left(\frac{\epsilon}{2J'} = \cos\frac{\phi}{2}\right). \tag{11.2}$$

This is valid for the quench in the BDI class, for which $\phi = 0$ and then $\epsilon = 2J'$ at the critical point, as well as for the one in the AIII class. The parameters of the Hamiltonian before the quench are chosen, as we explained in the previous section, in such a way that the corresponding edge state are:

$$\hat{l}^\dagger \approx \sum_n^N e^{ik_c n}\,\psi(n)\,\hat{x}^\dagger_{+,n}, \tag{11.3}$$

$$\hat{r}^\dagger \approx \sum_n^N e^{ik_c n}\,\psi(N+1-n)\,\hat{x}^\dagger_{-,n}, \tag{11.4}$$

where $\psi(n)$ a function localized at the left edge of the system, and being k_c the momentum at which the energy bands of the quench Hamiltonian cross each other. The initial state is prepared by populating both edge modes. Afterwards, the Hamiltonian parameters are quenched to the critical point and the system is let evolve in time.

Given that the edge states are well localized in momentum space at k_c, only the eigenstates of the quench Hamiltonian in a neighbourhood of k_c are involved in the time evolution and, therefore, we can make a first order expansion of the Hamiltonian matrix:

$$M(k_c + k) \approx kv\,\sigma_d, \tag{11.5}$$

where

$$\sigma_d = U_\theta\,\sigma_y\,U_\theta^\dagger, \tag{11.6}$$

$$v = 2\sqrt{J'^2\sin^2(\phi_c/2) + J^2}, \tag{11.7}$$

being $U_\theta = e^{i\theta\sigma_x/2}$ and $\tan\theta = \pm(J'/J)\sin\phi_c/2$ (here only the parameters after the quench are involved).

The edge modes are invariant under U_θ, as they are eigenstates of σ_x, therefore we can consider $M(k_c+k) \approx kv\,\sigma_y$, that corresponds to the case in which there is no flux penetrating the ladder, and then generalize the result by applying U_θ to the evolved states. The eigenmodes of this Hamiltonian matrix are $\hat{y}^\dagger_{\pm,k} = (\hat{a}^\dagger_k \pm i\hat{b}^\dagger_k)/\sqrt{2}$, with energies $\pm kv$, so that there is a correlation between spin and velocity. However, the eigenmodes of the effective Hamiltonian that governs the edge modes time evolution, H_{evol}, are not those but superpositions of them that satisfy the open boundary conditions. Thereby:

$$H_{\text{evol}} = \sum_k kv\,\hat{c}^\dagger_k \hat{c}_k, \tag{11.8}$$

being $\hat{c}^\dagger_k = (\,\hat{y}^\dagger_{+,k_c+k} - \hat{y}^\dagger_{-,k_c-k}\,)/\sqrt{2}$ the eigenstates of the time evolution Hamiltonian with energy $E(k) = kv$, and being the quantum number k quantized as $k(N+1) = m\pi$, with $m \in \mathbb{Z}$. Thus, modes with opposite spin can be coupled during the time evolution.

It is convenient to define the following states:

$$|l^\pm_j\rangle = \sum_n e^{ik_c n}\,\psi(n+1-j)\,\hat{y}^\dagger_{\pm,n}\,|0\rangle\,, \tag{11.9}$$

$$|r^\pm_j\rangle = \sum_n e^{ik_c n}\,\psi(j+1-n)\,\hat{y}^\dagger_{\pm,n}\,|0\rangle\,. \tag{11.10}$$

That is, $|l^\pm_j\rangle$ is an state with an spatial density distribution equal to the one of the left edge state $|l\rangle$, but shifted so that it reaches its maximum value at position $n = j$, and whose spin state is $\hat{y}^\dagger_{\pm,n}$. Analogously, $|r^\pm_j\rangle$ is an state with an spatial density distribution equal to the one of the right edge state $|r\rangle$, but shifted so that it reaches its maximum value at position $n = j$, and whose spin state is $\hat{y}^\dagger_{\pm,n}$. The initial edge states, $|j\rangle$ and $|r\rangle$, can then be written as:

$$|l\rangle = \frac{1}{\sqrt{2}}\big(\,|l^+_1\rangle + i\,|l^-_1\rangle\,\big), \tag{11.11}$$

$$|r\rangle = \frac{1}{\sqrt{2}}\big(\,|r^+_N\rangle - i\,|r^-_N\rangle\,\big). \tag{11.12}$$

As we see, since the initial edge states are eigenstates of σ_x, they are decomposed into a sum of two components, being each one an eigenstate of σ_y. Defining the function:

$$G(k) = \frac{1}{\sqrt{2N}}\sum_n e^{-ikn}\psi(n), \tag{11.13}$$

we can write the states $|l^\pm_j\rangle$ and $|r^\pm_j\rangle$ in terms of the eigenstates of the time evolution Hamiltonian as:

$$|l^\pm_j\rangle = \pm\sum_k e^{\mp ik(j-1)}\,G(\pm k)\,\hat{c}^\dagger_k\,|0\rangle\,, \tag{11.14}$$

$$|r^\pm_j\rangle = \pm\sum_k e^{\mp ik(j+1)}\,G(\mp k)\,\hat{c}^\dagger_k\,|0\rangle\,. \tag{11.15}$$

We can know easily compute the time evolution of the states $|l_1^{\pm}\rangle$ and $|r_N^{\pm}\rangle$, taking into account that the modes $\hat{c}_k^{\dagger}$ are eigenmodes of the time evolution Hamiltonian with energy $E(k) = kv$. We get:

$$U(t)\,|l_1^{\pm}\rangle = \pm \sum_k e^{-ikvt}\, G(\pm k)\, \hat{c}_k^{\dagger}\,|0\rangle\,, \tag{11.16}$$

$$U(t)\,|r_N^{\pm}\rangle = \pm \sum_k e^{-ikvt}\, e^{\mp ik(N+1)}\, G(\mp k)\, \hat{c}_k^{\dagger}\,|0\rangle\,. \tag{11.17}$$

Comparing Eq. (11.16) and Eq. (11.17) with Eq. (11.14) and Eq. (11.15) we obtain the following time evolution rules:

$$U(\pm t)\,|l_1^{\pm}\rangle = |l_{j=1+vt}^{\pm}\rangle\,, \tag{11.18}$$

$$U(\mp t)\,|r_N^{\pm}\rangle = |r_{j=N-vt}^{\pm}\rangle\,, \tag{11.19}$$

$$U(T)\,|l_1^{\pm}\rangle = |r_N^{\mp}\rangle\,, \tag{11.20}$$

$$U(T)\,|r_N^{\pm}\rangle = |l_1^{\mp}\rangle\,. \tag{11.21}$$

being $T = (N+1)/v$. Here we have used the fact that $k(N+1) = m\pi$, with $m \in \mathbb{Z}$. What do these results tell us? The state $|l_1^{+}\rangle$ is localized at the left edge of the system and its spin state is y_+. The time evolution Hamiltonian has a correlation between spin and velocity, so that the spin state $y_{\pm}$ corresponds to a velocity $\pm v$. Therefore, $|l_1^{+}\rangle$ propagates almost freely towards the bulk at constant velocity v. In contrast, the state $|j_1^{-}\rangle$ cannot move according to its velocity $-v$, as it is already at the left edge of the system. It propagates to the right if we let it evolve backwards in time. That is what Eq. (11.18) means. Something similar happens with states $|r_N^{\pm}\rangle$, but in the opposite direction, Eq. (11.19). Finally, Eq. (11.20) and Eq. (11.21), mean that for an evolution time $T = (N+1)/v$ each state becomes the state at the other edge and with the opposite spin.

Combining Eq. (11.18), Eq. (11.19) and Eq. (11.20) we obtain the time evolution of the left edge mode:

$$\begin{aligned} U(t)\,|l\rangle \overset{a}{=} & \frac{1}{\sqrt{2}}\left[U(t)\,|l_1^{+}\rangle + i\,U(t-T)\,U(T)\,|l_1^{-}\rangle\right] \overset{b}{=} \\ & \frac{1}{\sqrt{2}}\left[|l_{1+vt}^{+}\rangle + i\,U(t-T)\,|r_N^{+}\rangle\right] \overset{c}{=} \frac{1}{\sqrt{2}}\left[|l_{1+vt}^{+}\rangle + i\,|r_{vt-1}^{+}\rangle\right] = \\ & \frac{1}{\sqrt{2}}\sum_n e^{ik_c n}\left[\psi(n-vt) + i\,\psi(vt-n)\right]\hat{y}_{+,n}^{\dagger}\,|0\rangle\,. \end{aligned} \tag{11.22}$$

Here, we have first (a) separated $|l\rangle$ into the two different opposite spin components $|l_1^{+}\rangle$ and $|l_1^{-}\rangle$, as well as decomposed the time evolution operator that acts on the y_- component as the product of two time evolution operators: $U(t) = U(t-T)U(T)$. Then (b) the y_+ component $|l_1^{+}\rangle$ propagates during time t and becomes $|l_{1+vt}^{+}\rangle$, whereas the y_- component $|l_1^{-}\rangle$ evolves during time T and becomes $|r_N^{+}\rangle$, getting its spatial density distribution reflected and its spin inverted. Finally (c) the reflected component $|r_N^{+}\rangle$ evolves backwards in time and becomes $|r_{vt-1}^{+}\rangle$. In this way, the

two initial components form a wave packet centred at position vt with spin y_+, that moves towards the bulk at a constant velocity v.

The time evolution of the right edge state $|r\rangle$ can be analogously computed by combining Eq. (11.18), Eq. (11.19) and Eq. (11.21). We get:

$$\begin{aligned} U(t)\,|r\rangle \overset{a}{=} & \frac{1}{\sqrt{2}}\left[U(t-T)\,U(T)\,|r_N^+\rangle - i\,U(t)\,|r_N^-\rangle\right] \overset{b}{=} \\ & \frac{1}{\sqrt{2}}\left[U(t-T)\,|l_1^-\rangle - i\,|r_{N-vt}^-\rangle\right] \overset{c}{=} \frac{1}{\sqrt{2}}\left[|l_{N+2-vt}^-\rangle - i\,|r_{N-vt}^-\rangle\right] = \\ & \frac{1}{\sqrt{2}}\sum_n e^{ik_c n}\left[\psi(n-N-1+vt) - i\,\psi(N+1-vt-n)\right]\hat{y}_{-,n}^\dagger\,|0\rangle\,. \end{aligned} \tag{11.23}$$

Thus, the two components that constitute the initial edge state form a wave packet centred at position $N+1-vt$ with spin y_-, that moves towards the bulk at a constant velocity $-v$.

Finally, from Eq. (11.20) and Eq. (11.21), we can get the time evolution of the edge states at time T:

$$U(T)\,|l\rangle = i\,|r\rangle\,, \tag{11.24}$$

$$U(T)\,|r\rangle = -i\,|l\rangle\,., \tag{11.25}$$

In this way, after a time $T=(N+1)/v$, when each wave packet reaches the opposite end of the ladder, the initial states are restored. Therefore, the same process is repeated and, in conclusion, the edge modes dynamics consist on the free propagation of well defined wave packets, moving with constant velocity v, that bounce whenever they reach any end of the system and continue moving in the opposite direction. The spin and velocity are correlated, being the wave packet moving to the right in the spin state y_+, and the one moving to the left in the spin state y_-.

11.3 Chirality of the currents

In general, the spin states of the wave packets that propagate along the ladder are $U_\theta\,\hat{y}_\pm^\dagger$, which are the eigenmodes of σ_d. These modes are:

$$\hat{d}_{\pm,n}^\dagger = \frac{1}{\sqrt{2}}\left(\cos\frac{\theta}{2} \mp \sin\frac{\theta}{2}\right)\hat{a}_n^\dagger \pm \frac{i}{\sqrt{2}}\left(\cos\frac{\theta}{2} \pm \sin\frac{\theta}{2}\right)\hat{b}_n^\dagger. \tag{11.26}$$

In this way, the edge state dynamics consists of two wave packets travelling at constant velocity, one of them moves to the right and has spin state $\hat{d}_{+,n}^\dagger$, whereas the other one moves to the left and occupies the modes $\hat{d}_{-,n}^\dagger$. Therefore, there are two different currents in each leg of the ladder. Being j_a^+ and j_a^- the positive and negative currents in leg a; and j_b^+ and j_b^- the ones in leg b, we have:

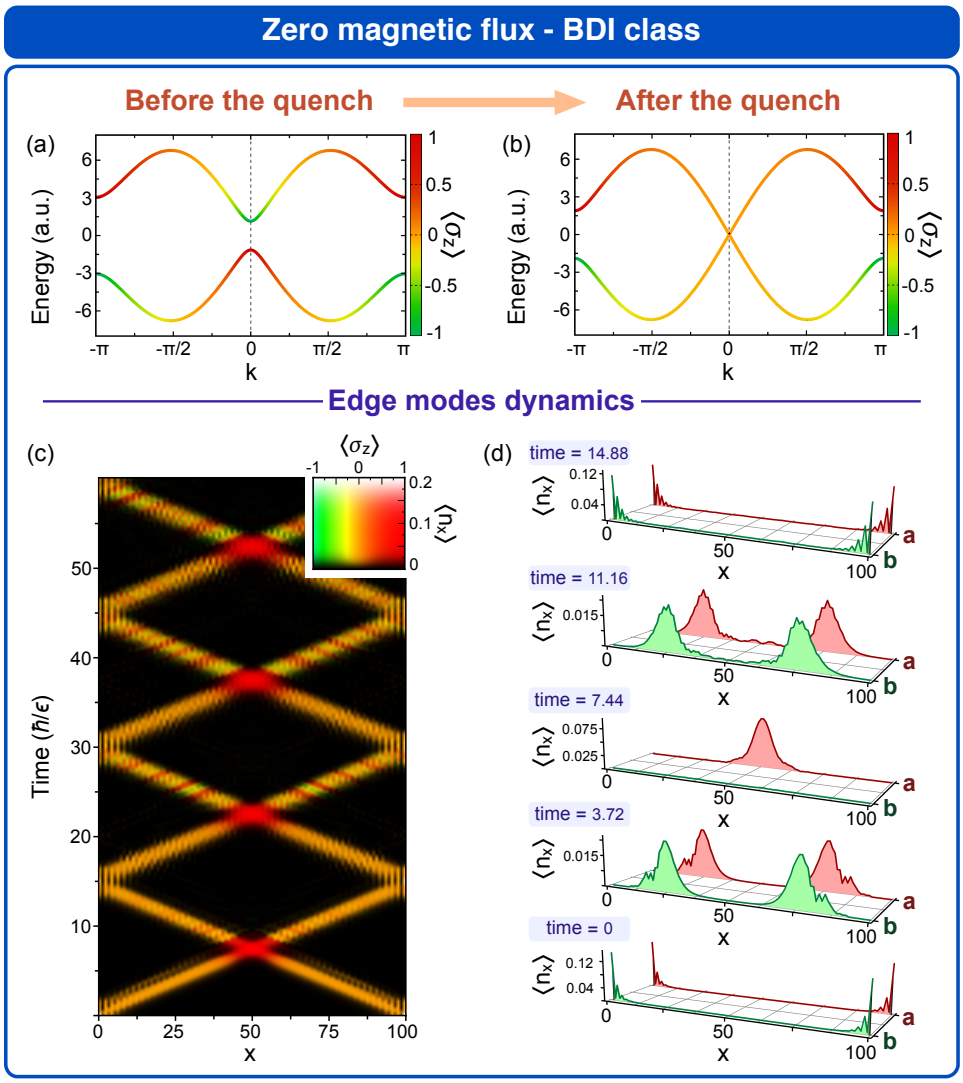

Figure 11.3: **Edge states dynamics in the BDI class.** Dynamics of the edge states after a quench to the critical point in the BDI symmetry class, when there is no magnetic flux penetrating the ladder. Parameters before the quench are $\epsilon = 0.95$, $J' = 1.05$, $J = 3.35$ and $\phi = 0$. (a) There are two gaps between the bands, at $q_1 = 0$ and $q_2 = \pi$. The parameters are chosen such that the gap at $q_2 = \pi$ is smaller enough for the corresponding edge modes to be mostly located in momentum space at $q = \pi$ (for the sake of clarity, we show the energy bands shifted by π, so that the crossing point between the two bands takes place at $k = 0$). (b) The quench to the critical point is performed by changing the value of J' to $\epsilon/2 = 0.475$, so that the bands touch each other at $q = \pi$, where the dispersion relation is linear. (c), (d) The edge modes form wave packets that propagate freely towards the bulk and whose spin states are the eigenmodes of σ_y. Therefore the generated currents are not chiral. When both edge states meet at the center of the system they interfere constructively in leg a and destructively in leg b, what is a consequence of their spin states.

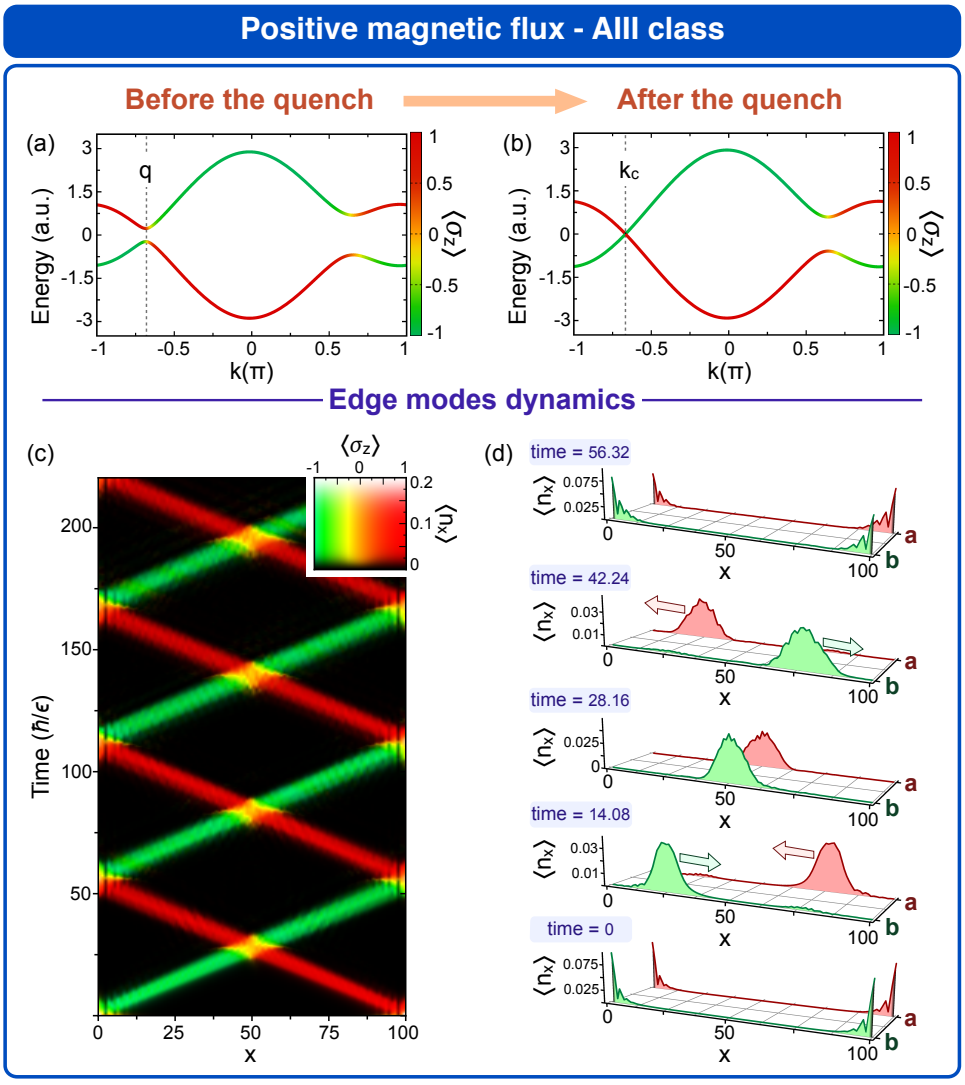

Figure 11.4: **Topologically protected chiral currents.** Dynamics of the edge modes after a quench to the critical point in the AIII symmetry class, when there is an effective magnetic flux penetrating the ladder. Parameters before the quench are $\epsilon = J' = 0.95$, $J = 0.35$ and $\phi = 7\pi/16$. (a) There are two gaps between the two bands, at momentum q_1 and q_2, being the edge modes located in momentum space close to q_1. (b) The quench to the critical point is performed by setting ϕ to $2\arccos\epsilon/2J' \approx 2.1$. After the quench, the bands close at $k_c \approx q_1$, where the dispersion relation is almost lineal and there is a high correlation between a-modes and b-modes and negative and positive velocity, respectively. (c), (d) In consequence, the edge modes move along the system freely giving rise to anticlockwise chiral currents ($\mathcal{J}_c = 0.92$). If we considered an opposite initial magnetic flux $\phi = -7\pi/16$, and then quenched it to the critical value $\phi = -\phi_c$, we would obtain the same dynamics but with opposite chirality $\mathcal{J}_c = -0.92$. In that case, the time evolution Hamiltonian would couple a-modes with positive velocity and b-modes with negative velocity.

$$j_a^+ = -j_b^- = \frac{1}{2}\left(\cos\frac{\theta}{2} - \sin\frac{\theta}{2}\right)^2, \tag{11.27}$$

$$j_a^- = -j_b^+ = -\frac{1}{2}\left(\cos\frac{\theta}{2} + \sin\frac{\theta}{2}\right)^2 \tag{11.28}$$

The total currents in each leg are $J_a = j_a^+ + j_a^-$ and $J_b = j_b^+ + j_b^-$. We have that $J_a = -J_b$, which is due to the fact that the two wave packets that move in opposite directions have orthogonal spin states. We characterize the chirality of these currents through the quantity $\mathcal{J}_c = -(j_a^+ + j_a^-) = j_b^+ + j_b^-$. A chirality of $\mathcal{J}_c = 1$, the maximum posible, means that the wave packet moving to the right occupies only b-modes and the one moving to the left occupies only a-modes. $\mathcal{J}_c = -1$ corresponds to the opposite situation, and $\mathcal{J}_c = 0$ means that the total current in each leg vanishes. The chirality of the currents can be written in terms of the Hamiltonian parameters as:

$$\mathcal{J}_c = \frac{\pm J' \sin(\phi_c/2)}{\sqrt{J'^2 \sin^2(\phi_c/2) + J^2}}, \tag{11.29}$$

where the $\pm$ corresponds to the sign of the effective magnetic flux at the critical point, $\phi = \pm\phi_c$. For a wide region in parameter space, the currents generated by the edge states dynamics have a high chirality (see Fig. 11.5).

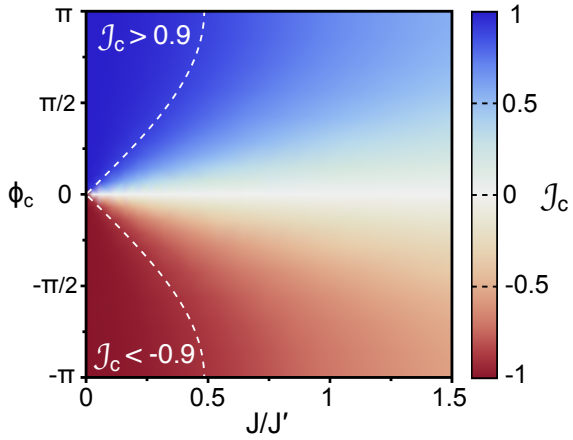

Figure 11.5: **Chirality of the edge states currents.** Chirality $\mathcal{J}_c$ of the currents generated by the edge states after, as a function of the ratio J/J' and ϕ_c. These parameters are not changed during the quench protocol in the AIII class, only the magnetic flux ϕ is changed. Therefore, we can compare this figure with Fig. 11.2(d) and see that the parameter values we need for the edge sates to have a momentum close to the critical momentum, at which the energy bands cross each other, correspond to a high chirality. The regions delimited by a dashed white curve correspond to a chirality higher than 0.9 or lower than -0.9.

In Fig. 11.3 and Fig. 11.4 we show the edge states dynamics in the BDI class, without any magnetic flux, and in the AIII class, respectively. In the first case,

$\sigma_d = \sigma_y$ and thus the wave packets formed by the edge states propagate occupying both legs equally [see Fig. 11.3(c) and (d)]. Therefore the currents are not chiral and we have $\mathcal{J}_c = 0$. In contrast, in the AIII case, $\hat{d}^\dagger_{+,n} \approx \hat{b}^\dagger_n$ and $\hat{d}^\dagger_{-,n} \approx \hat{a}^\dagger_n$, so that the wave packet moving to the right occupies mostly b-modes, whereas the one moving to the left is almost entirely in a-modes [see Fig. 11.4(c) and (d)]. For the chosen parameters, the chirality is $\mathcal{J}_c = 0.92$, close to the maximum value for an anticlockwise chiral current. If we changed the sign of the magnetic flux, the chirality would be inverted and the currents clockwise.

In addition to their chirality, what is a manifestation of the AIII symmetry class, the currents generated in this quench dynamics are also protected. That is, they stay in the system for quite long evolution times, what is a consequence of the properties of the edge states that form the currents. In fact, the initial edge states can be recover, Eq. (11.24) and Eq. (11.25), if we quench back the Hamiltonian at any time the currents hit the edges of the system [see Fig. 11.4(d)].

11.4 Experimental realization

We propose an experimental scheme for the realization of the hourglass Hamiltonian and observe the edge states quench dynamics using cold atoms in optical lattices. In particular, we use a recently developed atom-optics technique [46, 47] which uses momentum lattices for the study of single-particle transport phenomena in one-dimensional and lattice systems [38, 40, 21]. The control over all parameters, together with the capability to realize ladder models and implement all kind of tunneling terms, as well as the capacity for single-site detection, makes this experimental setup ideal for the experimental realization of our model and the observation of the edge states dynamics.

In this experimental scheme, each site in the ladder corresponds to a different free-particle momentum state of the atoms, and each leg of the ladder corresponds to a distinct internal state. All terms in the Hamiltonian can be implemented by means of two different types of optical processes. On one hand, two photon Bragg transition couple adjacent sites in the momentum lattice, without changing the internal state. This kind of transitions can be used to implement on-site energies and horizontal tunneling terms. On the other hand, two photon Raman transitions, which change the internal state of the atoms, can be used to implement diagonal tunneling terms of the Hamiltonian [see Fig. 11.6].

The edge states of the model can be prepared adiabatically (see Fig. 11.7). We start with two one-dimensional lattices, in which only the even tunnelings are implemented. In this situation, the atom cloud is loaded at the four sites at the edges of the two one-dimensional lattices [see Fig. 11.7(b)]. Then the odd tunneling terms are connected and adiabatically increased up to some value smaller than the even tunneling amplitudes. At this point, each ladder leg is a realization of the SSH mode, and the initial atoms are know occupying the edge states of such model [see Fig. 11.7(c)]. Afterwards, the diagonal couplings must be switched on

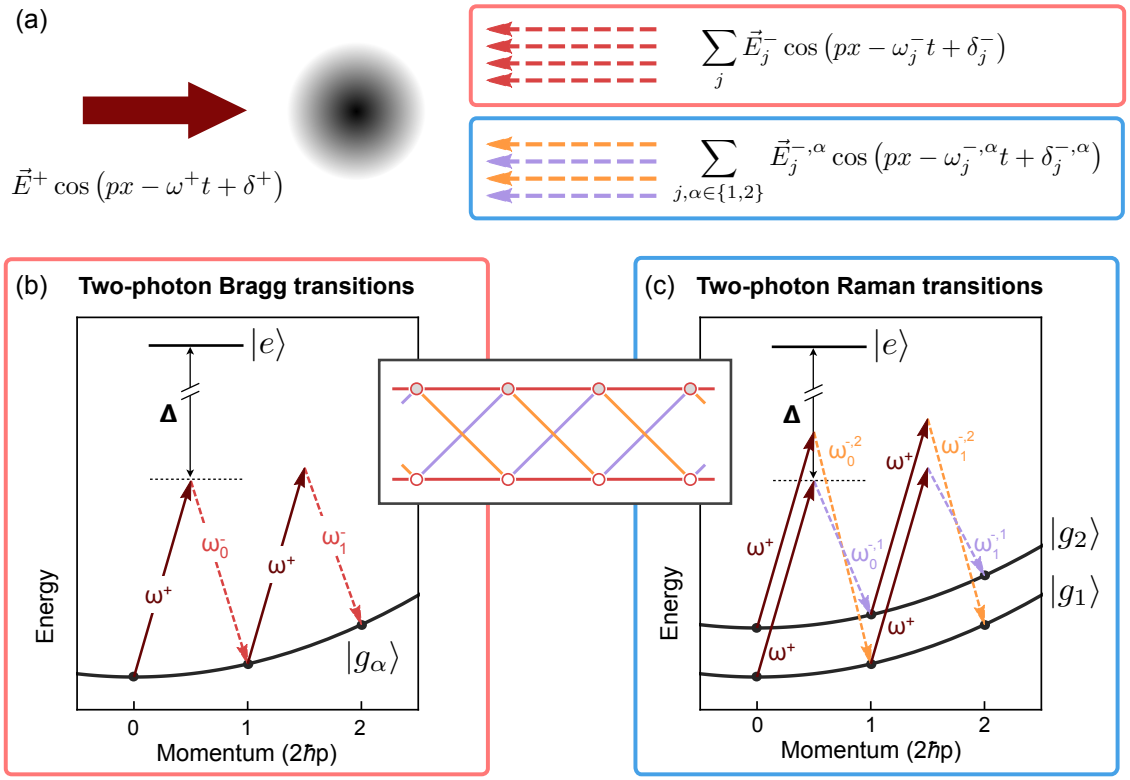

Figure 11.6: **Experimental scheme.** The experimental setup uses atoms with two low energy internal states $|g_1\rangle$ and $|g_2\rangle$, and an excited state $|e\rangle$.(a) The atomic cloud is driven by two counterpropagating laser fields. One of the laser fields is made of many different frequency components, being their phases, frequencies and amplitudes controllable. All laser fields are far detuned by Δ from atomic resonance between any of the low energy states and the excited state. (b) Two photon Bragg transitions, in which an atom absorbs or emits two photons, one from each counterpropagating laser field, couple states with a momentum difference of $2\hbar p$, while keeping the internal state of the atom invariant. This process generates a one-dimensional lattice of momentum states for each low energy state. Due to the quadratic dispersion relation of the atoms, each tunneling term in the lattice has a different resonance condition and thus, it is individually controlled by one of the left-moving laser field frequency components. On-site energy terms can also be introduced in this process. (c) Two photon Raman transitions allow for the implementation of couplings between different internal states. Since the resonance condition for each coupling is unique, they can be individually controlled by a single frequency component of the left-moving laser field. In this way, all terms in the hourglass ladder Hamiltonian can be implemented. The experimental scheme allows for the couplings to be complex, so that the effective magnetic flux ϕ can also be present in the experimental realization.

[see Fig. 11.7(d)], and finally, we can implement the on-site energies and make the even and odd horizontal tunneling amplitudes be the same [see Fig. 11.7(e)]. The

on-site energies can be implemented before or after making all horizontal tunneling amplitudes equal; the only requirement is that the diagonal couplings are already connected, otherwise the system would realize a non topological model with no edge modes and, thus, the prepared edge states would be destroyed.

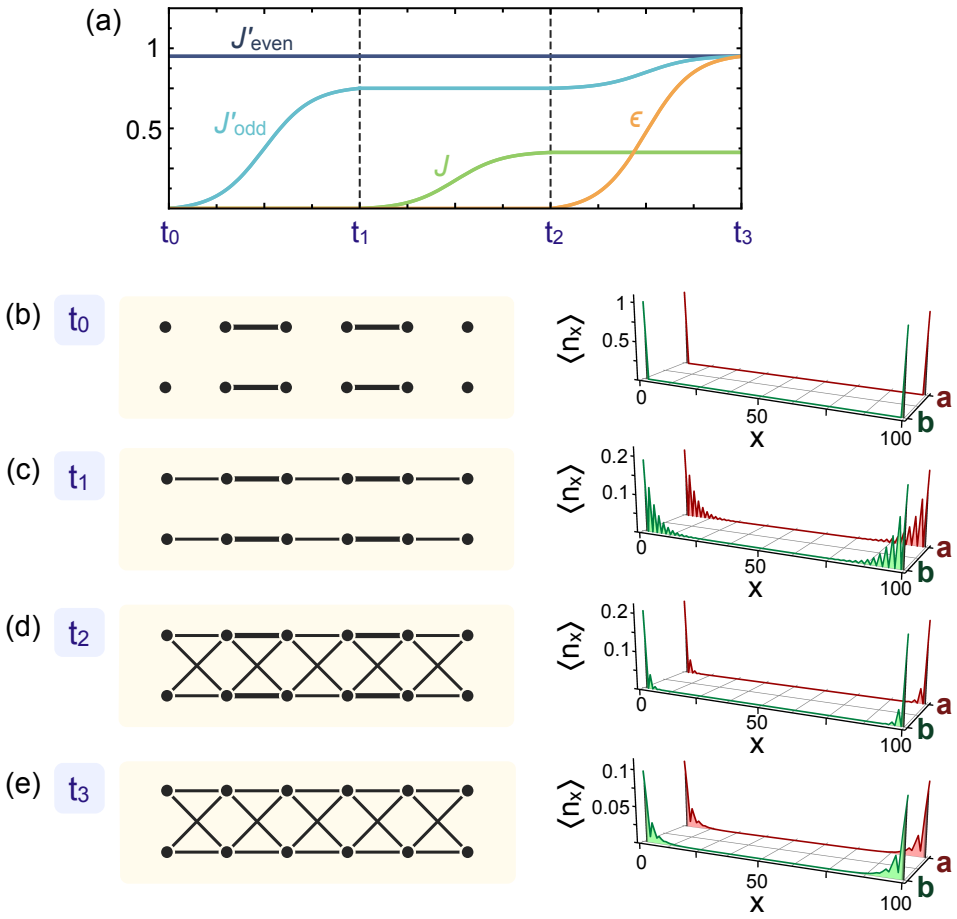

Figure 11.7: **Adiabatic preparation of the edge states.** In order to prepare the edge states of the Hamiltonian, we need to switch on each parameter of the model in a different step (a). First, only the even horizontal couplings are connected, and the atom cloud is loaded in the four edge sites (b). Then, the odd tunneling amplitudes are increased from zero to a certain value, so that each leg of the ladder realizes the SSH model (c). After that, the diagonal couplings need to be implemented (d) and, finally, the on-site energies are added and all horizontal tunneling amplitudes are set to the same value. Here we show the edge states spatial density distribution for each step. Parameters values are: (b) $J'_{\text{even}} = 0.95$ and $J'_{\text{odd}} = \epsilon = J = 0$; (c) $J'_{\text{even}} = 0.95$, $J'_{\text{odd}} = 0.75$ and $\epsilon = J = 0$; (d) $J'_{\text{even}} = 0.95$, $J'_{\text{odd}} = 0.75$, $J = 0.35$ and $\epsilon = 0$; and (e) $J'_{\text{even}} = J'_{\text{odd}} = \epsilon = 0.95$ and $J = 0.35$.

Summary and conclusions

The purposes of these thesis were, on one hand, to propose a one-dimensional model for a topological insulator in the AIII symmetry class, to find the properties that characterize it and distinguish it from the BDI class, and to open a new path for the observation of the phenomenon of fractionalization in one-dimensional topological insulators. On the other hand, we planned to extend our study of one-dimensional topological insulators and study also models with ladder structure. Our purposes regarding these second issue were: to know what is necessary for a ladder model to be topologically non trivial and what are the ingredients needed for it to belong to the BDI class or to the AIII class, to find all ladder architectures that realize a model for a topological insulator, and to know what kind of edge states can be found in a ladder model.

We have proposed a model for a one-dimensional topological insulator in the AIII symmetry class, which lacks experimental realization. Our model consists of a generalization of the well-known SSH model, a representative of the BDI class. We have analysed the topological zero energy edge states of our model and we have obtained two interesting results. First, the edge states can be localized in momentum space, in addition to their good localization in position space at the edges of the system. Second, the well defined momentum of the edge states is different from zero in the AIII class, while it is necessarily zero in the BDI class, due to the presence of time reversal symmetry. Thus, edge states with a nonzero momentum represent a characteristic property of the AIII class.

Furthermore, we have shown that, due to the edge states momentum localization, the phenomenon of fractionalization occurs also in momentum space. We have designed an experimental scheme for the realization of our model with cold atoms in optical lattices and we have shown how the edge states momentum properties in the AIII class open a new possibility for the detection of fractionalization, which has not been yet observed in one-dimensional topological insulators.

Motivated by the results we had already obtained, we developed a quench protocol in order to prove dynamically the consequences of the simultaneous good definition of the edge states position and momentum. Surprisingly, this led to the interference of fractionalized quasiparticles. The quench consists of changing the Hamiltonian parameters so that the system is taken to its critical point. In this situation the energy bands of the system cross each other at a critical momentum,

around which the dispersion relation is almost linear. This, combined with the edge states momentum properties, makes them propagate along the system, while preserving their identity as fractionalized quasiparticles, and interfere with each other.

As a further step, we continued our study of one-dimensional topological insulators by considering models with ladder structure. We have made a deep and detailed analysis of topological two leg ladder models. We have obtained the general form of a topological ladder Hamiltonian in the BDI class, as well as the general form of a topological ladder Hamiltonian in the AIII class. We have provided a compact way of writing the Hamiltonian matrix of any topological ladder model. In this way, all information about the model is encoded in three vectors, being the symmetry properties of the Hamiltonian easily red from their geometrical relations.

We have analysed the structure of these general Hamiltonians and classified all topological ladder models into six types, being each of them characterized by a different configuration of Wilson fermions. Three of these types of topological ladder models belong to the BDI class and the other three to the AIII class. We have shown how all topological ladder models can be obtained by performing a unitary transformation onto a particular ladder architecture, which thus serves as a canonical model. We have explored all parameter space of such model and obtained the two different systematic ways in which a topological ladder model can break time reversal symmetry and thus belong to the AIII class, namely: by introducing a shift in the momentum-isospin correspondence and by adding effective magnetic fluxes.

Besides that, we have obtained the wave function of the topological edge states of a general topological ladder model, and found an interesting connection between the edge states of a topological ladder and the set of Wilson fermions described by the model. On one hand, the edge states of a topological ladder model are made of several momentum components, corresponding each of them to a different Wilson fermion. On the other hand, the relative weights of each momentum component in the edge states wave function is directly related to the mass of the associated fermion. In this way, the six different types of topological ladder models result in six distinct types of edge states, which are characterized by their momentum density distributions.

Finally, we have provided a complete list with all ladder architectures that represent a model for a topological insulator. For each of them, we have specified which parameter configurations correspond to the BDI class and which to the AIII class.

After our analysis of topological ladder models we decided to focus on a particular ladder geometry, whose features lead to an interesting phenomenon: the emergence of protected chiral currents. The model consists of a two-leg ladder subjected to a magnetic field, which is implemented in the model by means of complex diagonal couplings that result in an effective magnetic flux. In the presence of such magnetic flux the model breaks time reversal symmetry, while preserving its chiral symmetry, and thus belongs to the AIII symmetry class.

We have designed a quench protocol that makes the edge states propagate along the system nearly without dissipation. This dynamics is a consequence of the combination of two ingredients: the edge states simultaneous position and momentum localizations, and the almost linear dispersion relation at precisely the location of the edge states in momentum space. Furthermore, the currents generated in this process are chiral when there is an effective magnetic flux penetrating the ladder, what is a manifestation of the AIII symmetry class. In addition, these chiral currents stay in the ladder for quite long evolution times and it is possible to recover the initial edge states by performing the inverse quench any time the currents reach the edges of the ladder, what stands for a protection feature.

In conclusion, we have carried out a quite complete analysis of one-dimensional topological insulators, both with dimerized lattice structure and with ladder geometry. Our results include a list of all topological ladder models and all types of edge states to which they can give rise, providing a way of characterizing the symmetry class of a ladder model through their edge states momentum density distributions. Moreover, we have designed protocols that allow us to prove the topological protection of edge states, as well as their chirality under an effective magnetic flux, through quench dynamics.

Resumen y conclusiones

Los objetivos de esta tesis consistían, por un lado, en: proponer un modelo de aislante topológico unidimensional en la clase de simetría AIII, identificar sus propiedades características que lo diferencian de un modelo en la clase BDI, y abrir un nuevo camino hacia la observación del fenómeno de fraccionalización en aislantes topológicos unidimensionales. Por otro lado, planeamos ampliar nuestro estudio de aislantes topológicos unidimensionales y estudiar también modelos con estructura de escalera. Nuestros objetivos, en relación a este segundo asunto, eran: conocer qué requiere un modelo de escalera para ser topológicamente no trivial y qué elementos son necesarios para que pertenezca a la clase de simetría BDI o a la clase de simetría AIII, encontrar todas las arquitecturas de escalera que representan un modelo de aislante topológico, y conocer cuáles son las características de los estados de borde que pueden ser encontrados en este tipo de modelos.

Hemos propuesto un modelo de aislante topológico unidimensional en la clase de simetrlía AIII, la cual aún no ha sido realizada experimentalmente. Nuestro modelo consiste en una generalizacilón del ampliamente conocido modelo SSH, que es un representante de la clase BDI. Hemos analizado los estados de borde topológicos presentes en el modelo y hemos obtenido dos resultados interesantes. Por un lado, los estados de borde pueden estar localizados en el espacio de momentos, además de estar bien localizados en el espacio de posiciones en los extremos del sistema. De este modo, podemos decir que los estados de borde presentan un cierto momento, estando este bien definido. Por otro lado, su momento es diferente de cero en la clase AIII, lo cual no es posible en la clase BDI, debido a la presencia de simetría de inversión temporal. Esto quiere decir que la presencia de estados de borde con un momento diferente de cero representa una propiedad caracterlística de la clase AIII.

Además, la buena definición del momento de los estados de borde hace posible que el fenómeno de fraccionalización también tenga lugar en el espacio de momentos. Hemos diseñado un procedimiento experimental que permite la realización de nuestro modelo con átomos fríos en redes ópticas y hemos mostrado cómo las propiedades de los estados de borde en el espacio de momentos características de la clase AIII abren una nueva alternativa para la observación del fenómeno de fraccionalización, que todavía no ha sido detectado en aislantes topológicos unidimensionales.

Motivados por los resultados obtenidos, hemos analizado cómo la localización de los estados de borde en los espacios de posiciones y de momentos se puede man-

ifestar a través de la dinámica de los estados de borde tras un quench. Esto es, realizar el Hamiltonian del sistema y preparar los estados de borde, de tal manera que se mantienen constantes al ser estados propios del modelo, modificar de manera abrupta algún parámetro del sistema y dejar que los estados de borde evolucionen bajo el nuevo Hamiltoniano. En particular, hemos diseñado un quench en el que tiene lugar una interferencia de cuasipartículas. Dicho quench consiste en cambiar una de las amplitudes de salto de la red de tal manera que el sistema pase a encontrarse en su punto crítico. En esta situación, las bandas de energía se cortan en un momento crítico, en torno al cual la relación de dispersión es aproximadamente lineal. Esto, junto con las propiedades de localización de los estados de borde, hace que estos se propaguen a lo largo del sistema preservando su identidad de cuasipartículas fraccionalizadas, e interfieran entre ellos.

Posteriormente, hemos continuado nuestro estudio sobre aislantes topológicos unidimensionales considerando modelos con estructura de escalera. Hemos obtenido la forma general del Hamiltoniano de un modelo de escalera topológico en la clase BDI, así como del Hamiltonian de un modelo de escalera topológico en la clase AIII. Nuestro estudio proporciona una manera compacta de escribir el Hamiltoniano de cualquier modelo de escalera en la que toda la información del sistema se encuentra contenida en tres vectores, cuyas relaciones geométricas permiten conocer fácilmente las propierdades de simetría del modelo.

Hemos analizado la estructura de estos Hamiltonianos generales y clasificado todos los modelos topológicos de escalera en seis tipos diferentes, estando cada uno de ellos caracterizado por una configruación distinta de fermiones de Wilson. Tres de estos tipos de modelos pertenecen a la clase BDI, mientras que los otros tres pertenecen a la clase AIII. En nuestro trabajo, hemos presentado un modelo topológico de escalera canónico, a partir del cual se puede obtener cualquier otro modelo de escalera topológico mediante la aplicación de una transformación unitaria. Analizando el espacio de parámetros de dicho modelo canónico, hemos descubierto que hay dos formas sistemáticas en las que un modelo de escalera topológico puede romper la simetría de inversión temporal y, por tanto, pertenecer a la clase AIII. Por un lado, mediante la introducción de un desfase en la relación entre el momento y el isospín, presente en la matriz del Hamiltoniano, y por otro lado, mediante la presencia de flujos magnéticos efectivos en el sistema.

Por otra parte, hemos obtenido la función de onda de los estados de borde de un modelo topológico de escalera general, y encontrado una interesante conexión entre los estados de borde de un modelo de escalera topológico y el conjunto de fermiones de Wilson descritos por el modelo. Por un lado, los estados de borde están formados por varias componentes de momento, correspondiendo cada una de ellas a un fermión de Wilson diferente. Por otro lado, los pesos relativos de cada componente en la función de onda de los estados de borde está directamente relacionada con las masas de los fermiones asociados. De esta manera, los seis tipos diferentes de modelos de escalera topológicos dan lugar a seis tipos diferentes de estados de borde, caracterizados por sus distribuciones de densidad en el espacio de

momentos.

Por último, hemos presentado una lista completa de todas las arquitecturas de escalera que representan un modelo de aislante topológico. Para cada una de ellas, hemos especificado qué configuraciones de parámetros dan lugar a un modelo en la clase BDI, y cuáles a un modelo en la clase AIII.

Tras completar nuestro análisis sistemático de modelos de escalera topológicos, decidimos estudiar en mayor detalle una geometría de escalera concreta, cuyas características dan lugar a la aparición de corrientes quirales protegidas. El modelo consiste en una escalera sometida a un campo magnético, implementado a través de términos de acoplo diagonales complejos que dan lugar a un flujo magnético efectivo. En la presencia de dicho flujo, el modelo rompe la simetría de inversión temporal, manteniendo la symetría quiral, y por tanto pertenece a la clase AIII.

Hemos diseñado un protocolo de quench en el que los estados de borde se propagan a lo largo del sistema prácticamente sin disipación. Esta dinámica es la consecuencia de la combinación de dos ingredientes: la simultánea buena localización de la posición y el momento de los estados de borde, y una relación de dispersión aproximadamente lineal en torno al momento en el que se encuentran los estados de borde en el espacio de momentos. Las corrientes que se generan en este proceso son quirales cuando el modelo está sometido a un flujo magnético efectivo, lo que representa una manifestación de la clase de simetría AIII. Además, estas corrientes permanecen en el sistema durante largos tiempos de evolución, siendo posible recuperar los estados de borde iniciales invirtiendo el quench en cualquier momento en el que las corrientes alcanzan los extremos del sistema, lo que representa una propiedad de protección.

En conclusión, hemos llevado a cabo un análisis bastante completo sobre aislantes topológicos unidimensionales, tanto con estructura de red dimerizada como de escalera. Nuestros resultados incluyen una lista con todos los modelos de escalera topológicos y todos los tipos de estados de borde a los que dichos modelos pueden dan lugar, proporcionando una manera de caracterizar la clase de simetría de un modelo de escalera a través de la distribución de momentos de los estados de borde. Además, hemos diseñado procedimientos para probar la protección topológica de los estados de borde, así como su quiralidad bajo un campo magnético efectivo, mediante su dinámica tras un quench.

Aknowledgements

This research was funded by the grant BES-2013-064443 of the Spanish MINECO, as well as by the Deutsche Forschungsgemeinschaft (DFG, German Research Foundation) via Research Unit FOR 2414 under project number 277974659.

Appendix A: Chiral symmetry and time reversal conditions

In order to prove the conditions for chiral symmetry, 5.6 and 5.7, and for T symmetry, 5.10 and 5.11, we first show two useful results. We consider a general 2×2 hermitian matrix H and a genaral 2×2 unitary matrix U, which can be written as:

$$H = \alpha\mathbb{I} + \beta\,\boldsymbol{n}\cdot\boldsymbol{\sigma} \tag{11.30}$$

$$U = e^{i\varphi}\left(\cos\frac{\theta}{2}\mathbb{I} + i\sin\frac{\theta}{2}\boldsymbol{m}\cdot\boldsymbol{\sigma}\right), \tag{11.31}$$

where $\boldsymbol{n}$ and $\boldsymbol{m}$ are unit vectors in $\mathbb{R}^3$, α and β are two real numbers, θ an angle and φ a global phase. We compute the transformation of H under U and get:

$$UHU^\dagger = \alpha\mathbb{I} + \beta\,\boldsymbol{n'}\cdot\boldsymbol{\sigma}, \tag{11.32}$$

with $\boldsymbol{n'} = \cos\theta\,\boldsymbol{n} - \sin\theta\,\boldsymbol{m}\times\boldsymbol{n} + 2\sin^2\frac{\theta}{2}(\boldsymbol{m}\cdot\boldsymbol{n})\,\boldsymbol{m}$. We are interested in those unitary transformations that leave H invariant and those that produce a change in its sign. In the second case we want that $UHU^\dagger = -H$. Comparing 11.30 and 11.32 we see that this implies: $\alpha = 0$ and $\boldsymbol{n'} = -\boldsymbol{n}$. If $\boldsymbol{m}$ is codirectional to $\boldsymbol{n}$, $\boldsymbol{n'} = \boldsymbol{n}$ and there is no solution. Otherwise the set $\{\,\boldsymbol{n}, \boldsymbol{m}, \boldsymbol{m}\times\boldsymbol{n}\,\}$ constitutes a basis of $\mathbb{R}^3$ and we can get the solution by comparing coefficients, getting three equations:

$$\cos\theta = -1 \tag{11.33}$$

$$2\sin^2\frac{\theta}{2}\,\boldsymbol{m}\cdot\boldsymbol{n} = 0 \tag{11.34}$$

$$\sin\theta = 0. \tag{11.35}$$

The only solution to them is $\theta = \pi$ and $\boldsymbol{m}\cdot\boldsymbol{n} = 0$, so we get the following result. *Result 1*: given a 2×2 hermitian matrix H, there exists a unitary transformation U such that $UHU^\dagger = -H$ if and only if $H = \beta\,\boldsymbol{n}\cdot\boldsymbol{\sigma}$. Moreover, the unitary transformation U has the form $U = e^{i\varphi}\,\boldsymbol{m}\cdot\boldsymbol{\sigma}$ for any φ and being $\boldsymbol{m}$ such that $\boldsymbol{m}\cdot\boldsymbol{n} = 0$.

On the other hand, for H to be invariant under U we need that $\mathbf{n}' = \mathbf{n}$, which is

the case if $\boldsymbol{m}$ is codirectional to $\boldsymbol{n}$. Otherwise we have that:

$$\cos\theta = 1 \tag{11.36}$$

$$2\sin^2\frac{\theta}{2}\,\mathbf{m}\cdot\mathbf{n} = 0 \tag{11.37}$$

$$\sin\theta = 0, \tag{11.38}$$

whose only solution is $U = e^{i\varphi}\mathbb{I}$. As a consequence we obtain the second result. *Result 2*: given a 2×2 hermitian matrix $H = \alpha\mathbb{I} + \beta\,\boldsymbol{n}\cdot\boldsymbol{\sigma}$, the only unitary transformations U such that $UHU^\dagger = H$ are those with the form $U = e^{i\varphi}\left(\cos\frac{\theta}{2}\mathbb{I} + i\sin\frac{\theta}{2}\boldsymbol{n}\cdot\boldsymbol{\sigma}\right)$.

Now we can easily derive the chiral conditions 5.6 and 5.7 and the T conditions 5.10 and 5.11. The Hamiltonian matrix of a general ladder model is:

$$M(k) = \lambda(k)\mathbb{I} + (\boldsymbol{n}_0 + \boldsymbol{n}_c\cos k + \boldsymbol{n}_s\sin k)\cdot\boldsymbol{\sigma}, \tag{11.39}$$

Using *result 1* we see that the Hamiltonian matrix fulfils the chiral condition (7) only if $\lambda(k) = 0$ and there exists a vector $\boldsymbol{a}$ such that $\boldsymbol{a}\cdot(\boldsymbol{n}_0 + \boldsymbol{n}_c\cos k + \boldsymbol{n}_s\sin k) = 0 \quad \forall k$. Therefore, the model will be chiral symmetric if the vectors $\boldsymbol{n}_0$, $\boldsymbol{n}_c$ and $\boldsymbol{n}_s$ lie in a common plane.

The model has T symmetry (condition 5) if there is a unitary transformation U_T such that $U_T\,M(-k)^\dagger U_T^\dagger = M(-k)$. Using $\boldsymbol{\sigma}^* = -\sigma_y\boldsymbol{\sigma}\sigma_y$ and defining $\widetilde{U}_T = U_T\sigma_y$, this implies:

$$\widetilde{U}_T\,(\boldsymbol{n}_0\cdot\boldsymbol{\sigma})\,\widetilde{U}_T^\dagger = -\boldsymbol{n}_0\cdot\boldsymbol{\sigma} \tag{11.40}$$

$$\widetilde{U}_T\,(\boldsymbol{n}_c\cdot\boldsymbol{\sigma})\,\widetilde{U}_T^\dagger = -\boldsymbol{n}_c\cdot\boldsymbol{\sigma} \tag{11.41}$$

$$\widetilde{U}_T\,(\boldsymbol{n}_s\cdot\boldsymbol{\sigma})\,\widetilde{U}_T^\dagger = \boldsymbol{n}_s\cdot\boldsymbol{\sigma}. \tag{11.42}$$

For the first two equations to be fulfilled, using *result 1*, the unitary transformation $\widetilde{U}_T$ must have the form $\widetilde{U}_T = \boldsymbol{b}\cdot\boldsymbol{\sigma}$ with $\boldsymbol{b}\cdot\boldsymbol{n}_0 = \boldsymbol{b}\cdot\boldsymbol{n}_c = 0$. However, from the last equation, using *result 2*, $\boldsymbol{b}$ must be proportional to $\boldsymbol{n}_s$, therefore the condition for time reversal symmetry is fulfilled if: $\boldsymbol{n}_s\cdot\boldsymbol{n}_0 = \boldsymbol{n}_s\cdot\boldsymbol{n}_c = 0$. In other words, the even and odd components of the Hamiltonian matrix must be perpendicular to each other for the system to exhibit time reversal symmetry.

Bibliography

[1] R. Jackiw and C. Rebbi, Solitons with fermion number 1/2, *Phys. Rev. D* **13**, 3398 (1976).

[2] J. Goldstone and F. Wilczek, Fractional quantum numbers of solitons, *Phys. Rev. Lett.* **47**, 986 (1981).

[3] W. P. Su, J. R. Schrieffer and A. J. Heeger, Solitons in polyacetylene, *Phys. Rev. Lett.* **42**, 1698 (1979).

[4] S. A. Kivelson, Electron fractionalization, *Synthetic Metals* **125**, 99 (2002).

[5] M. J. Rice and E. J. Mele, Elementary excitations of a linearly conjugated diatomic polymer, *Phys. Rev. Lett.* **49**, 1455 (1982).

[6] A. J. Heeger, S. Kivelson, J. R. Schrieffer and W. P. Su, Solitons in conducting polymers, *Rev. Mod. Phys.* **60**, 781 (1988).

[7] M. Z. Hasan and C. L. Kane, *Colloquium*: Topological insulators, *Rev. Mod. Phys.* **82**, 3045 (2010).

[8] X.-L. Qi and S.-C. Zhang, Topological insulators and superconductors, *Rev. Mod. Phys.* **83**, 1057 (2011).

[9] J. Zak, Berry's phase for energy bands in solids, *Phys. Rev. Lett.* **62**, 2747 (1989).

[10] S. Ryu and Y. Hatsugai, Topological origin of zero-energy edge states in particle-hole symmetric systems, *Phys. Rev. Lett.* **89**, 077002 (2002).

[11] J. C. Y. Teo and C. L. Kane, Topological defects and gapless modes in insulators and superconductors, *Phys. Rev. B* **82**, 115120 (2010).

[12] P. Delplace, D. Ullmo and G. Montambaux, Zak phase and the existence of edge states in graphene, *Phys. Rev. B* **84**, 195452 (2011).

[13] A. Altland and M. R. Zirnbauer, Nonstandard symmetry classes in mesoscopic normal-superconducting hybrid structures, *Phys. Rev. B* **55**, 1142 (1997).

[14] A. P. Schnyder, S. Ryu, A. Furusaki and A. W. W. Ludwig, Classification of topological insulators and superconductors in three spatial dimensions, *Phys. Rev. B* **78**, 195125 (2008).

[15] S. Ryu, A. P. Schnyder, A. Furusaki and A. W. W. Ludwig, Topological insulators and superconductors: ten-fold way and dimensional hierarchy, *New J. Phys.* **12**, 065010 (2010).

[16] I. Bloch, J. Dalibard and W. Zwerger, Many-body physics with ultracold gases, *Rev. Mod. Phys.* **80**, 885 (2008).

[17] W. S. Bakr, J. I. Gillen, A. Peng, S. Fölling and M. Greiner, A quantum gas microscope for detecting single atoms in a Hubbard-regime optical lattice, *Nature* **462**, 74 (2009).

[18] J. F. Sherson, C. Weitenberg, M. Endres, M. Cheneau, I. Bloch and S. Kuhr, Single-atom-resolved fluorescence imaging of an atomic Mott insulator, *Nature* **467**, 68 (2010).

[19] I. Bloch J. Dalibard and S. Nascimbène, Quantum simulations with ultracold quantum gases, *Nat. Phys.* **8**, 267 (2012).

[20] M. Atala, M. Aidelsburger, J. T. Barreire, D. Abanin, T. Kitagawa, E. Demler and I. Bloch, Direct measurement of the Zak phase in topological Bloch bands, *Nat. Phys.* **9**, 795 (2013).

[21] E. J.Meier, F. A. An and B. Gadway, Observation of the topological soliton state in the Su-Schrieffer-Heeger model, *Nat. Commun.* **7**, 13986 (2016).

[22] C. G. Velasco and B. Paredes, Realizing and detecting a topological insulator in the AIII symmetry class, *Phys. Rev. Lett.* **119**, 115301 (2017).

[23] M. Creutz, End states, ladder compounds, and domain-wall fermions, *Phys. Rev. Lett.* **83**, 2636 (1999).

[24] J. Jünemann, A. Piga, S.-J. Ran, M. Lewenstein, M. Rizzi and A. Bermudez, Exploring interacting topological insulators with ultracold atoms: the synthetic Creutz-Hubbard model, *Phys. Rev. X* **7**, 031057 (2017).

[25] S. Gholizadeh, M. Yahyavi and B. Hetényi, Extended Creutz ladder with spin-orbit coupling: a one dimensional analog of the Kane-Mele model, *EPL*, **122**, 27001 (2018).

[26] O. Boada, A. Celi, J. I. Latorre and M. Lewenstein, Quantum simulation of an extra dimension, *Phys. Rev. Lett.* **108**, 133001 (2012).

[27] A. Celi, P. Massignan, J. Ruseckas, N Goldman, I. B. Spielman, G. Juzeliūnas and M. Lewenstein, Synthetic gauge fields in synthetic dimensions, *Phys. Rev. Lett.* **112**, 043001 (2014).

[28] Y.-J. Lin, K. Jiménez-García and I. B. Spielman, Spin-orbit-coupled Bose-Einstein condensates, *Nature* **471**, 83 (2011).

[29] L. W. Cheuk, A. T. Sommer, Z. Hadzibabic, T. Yefsah, W. S. Bakr, and M. W. Zwierlein, Spin-injection spectroscopy of a spin-orbit coupled Fermi gas, *Phys. Rev. Lett.* **109**, 095302 (2012).

[30] V. Galitski and I. B. Spielman, Spin-orbit coupling in quantum gases, *Nature* **494**, 49 (2013).

[31] D. Hügel and B. Paredes, Chiral ladders and the edges of quantum Hall insulators, *Phys. Rev. A* **89**, 023619 (2014).

[32] M. Aidelsburger, M. Atala, S. Nascimbène, S. Trotzky, Y.-A. Chen and I. Bloch, Experimental realization of strong effective magnetic fields in an optical lattice, *Phys. Rev. Lett.* **107**, 255301 (2011).

[33] M. Aidelsburger, M. Atala, M. Lohse, J. T. Barreiro, B. Paredes and I. Bloch, Realization of the Hofstadter Hamiltonian with ultracold atoms in optical lattices, *Phys. Rev. Lett.* **111**, 185301 (2013).

[34] M. Atala, M. Aidelsburger, M. Lohse, J. T. Barreiro, B. Paredes and I. Bloch, Observation of chiral currents with ultracold atoms in bosonic ladders, *Nat. Phys.* **10**, 588 (2014).

[35] M. Mancini, G. Pagano, G. Cappellini, L. Livi, M. Rider, J. Catani, C. Sias, P. Zoller, M. Inguscio, M. Dalmonte and L. Fallani, Observation of chiral edge states with neutral fermions in synthetic Hall ribbons, *Science* **349**, 1510 (2015).

[36] B. K. Stuhl, H.-I. Lu, L. M. Aycock, D. Genkina and I. B. Spielman, Visualizing edge states with an atomic Bose gas in the quantum Hall regime, *Science* **349**, 1514 (2015).

[37] L. F. Livi, G. Cappellini, M. Diem, L. Franchi, C. Clivati, M. Frittelli, F. Levi, D. Calonico, J. Catani, M. Inguscio and L. Fallani, Synthetic dimensions and spin-orbit coupling with an optical clock transition, *Phys. Rev. Lett.* **117**, 220401 (2016).

[38] F. A. An, E. J. Maier and B. Gadway, Direct observation of chiral currents and magnetic reflection in atomic flux lattices, *Sci. Adv.* **3**, e1602685 (2017).

[39] E. Anisimovas, M. Račiūnas, C. Sträter, A. Eckardt, I. B. Spielman and G. Juzeliūnas, Semisynthetic zigzag optical lattice for ultracold bosons, *Phys. Rev. A* **94**, 063632 (2016).

[40] F. A. An, E. J. Maier and B. Gadway, Engineering a flux-dependent mobility edge in disordered zigzag chains, *Phys. Rev. X* **8**, 031045 (2018).

[41] M. Stone, Elementary derivation of one-dimensional fermion-number fractionalization, *Phys. Rev. B* **31**, 6112 (1985).

[42] A. L.Niemi, G. W. Semenoff, Fermion number fractionalization in quantum field theory, *Phys. Reports* **135**, 99 (1986).

[43] M. Creutz and I. Horváth, Surface states and chiral symmetry on the lattice, *Phys. Rev. D* **50**, 2297 (1994).

[44] M. Creutz, Aspects of chiral symmetry and the lattice, *Rev. Mod. Phys.* **73**, 119 (2001).

[45] K. Wilson, in *New Phenomena in Subnuclear Physics*, edited by A. Zichichi (Plenum, New York, 1977).

[46] B. Gadway, Atom-optics approach to studying transport phenomena, *Phys. Rev. A* **92**, 043606 (2015).

[47] E. J. Meier, F. A. An and B. Gadway, Atom-optics simulator of lattice transport phenomena, *Phys. Rev. A* **93**, 051602 (2016).